

**MODELING STUDIES OF ATMOSPHERIC PRESSURE MICROPLASMAS:
PLASMA DYNAMICS, SURFACE INTERACTION AND APPLICATIONS**

by
Jun-Chieh Wang

A dissertation submitted in partial fulfillment
of the requirements for the degree of
Doctor of Philosophy
(Electrical Engineering)
in the University of Michigan
2014

Doctoral Committee:

Professor Mark J. Kushner, Chair
Professor John E. Foster
Professor Brian E. Gilchrist
Professor Yogesh B. Gianchandani
Professor Euisik Yoon

*To those who always stand behind me,
Thanks for your continued support and encouragement.
To those who stick by me through tough times,
I cannot accomplish any of these on my own.*

ACKNOWLEDGEMENTS

Five years has gone so fast. It feels like I just came here as a newbie yesterday, felt excited about everything I saw and everyone I met, and all of a sudden, I am standing here bragging about my research and begging for a PhD degree. It seems crazy that one thing just leads to another like it was planned way before I was born. In fact, none of these can be done without a great deal of assistance and support from all of my family, professors, collaborators and friends.

In some particular order, I would like to thank my parents. It's impossible to thank them adequately for everything they have done and sacrificed for me from raising me in a stable household to unconditionally loving me.

A great deal of credit is due to my dissertation committee: Professor John E. Foster, Professor Yogesh B. Gianchandani, Professor Euisik Yoon, and Professor Brian Gilchrist for serving on my committee and all the insightful comments they provide me throughout the process; this work will not be possible without their help.

To my current and former labmates: Juline Shoeb, Mingmei Wang, Michael Logue, Seth Norberg, Sang-Heon Song, Pen Tian, Wei Tian, Yiting Zhang; your companionship is invaluable. Special thanks go to Dr. Zhongmin Xiong and Dr. Natalia Babaeva for all the guidance and useful conversation we had; thanks to Yan Yang for serving as a good example for me; and Julia for helping me through all the processes and paper work. I would also like to acknowledge my collaborators at HP Lab: Daihua Zhang, Henryk Birecki, Michael Lee, Napoleon Leoni, Omer Gila, Seongsik Chang, and Tom Anthony; and graduate students at Prof. Gianchandani's group:

Christine Eun and Xin Luo, who have contributed greatly to the development, fabrication, testing and validation of the devices that we are interested. I appreciate this great opportunity to work with them on such challenging and interesting topics.

I would like to extend my gratitude to my teachers at the National Cheng Kung University: Prof. Kuan-Ren Chen, Prof. Sunny Wing-Yee Tam, Prof. Ker-Chung Shaing, Prof. C. Z. Frank Cheng and Prof. Jang-Yu Hsu. Your training and lectures not only broadened my horizons, but also equipped me with the necessary knowledge and skills to pursue my research career.

I also wish to thank all my wonderful friends for being always right behind me. It was at times a long, difficult road, but I am glad it was long and difficult because if I hadn't gone through it to get there, the memories and lessons might not be so clear. I will cherish all the great moments we shared: stupid drinking game at parties, BBQs at Gallup Park, studying at library, every Christmas Eve and sleepy Sunday afternoon-I will carry that with me.

I have saved the best for last: I would like to express my deepest gratitude to my research supervisor, Prof. Mark Kushner who has supported and encouraged me for all these years. Mark is always actively involved in the work of all his students. Time after time, his easy grasp of physics at its most fundamental level helped us in the struggle for understanding. As a successful and world-leading scientist, Mark is still the most diligent and enthusiastic researcher than everyone I know. Day and night, weekday and weekend, he is always passionate, hardworking and eager about making a positive contribution to this society. Just when I thought that comfort and luxury were the chief requirements of life, his passion for science and education reminds me that all we need to make us really happy is something to be enthusiastic about. I am fortunate to have him as my mentor, and I could not ask for a better supervisor and role-model.

TABLE OF CONTENTS

DEDICATION.....	ii
ACKNOWLEDGEMENTS	iii
LIST OF FIGURES	viii
ABSTRACT	xviii
CHAPTER 1 INTRODUCTION.....	1
1.1 Plasmas: The Fourth State of Matter.....	2
1.2 Plasmas: The Definition.....	3
1.3 Plasmas: 99% of the Entire Visible Universe	4
1.4 Townsend Breakdown.....	5
1.5 Spark Breakdown.....	7
1.6 Dielectric Barrier Discharge (DBDs).....	9
1.7 Microdischarges and Electrophotography.....	11
1.8 Microdischarge-based Pressure Sensor.....	13
1.9 Issues to Be Discussed	14
1.10 Figures.....	18
1.11 References.....	26
CHAPTER 2 DESCRIPTION OF THE MODEL	30
2.1 Introduction.....	30
2.2 Geometry, Mesh Generation, and Discretization.....	31
2.3 Interpolation of E/N	34
2.4 Plasma Dynamics.....	35
2.5 Transport Coefficients, Rate Coefficients, and Electron Temperature	40
2.6 Radiation Transport.....	43
2.7 Secondary Electrons and Field Emission.....	44
2.8 Monte Carlo Simulation.....	45
2.9 Parallel Implementation of EMCS.....	46
2.10 Figures.....	49
2.11 References.....	59
CHAPTER 3 ELECTRON CURRENT EXTRACTION FROM RADIO FREQUENCY EXCITED MICRO-DIELECTRIC BARRIER DISCHARGES	61

3.1	Introduction.....	61
3.2	Description of the Model and Reaction Mechanism.....	63
3.3	Plasma Dynamics and Current Extraction from the mDBD	65
3.4	Dielectric Charging Characteristics and Ionization Processes.....	69
3.5	Total Charge Collection.....	75
3.6	Concluding Remarks.....	78
3.7	Figures.....	80
3.8	References.....	96

CHAPTER 4 CHARACTERISTIC OF A RF MICRO-DIELECTRIC BARRIER DISCHARGE ARRAY..... 100

4.1	Introduction.....	100
4.2	Description of the Model and Reaction Mechanism.....	101
4.3	mDBD Plasma Properties	103
4.4	Small Arrays of mDBDs.....	104
4.5	Concluding Remarks.....	111
4.6	Figures.....	114
4.7	References.....	124

CHAPTER 5 CHARGING OF MOVING SURFACES BY CORONA DISCHARGES SUSTAINED IN AIR..... 126

5.1	Introduction.....	126
5.2	Description of the Model and Reaction Mechanism.....	129
5.3	Corona Properties and Charging of a Stationary Surface	131
5.4	Charging of a Moving Surface.....	136
5.5	Concluding Remarks.....	141
5.6	Figures.....	143
5.7	References.....	155

CHAPTER 6 ATMOSPHERIC PRESSURE MICRODISCHARGES PRODUCED BY CONDUCTIVE CHARGE ROLLER..... 158

6.1	Introduction.....	158
6.2	Description of the Model and Reaction Mechanism.....	161
6.3	Characteristics of Microplasmas and Charging of a Stationary PC Surface.....	163
6.4	Charging of a Moving Surface.....	170
6.5	Concluding Remarks.....	175
6.6	Figures.....	177
6.7	References.....	191

CHAPTER 7 SIMULATION OF MICRODISCHARGE-BASED PRESSURE SENSORS..... 193

7.1	Introduction.....	193
-----	-------------------	-----

7.2	Description of the Model and Reaction Mechanism.....	196
7.3	Plasma Dynamics in the Microdischarge Pressure Sensor.....	198
7.4	Periodic IW and Current Collection.....	200
7.5	Differential Current and External Pressure.....	202
7.6	Concluding Remarks.....	204
7.7	Figures.....	206
7.8	References.....	214
CHAPTER 8 SUMMARY AND FUTURE WORK		216
8.1	Summary and Future Work.....	216
8.2	Publications.....	221
APPENDIX: AUTHOR'S BIOGRAPHY.....		226

LIST OF FIGURES

Figure 1.1	Plasma can be characterized by electron density and temperature. Electron Debye length λ_D (constant along the dashed lines) and the number of charged particles in a Debye cube N_D (constant along solid lines) are also indicated in the figure.[5].....	18
Figure 1.2	Illustration of avalanche and Townsend breakdown.[12-13].....	19
Figure 1.3	The charge distribution and electric field in the gap (a) before and (b) after the avalanche reaches the anode. E_0 , E' , and E represent the applied electric field, the field produced by space charges, and the total field ($E = E_0 + E'$), respectively.[6,10-11].....	20
Figure 1.4	Schematics of a (a) cathode-directed (or positive) streamer and (b) anode-directed (or negative) streamer at t_1 and t_2 ($t_2 > t_1$). The anode-directed (or negative) streamer occurs in a longer gap.[6,10-11].....	21
Figure 1.5	A time evolution of DBDs between a pair of parallel electrodes biased with AC voltage. The DBD prevents the formation of an arc.	22
Figure 1.6	Elements of electrophotography (EP). (a) Six steps of EP printing.[43] (b) Surface charging by a charge roller (CR) and a corona discharge.	23
Figure 1.7	Schematic of ionography. (a) A typical printing head. (a) Printing process of ionography.....	24
Figure 2.1	Block diagram of nonPDPSIM.	49
Figure 2.2	Model geometry and unstructured mesh used for the simulation of microdischarge-based pressure sensor. The refinement zones are highlighted by red rectangles. ..	50
Figure 2.3	Control volume (CV) mesh and actual mesh. (a) The vertex-centered control volume is constructed by identifying the intersections of the perpendicular bisectors between a node and its nearest neighbors; the “cell corners” (A, B, C, D, E, or F) are defined as the intersections of the perpendicular bisectors. Actual mesh consists of vertices, faces, and cells. Nodes (no. 1–7) and solid lines which connect the nodes are output from the mesh generator. (b) The CV is centered around the vertex.	51

Figure 2.4	An example of the interpolation technique used to obtain electric field and E/N on an unstructured mesh.....	53
Figure 2.5	A schematic of the Newton-Raphson iterative method.....	54
Figure 2.6	Schematic of radiation transport. Seeding of electrons far away from the avalanche is produced by photons from excited species in the ionization. Both photoionization and photoemission (ϕ_s) from the surface result from photons emitted by species j	55
Figure 2.7	An electron Monte Carlo simulation is used to follow trajectories of secondary electrons from surfaces. The structured Cartesian mesh (CM) is overlaid onto the unstructured mesh (UM). The CM overlays only the portion of the UM in which beam electron transport is expected to be important. The resolution of the CM is chosen to be fine enough to capture the small scale feature of the UM.....	56
Figure 2.8	A schematic of original and optimized particle trajectory algorithms in the EMCS. In the original algorithm, particles are (a) first launched and from node 1. After all particles from node 1 are tracked and removed from EMCS domain, new particles are then released from (b) node 2 and then (c) node 3. The process repeats until particles are launched and recorded from all emission nodes. In the optimized algorithm (d), particles are simultaneously released from all emission nodes.....	57
Figure 2.9	The speedup and efficiency for (a) $N_p = 400$; and (b) $N_p = 40,000$ from each emission node.	58
Figure 3.1	Schematic of the cylindrical symmetric mDBD device. (a) Entire device and full computational domain. (b) Enlargement of mDBD cavity and location of sites A, B, C and D that are used to provide surface properties and ionization characteristics.....	80
Figure 3.2	Time evolution of electron density (log scale, cm^{-3}) and E/N (at the center of contour labels, Td) in the mDBD cavity at different phases of the rf driving voltage of 1.4 kV during a 40 ns (25 MHz) cycle. The cycle begins with 0 V on the buried rf electrode. The top electrode is biased with +2 kV. At high electron density, the electric field is shielded and E/N is reduced.	81
Figure 3.3	Electron density in the plume (log scale, cm^{-3}) in the gap at different phases of the rf driving voltage of 1.4 kV during a 40 ns (25 MHz) cycle.	82
Figure 3.4	Electron temperature (eV), electron impact ionization sources from bulk electrons (S_e) and ionization source by sheath accelerated secondary electrons (S_{sec}) in the mDBD cavity during a 40 ns (25 MHz) cycle for $V_{rf} = 1.4$ kV and extraction voltage of 2 kV. The ionization sources are plotted on a log scale.....	83

Figure 3.5	The total charge density, charge density due to positive ions and charge density due to electrons and negative ions (log scale cm^{-3}) in the mDBD cavity at different times during a 25 MHz cycle for $V_{rf} = 1.4$ kV and extraction voltage of 2 kV. Positive ions alternately strike the cathode-like negatively charged dielectric or discharge electrode and release secondary electrons for re-ignition.	84
Figure 3.6	Density of excited states $\text{N}_2(\text{C})$ and $\text{N}_2(\text{A,B})$ in the mDBD cavity (log scale, cm^{-3}) at different times during a 25 MHz cycle for $V_{rf} = 1.4$ kV and extraction voltage of 2 kV. UV photons emitted from excited states of nitrogen produce secondary electrons which aid in re-ignition of the plasma especially at low frequency.....	85
Figure 3.7	The surface charge density σ_S (dash-dotted, cm^{-3}), surface voltage on the dielectric (solid, V) and voltage on the buried rf electrodes (dashed, V) are shown for frequencies of a) 25, b) 5 and c) 2.5 MHz at site A (see Fig. 3.1) for $V_{rf} = 1.4$ kV and extraction voltage of 2 kV. Oscillations in charging of the dielectric appear at low frequencies.	86
Figure 3.8	mDBD characteristic are shown at site B as a function of time (see Fig. 3.1) for $V_{rf} = 1.4$ kV and extraction voltage of 2 kV for a) 25 MHz and b) 2.5 MHz: rf voltage (dashed, V), local potential (dash-dotted, V) and E/N (solid, Td), electron density (dash-dotted, cm^{-3}) and electron ionizations source S_e and S_{sec} (solid and dotted, $\text{cm}^{-3}\text{s}^{-1}$).	87
Figure 3.9	Current collection on the top electrode. a) Experimentally observed triple current pulsed obtained at 2.5 MHz and b) simulation results in a similar sandwich mDBD device for equivalent biasing.....	88
Figure 3.10	Charge density at site D and current collection on the top electrode at 25 MHz. a) Electron (solid, cm^{-3}) and positive ion density (dash, cm^{-3}) at site D for top bias voltage $V_{top} = 2, 1.5$ and 1 kV. b) Electron current collected by the top biased electrode for $V_{top} = 2, 1.5$ and 1 kV. A pulsed modulated dc current is collected at $V_{top} = 2$ kV.	89
Figure 3.11	Charge collection as a function of time for 25 MHz to 2.5 MHz (1.4 kV rf bias) and a 2 kV biased collection electrode. a) Charge collected per pulse and b) time integrated charge collection. Charge collection per pulse is relatively independent of frequency until positive charge builds up in the gap at the higher frequencies, which then transitions to a modulated dc discharge.....	90
Figure 3.12	Charge collection as a function of time for 25 MHz at $V_{rf} = 1.4, 2.8, 4.2$ and 5.6 kV and a 2 kV biased collection electrode.....	91

Figure 3.13	Charge collection as a function of time for 25 MHz at $V_{rf} = 1.4, 2.8, 4.2$ and 5.6 kV and a 2 kV biased collection electrode.....	92
Figure 3.14	Surface properties at site A and gas phase properties at site B as a function of time at 25 MHz for $V_{rf} = 1.4, 2.8, 4.2$ and 5.6 kV. The location is noted in each frame. a) Surface charge density and applied rf voltage, b) surface potential, c) E/N , d) electron density, e) ionization by bulk electrons and f) ionization by secondary electrons..	93
Figure 3.15	Charge collection/pulse and total charge collected by the top 2 kV biased electrode as a function of time for 25 MHz with $\epsilon/\epsilon_0=20, 10, 5$ and 2 with 1.4 kV on the rf electrode. The charge per pulse is normalized by $\epsilon_r = \epsilon/\epsilon_0$	94
Figure 3.16	Surface properties at site A and gas phase properties at sites B and C as a function of time at 25 MHz for $\epsilon/\epsilon_0=20, 10, 5$ and 2. The location is noted in each frame. a) Surface charge density normalized by ϵ_r and rf voltage, b) surface potential, c) E/N , d) electron density, e) ionization by bulk electrons and f) ionization by secondary electrons.	95
Figure 4.1	Schematic of the mDBD device. (a) A single mDBD single aperture. (b) Multiple mDBD apertures and top grounded electrode covered with dielectric.	114
Figure 4.2	Electron current extraction produced by an rf voltage of 25 MHz. (a) Time evolution of electron density (color flood, cm^{-3}) and electric potential (contour lines, V) during a 40 ns rf period. The electron density is plotted on a log-scale over 4 decades ($2 \times 10^{11} - 2 \times 10^{15} \text{ cm}^{-3}$). (b) Electron density (color flood, cm^{-3}), electric field (vector, $\text{V}\cdot\text{cm}^{-1}$) and potential (contour lines, V) at $t = 13.5$ ns when electrons are extracted. (c) rf driving voltage. The instantaneous electric field vectors show only the orientation but not the magnitude of the field which help extract and focus the electron beam.	115
Figure 4.3	mDBD array with a spacing of 300 μm and target dielectric constant of $\epsilon/\epsilon_0 = 1.25$. Electron density (color flood, cm^{-3}) and electric potential (contour lines, V) at the peak of electron current extraction for the (a) 1 st , (b) 3 rd , (c) 5 th , (d) 7 th and (e) 12 th rf pulse. The electron density is plotted on a log-scale over 4 decades ($2 \times 10^{11} - 2 \times 10^{15} \text{ cm}^{-3}$). The electron plume is largely warped toward less charged dielectric by the 12 th pulse.....	116
Figure 4.4	mDBD array with spacing of 300 μm and larger target dielectric constant $\epsilon/\epsilon_0 = 12.5$. Electron density (color flood, cm^{-3}) and electric potential (contour lines, V) at the peak of electron current extraction for the (a) 1 st , (b) 3 rd , (c) 5 th , (d) 7 th and (e) 12 th rf pulse. The electron density is plotted on a log-scale over 4 decades ($2 \times 10^{11} - 2$	

	$\times 10^{15} \text{ cm}^{-3}$). Divergence of the current begins later due to the longer charging time of target dielectric.....	117
Figure 4.5	Total charge density (color flood, cm^{-3}) and electric potential (contour lines, V) for the (a) 1 st , (b) 3 rd , (c) 5 th , (d) 7 th and (e) 11 th rf pulse. The charge density is plotted on a log-scale over 5 decades ($10^{10} - 10^{15} \text{ cm}^{-3}$). Electrons in the plumes are accelerated towards the top dielectric and only heavy positive ions are left in the gap. A concavity in the potential is produced by the net positive charge in the gap which helps to extract and focus the electron current beam before surface charging become dominant.....	118
Figure 4.6	Net negative (ρ^-) and positive (ρ^+) total charge density (color floods cm^{-3}) and electric potential (contour lines, V) in a gap filled with N_2/O_2 mixtures with O_2 content of (a) 0.01%, (b) 0.1 %, (c) 1% and (d) 10%. The charge density is plotted on a log-scale over 5 decades ($10^{10} - 10^{15} \text{ cm}^{-3}$) after the 12 pulse. A white line separates regions of positive and negative charge. The resulting (e) potential (V) on the top dielectric surface and (f) time integrated electron flux (cm^{-2}) decrease with increasing O_2 content.	119
Figure 4.7	A more uniform current beam with higher intensity can be achieved by reducing the mDBD spacing. Electron density (color flood, cm^{-3}) and electric potential (contour lines, V) for (a) 1 st , (b) 3 rd , (c) 5 th , (d) 7 th , (e) 9 th and (f) 12 th rf pulse. The electron density is plotted on a log-scale over 4 decades ($2 \times 10^{11} - 2 \times 10^{15} \text{ cm}^{-3}$). (g) Electron density and potential after the 12 th pulse for a 600 μm spacing. (h) Surface potential on top dielectric after the 12 th pulse for spacing of 100 μm , 300 μm and 600 μm between the microdischarge cavities. A less modulated and higher peak potential results from merging of the closely spaced electron plumes.	120
Figure 4.8	Electron density (color flood, cm^{-3}) and electric potential (contour lines, V) during peak current extraction on the 4 th rf cycle for frequencies of (a) 25 MHz, (b) 10 MHz, (c) 6 MHz and (d) 2.5 MHz. The electron density is plotted on a log-scale over 5 decades ($10^{11} - 10^{16} \text{ cm}^{-3}$). More negative voltage and charge density result on the top dielectric at lower frequency due to the longer rf period.	121
Figure 4.9	Plasma and charging characteristics for different rf frequencies. (a) Peak electron density (cm^{-3}) at site A (see Fig. 4.1) as a function of pulse number, (b) surface potential (V) at $t = 500 \text{ ns}$ and (c) surface potential after the 4 th pulse. At higher frequencies, the peak electron density initially increases due to enhancements in the extracting field produced by positive ion accumulation. The electron density then decreases due to charging of the top dielectric. At lower frequencies, positive ions are collected by the screen electrode and the electron density decreases with increasing pulses.	122

- Figure 4.10 Independently controlled mDBDs demonstrated by delaying starting rf voltage on the center microdischarge by 2 rf periods. Electron density (color flood, cm^{-3}) and electric potential (contour lines, V) for (a) 1st, (b) 3rd, (c) 5th, (d) 7th and (e) 12th rf pulse. The electron density is plotted on a log-scale over 4 decades ($2 \times 10^{11} - 2 \times 10^{15} \text{ cm}^{-3}$). (f) Surface potential on the top dielectric at $t = 500 \text{ ns}$ (12th pulse) for in-phase and center delayed rf excitation. Tuning of the surface potential is enabled by controlling the onset of individual microdischarges, in this case a decrease in the potential of the center peak 100 V due to the two period delay. 123
- Figure 5.1 Schematics of corona devices. (a) A, B and C are 3-wire corotron, scorotron and shielded corotron, respectively.[16] (b) Entire device and full computational domain of negatively dc-biased blade corona discussed in this chapter. (c) Enlargement of corona electrode and underlying ground electrode covered with a dielectric photoconductor (PC). 143
- Figure 5.2 Charging of PC surface by a dc biased corona blade. (a) Time evolution of electron density (color flood, cm^{-3}) and electric potential (contour lines, V) produced by a -3 kV dc biased corona blade. (b) Time evolution of surface charge density (solid, cm^{-3}) and surface voltage (dashed, V) on the PC dielectric. The electron density is plotted on a log-scale over 4 decades ($10^{11} - 10^{15} \text{ cm}^{-3}$). The discharge is terminated by surface charging. 144
- Figure 5.3 Electron impact ionization sources from bulk electrons (S_e), and ionization source by sheath accelerated secondary electrons (S_{sec}) at different times after initiation of the discharge. The ionization sources are plotted on a log scale over 3 decades. The charging of the surface far from electrode results from a surface ionization wave. 145
- Figure 5.4 Ionization by secondary electrons S_{sec} helps maintain the corona discharge. (a) Electron density (color flood, cm^{-3}) and electric potential (contour lines, V) produced by a -3 kV dc biased wire corona at $t = 30 \text{ ns}$ with and without ionization sources by sheath accelerated secondary electrons (S_{sec}). (b) Surface charge density (solid, cm^{-3}) and surface voltage (dashed, V) with and without S_{sec} showing the contribution of secondary electrons. 146
- Figure 5.5 Residual electrons and negative ions produce nominal charging of the PC after the discharge is terminated. (a) Time evolution of electron and negative ion density (color flood, cm^{-3}), and electric potential (contour lines, V) at $t = 50, 200, 400$ and 600 ns . (b) Time evolution of surface charge density (solid, cm^{-3}) and surface voltage (dashed, V) at $t = 50, 200$ and 600 ns 147

Figure 5.6	Plasma properties produced by a -3 kV dc biased wire corona at $t = 30$ ns with and without volumetric photoionization source S_{ph} and photoemission from the corona and PC surface. (a) Electron density (color flood, cm^{-3}) and electric potential (contour lines, V). (b) Surface charge density (solid, cm^{-3}) and surface voltage (dashed, V).	148
Figure 5.7	Plasma properties produced by a -3 kV dc biased wire electrode at $t = 60$ ns on dielectric sheets with relative permittivities ϵ_r of 5, 10, and 20. (a) Electron density (color flood, cm^{-3}) and electric potential (contour lines, V). (b) Surface charge density (solid, cm^{-3}) and surface voltage (dashed, V) on the dielectric surface after termination of the discharge.	149
Figure 5.8	Time evolution of electron density (flood, cm^{-3}), ionization sources from bulk electrons S_e , ionization by secondary electrons S_{sec} (flood, $\text{cm}^{-3}\text{-s}^{-1}$) and electric potential (contour lines, V) produced during reignition after the first symmetric surface charge density was shifted to the left by $500 \mu\text{m}$	150
Figure 5.9	The total surface charge density (solid, cm^{-3}) and surface potential (dashed, V) before and after re-ignition of the secondary discharge with a shift of initial surface charge density by (a) $500 \mu\text{m}$, (b) $600 \mu\text{m}$, and (c) $700 \mu\text{m}$	151
Figure 5.10	The total charge density (solid, cm^{-3}) and surface potential (dashed, V) on the dielectric surface after 5 discharge pulses (4 re-ignitions).	152
Figure 5.11	Time evolution of (a) electron density (flood, cm^{-3}) and electric potential (contour lines, V) and (b) total surface charge density (solid, cm^{-3}) and surface potential (dashed, V) on a rapidly moving surface. The discharge is continuously re-ignited by the rapidly moving surface in a quasi-dc manner.	153
Figure 5.12	Time evolution of (a) electron density (flood, cm^{-3}) and electric potential (contour lines, V) during the charging process at $t = 20$ ns and (b) total surface charge density (solid, cm^{-3}) and surface potential (dashed, V) after the termination of discharge for $V_a/d_g = -1.5 \text{ kV}/0.1 \text{ mm}$, $-3 \text{ kV}/0.2 \text{ mm}$ and $-4.5 \text{ kV}/0.3 \text{ mm}$, where V_a is the applied dc voltage and d_g is the gap size.	154
Figure 6.1	Schematic of a charge roller (CR) and a photoconductor (PC) drum. (a) Microdischarges and surface charging in the entire device consist of a cylindrical CR and a PC drum. (b) A non-uniform periodic surface charging pattern with period of 1 mm. An idealized device of its original scale is shown in (c); the idealized device with its vertical scale expanded by a factor of 2 is shown in (d). A more sophisticated geometry that is vertically expanded by a factor of 4 is shown in (e).	177

Figure 6.2	Time evolution of electron density (color flood, cm^{-3}) and electric potential (contour lines, V) produced by a -1.6 kV dc-biased conductive charge roller. The electron density is plotted on a log scale over 4 decades, the maximum density is shown in the upper-left corner of each time frame. The discharge is terminated by surface charging.	178
Figure 6.3	Electron impact ionization sources from bulk electrons (S_e) at different times during the charging process. The ionization sources are plotted on a log scale over 5 decades.	179
Figure 6.4	The time evolution of an ionization source by sheath-accelerated secondary electrons (S_{sec}) during the charging process. After the sheath is fully formed, S_{sec} is in general comparable to or an order of magnitude larger than S_e	180
Figure 6.5	The time evolution of photoionization (S_{ph}) plotted on a log scale over 5 decades. Although relatively smaller compared to the electron impact ionization source, the remote secondary electrons provided by UV photon flux help initiate the microplasmas at the narrowing gap.	181
Figure 6.6	The time evolution of surface voltage (solid, V) on photoconductive dielectric for $\gamma_p = 0.01$. Microplasmas are initiated by emission current from nodes A, B, and C.	182
Figure 6.7	The time evolution of surface voltage (solid, V) on photoconductive dielectric for $\gamma_p = 0$ (no photoemission from surface). Microplasmas are initiated by emission current from nodes A, B, and C. The surface potential is less smooth without photoemissions.	183
Figure 6.8	The time evolution of electron density (color flood, cm^{-3}) and electric potential (contour lines, V) triggered by a field emission current density of $10^{-3} \text{ A}\cdot\text{cm}^{-2}$ from emission node A. CR is biased with -1.6 kV dc voltage; photoionization and photoemission are not considered. The electron density is plotted on a log scale over 4 decades.	184
Figure 6.9	The time evolution of surface voltage (solid, V) on a photoconductive dielectric without photoionization and photoemission. Microplasmas are initiated underneath the emission node A, B, or C if the local field is sufficient.	185
Figure 6.10	Microdischarges produced by a charge roller having a conductivity of $\sigma = 10^{-4} \Omega^{-1}\cdot\text{cm}^{-1}$. (a) The time evolution of electron density (color flood, cm^{-3}), and electric potential (contour lines, V) at $t = 4, 10, 40,$ and 180 ns . (b) Surface voltage (solid, V) after the discharge is terminated for $\sigma = 10^{-2}$ and $10^{-4} \Omega^{-1}\cdot\text{cm}^{-1}$	186

- Figure 6.11 The time evolution of electron density (flood, cm^{-3}) and electric potential (contour lines, V). The discharge is re-ignited continuously by a rapidly moving surface. 187
- Figure 6.12 Characteristics of microplasmas and surface potential on PC dielectric at steady state. (a) The electron density (flood, cm^{-3}) and electric potential (contour lines, V). (b) The corresponding spatial distribution of electric potential and charge density over the cross section of the streamer. (c) The corresponding spatial distribution of electric potential and electric field over the cross section of the streamer. (d) The surface potential on the PC sheet before and after the steady state for a rapidly and slowly moving surface. 188
- Figure 6.13 The time evolution of electron density (flood, cm^{-3}) and electric potential (contour lines, V) produced by a conductive CR biased with -700 dc voltage. The discharges of low electron density are continuously produced by lower applied voltage and seed secondary electrons. 189
- Figure 6.14 The Townsend-like discharge and quasi-constant electric field in the narrowing gap. (a) The microplasma and electric potential at steady state. (b) The corresponding spatial distribution of electric potential and the charge density over the cross section of the discharge. (c) The corresponding spatial distribution of electric potential and the electric field over the cross section of the discharge. (d) The surface potential at steady state for a rapidly and slowly moving (10 times slower) PC surface. 190
- Figure 7.1 Schematic of the microdischarge-based pressure sensor device. (a) The whole computational domain. (b) The deflected microdischarge chamber with a 10- μm gap. (c) A deflection example of a discharge chamber with a 7- μm gap (i.e., 3- μm deflection). The vertical scale for Fig. 7.1(b) and 7.1(c) is expanded by a factor of 2 for clarity. 206
- Figure 7.2 Time evolution of electron density (color flood, cm^{-3}) and electric potential (contour lines, V) produced by a 400 V dc-biased anode in the microdischarge-based pressure sensor. The electron density is plotted on a log-scale over 4 decades. The density shown on the left in the figures is the maximum level of electron density. 207
- Figure 7.3 Time evolution of E/N (color flood, Td) and electric potential (contour lines, V) produced by a 400 V dc-biased anode in the microdischarge-based pressure sensor. The E/N (Td) is plotted on a linear scale from 20 to 2,500 Td. 208
- Figure 7.4 Electron impact ionization from bulk electrons (S_e). (a) The time evolution of electron impact ionization S_e (color flood, $\text{cm}^{-3} \text{ s}^{-1}$) and electric potential (contour lines, V). The ionization source is plotted on a log-scale over 5 decades. (b) A line

	plot of ionization source S_e at mid-gap in the chamber at $t = 34$ ns, 36 ns, and 43 ns. Bullet-like ionization waves propagate to the left.	209
Figure 7.5	The time evolution of ionization by secondary electrons S_{sec} (color flood, $\text{cm}^{-3} \text{s}^{-1}$) and electric potential (contour lines, V). The ionization source is plotted on a log-scale over 5 decades. The secondary electrons emitted from K_1 help trigger the ionization waves between A- K_1	210
Figure 7.6	The periodic steady-state current collection and its corresponding electron density. (a) I_{K1} , I_{K2} , and their differential current as a function of time. (b) A time evolution of electron density (color flood, cm^{-3}) and electric potential (contour lines, V). The electron density is plotted on a log-scale over 4 decades.....	211
Figure 7.7	The current collection and plasma dynamics can be shaped to optimize the signal output by adjusting the ballast resistor. (a) A time series of current collected on the cathodes connected to three resistor sets (Ω_{Small} : 250 Ω on the anode and 50 Ω on cathodes; Ω_{Median} : 500 Ω on the anode and 100 Ω on cathodes; Ω_{Large} : 1,000 Ω on the anode and 200 Ω on cathodes). (b) Electron density at steady state sustained by electrodes connected to Ω_{Large}	212
Figure 7.8	The time series of current collection on cathodes (I_{K1} and I_{K2}) and its differential current $(I_{K2} - I_{K1})/(I_{K2} + I_{K1})$ for deflection up to 3 μm . The external applied pressure (atm.) corresponding to the deflection is shown on the top x-axis.....	213

ABSTRACT

Technologies based on atmospheric-pressure microplasmas (APMs) have been widely developed due to their unique nature such as its non-equilibrium state and capability for high pressure operation. Electrophotographic printing, sensors, surface functionalization and plasma medicine are typical applications of APMs. However, obtaining accurate measurements of key plasma parameters is challenging due to the complicated plasma dynamics and the small spatial and temporal scales. In this work, results from a computational investigation of APMs using a two-dimensional, multi-fluid simulation platform are discussed with the goal of improving our fundamental understanding of the nonlinear plasma kinetics of APMs, and to provide design rules for the devices of interest. In this thesis, the following problems are discussed:

Micro-dielectric barrier discharges (mDBD's) consist of micro-plasma devices (10-100 μm diameter) are finding continued use in the printing technologies. In a print head used for ionography, for example, a third electrode is desirable to extract electron current out of the mDBD. As a result, the physical structure of micro-DBD and the electron emitting properties are important to its operation. The characteristics of mDBD current extraction for frequencies from 2.5 to 25 MHz are discussed. After an electron avalanche in the mDBD cavity, the plasma can be attracted to the bottom dielectric or expelled from the mDBD's cavity towards the extraction electrode as the rf voltage varies. The electron current extraction and charge collection can be controlled by choice of rf frequency, rf driving voltage and permittivity of the dielectric barrier.

Independently controlled mDBD arrays consist of micro-plasma devices have been developed for high definition surface treatment and charging in ionography. During the charging process, the direct or indirect interactions between the mDBD devices and target dielectric are important to operation. The characteristics of atmospheric mDBD's arrays sustained in N₂ with an O₂ impurity are discussed. After electron plumes charge the target dielectric, a negative potential is generated by surface charging which deflects the incoming electron plumes. This blooming effect can be mitigated by increasing the capacitance (or dielectric constant) of the target sheet. Current extraction and surface charging are found to be sensitive to the adjacent of the mDBDs, dielectric properties of the materials being treated, gas mixture and rf driving frequencies.

An atmospheric pressure corona discharge consists of a corona wire biased with 100s V dc plus a few kV of ac voltage are used in electrophotographic (EP) printing technologies for charging imaging surfaces. After plasmas produced around the corona wire charge the underlying dielectric surface, the surface charging reduces the voltage drop across the gap between the corona wire and the dielectric surface which then terminates the discharge. As this underlying surface moves during the charging process, previously charged surfaces are translated out of the field of view and are replaced with uncharged surface. As a result, the uncharged fresh surface produces a rebound in the electric field which re-ignites the discharge. This discharge is then asymmetric. Depending on the speed of the underlying surface and its dielectric properties, the periodic re-ignition of the discharge can produce a periodic charging pattern on the moving surface.

Atmospheric pressure microdischarges produced by conductive charge rollers (CR) are used in electrophotographic (EP) printing technologies for the surface charging of the cylindrical photoconductor (PC). The characteristics of APMs sustained in dry air in the narrowing gap between a dc-biased CR and PC, and the charging properties on the PC surface are discussed. It

was found that surface charging and surface potential of the PC has varying degrees of uniformity and speed of charging depends on where the discharge is initiated and the degree of photoionization and photoelectron emission that provides remote seed electrons. In real printing applications, the surfaces of both the CR and PC are rotating. It was found that the rotation of the PC brings in uncharged surface, which restores the voltage drop in the gap and then re-ignites the plasma. As the process repeats, self-pulsing microplasmas may be produced to form an oscillatory charging pattern on the PC surface.

Pressure sensors in harsh environments often use piezoresistive and capacitive approaches to measure the pressure-produced deflection of a surface. The smallest dimension of this class of sensors is about 1 mm. To further reduce the size of such sensors, a microdischarge-based pressure sensor that is potentially capable of being an order of magnitude smaller has been recently proposed. In these sensors, a microdischarge is initiated between an anode and two competing cathodes (a reference and sensing cathode) in a sealed chamber. The sensing cathode is attached to a flexible diaphragm whose opposite surface is exposed to ambient. As the external pressure deforms the diaphragm, the resulting change in inter-electrode spacing redistributes the current collected by the two competing cathodes. The difference in current is a measure of the external pressure. The plasma dynamics of microdischarge-based pressure sensors are discussed. Following the electron avalanche, a conductive plasma transfers the anode voltage to the cathodes. A periodic bullet-like ionization wave is then generated which in turn produces a pulse-modulated dc current collected on the cathodes. The current collection varies with deflection of the diaphragm due to the external pressure and can also be optimized by adjusting the series impedance.

CHAPTER 1 INTRODUCTION

The research and development of technologies using atmospheric-pressure plasmas (AP plasma) have been rapidly accelerating. The literature published in the last two decades reveals a significant growth in plasma-assisted research and technologies. Due to its unique nature of being non-equilibrium and its ability to operate at atmospheric pressure, AP plasma forms the basis of a wide range of applications, such as plasma display panel (PDP), UV/VUV photon sources, current and charge sources, plasma-assisted combustion, remediation of toxic gases, surface functionalization, plasma actuator, and plasma medicine. This multi- and interdisciplinary effort encompasses fields of science and technology such as physics, chemistry, biology, electrical engineering, nuclear engineering, and chemical engineering.

Despite the fact that AP plasmas are relatively straightforward to generate, maintaining the system in a stable region and obtaining accurate measurements of plasma parameters is challenging due to their complicated dynamics and small spatial and temporal scales. In this thesis, a numerical simulation model, *nonPDPSIM*, is used to improve the fundamental understanding of the nonlinear plasma kinetics, and to provide design rules of the devices of interest. In this chapter, the fundamentals of plasmas will be introduced, and then a brief description of plasma technologies used for the printing industry and pressure sensors will be presented.

1.1 Plasmas: The Fourth State of Matter

Since ancient times, there has been a classification of the states of matter: solid, liquid, and gas. These states of matter occur as the substance is heated (heating means putting energy into the system) to a temperature above the bonding energy corresponding to a particular state, and then a phase transition occurs to transform the substance to the next state of matter. For example, the state of H₂O is in a crystal solid form known as ice when the temperature is below $T = 273$ K (i.e. $T \approx 0.0235$ eV, $1 \text{ eV} \approx 11,600$ K). The solid (A.K.A. the first state of matter) is a strongly coupled medium in which the bonding energy is higher than thermal energy. As the temperature is raised to a temperature between $T = 273\text{--}373$ K, the thermal energy breaks the crystalline bond. The solid melts to form a liquid in which intermolecular bonds are constantly broken and reformed. This H₂O liquid is known as water—the second state of matter. If the temperature is increased above $T = 373$ K, the intermolecular bonds are broken, and the H₂O molecules becomes independent and free to move—it exists in the gas state known as steam. By further heating the gas to the temperature in which the molecules and atoms are dissociated and the atomic bonds are broken, negative charges (electrons and negative ions) and positive ions are produced to form an ionized gas. In 1900's, the term “plasma” was first introduced by Lewi Tonks and Irving Langmuir to designate the portion of an glow discharge that embraces the whole space not occupied by sheaths. In this portion, the density of ions and electrons are high but substantially equal. The nature of high-conductivity and space-charge neutralization reminded Lewi Tonks and Irving Langmuir of blood plasma. The plasma is thus referred to as the “fourth state of matter.”[1-5]

1.2 Plasmas: The Definition

Not just any ionized gas can be called plasma since there is always some small degree of ionization in any gas. For example, an ionization rate on the order of $10 \text{ cm}^{-3}\text{-s}^{-1}$ is generated in the air at sea level by energetic cosmic rays and natural radioactivity. After electron-ion pairs are produced, electrons are attached to oxygen immediately, and an ion density on the order of 10^3 cm^{-3} is left in the air while the air density is on the order of $2.4 \times 10^{19} \text{ cm}^{-3}$. In general, plasma is defined as a quasi-neutral gas of charged and neutral particles that exhibits collective behavior. More rigorously, three general criteria must be satisfied for charged particles to be called plasma:

- (i) Debye Shielding: Plasma has the ability to shield out the electric potential applied to it.

The Debye length λ_D , a measure of shielding distance or the thickness of the sheath, must be smaller than the dimension of system L ($\lambda_D \ll L$). This criterion indicates that whenever an electric potential is locally or externally introduced into the system, the shielding process occurs within λ_D ; outside of λ_D , the plasma is “*quasi-neutral*,” that is $n_e \approx n_i$, where n_e and n_i are electron and ion density, respectively.

- (ii) Collective behavior: As the charges in the plasma are in motion, they can generate local net charges and electric current, which might produce electric and magnetic fields. As a result, the motion of charged particles far away depends not only on the local binary collisions but also on the electromagnetic force generated by the plasma in remote regions. This collective behavior and the Debye shielding effect would be statically valid only if there are enough particles in the Debye sphere (a sphere with a radius equal to the Debye length) or a Debye cube; that is $N_D \gg 1$, where N_D is the number of particles in a Debye sphere or a Debye cube.

(iii) Plasma frequency: the inertial response frequency of typical plasma oscillation, the electron plasma frequency, ω_{pe} , must be larger than electron-neutral collision frequency, ν_c , so that the plasma oscillation effects on electrostatic (ES) and electromagnetic (EM) waves are not damped by the electron-neutral collision effect, and plasma can rapidly respond and shield out electric potential

Among the three general criteria, the requirement of a large number of charged particles in a Debye sphere ($N_D \gg 1$) is the most essential condition. The concepts of Debye shielding, collective behavior, and wave behavior will not be valid if this condition is not satisfied.[4-7]

1.3 Plasmas: 99% of the Entire Visible Universe

Plasmas exist as various types of laboratory and extraterrestrial plasmas. As shown in Fig. 1.1, the plasma density, n_e , spans the range between $10^{-2} - 10^{28} \text{ cm}^{-3}$, and the electron temperature, T_e , varies between $10^{-2} - 10^5 \text{ eV}$. For example, solar wind is a stream of charge particles with $n_e \approx 5 \text{ cm}^{-3}$ and $T_e \approx 50 \text{ eV}$; in the controlled nuclear fusion reactor, an electron temperature of $T_e \approx 10 \text{ keV}$ and electron density of $n_e \approx 10^{14} \text{ cm}^{-3}$ are required to maintain the nuclear fusion reaction.

According to the wide range of parameters, plasma is classified into several categories:

- (i) Complete Thermodynamic Equilibrium (CTE) plasma: In CTE plasmas, all temperatures of charge species, neutral particles, and radiation temperature are equal. The CTE plasmas cannot be easily achieved, hence only exist in stars or during a short interval of strong explosion.
- (ii) Local Thermodynamic Equilibrium (LTE) plasma: In LTE plasmas (A.K.A. thermal plasmas) all temperature except the radiation temperature are equal if operating under the conditions of atmospheric pressure and heavy particles having a high energy of 10^2

– 10^4 eV. Since the collision frequency between electrons and heavy particles increases with pressure, two systems (electrons and heavy particles) reach equilibrium easily at atmospheric pressure. An example of LTE-plasma is the high intensity of an electric arc at atmospheric pressure.

(iii) Non-Local Thermodynamic Equilibrium (non-LET) plasma: In non-LTE plasmas (A.K.A. cold plasmas) the thermodynamic equilibrium between electrons and heavy particles is not reached. The electron temperature ($T_e \approx 1 - 10$ eV) is much higher than the temperature of ions and neutral particles ($T_g \approx T_i \approx 0.0235$ eV) that are usually at room temperature.

The non-LTE cold plasmas have been investigated for decades due to their non-equilibrium properties, high selectivity, and energy efficiency in plasma chemical reactions, as well as their potential applications in a variety of fields such as microelectronic fabrication, surface treatment, and UV/VUV photon sources. This thesis focuses only on the non-LTE atmospheric pressure plasmas and their applications.[5,7,8,9]

1.4 Townsend Breakdown

Although plasmas have various types of applications and characteristics, the plasma discharges usually start with an electron avalanche. A simplified model of an avalanche at steady state is shown in Fig. 1.2. A cathode is separated from an anode by a gap of distance d , and the electrode is biased with voltage V . A uniform electric field, E , is formed in the gap ($E = V/d$). Assume that the number of initial photoelectrons, n_0 , are induced by external UV photons at the cathode, and the number of secondary electrons, $n_{0,sec}$, are produced at the cathode due to the secondary process. The total number of electrons leaving the cathode is defined as $n_{0,tot} = n_0 +$

$n_{0,sec}$. These primary electrons near the cathode drift along the electric field to the anode, gaining energy and ionizing the gas. This multiplication of electrons in cascade ionization is named *avalanche*. The total number of electrons at the anode can be obtained by $n_{tot} = n_{0,tot} e^{\alpha d}$ where α is the *Townsend first ionization coefficient* that gives electron production per unit length. The secondary electrons produced by ion impact are defined as $n_{0,sec} = \gamma n^+$, where γ is the *secondary emission coefficient* (the probability of secondary electron generation on the cathode by an ion impact), and n^+ is the number of positive ions produced during the ionization process ($n^+ = n_{tot} - n_0 - n_{0,sec}$). It is straightforward to obtain the total number of electrons reaching anode $n_{tot} = n_0 e^{\alpha d} / [1 - \gamma(e^{\alpha d} - 1)]$, and the total average current in the gap can be written as $I_{tot} = I_0 e^{\alpha d} / [1 - \gamma(e^{\alpha d} - 1)]$. Notice that $\gamma(e^{\alpha d} - 1)$ in the denominator represents the number of secondary electrons induced by positive ions that are produced after an avalanche by a primary electron. The number of secondary electrons increases with first ionization coefficient α and secondary emission coefficient γ . If a primary electron can produce one secondary electron, that is $\gamma(e^{\alpha d} - 1) = 1$, theoretically the current becomes infinitely large but practically it is limited by the resistance of the circuits; the electric current due to an avalanche becomes sufficiently measurable and *self-sustained* (self-sustained means the discharge will sustain itself even if the initial current I_0 produced by the external source is removed), the gas becomes conductive, and the *breakdown* occurs. As a result, the *Townsend breakdown criterion* for the stable state of a self-sustaining discharge can be expressed as $\gamma(e^{\alpha d} - 1) = 1$ or $\alpha d = \ln(1/\gamma + 1)$; it is also the threshold or lower limit below which a spark cannot pass. If $\gamma(e^{\alpha d} - 1) < 1$ (or $\alpha d < \ln(1/\gamma + 1)$), the current in the gap is *non-self-sustained*, the external source producing I_0 is required to maintain the discharge. This mechanism of ignition of self-sustained discharge is referred to as the *Townsend breakdown mechanism*—the breakdown is based on the avalanche via secondary electron emission at a low pressure or smaller gap (low

pd), and the applied electric field is not disturbed by the space charges produced by the electron avalanche. Combining the breakdown condition and a conventional semi-empirical expression for α , a formula for the calculation of the breakdown-reduced electric field (E/p) as a function of pd can be obtained:

$$\frac{E}{p} = \frac{B}{C + \ln(pd)}$$

where E , p , and d stand for electric field, pressure, and gap distance, respectively; and B and C are constants that depend on the gas mixture and the secondary electron coefficient γ . This expression is also referred as the *Paschen curve*. [6,10-12,14]

1.5 Spark Breakdown

The Townsend breakdown mechanism usually occurs in a low-pressure environment or in a smaller gap (low pd) in which the avalanches (e^{ad}) do not disturb the applied electric field in both cases, and the discharge is sustained by secondary electron emission from the cathode. Under certain conditions such as operating in a large gap, higher pressure, or applied with overvoltage (applied voltage above the breakdown voltage), a *spark breakdown mechanism* might become dominant. In contrast to the Townsend breakdown mechanism, the spark breakdown is based on the concept of the growth of a local and narrow ionized channel (A.K.A a streamer). The streamer at a high pd develops faster than the characteristic time of an ion traveling through the gap generating secondary electrons. As a result, the spark breakdown and a streamer are relatively independent to the cathode materials and secondary emission process.

When the avalanche occurs at a high pd or overvoltage, the space-charge effect might become important. The charge distributions and electric field are illustrated in Fig. 1.3 before and after the avalanche reaches the anode. As the electron avalanche occurs between electrodes, a

dipole-like field (E') is formed by the fast-moving electrons at the head of avalanche and the massive positive ions that are left behind. If the amplification (e^{ad}) proceeds, the space-charge density increases in the gap, and E' starts to distort the external field E_0 . As a result, the total electric field ($E = E_0 + E'$) in front of the avalanche head becomes stronger due to this space-charge effect, which then accelerates the amplification of the space-charge density and ionization process. When the avalanche reaches the anode, the electrons are collected by the anodic metal, and only the massive ions of the *ionic trail* remain in the gap. At this time, the total field, E , is then produced by the positive ions and its negative image charges in the electrodes.

As the charge amplification (e^{ax}) reaches a sufficiently high value so that the space-charge field becomes comparable to the external field ($E' \approx E_0$), the avalanche starts to transform into a streamer—a local and thin ionized plasma channel formed from the primary avalanche. The streamer stretches toward one or both electrodes connecting the anode-cathode pair, which then leads to a spark discharge. Schematics of cathode-directed and anode-directed streamers are shown in Fig. 1.4. In a relatively short gap biased with overvoltage, the avalanche-to-streamer transformation occurs at the anode. The electrons produced by photoionization or the electron detachment process near the anode, or photoemission from the cathode, are attracted into the ionic trail, initiating a secondary avalanche. The electrons from the secondary avalanche pulled into the ionic trail form a quasi-neutral plasma channel, while the positive charges that are left behind enhance the space-charge effect. The process repeats to trigger sequential avalanches and to provide a propagation of the streamer in the direction of the cathode. As a result, this needle-like *cathode-directed streamer* (A.K.A. *positive streamer*) stretches from the anode carrying part of the anode potential toward the cathode. The enhanced electric field in front of the needle-like streamer head triggers fast streamer propagation with a speed of 10^8 cm/s. If the primary avalanche

transforms into a streamer halfway to the anode in a longer gap biased with a high overvoltage, the streamer then propagates toward both electrodes; if the transformation occurs near the cathode, the streamer mostly propagates toward the anode, and it is referred to as an *anode-directed streamer* (A.K.A. *negative streamer*). In these cases, the mechanism of streamer propagation toward the cathode is the same as the cathode-directed streamer. However, the propagation to the anode can be initiated by electrons provided not only by photoionization, photoemission, and the electron detachment process, but also by fast electrons moving in front of the primary avalanche, which indicates that the propagation of an anode-directed streamer without a photon source is possible.

When the streamer approaches the cathode, a strong electric field between the streamer head and cathode stimulates an intense *back ionization wave* propagating from the cathode back toward the anode forming a stronger ionized plasma channel. After the wave front reaches the anode and the conductive plasma channel connects the electrodes, the *spark* channel is then established.[6,10-11,15]

1.6 Dielectric Barrier Discharge (DBDs)

As the spark breakdown occurs at high pressure, a large current (typically 10^4 – 10^5 A) can flow through the conductive spark channel, which can lead to local Joule heating, the formation of shock waves, and eventually an arc. To avoid the formation of sparks and the growth of a high-density current in a streamer channel, a nanosecond-pulse power supply or a dielectric barrier discharge (DBD) are widely used in industrial applications especially at atmospheric pressure.[10-11] The ns-pulse power supply generates pulses with the duration of a few hundred nanoseconds,

which is sufficiently short to avoid the formation of a spark. Using dielectric barrier discharges (DBDs) [16] is an alternative approach to avoid the formation of an arc.

DBDs have been developed as stable, high-pressure and non-thermal plasma sources.[16] Conventional DBDs with large area electrodes sustained at atmospheric pressure typically have gap spacing of a few mm. The electrodes are biased with an AC voltage of tens of Hz to as high as tens of MHz. At low frequencies, the plasma in these devices operates in a filamentary mode with each individual filament having a diameter of tens to hundreds of μm . When operating at a high frequency (tens of kHz or above) or with rapidly rising voltage pulses in mildly attaching gas mixtures, DBDs often visually appear to be a uniform plasma since the rapid onset of voltage and preionization from the prior pulse tend to work against the formation of large filaments.[17-18]

A time evolution of a DBD is shown in Fig. 1.5. In principle, when a DBD operates in a filamentary mode, upon initiation the filament propagates across the gap as a streamer. When the streamer strikes the opposite surface, it electrically charges the dielectric surface and so removes the local potential drop across the gap. As the gap voltage falls below its self-sustaining value, the plasma is quenched, thereby preventing the formation of an arc. The surface charges on the dielectrics, excited states and ions left in the plasma channel are often referred to as microdischarge remnants.[10-11] When the polarity changes on the following half ac cycle, a more intense electron avalanche may occur at the same location due to the higher voltage across the gap from the previously charged dielectrics. This discharge occurs in many individual breakdown channels, which are referred to as *microdischarges*. At atmospheric pressure, particularly in attaching gases, the plasma formation and decay times can be as short as a few to tens of ns whereas the ac period, even at rf frequencies, may be tens to hundreds of ns. As a result, the micro-plasma may need to be re-ignited with each rf cycle.

DBDs form the basis of a wide range of applications due the unique features.[16,19] For example, ozone generation and remediation of toxic gases [20-21], UV/VUV photon sources and polymer functionalization [22-24], and plasma display panels [25-26] are typical DBD applications. Recently, DBDs are being implemented as plasma sources in biomedical medical applications [27-28], area-selective surface modification [29-31], investigations of nonlinear behavior [32], self-organized pattern formation[33-34] and large arrays of DBDs having apertures of tens of microns as lighting sources.[35-37] In Chapters 3–6 of this thesis, I will further discuss the DBD-based technologies used in the printing industry.

1.7 Microdischarges and Electrophotography

The invention of electrophotography has introduced a worldwide revolution in document processing.[38-42] It is the fundamental technology of virtually all office copiers and laser printers. As shown in Fig. 1.6, the electrophotographic process generally consists of six steps: (1) charging, (2) exposure, (3) development, (4) transfer, (5) fusing, and (6) a cleaning step. In the charging step, a charge roller or a corona discharge uniformly charges the surface of the photoconductor (PC) negatively. In the exposure step, a laser beam forms a latent image on the PC surface. The charged toner particles are then electrically attracted to the latent image on the PC in the development step. In the transfer and fuse steps, the toner particles are transferred from the PC surface to a uniformly charged paper, and are fused by heating. The residue charges and toner particles are then removed in the cleaning step. After the cleaning of residue particles, the six steps repeat until the printing process is finished.

Among all of the steps, the charging of the PC surface is the key step to printing quality. Two charging methods shown in Fig. 1.6(b) are commonly used in electrophotography: charge

roller (CR) and corona discharge. A Charge roller is a cylindrical conducting rubber biased with dc, pulsed dc, or ac voltage up to 1 kV. In the charging process, microdischarges are generated in the narrowing gap of the converging CR and PC to charge the photoconductor surface negatively. Although the charging process in a charge roller can be achieved with relatively low voltage, a non-uniform periodic charged pattern was reported, which reduces the printing quality. Corona discharge contains a corona wire biased with a relatively larger potential up to a few kV dc plus ac voltage. The wire is separated from the PC surface by a gap of tens of microns to millimeters. A large electric field is produced around the wire by geometric enhancement, and the discharge is initiated to charge the underlying PC surface. Although the corona discharge charges the PC surface more uniformly compared to a charge roller, the corona consumes more power and produces a great amount of ozone that pollutes the environment and damages the photoconductor.

Ionography is a simplification of the electrophotographic process, in that the exposure step is eliminated. Schematics of ionography are shown in Fig. 1.7. After microdischarges are generated and controlled in a print head, as shown in Fig. 1.7(a), charge beams extracted from the print head form charge dots at selected locations on an image carrier, a dielectric cylinder, to create the latent image. The charged toner particles are then electrically attracted to the latent images. Several different charge sources have been employed for ionography; mDBD (micro— dielectric barrier discharge) -based print heads are the most successful, and are still being used by high-end digital printers. Through MEMS technology, mDBDs in print heads with aperture sizes of tens of microns have been developed for electrographic surface patterning at atmospheric pressure. The key challenges for a print head-based print engine are (1) high current and (2) resolution requirements. Since high current extraction is desirable in a print head for high-speed printing, plasma dynamics in mDBDs and current extraction mechanism are important to the operation. The

resolution is also required but limited by extracted current beam size and blooming (dielectric effect) on the dielectric surface. In this thesis, a 2-D multi-fluid model, *nonPDPSIM*, is used to understand the plasma dynamics and its interaction with surfaces.

1.8 Microdischarge-based Pressure Sensor

Microscale pressure sensing solutions have been widely investigated in the past five decades; the most commonly used mechanisms are piezoresistive and capacitive pressure sensors.[44] Piezoresistive sensors typically measure stress in a diaphragm as it was deflected by applied pressure; capacitive pressure sensors measure displacement (or variance of capacitance) between the deflected metal diaphragm and a reference electrode. The smallest micromachined pressure sensors that have been reported—e.g., for use within cardiac catheters—use these transduction techniques.[44] For both types of sensors, the dimensions of the diaphragms of the smallest devices have been about 1 mm long. A further reduction in size has been a challenge for both approaches. Recently, a pressure-sensing approach based on microdischarges has been reported.[45-47] Microdischarge-based pressure sensors operate by measuring the change in the spatial current distribution of confined microdischarges within the pressure sensors. The microdischarge-based transducers have many potential attractive features. For example, the inherent signal levels are large compared to both capacitive and piezoresistive devices, which eliminates the need for an interface circuit, and substantially reduces the need for amplification. This is very appealing from the viewpoint of miniaturization. In this regard, the microdischarge cells that have been reported to date are at least 100× smaller in area than the smallest capacitive and piezoresistive pressure sensors that have been reported. For example, the discharge gap in cells used for plasma display panels can be less than 100 μm.[48] Having said that, the plasma

properties are not well understood in the microdischarge-based pressure sensors, which has motivated further investigation into optimizing their performance and reducing the dimension.

1.9 Issues to Be Discussed

The goal of this thesis is to improve the fundamental understandings of plasma dynamics and the plasma-surface interaction in the device of interest, and also to provide design rules to optimize the performance using a 2-D multi-fluid simulation platform, *nonPDPSIM*, which will be discussed in Chapter 2.

In Chapter 3, micro—dielectric barrier discharges (mDBDs) sustained in atmospheric pressure N_2 , driven with radio frequency (rf) waveforms will be discussed. The mDBDs are sandwich structures with an opening of tens of microns excited with rf voltage waveforms of up to 25 MHz. Following the avalanche by electron impact ionization in the mDBD cavity, the plasma can be expelled from the mDBDs cavity toward the extraction electrode during the part of the rf cycle when the extraction electrode appears to be anodic. The electron current extraction can be enhanced by biasing this electrode. The charge collection can be controlled by choice of rf frequency, rf driving voltage, and permittivity of the dielectric barrier.

In Chapter 4, independently controlled mDBD arrays used for the charge extraction and surface treatment of a dielectric sheet will be discussed. When using the mDBDs to produce plumes of charged species, there are potential direct or indirect interactions between the mDBD devices. In this chapter, the characteristics of atmospheric mDBDs arrays sustained in N_2 with an O_2 impurity using results from a 2-D simulation will be discussed. The device of interest consists of a sandwich structure using layers of dc- and rf-biased electrodes to help shape the plume. It was found that the adjacency of the mDBDs and the dielectric properties of the materials being

treated are important to the interactions between mDBDs in the array. Scaling laws will be presented for the operating characteristics of these mDBDs arrays as a function of material properties, geometry, driving voltage waveform, and gas mixture.

In Chapter 5, atmospheric pressure corona discharges used in electrophotographic (EP) printing technologies for charging imaging surfaces, such as photoconductors (PC), will be discussed. An electric discharge is produced around the corona wire from which electrons drift toward and charge the underlying dielectric surface. The surface charging reduces the voltage drop across the gap between the corona wire and the dielectric surface, which then terminates the discharge, as in a dielectric barrier discharge. In printing applications, this underlying surface is continuously moving throughout the charging process. For example, previously charged surfaces that had reduced the local electric field and terminated the local discharge are translated out of the field of view and are replaced with the uncharged surface. The uncharged surface produces a rebound in the electric field in the vicinity of the corona wire, which in turn results in re-ignition of the discharge. The discharge, so reignited, is then asymmetric. It was found that in the idealized corona charging system I investigated, a negatively dc-biased corona blade with a dielectric-covered ground electrode, the discharge is initially sustained by electron impact ionization from the bulk plasma and then dominated by ionization from sheath-accelerated secondary electrons. Depending on the speed of the underlying surface and its dielectric properties, the periodic re-ignition of the discharge can produce a periodic charging pattern on the moving surface.

In Chapter 6, the behavior of atmospheric pressure microdischarges sustained in dry air between a dc-biased charge roller (CR) and photoconductor (PC) will be discussed, as will the charging properties on the PC surface using results from a 2-D simulation. In general, these microdischarges behave like a dielectric-barrier-discharge (DBD). Microdischarges are produced

in the narrowing gap between the CR and PC, where the CR is biased with hundreds of volts plus a few kilovolt ac voltages. After charging the underlying PC surface to a predetermined potential, these cathode-directed streamers can be terminated by the surface charging of the PC if operated with a dc or quasi-dc voltage on the CR. In real printing applications, the surfaces of both the CR and PC are rotating. The rotation of the PC brings in an uncharged surface, which restores the voltage drop between the CR and PC. The rebound of E/N then re-ignites the plasma. As the process repeats, self-pulsing microdischarges are produced to form an oscillatory charging pattern on the PC surface. Under certain operating conditions, a Townsend-like discharge is observed in which a quasi-constant electric field in the gap and a uniform surface charging are produced. I find that photoionization and photoemission are significant in the charging process. When the PC surface is in motion, by varying applied voltage and the speed of the PC surface, a microdischarge and a Townsend-like discharge can be produced in the CR-PC gap. With a higher applied voltage and a rapidly moving surface, an oscillatory charging pattern is formed by self-pulsing microdischarges. With a relatively smaller voltage, a Townsend-like discharge becomes more dominant and a uniform charging pattern can be formed.

In Chapter 7, a microdischarge-based pressure will be discussed. A 3-D model is shown in Fig. 1.8. In this sensor, a microdischarge is initiated between an anode (A) and two competing cathodes (a reference cathode, K_1 , and a sensing cathode, K_2) in a sealed chamber. The sensing cathode is attached to a flexible diaphragm that serves as a surface of the chamber. As the external pressure deflects the diaphragm, the changing of inter-electrode spacing redistributes the current collected by the two competing cathodes. In this chapter, I will discuss the plasma dynamics of microdischarge-based pressure sensors using results from a 2-D simulation. I find that following the electron avalanche in the geometrically enhanced electric field at the edge of the anode, a

conductive plasma is created within tens of nanoseconds, which transfers the anode voltage to the cathodes. A periodic bullet-like ionization wave (IW) is then generated in the chamber and produces a pulse-modulated dc current collected on K_1 and K_2 . The current collection varies with inter-electrode spacing (A- K_2) that is changed by deflection of the diaphragm due to the external pressure; the current distribution can also be optimized by adjusting the impedance connected to electrodes.

1.10 Figures

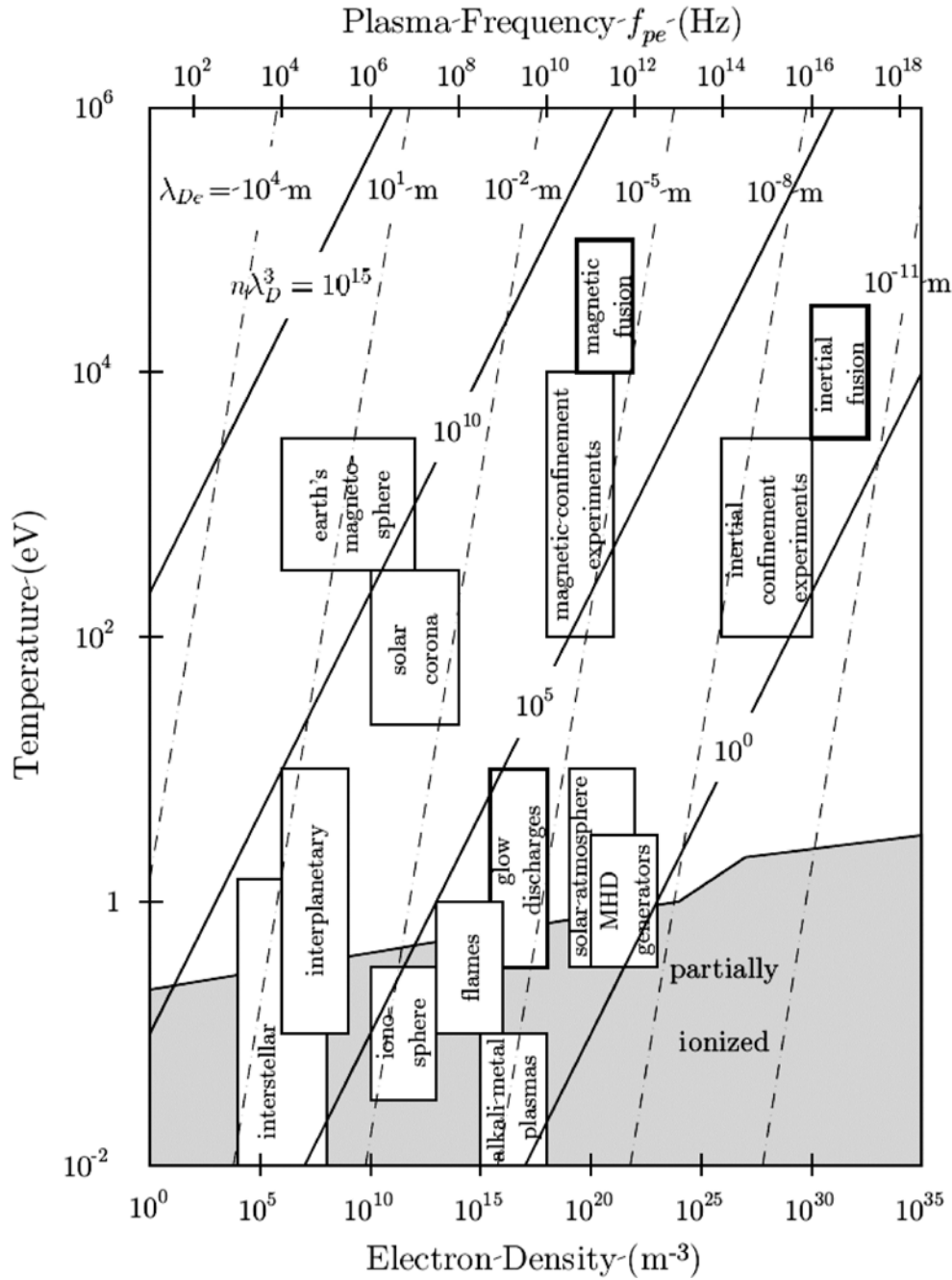


Figure 1.1 Plasma can be characterized by electron density and temperature. Electron Debye length λ_D (constant along the dashed lines) and the number of charged particles in a Debye cube N_D (constant along solid lines) are also indicated in the figure.[5]

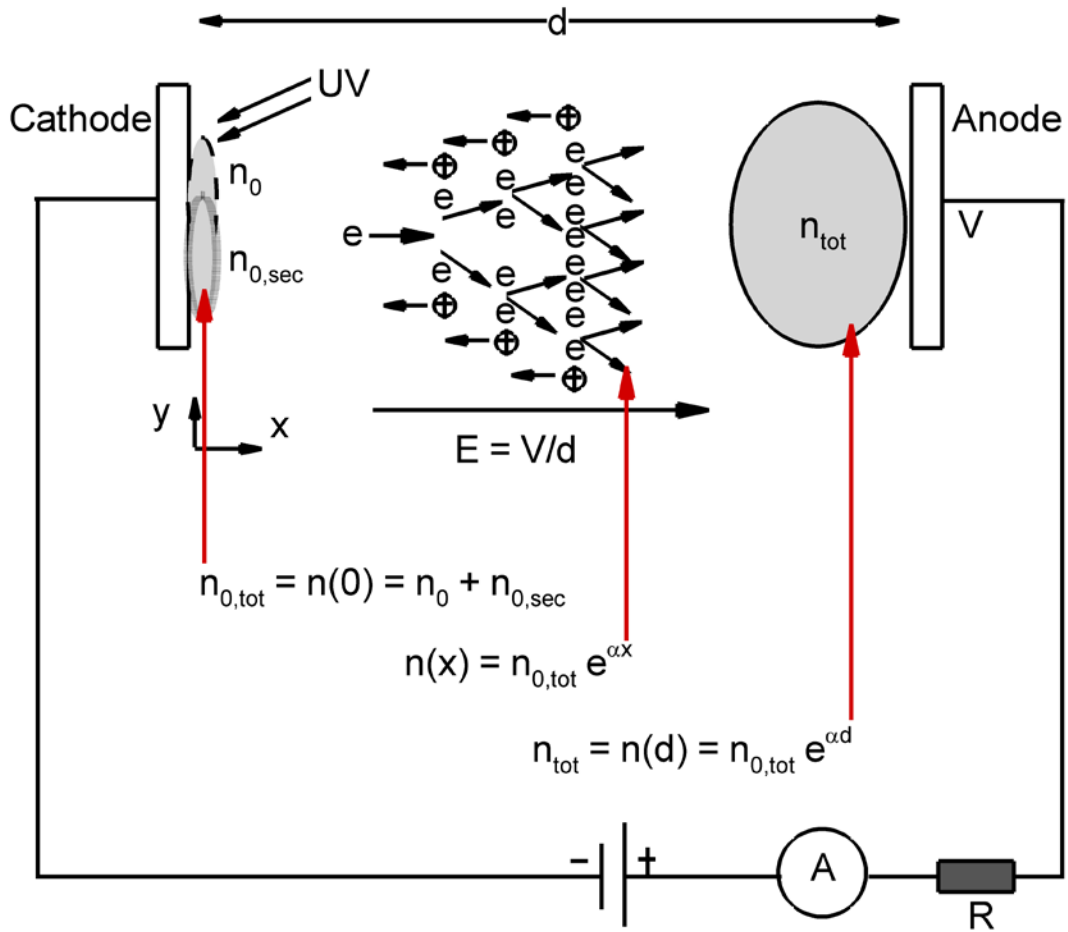
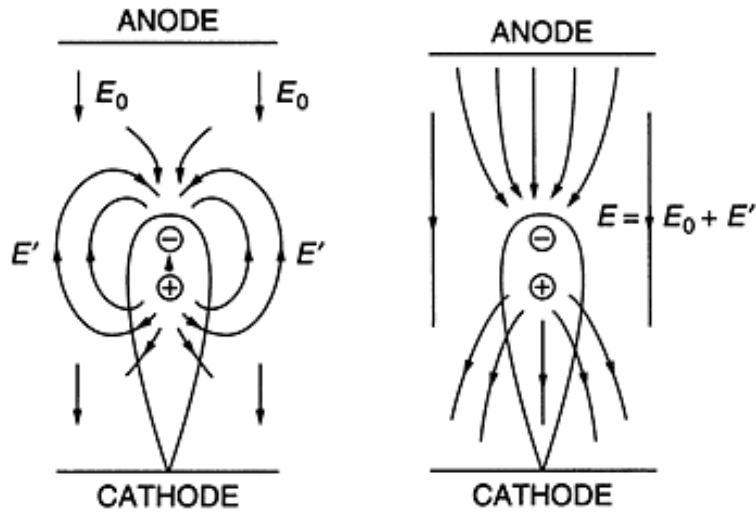
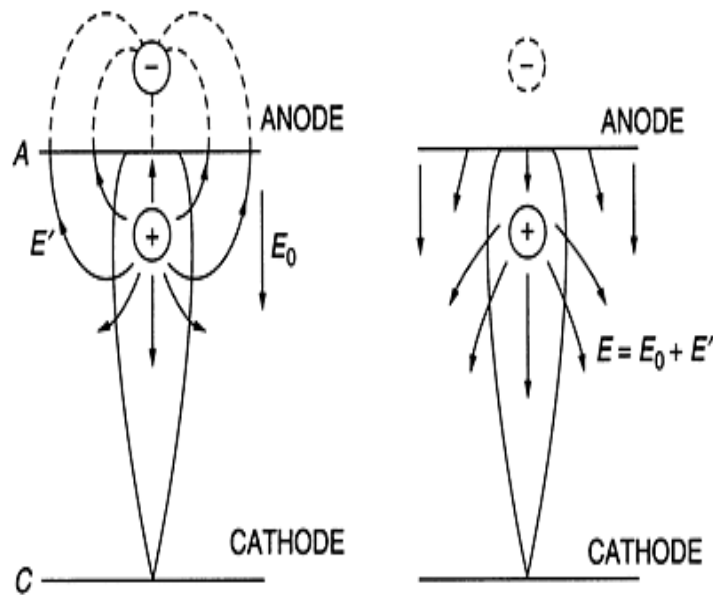


Figure 1.2 Illustration of avalanche and Townsend breakdown.[12-13]



(a)



(b)

Figure 1.3 The charge distribution and electric field in the gap (a) before and (b) after the avalanche reaches the anode. E_0 , E' , and E represent the applied electric field, the field produced by space charges, and the total field ($E = E_0 + E'$), respectively.[6,10-11]

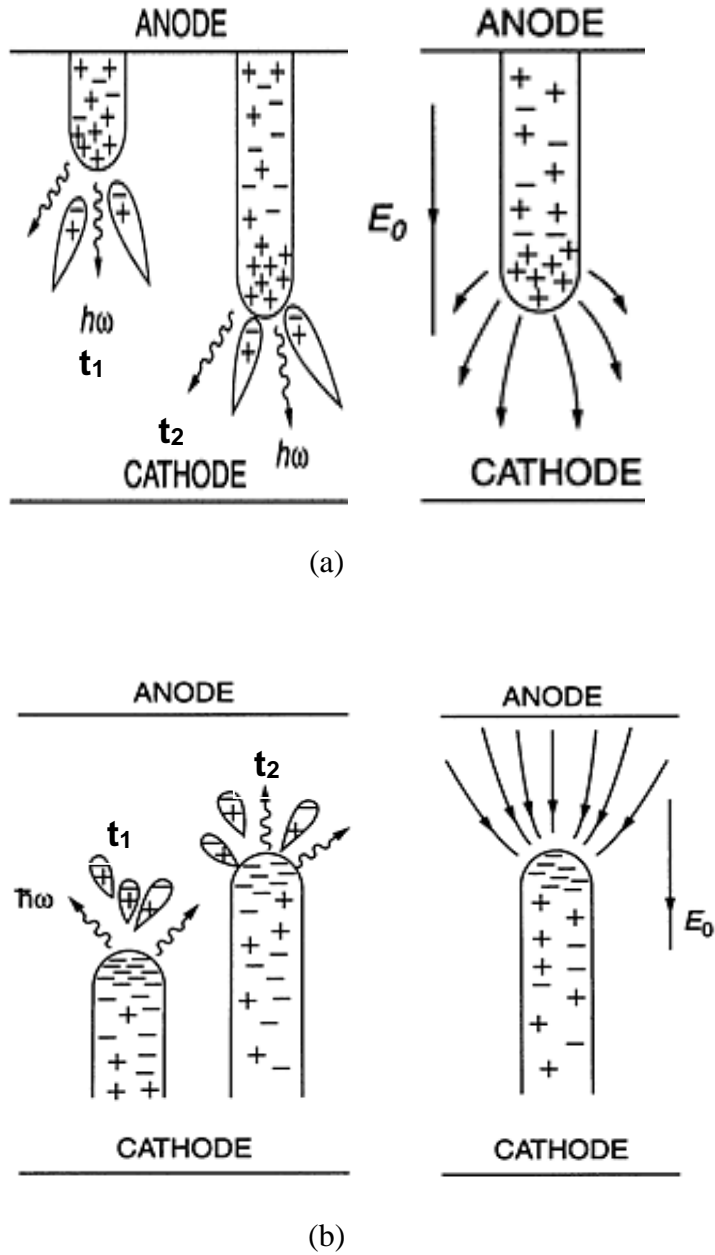


Figure 1.4 Schematics of a (a) cathode-directed (or positive) streamer and (b) anode-directed (or negative) streamer at t_1 and t_2 ($t_2 > t_1$). The anode-directed (or negative) streamer occurs in a longer gap.[6,10-11]

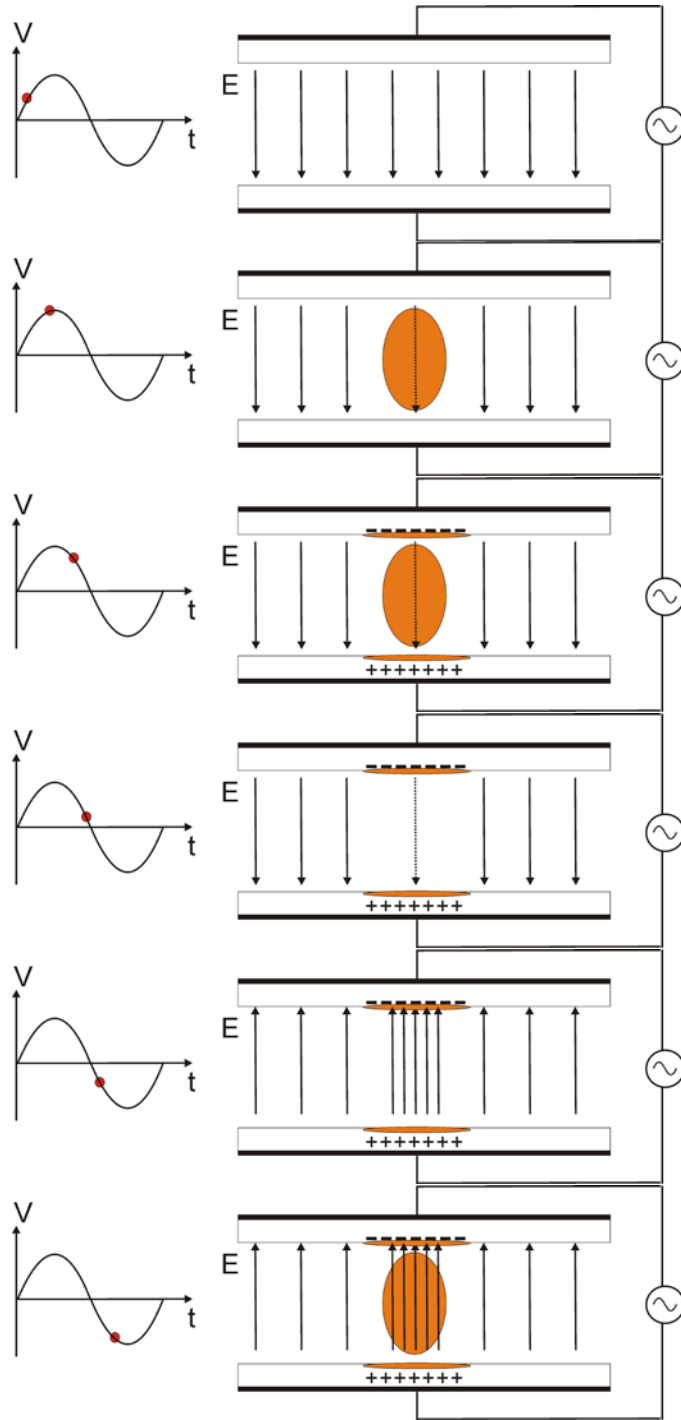


Figure 1.5 A time evolution of DBDs between a pair of parallel electrodes biased with AC voltage. The DBD prevents the formation of an arc.

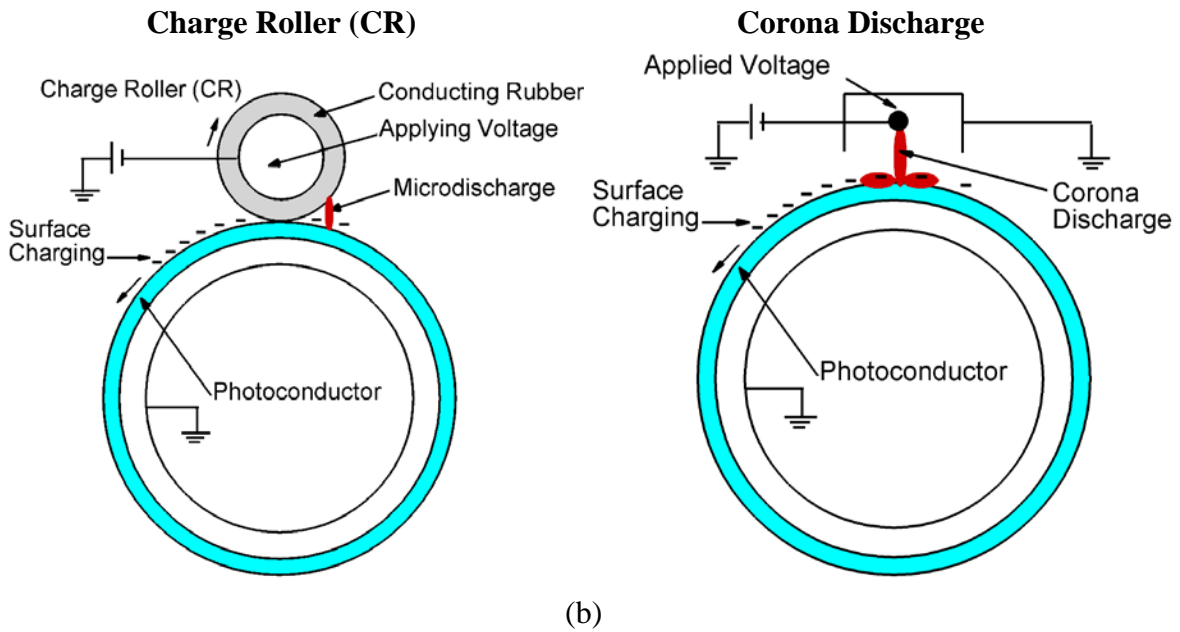
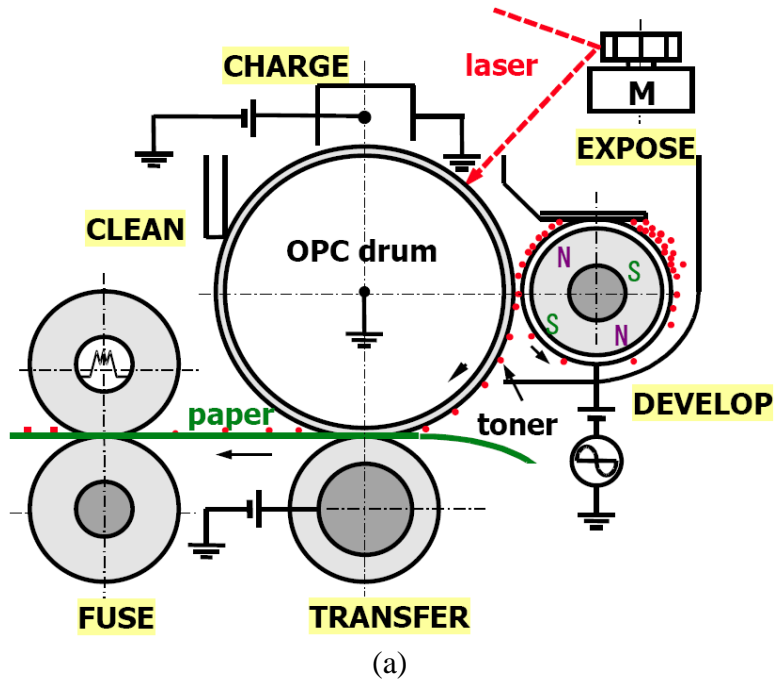
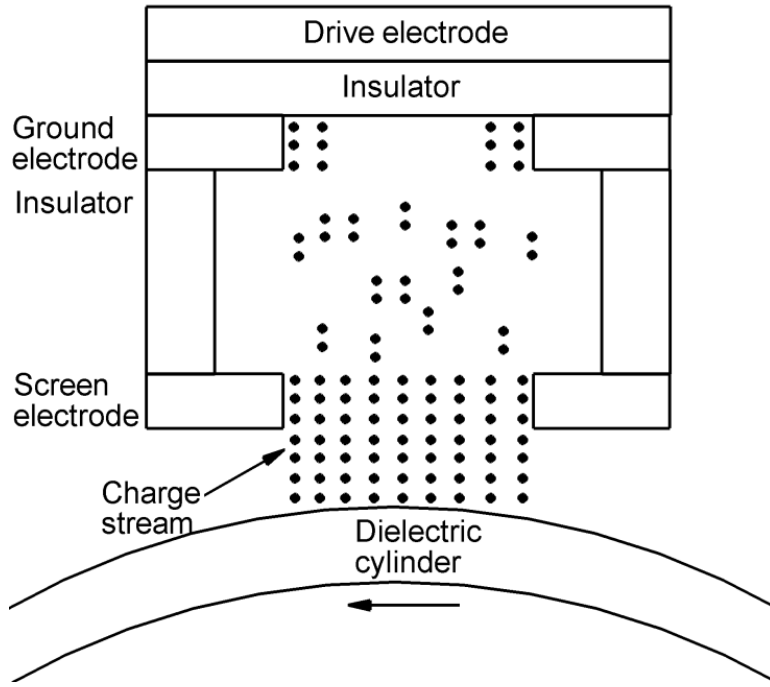
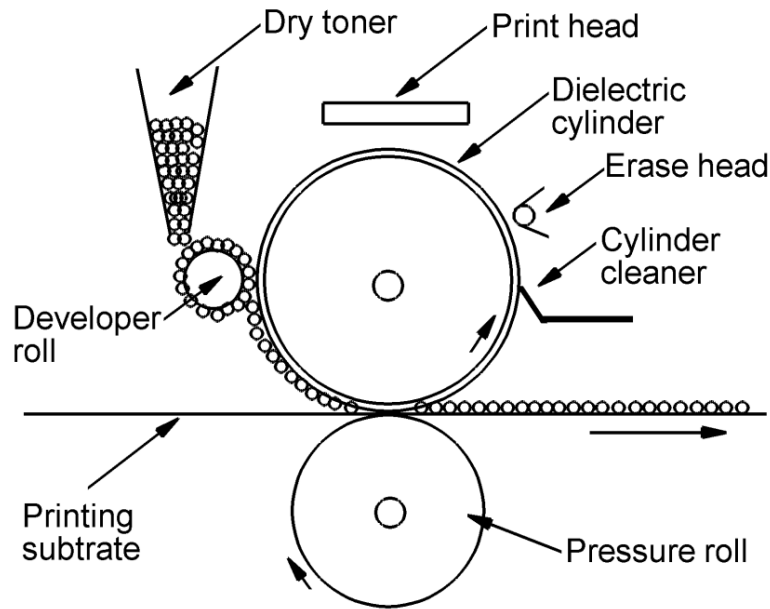


Figure 1.6 Elements of electrophotography (EP). (a) Six steps of EP printing.[43] (b) Surface charging by a charge roller (CR) and a corona discharge.

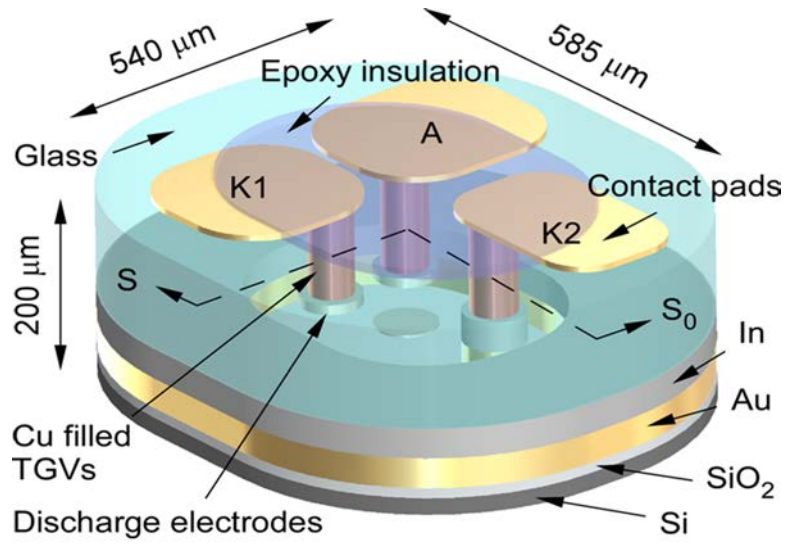


(a)

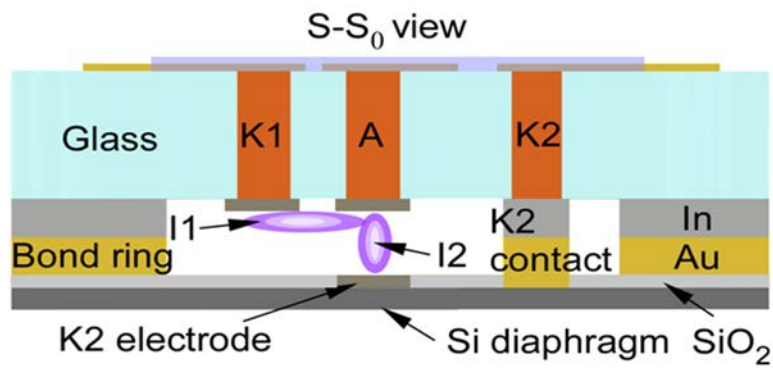


(b)

Figure 1.7 Schematic of ionography. (a) A typical printing head. (a) Printing process of ionography.



(a)



(b)

Figure 1.8 Schematic of microdischarge-based pressure sensor. (a) 3-D model of the pressure sensor. (b) S-S₀ view of the structure. I₁ and I₂ are discharge currents from two discharge paths.

1.11 References

- [1] L. Tonks, Am. J. Phys. **35**, 857 (1967).
- [2] I. Langmuir, Proc. Nat. Acad. Sci. U.S., **14**, 628 (1928).
- [3] L. Tonks and I. Langmuir, Phys. Rev. **33**, 195 (1929).
- [4] F. F. Chen, Introduction to Plasma Physics and Controlled Fusion. Vol. I: Plasma Physics, Springer, 2006.
- [5] James D. Callen, Fundamentals of Plasma Physics, University of Wisconsin, Madison, 2006.
- [6] Y. P. Raizer, Gas Discharge Physics, Springer, 1991.
- [7] M. A. Lieberman and A. J. Lichtenberg, Principles of Plasma Discharges and Materials Processing, 2nd Edition, Wiley-Interscience, 2005.
- [8] S. Eliezer and Y. Eliezer, The Fourth State of Matter: An Introduction to Plasma Science, 2nd Edition, IOP Publishing Ltd, 2001.
- [9] A. Grill, Cold Plasma Materials Fabrication: From Fundamentals to Applications, Wiley-IEEE Press, 1994
- [10] A. Fridman, A. Chirokov, and A. Gutsol, J. Phys. D: Appl. Phys. **38**, R1 (2005).
- [11] A. Fridman and L. A. Kennedy, Plasma Physics and Engineering, 2nd Edition, CRC Press, 2011.
- [12] M. Naidu and V. Kamaraju, High Voltage Engineering, 4th Edition, Tata McGraw-Hill, 2008.
- [13] H. Raether, Electron Avalanches and Breakdown in Gases, Butterworths Advanced Physics Series, Butterworth Inc., Washington, D.C. 1964.
- [14] L. B. Loeb and A. F. Kip, J. App. Phys. **10**, 142 (1939).
- [15] J. M. Meek, Phys. Rev. **57**, 722 (1940).
- [16] U. Kogelschatz, Plasma Chem. Plasma Process. **23**, 1 (2003).

- [17] S. Kanazawa, M. Kogoma, T. Moriwaki, and S. Okazaki, *J. Phys. D: Appl. Phys.* **21**, 838 (1988).
- [18] T. Yokoyama, M. Kogoma, T. Moriwaki, and S. Okazaki, *J. Phys. D: Appl. Phys.* **23**, 1125 (1990).
- [19] E. E. Kunhardt, *IEEE Trans. Plasma Sci.* **28**, 189 (2000).
- [20] H. H. Kim, *Plasma Process. Polym.* **1**, 91 (2004).
- [21] B. Eliasson, M. Hirth and U. Kogelschatz, *J. Phys. D: Appl. Phys.* **20**, 1421 (1987).
- [22] G. Borcia, C. A. Anderson and N. M. D. Brown, *Plasma Sources Sci. Technol.* **12**, 335 (2003).
- [23] M. Sira, D. Trunec, P. Stahel, V. Bursikova, Z. Navratil and J. Bursik, *J. Phys. D: Appl. Phys.* **38**, 621 (2005).
- [24] Z. Fang, X. Xie, J. Li, H. Yang, Y. Qiu and E. Kuffel, *J. Phys. D: Appl. Phys.* **42**, 085204 (2009).
- [25] J. P. Boeuf, *J. Phys. D: Appl. Phys.* **36**, R53 (2003).
- [26] J. Meunier, Ph. Belenguer and J. P. Boeuf, *J. Appl. Phys.* **78** (2), 731 (1995).
- [27] M. G. Kong, G. Kroesen, G. Morfill, T. Nosenko, T. Shimizu, J. van Dijk, and J. L. Zimmermann, *New J. Phys.* **11**, 115012 (2009).
- [28] H. Ayan, G. Fridman, A. F. Gutsol, V. N. Vasilets, A. Fridman and G. Friedman, *IEEE Trans. Plasma Sci.* **36**, 504 (2008).
- [29] C. Penache, C. Gessner, T. Betker, V. Bartels, A. Hollaender and C.-P Klages, *IEE Proc. Nanobiotechnol.* **151**, 139 (2004).
- [30] S. Kreitz, C. Penache, M. Thomas, and C. -P. Klages, *Surf. Coat. Technol.* **200**, 676 (2005).
- [31] N. Lucas, A. Hinze, C. P. Klages and S. Büttgenbach, *J. Phys. D: Appl. Phys.* **41**, 194012

(2008)

- [32] J. Zhang, Y. H. Wang and D. Z. Wang, *Phys. Plasmas* **17**, 043507 (2010).
- [33] A. Chirokov, A. Gutsol, A. Fridman, K. D. Sieber, J. M. Grace and K. S. Robinson, *Plasma Chem. Plasma Process.* **26**, 127 (2006).
- [34] L. Stollenwerk, J. G. Laven and H. G. Purwins, *Phys. Rev. Lett.* **98**, 255001 (2007).
- [35] S.-J. Park, J. G. Eden, K. Jain and M. A. Klosner, *Jpn. J. Appl. Phys.* **45**, 8221 (2006).
- [36] J. D. Readle, K. E. Tobin, K. S. Kim, J. K. Yoon, J. Zheng, S. K. Lee, S.-J. Park, and J. G. Eden, *IEEE Trans. Plasma Sci.* **37**, 1045 (2009).
- [37] S.-J. Park, P. A. Tcherchian, S. H. Sung, T. M. Spinka, J. G. Eden, *IEEE Trans. Plasma Sci.* **35**, 215 (2007).
- [38] D. M. Pai and B. E. Springett, *Rev. Mod. Phys.* **65**, 163 (1993).
- [39] L. B. Schein, *J. Vac. Sci. Technol. A* **25**, 1256 (2007).
- [40] C. B. Duke, J. Noolandi, and T. Thieret, *Surf. Sci.* **500**, 1005 (2002).
- [41] R. M. Schaffert, *Electrophotography* (Focal Press, London, 1965).
- [42] J. S. Chang, P. A. Lawless, and T. Yamamoto, *IEEE Trans. Plasma Sci.* **19**, 1152 (1991).
- [43] H. Kawamoto, *NIP24: International Conference on Digital Printing Technologies: September 6 – 11, 2008, Pittsburgh, Pennsylvania: Technical Program and Proceedings: Digital Fabrication 2008 (IS&T, 2008).*
- [44] Y. B. Gianchandani, C. Wilson, and J.-S. Park, "Micromachined Pressure Sensors: Devices, Interface Circuits, and Performance Limits," in *The MEMS Handbook*, ed: M. Gad-el-Hak, CRC Press, 2006, pp. 3.1-3.44.
- [45] S. A. Wright and Y. B. Gianchandani, *J. Vac. Sci. Technol., B* **25**, 1711 (2007).
- [46] S. A. Wright and Y. B. Gianchandani, *J. Microelectromech. Syst.* **18**, 736 (2009).

[47] S. A. Wright, H. Z. Harvey, and Y. B. Gianchandani, *J. Microelectromech. Syst.* **22**, 80 (2013).

[48] K. Ishii, Y. Hirano, and Y. Murakami, *IEEE Trans. Plasma Sci.* **36**, 1192 (2008).

CHAPTER 2 DESCRIPTION OF THE MODEL

2.1 Introduction

This research utilizes *nonPDPSIM* to study a wide range of plasma systems. An overview of *nonPDPSIM* along with a detailed explanation of modules and a block diagram of the code (see Fig. 2.1) is necessary to appreciate the scope and context of the following analysis of the various discharge systems. *nonPDPSIM* is a two-dimensional, multi-fluid hydrodynamic simulation code. It was originally written by Dr. Shahid Rauf and Prof. Mark J. Kushner in FORTRAN 77 to simulate plasma display panel (PDP) cells, but its application has grown in scope.[1] In this code, the continuity equations and Poisson's equation are simultaneously solved for densities of all charged species (electrons and ions), the charge density (in and on materials), and electric potential. The time evolution of the charged species densities and surface charges are simultaneously integrated with Poisson's equation using a fully implicit Newton-Raphson iterative method. The electron energy equation for the bulk electron temperature and neutral continuity equations are then also implicitly solved. Rate coefficients and transport coefficients for bulk electrons are obtained from local solutions of Boltzmann's equation for the electron energy distribution (EED). Once the electric potential, charge density, and electron temperature have been updated, radiation transport is addressed by using Greens function propagator. The radiation is produced by relaxation of high-lying excited states of gas species. An electron Monte Carlo simulation is applied to track the ionization sources produced by sheath-accelerated secondary electrons. Sources of secondary electrons include ion and photon fluxes onto surfaces. The differential

equations are discretized using finite volume techniques. The numerical grid uses a boundary fitting unstructured mesh with triangle elements with multiple refinement zones. Algorithms used in the model will be described in more detail in the following sections.[2-5]

2.2 Geometry, Mesh Generation, and Discretization

The differential equations in *nonPDPSIM* are discretized using finite volume techniques. The numerical grid uses a boundary fitting unstructured mesh with triangle elements with multiple refinement zones. The unstructured mesh, consisting of vertices (or nodes) and faces and cells with triangular elements was generated offline using the software SKY/Mesh2. SKY/Mesh2, an automatic mesh generator for surface meshes, was produced by SkyBlue systems. This software is no longer commercially available. To build a correct geometric model, the following data files are required: the geometry file, which defines the adjustable parameters of the model geometry; the points file, which defines the coordinates of the vertices of the model geometry; the edges file, which defines the connectivity of the geometry regions; the boundary conditions file, which defines the boundary conditions, such as material identities of the faces, edges and vertices, and zone numbers used for different initial conditions such as gas mixtures, pressure, and temperature. For applications that require high resolution modeling, SKY/Mesh2 provides an easy way to locally control the density and resolution of meshes using the refinement file. Once all the input files are accurately created, the unstructured mesh with triangular elements containing the coordinates, connectivity, and boundary conditions of each node, edges and faces can be generated using SKY/Mesh2. After the information of the mesh is fed into the *nonPDPSIM*, it is kept static throughout the simulation process. A typical example of model geometry and its mesh is shown

in Fig. 2.2. This model geometry is used for simulation of microdischarge-based pressure sensor and it will be discussed in Chapter 7.

The Vertex-Centered Finite Volume Method (VC-FVM) is used to discretize the partial differential equations addressing the plasma and fluid behavior in *nonPDPSIM*. The variables of interest in the Finite Volume Method (FVM) are averaged over control volumes (CVs) which are defined using the vertex-centered approach. Examples of control volume mesh (CV mesh) and actual mesh are shown in Fig. 2.3. In an actual mesh, the vertices of each triangle are called “nodes” (e.g., nodes 1–7 in which nodes 2–7 are the “neighbors” of node 1). The nodes and the solid lines that connect nodes are the output from the mesh generator. In a vertex-centered approach, the CVs are around the vertices (e.g., node 1) and the average variables over the CVs are stored on the nodes. The CV that is associated with each node is constructed by identifying the intersection of the perpendicular bisectors between node 1 and its nearest neighbors (e.g., nodes 2-7); the “cell corners” (e.g. A, B, C, D, E, or F) are defined as the intersections of the perpendicular bisectors. The area enclosed by the dashed lines and cell corners (e.g., area ABCDEF) is referred to as “cell”. The volume of CV is obtained by $V_{CV} = A_{cell} \times D_{CV}$ where V_{CV} , A_{cell} , and D_{CV} represent volume of CV, area of the cell, and depth of CV respectively. Since it is a 2-D simulation, volume of CV is referred to as the area of the cell, A_{cell} , and D_{CV} is cancelled from the equations.

Once the coordinates of cell corners are obtained, the control volume ($V_{i,j}$) and area ($A_{i,j}$) between node i and node j used for FVM can be calculated. For example, $A_{1,2}$ is the area between node 1 and node 2 is,

$$A_{1,2} = L_{A,B} \times D_{CV} = \sqrt{(x_B - x_A)^2 + (y_B - y_A)^2} \times D_{CV}, \quad (2.1)$$

where $L_{A,B}$ is the length between cell corners A and B; x and y are coordinates; $V_{1,2}$ is the volume between node no. 1 and no. 2 is,

$$V_{1,2} = \frac{ab \sin(\alpha)}{2} \times D_{CV}, \quad (2.2)$$

where a , b , and α are the lengths and angle indicated in Fig. 2.3(b). The total control volume associated with node 1 can be obtained by the summation of the volumes shared between node 1 and each of its neighbors (e.g. nodes 2–7):

$$V_1 = V_{CV} = A_{cell} \times D_{CV} = \sum_{j=2}^{j=7} V_{1,j}, \quad (2.3)$$

Practically, the depth of a CV (D_{CV}) is cancelled out as the ratio of area to volume in FVM is used. The depth becomes irrelevant in this 2-D simulation. All the geometrical factors such as volumes and areas associated with nodes in the model geometry are computed at the beginning of the execution of the program. The typical numerical operator of gradient, divergent, and Laplacian for FVM can be obtained by

$$\bar{\nabla} \phi_i = \frac{1}{N} \sum_{j=1}^N \left[\frac{\phi_j - \phi_i}{l_{i,j}} (\cos \theta_{i,j} \hat{x} + \sin \theta_{i,j} \hat{y}) \right], \quad (2.4)$$

$$\bar{\nabla} \cdot \bar{\phi}_i = \frac{1}{V_i} \sum_{j=1}^N [\phi_{i,j} A_{i,j}], \quad (2.5)$$

$$\nabla^2 \phi_i = \frac{1}{V_i} \sum_{j=1}^N \left[\frac{\phi_j - \phi_i}{l_{i,j}} A_{i,j} \right], \quad (2.6)$$

where ϕ_i and ϕ_j are scalar variables on nodes i and j ; $l_{i,j}$, $\theta_{i,j}$, $\phi_{i,j}$ and $A_{i,j}$ refers to distance, angle, flux, and surface area between nodes i and j ; N and V_i are the number of neighbors and the control volume for node i ; $\bar{\phi}_i$ is a vector variable on node i . [6,9,11]

2.3 Interpolation of E/N

The value of E/N (electric field/total density) is a fundamental parameter in low temperature plasma. However, it is not that straightforward on an unstructured mesh. In *nonPDPSIM*, an interpolation technique is used to interpolate the potential on the unstructured nodes back to the x-y axis. An example of interpolation technique is shown in Fig. 2.4. The algorithm goes through four quadrants of each node (e.g., node 1) and searches for two neighbors closest to each axis (+x, +y, -x and -y) based on the angle of the neighbor respect to the axes. A line (e.g., dashed line) connecting these two nodes crosses the axis and gives an interpolated node (e.g., node a, b, c, and d) on the axis. A linear interpolation is then performed to obtain the potential on the interpolated node. For example, the voltage (Φ_a) on the interpolated node a can be obtained by

$$\Phi_a = \frac{\Phi_3 l_3 + \Phi_2 l_2}{l_3 + l_2}, \quad (2.7)$$

Electric field on the central node (e.g., node 1) can be computed using a finite difference method based on electric potential on nodes a – d. Once the electric field is computed, E/N at each node is obtained by

$$\frac{E}{N} = \frac{\sqrt{E_x^2 + E_y^2}}{N}, \quad (2.8)$$

where E_x and E_y are electric fields in x and y direction and N is the total density. In certain situations where the electric field along the central node i and its neighbor node j is required, the field can be computed by $E_{i,j} = -(\Phi_i - \Phi_j)/l_{i,j}$, where $l_{i,j}$ ($l_{i,j}$ is always positive) is the distance between node i and j , where the positive $E_{i,j}$ represents the electric field vector pointing outward

from the central node i to its neighbor node j , while the negative $E_{i,j}$ represents the vector pointing inward from the neighbor node j to the central node i . [6,8]

2.4 Plasma Dynamics

The fundamental equations we solved simultaneously for charged species and electric potential are,

$$-\nabla \cdot (\epsilon \nabla \Phi) = \sum_j N_j q_j + \rho_s, \quad (2.9)$$

$$\frac{\partial N_i}{\partial t} = -\nabla \cdot \bar{\phi}_i + S_i, \quad (2.10)$$

$$\frac{\partial \rho_s}{\partial t} = \left[\sum_i q_i (-\nabla \cdot \bar{\phi}_i + S_i) - \nabla \cdot (\sigma (-\nabla \Phi)) \right]_{material}, \quad (2.11)$$

where i , ϵ , Φ , ρ_s , N , ϕ , σ , S , and q refer to charged species, permittivity, electric potential, surface charge density, charged species number density, species flux, material conductivity, source terms, and elementary charge respectively. The source term, S_i , includes the production and loss of species i due to electron impact excitation and ionization, heavy particle reactions, photoionization, secondary electron emission, field emission, and surface reaction. Poisson's equation (Eq. (2.9)) is solved to determine the electric potential (Φ) for the whole computational domain except for the electrodes where potential is given as a boundary condition. The highly conductive materials or floating electrodes are treated as a dielectric with a high conductivity. Charge species number densities (N) are obtained by solving the continuity equation (Eq. (2.10)). The total charge density accumulated on the dielectric surface (ρ_s) is computed using a surface charge balance equation (Eq. (2.11)) that includes fluxes of charged species onto the surface and the dielectric relaxation (or conduction process) by conductivity of materials. Once the flux strikes a surface, a

flux-in/flux-out boundary condition is used for surface chemistry. For example, as a flux strikes the surface, a certain portion of the flux will be returned and/or converted to other returning species governed by specifications selected by the user. The flux returned to the plasma from the surface can be written as,

$$\phi_i = \phi_i^0 (1 - \alpha_i) + \sum_k \phi_k^0 \beta_{k,i}, \quad (2.12)$$

where ϕ_i^0 and ϕ_k^0 are flux of species i and k into the surface, α_i is the fraction of species i that disappears on the surface, and $\beta_{k,i}$ is the fraction that the species k is converted to species i . When the striking species are ions, the returning species are typically neutral species and secondary electron emission from the surface due to ion bombardment.

When the momentum transfer collisional frequency is larger than the driving frequency of external electric field, the drift-diffusion (DD) approximation can be used instead of the momentum conservation equation. The inertia of charged particles is neglected and the drift velocity instantaneously responds to the external electric field and diffusion. In the high pressure environment (pressure ≈ 100 's Torr), it is not necessary to solve the momentum equation for charged particle transport. In *nonPDPSIM*, the electron flux $\bar{\phi}_e$ is expressed using DD approximation, which considerably reduces the simulation time, while the ion flux $\bar{\phi}_i$ can be obtained by using DD approximation or solving the momentum conservation equation. The DD approximation is given by

$$\bar{\phi}_{DD} = \frac{q}{|q|} \mu N \bar{E} - D \nabla N \quad (2.13)$$

where D , μ , and E are diffusion coefficients, mobility, and electric field. When using the DD approximation, two methods are implemented to compute the flux: Eq. (2.13) can be directly

computed for drift-diffusion flux, or numerically implemented using the Scharfetter-Gummel scheme [12-13] which provides an optimized and stable approach. The Scharfetter-Gummel flux has the properties of being upwind or downwind according to the direction and the magnitude of the drift flux compared to the diffusion flux. In this method, the flux ($\phi_{i,j}$) between node i and j is given by

$$\bar{\phi}_{i,j} = v_{i,j} \left(\frac{N_i - N_j \exp(-v_{i,j} \Delta_{i,j} / D_{i,j})}{1 - \exp(-v_{i,j} \Delta_{i,j} / D_{i,j})} \right),$$

$$v_{i,j} = \frac{q}{|q|} \mu_{i,j} \bar{E}_{i,j}, \quad D_{i,j} = \frac{D_i + D_j}{2}, \quad \mu_{i,j} = \frac{\mu_i + \mu_j}{2} \quad (2.14)$$

where $v_{i,j}$ and $\Delta_{i,j}$ are drift velocity and distance between nodes i and j , respectively.

Due to dielectric relaxation, the maximum time step for explicit time integration in typical low temperature plasma simulations during the discharge pulse is on the order of 10^{-12} second, which makes the simulations slow for modeling practical devices and complicated gas mixtures. To overcome this time constraint, the equations (Eq. (2.9) – Eq. (2.11)) are solved simultaneously for time evolution of Φ , N , and ρ_s on each node using a fully implicit Newton-Raphson iterative method. A schematic of this method is shown in Fig. 2.5. The variables at time $(t + \Delta t)$ are obtained from

$$X(t + \Delta t) = X(t) + \frac{\partial X(t)}{\partial t} \Delta t = X(t) + \Delta X, \quad (2.15)$$

where X represents Φ , N , and ρ_s . Eq.(2.9) – Eq.(2.11) are rewritten in terms of new functions F_1 , F_2 and F_3

$$F_1 = \nabla \cdot (\epsilon \nabla \Phi) + \sum_j N_j q_j - \rho_s = 0, \quad (2.16)$$

$$F_2 = \frac{\partial N_i}{\partial t} + \nabla \cdot \bar{\phi}_i - S_i = 0, \quad (2.17)$$

$$F_3 = \frac{\partial \rho_s}{\partial t} - \left[\sum_i q_i (-\nabla \cdot \bar{\phi}_i + S_i) - \nabla \cdot (\sigma(-\nabla \Phi)) \right]_{material} = 0, \quad (2.18)$$

which can be linearized using first order Taylor series expansion

$$F_i(X_j(t + \Delta t)) = F_i(X_j(t)) + \frac{\partial F_i(X_j(t))}{\partial X_j} \Delta X_j$$

$$\Delta X_j = X_j(t + \Delta t) - X_j(t) \quad (2.19)$$

where $F_i(X_j(t + \Delta t))$ is function F_i and variable X_j at time $(t + \Delta t)$. For example, expansion of

Eq. (2.16) can be linearized as shown as,

$$\begin{aligned} & \frac{\partial F_{1,i}}{\partial \Phi_i} \Delta \Phi_i + \frac{\partial F_{1,i}}{\partial N_i} \Delta N_i + \frac{\partial F_{1,i}}{\partial \rho_{s,i}} \Delta \rho_{s,i} + \dots + \frac{\partial F_{1,i}}{\partial \Phi_{i+k}} \Delta \Phi_k + \frac{\partial F_{1,i}}{\partial N_{i+k}} \Delta N_{i+k} + \frac{\partial F_{1,i}}{\partial \rho_{s,i+k}} \Delta \rho_{s,i+k} \\ & = -F_{1,i}(\Phi_i(t), \rho_{s,i}(t), N_i(t)), \end{aligned} \quad (2.20)$$

where i is the node being solved and $i+k$ is the dependence of the node i on all other nodes in the mesh. Expansion of Eq. (2.16) – Eq. (2.18) can be rewritten in a matrix form $\vec{J} \cdot \Delta X = B$, where matrix \vec{J} is the Jacobian matrix, ΔX is a vector which contains the unknown variables, and B is a vector that contains evaluation of functions F_1 to F_3 at time t on node i to k . For example, the matrix form can be written as

$$\begin{bmatrix}
\frac{\partial F_{1,i}}{\partial \Phi_i} & \frac{\partial F_{1,i}}{\partial N_i} & \frac{\partial F_{1,i}}{\partial \rho_{s,i}} & \dots & \frac{\partial F_{1,i}}{\partial \Phi_{i+k}} & \frac{\partial F_{1,i}}{\partial N_{i+k}} & \frac{\partial F_{1,i}}{\partial \rho_{s,i+k}} \\
\frac{\partial F_{2,i}}{\partial \Phi_i} & \frac{\partial F_{2,i}}{\partial N_i} & \frac{\partial F_{2,i}}{\partial \rho_{s,i}} & \dots & \frac{\partial F_{2,i}}{\partial \Phi_{i+k}} & \frac{\partial F_{2,i}}{\partial N_{i+k}} & \frac{\partial F_{2,i}}{\partial \rho_{s,i+k}} \\
\frac{\partial F_{3,i}}{\partial \Phi_i} & \frac{\partial F_{3,i}}{\partial N_i} & \frac{\partial F_{3,i}}{\partial \rho_{s,i}} & \dots & \frac{\partial F_{3,i}}{\partial \Phi_{i+k}} & \frac{\partial F_{3,i}}{\partial N_{i+k}} & \frac{\partial F_{3,i}}{\partial \rho_{s,i+k}} \\
\dots & \dots & \dots & \dots & \dots & \dots & \dots \\
\frac{\partial F_{1,i+k}}{\partial \Phi_i} & \frac{\partial F_{1,i+k}}{\partial N_i} & \frac{\partial F_{1,i+k}}{\partial \rho_{s,i}} & \dots & \frac{\partial F_{1,i+k}}{\partial \Phi_{i+k}} & \frac{\partial F_{1,i+k}}{\partial N_{i+k}} & \frac{\partial F_{1,i+k}}{\partial \rho_{s,i+k}} \\
\frac{\partial F_{2,i+k}}{\partial \Phi_i} & \frac{\partial F_{2,i+k}}{\partial N_i} & \frac{\partial F_{2,i+k}}{\partial \rho_{s,i}} & \dots & \frac{\partial F_{2,i+k}}{\partial \Phi_{i+k}} & \frac{\partial F_{2,i+k}}{\partial N_{i+k}} & \frac{\partial F_{2,i+k}}{\partial \rho_{s,i+k}} \\
\frac{\partial F_{3,i+k}}{\partial \Phi_i} & \frac{\partial F_{3,i+k}}{\partial N_i} & \frac{\partial F_{3,i+k}}{\partial \rho_{s,i}} & \dots & \frac{\partial F_{3,i+k}}{\partial \Phi_{i+k}} & \frac{\partial F_{3,i+k}}{\partial N_{i+k}} & \frac{\partial F_{3,i+k}}{\partial \rho_{s,i+k}} \\
\frac{\partial \Phi_i}{\partial \Phi_i} & \frac{\partial \Phi_i}{\partial N_i} & \frac{\partial \Phi_i}{\partial \rho_{s,i}} & \dots & \frac{\partial \Phi_i}{\partial \Phi_{i+k}} & \frac{\partial \Phi_i}{\partial N_{i+k}} & \frac{\partial \Phi_i}{\partial \rho_{s,i+k}}
\end{bmatrix}
\begin{bmatrix}
\Delta \Phi_i \\
\Delta N_i \\
\Delta \rho_i \\
\dots \\
\Delta \Phi_{i+k} \\
\Delta N_{i+k} \\
\Delta \rho_{i+k}
\end{bmatrix}
=
\begin{bmatrix}
-F_{1,i} \\
-F_{2,i} \\
-F_{3,i} \\
\dots \\
-F_{1,i+k} \\
-F_{2,i+k} \\
-F_{3,i+k}
\end{bmatrix}, \quad (2.21)$$

Each row in the Jacobian matrix represents the effect of perturbation of variables on the functions F_1 to F_3 . For example, the first row in the Jacobian matrix describes how the perturbations of variables (Φ , N , and ρ_s) on node i to node k affect the evolution of function F_1 on node i . Once the Jacobian matrix \bar{J} is computed, the unknown vector ΔX can be obtained by inverting the Jacobian matrix and solving $\Delta X = (\bar{J})^{-1} \cdot B$. The variables at time $(t + \Delta t)$ can be updated using $X(t + \Delta t) = X(t) + \Delta X$. The process will be iterated until the variables converge to $\Delta X_j / X_j \leq \varepsilon_{\max}$, where ε_{\max} is the error criterion which is the specified tolerance.

Once the density and potential (Φ , N , ρ_s) are updated, time is incrementally increased and the Eq. (2.16) – Eq. (2.18) are linearized and solved for that time step. The time step used in the model can be a fixed time step (the time step is specified in the input file) or a dynamic time step (time step is determined according to the difficulty that the matrix solver encountered). If the number of iterations for the matrix solver to find a converged solution increases (or decreases), the

time step for the next subsequent calculation will be reduced (increased) accordingly. The typical time step for atmospheric pressure plasma simulations is $10^{-12} - 10^{-11}$ seconds and the typical number of iterations is 10 – 20.[5,6-10,12-14,16]

2.5 Transport Coefficients, Rate Coefficients, and Electron Temperature

Several methods are used in the *nonPDPSIM* to compute electron transport coefficients and source functions for electron impact reactions using the electron energy distribution $f(\varepsilon)$ (EED). The simplest approach is to assume that the energy gained by charged particles from the electric field is locally balanced by the energy loss in collisional process. The transport and reaction coefficients then depend only on the local E/N . It is known as local field approximation (LFA). The LFA is valid if

$$v_{eq} > \frac{1}{E} \frac{\partial E}{\partial t} \text{ or } \frac{1}{\lambda_{eq}} > \frac{1}{E} \frac{\partial E}{\partial x} \quad (2.22)$$

where v_{eq} is the rate of energy (or momentum) relaxation and λ_{eq} is the distance over which the EED equilibrates. In this method, the spatially independent ($\nabla_x \cdot (\bar{v}f(\bar{v})) = 0$) and stationary ($\partial f(\bar{v})/\partial t = 0$) Boltzmann equation are solved for the local solution (the electron energy distribution $f(\varepsilon)$ (EED)) in a Boltzmann module using a two-term spherical harmonic expansion for a wide range of values for E/N . The EED is used to generate a lookup table of transport coefficients, electron impact reaction rates, electron temperature (T_e), and momentum transfer collision frequency (ν_m) as a function of E/N . This lookup table is interpolated and periodically updated during execution of the model as the composition of the electron collision partners varies.

In certain applications such as cathode fall (a region of strong field gradient) of glow discharges or high-frequency low pressure discharges used for plasma processing, Eq. (2.22) is

not valid and LFA cannot provide satisfactory results. To improve the accuracy, an alternative approach – an electron energy equation – is implemented to capture to some extent non-local effects by including the conduction and convection of electron energy. The electron energy equation [15] is solved to obtain the average energy (ε) and electron temperature (T_e):

$$\frac{\partial}{\partial t} \left(\frac{3}{2} n_e T_e \right) = \vec{j} \cdot \vec{E} - \nabla \cdot \vec{q}_e - n_e \sum_i \Delta \varepsilon_i k_i N_i,$$

$$\vec{q}_e = \frac{5}{2} \bar{\phi}_e T_e - \lambda \nabla T_e, \text{ and } \vec{j} = q_e \bar{\phi}_e, \quad (2.23)$$

where n_e is electron density, k_i is the rate coefficient for power loss for collision of electrons with species i having density N_i and electron energy loss $\Delta \varepsilon_i$, $\bar{\phi}_e$ is the electron flux obtained using the Scharfetter-Gummel scheme (as described in Sec. 2.4), λ is electron thermal conductivity, and T_e is the electron temperature expressed in terms of average energy defined as $\varepsilon = 3T_e/2 = \int_0^\infty f(\varepsilon') \varepsilon' d\varepsilon'$. The flux density of electron energy \vec{q}_e is composed of the hydrodynamic flux of enthalpy and the heat conduction flux. This equation is implicitly integrated in time using the successive over-relaxation technique (SOR) with an SOR parameter α_{SOR} of 1.7 – 1.8 specified in the input file. The electron temperature of node i at the next time step and the $(k+1)^{\text{th}}$ iteration can be obtained by

$$T_{e,i}^{n+1,k+1} = (1 - \alpha_{SOR}) T_{e,i}^{n+1,k} + \alpha_{SOR} \frac{T_{e,i}^n + \Delta t \left(\sum_{j=1}^{\text{all neighbors}} f_{1,j} T_{e,j}^{n+1,k} + f_{2,i} \right)}{1 + \Delta t \left(f_{3,i} + \sum_{j=1}^{\text{all neighbors}} f_{4,j} \right)}, \quad (2.24)$$

where i and j are the central node and its neighbor, n and $(n+1)$ are the current and next time steps, k and $(k+1)$ are the old and updated iterations, Δt is the same time step as used in Newton-Raphson iterative method as described in Sec. 2.4, The functions $f_{1,j}$ and $f_{4,j}$ contain the geometrical factors,

thermal conduction, and convection between node i and its neighbor node j ; the function $f_{2,i}$ contains the power deposition by Joule heating and power loss by collisions; the function $f_{3,i}$ contains the energy change due to collisions and variation of dn_e / dt . The electron transport coefficients, rate coefficients, and collision frequency for use in solving Eq. (2.23) and Eq. (2.24) are obtained by solving Boltzmann's equation for EED using a two-term spherical harmonic expansion, as in the LFA. Once the electron temperature is obtained, a lookup table of the collision frequency and reaction rate coefficients is constructed using the new electron temperature as the lookup factor. This table is also interpolated and periodically updated during simulation.

The mobility and diffusion coefficients for ions and neutral species do not dramatically change over the range of E/N of our interest, hence constant values are used for ion mobility at a given pressure, and the ion diffusion coefficient is given by the Einstein relation. The diffusion coefficients for neutral species are determined by the Lennard-Jones approximation.

The reaction mechanisms used for this simulation are specified in a separate input file entered into *nonPDPSIM*. If the reaction is an electron impact reaction, the rate coefficients are obtained from the Boltzmann module as a function E/N or electron temperature. If the reactions involve only heavy ions, the Arrhenius equation is used to compute the rate coefficient

$$k = A \left(\frac{T_g}{300} \right)^n \exp\left(-\frac{E_a}{T_g}\right) \quad (2.25)$$

where k , A , T_g and E_a are rate coefficient, Arrhenius coefficient, gas temperature, and activation energy respectively. During each time step the rates for all the reactions are calculated and the rate of production of charge and neutral species are coupled to the continuity equations via the source term in Eq. (2.17).[7-10,16-17]

2.6 Radiation Transport

Seed electrons far away from the avalanche can be generated by the photons from highly excited states in the ionized regions. This radiation transport is addressed using a Green's function approach, the end product of which is photoionization in the gas phase and photoelectron emission from selected surfaces. A schematic of radiation transport is shown in Fig. 2.6. In our model, the photo-ionization source ($\text{cm}^{-3}\text{s}^{-1}$) for species i at location \vec{r}_i resulting from photon emission by species j at location \vec{r}'_m is

$$S_i(\vec{r}_i) = N_i(\vec{r}_i) \sum_j A_j \int \sigma_{ji} N_j(\vec{r}'_m) G_j(\vec{r}'_m, \vec{r}_i) d^3 \vec{r}'_m,$$

$$G_j(\vec{r}'_m, \vec{r}_i) = \frac{\exp(-|\vec{r}'_m - \vec{r}_i|/\lambda_j)}{4\pi|\vec{r}'_m - \vec{r}_i|^2} = \frac{\exp\left(-\sum_k \int_{\vec{r}'_m}^{\vec{r}_i} \sigma_{jk} N_k(\vec{r}''_n) d\vec{r}''_n\right)}{4\pi|\vec{r}'_m - \vec{r}_i|^2}, \quad (2.26)$$

where N_j is the radiating species density with Einstein coefficient A_j , and σ_{ji} is the photoionization cross section for species i by photons emitted from species j . In traversing the plasma, the photons are absorbed by species k with cross section σ_{jk} . This is addressed by the Green function propagator $G_j(\vec{r}'_m, \vec{r}_i)$ which accounts for the probability of survival of the photons emitted at \vec{r}'_m to reach location \vec{r}_i with absorption length λ_j . $G_j(\vec{r}'_m, \vec{r}_i)$ also accounts for physical obstructions and view angles that might block the radiation. In practice, $G_j(\vec{r}'_m, \vec{r}_i)$ is computed only for a specified volume around \vec{r}'_m . The radiation transport model is an offline module, which is periodically called during the simulation to compute the photo-ionization and photoemission.[7-8,10]

2.7 Secondary Electrons and Field Emission

The algorithm used for radiation transport is also used to generate secondary electrons by photoemission from surfaces. The flux of secondary electrons ($\text{cm}^{-2}\text{s}^{-1}$) from surface location \vec{r}_i is

$$\phi_s(\vec{r}_i) = \sum_j A_j \int \gamma_j(\vec{r}_i) N_j(\vec{r}'_m) G_j(\vec{r}'_m, \vec{r}_i) d^3\vec{r}'_m, \quad (2.27)$$

where $\gamma_j(\vec{r}_i)$ is the photoemission probability for photon j . As the ion flux strikes the dielectric surface, the flux of returning secondary electrons is given by

$$\phi_s = -\sum_i \gamma_i \phi_i, \quad (2.28)$$

where γ_i and ϕ_i are the secondary electron emission coefficients and flux for species i . ϕ_s is then used as a boundary condition for electron flux at surfaces. The secondary emission coefficients used in these simulations were generally between 0.1 and 0.15 for all positive ions and photons.

The electric field-enhanced thermionic emission from metal surfaces was also included in the model using the Richard Dushman equation (Eq. (2.29)) to provide the locally emitted electron current density as a function of the work function of the metal and the electric field at the surface of the metal

$$j_e = AT_s^2 \exp\left(\frac{-\left(\Phi_w - \sqrt{q^3 \eta E_s / \epsilon_0}\right)}{KT_s}\right), \quad (2.29)$$

where T_s is the surface temperature, A is the Richardson-Dushman constant ($120 \text{ A K}^{-2} \text{ cm}^2$), Φ_w is the material work function, and η represents the local surface roughness that cannot be resolved by the mesh.[10]

2.8 Monte Carlo Simulation

In certain applications, secondary electron emission is an important process which might dramatically change the plasma dynamics.[5] In addition to the flux of secondary electrons represented using a fluid approximation, the Electron Monte Carlo Simulation (EMCS), a kinetic approach, is also implemented to more accurately resolve the energy transport and electron impact source results from the secondary electrons by tracking the trajectories of these secondary electrons emitted from surfaces. Based on local ion and UV photon fluxes and their secondary electron emission coefficients, electron pseudo-particles are released with an initial energy of 4 eV from numerical mesh nodes on surfaces. These pseudo-particles are weighted (with unit of electron/s) by the magnitude of the local ion flux, the secondary electron emission coefficient, and the number of particles released at each node. The trajectories of the sheath accelerated secondary electrons and their ionization progeny are tracked until they hit boundaries, move out of the region allocated for the EMCS region or fall below a specified energy, thereby being removed from EMCS and join the bulk electron distribution. The pseudo-particle energies are recorded during their trajectories to compute EEDs for the secondary electrons as a function of position $f(\epsilon, \mathbf{r})$ and from these EEDs, electron impact source functions are computed. Electrons emitted from surfaces (called primary electrons that represent injected current) which join the bulk electrons are recorded as sources of current and are included in the continuity equations for the bulk electron distribution. Primary electrons which strike surfaces are summed into sources for surface charging or, if the surface is an electrode, as a source of current.

The underlying computational mesh used in *nonPDPSIM* is unstructured, which makes integrating the trajectories of pseudo-particles in the EMCS difficult. To facilitate these integrations, a spatially fine rectangular Cartesian mesh is overlaid onto the unstructured mesh. A

schematic of unstructured and structured EMCS mesh is shown in Fig. 2.7. Electric field quantities are interpolated onto the structured mesh for use in advancing the trajectories of the pseudo-particles. The EEDs and electron impact source functions are computed on the structured mesh. These results are interpolated back onto the unstructured mesh. The EMCS is called periodically during the simulation and the source functions produced by the EMCS are held constant during that call to the EMCS.

2.9 Parallel Implementation of EMCS

The EMCS is computationally demanding. The computation time required to track all the pseudo-particles and to statistically determine the collisions and their scattered velocities increases with the number of pseudo-particles launched from the emission nodes. Therefore, launching fewer pseudo-particles is preferable. However, a sufficiently large number of particles need to be simulated to accurately resolve the energy transport (or electron impact source) and reduce the intrinsic noise produced by a finite number of pseudo-particles. In order to properly represent the electrons emitted from the emission nodes using pseudo-particles while reducing the computation time, an optimized particle trajectory algorithm has been implemented and parallelized using Open Multi-Processing (Open MP). OpenMP is an application programming interface (API) that supports multi-platform shared memory multiprocessing programming. It provides a portable and scalable model that enables programmers to develop shared memory parallel applications.[18]

A schematic of original and optimized particle trajectory algorithms in the EMCS is shown in Fig. 2.8. In the original algorithm, the pseudo-particles are “sequentially” launched from each emission node for which secondary emission occurs. This process is shown in Fig. 2.8(a)-(c). For example, the particles are first released from node 1 (the number of particles launched from each

node is N_p). The trajectories of particles are then tracked until they are removed from EMCS domain and join the bulk electron distribution (see Fig. 2.8(a)). After all the particles from node 1 are removed, the same amount of new particles (N_p) are then released from node 2 (see Fig. 2.8(b)). The process repeats until the pseudo-particles are released and recorded sequentially from all the emission nodes (the number of emission nodes is N_n).

An optimized particle trajectory algorithm is illustrated in Fig. 2.8(d). In this algorithm, particles are “simultaneously” launched from all emission nodes, N_n , for which secondary emission occurs. The number of total particles can be as large as $N_p \times N_n$. In general, the number of pseudo-particles launched from each node, N_p , is on the order of a few hundreds and the number of emission nodes in EMCS domain, N_n , is typically tens to hundreds of nodes. In the optimized algorithm, the large number of pseudo-particles ($N_p \times N_n$) simultaneously released from all emission nodes can be simulated using serial execution or OpenMP parallelization. The performance of the optimized algorithm with OpenMP parallelization is demonstrated using an idealized testing case and the result is shown in Fig. 2.9(a) and (b) for $N_p = 400$ and $N_p = 40,000$ particles released from each emission node. The number of emission nodes in this idealized testing case is $N_n = 59$. The speedup and efficiency are defined by

$$\begin{aligned}
 \text{speedup} &= \frac{T_{\text{original}}}{T_{\text{optimized+parallelized}}}, \\
 \text{and efficiency} &= \frac{\text{speedup}}{\text{Number of threads}}, \tag{2.30}
 \end{aligned}$$

where T_{original} is the total elapsed time spent on the original particle trajectory algorithm and $T_{\text{optimized+parallelized}}$ is the total elapsed time spent on the optimized algorithm using OpenMP parallelization with 1 – 8 threads of execution. In general, the speedup increases with number of threads and then reaches a plateau of speedup $\approx 2 - 3$ at 4 – 5 threads. It is expected that the

parallel performance is not scalable because of the general nature of *nonPDPSIM* – the code is written in a very general manner to enable use of many different options. This makes parallelization very difficult. I also find that the speedup decreases with increasing N_p and it might be because the size of the array for the particles becomes significantly large and the memory/cache cannot be sufficiently used when a large number of particles are launched ($N_p = 4,000$ shown in Fig. 2.9(b)). As a result, the total particles simultaneously emitted is so large ($N_p \times N_n = 4,000 \times 59 = 236,000$) that the idle threads, memory allocation or memory/cache synchronization might start to limit the scalability. In addition, the speedup for optimized algorithm using OpenMP parallelization with only one thread is higher than the speedup using original algorithm with serial execution. It is also expected, since the optimized algorithm (shown in Fig. 2.8(d)) is more efficient than the original version (shown in Fig. 2.8(a) to (c)). The serial execution should also run faster.

2.10 Figures

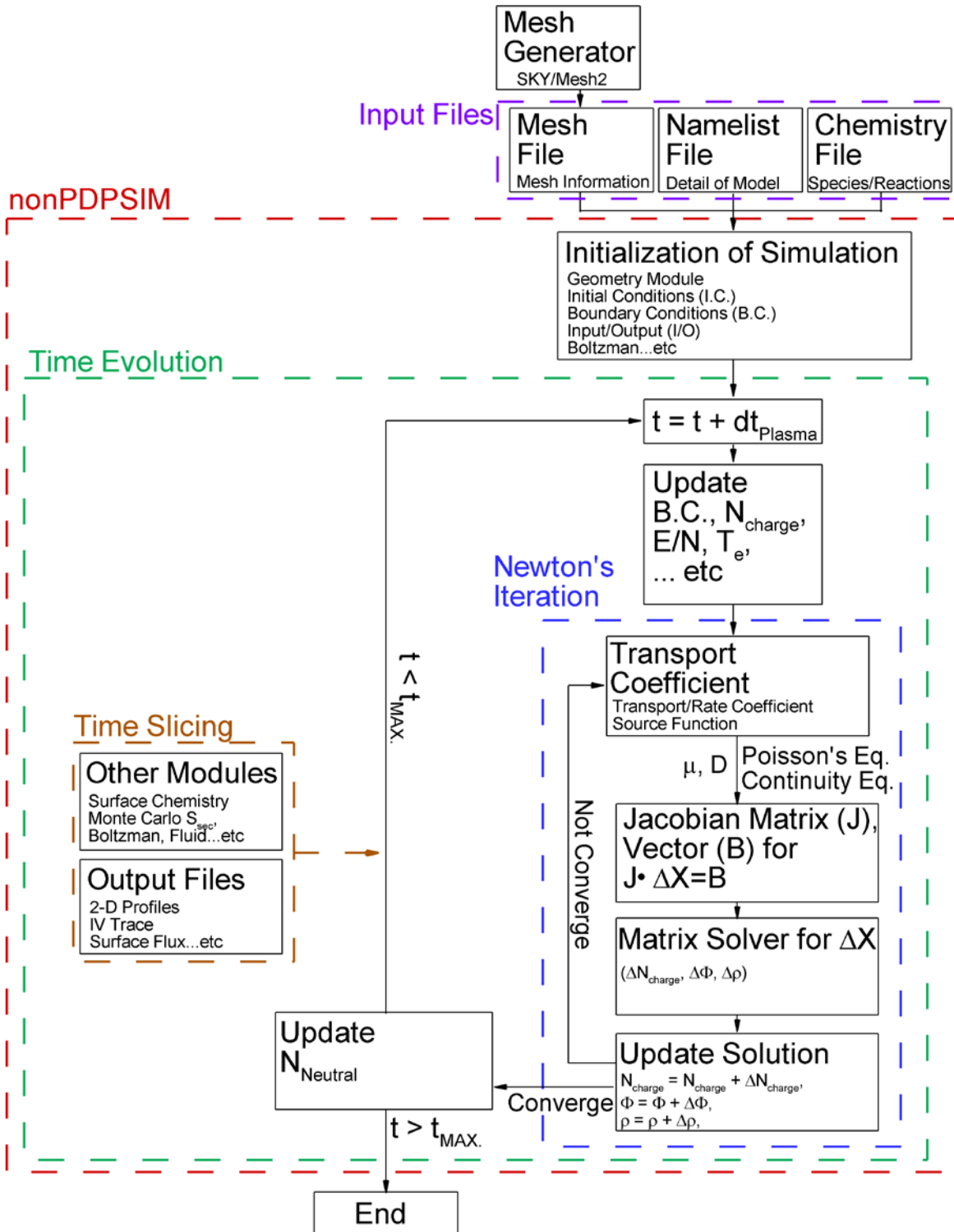


Figure 2.1 Block diagram of nonPDPSIM.

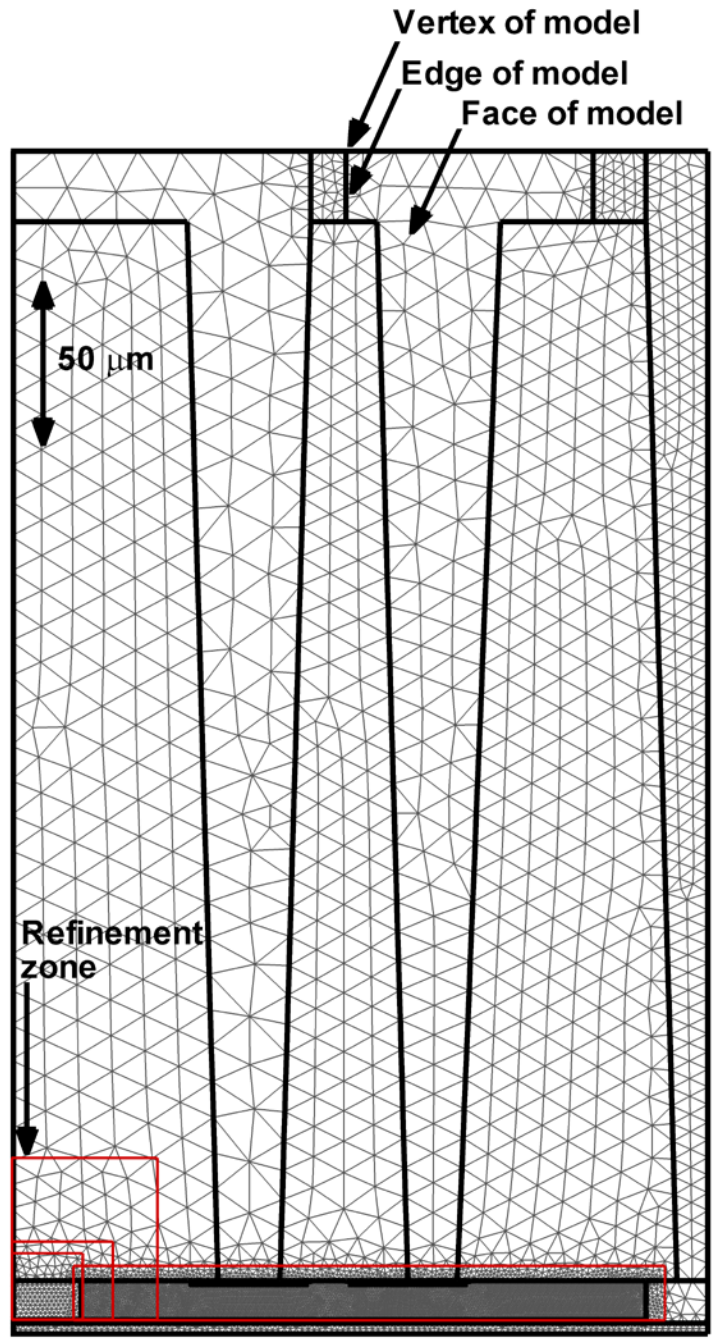


Figure 2.2 Model geometry and unstructured mesh used for the simulation of microdischarge-based pressure sensor. The refinement zones are highlighted by red rectangles.

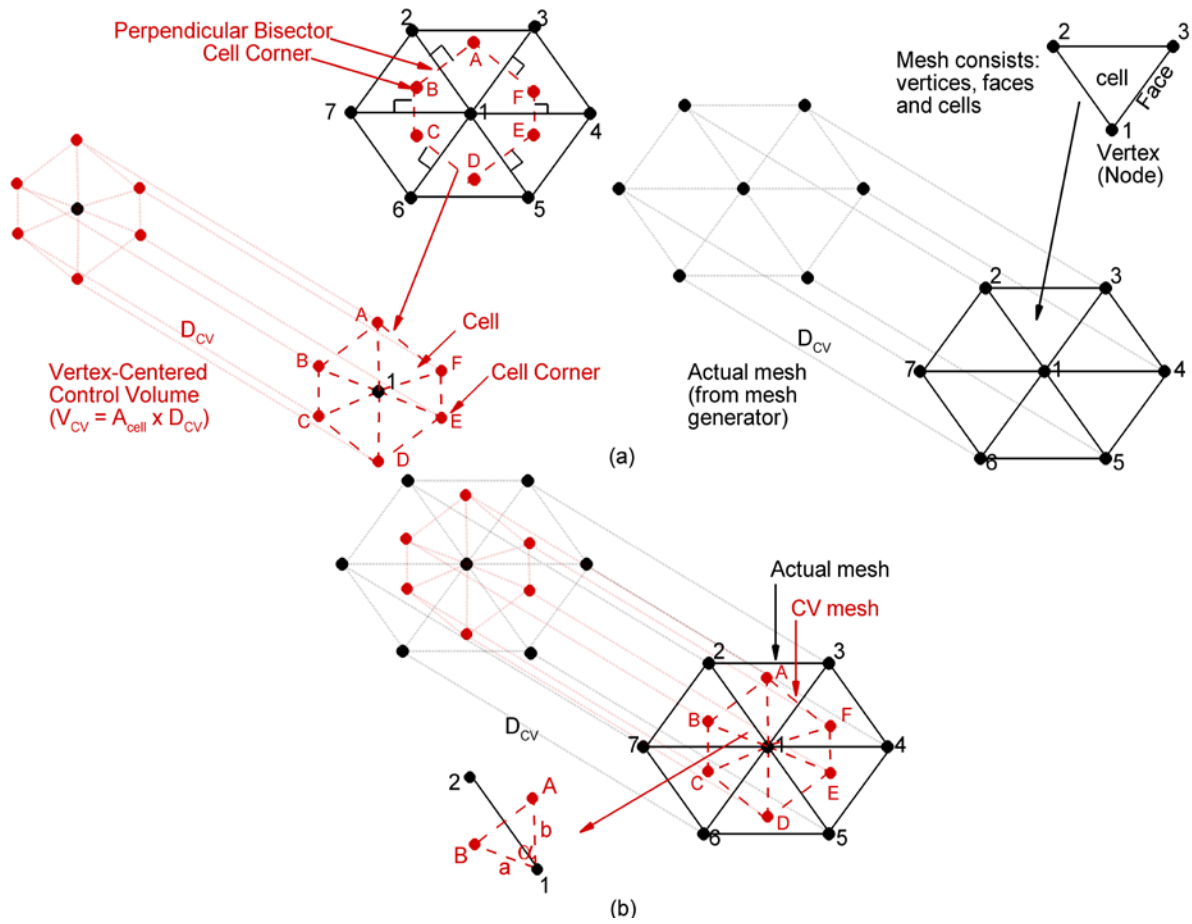


Figure 2.3 Control volume (CV) mesh and actual mesh. (a) The vertex-centered control volume is constructed by identifying the intersections of the perpendicular bisectors between a node and its nearest neighbors; the “cell corners” (A, B, C, D, E, or F) are defined as the intersections of the perpendicular bisectors. Actual mesh consists of vertices, faces, and cells. Nodes (no. 1–7) and solid lines which connect the nodes are output from the mesh generator. (b) The CV is centered around the vertex.

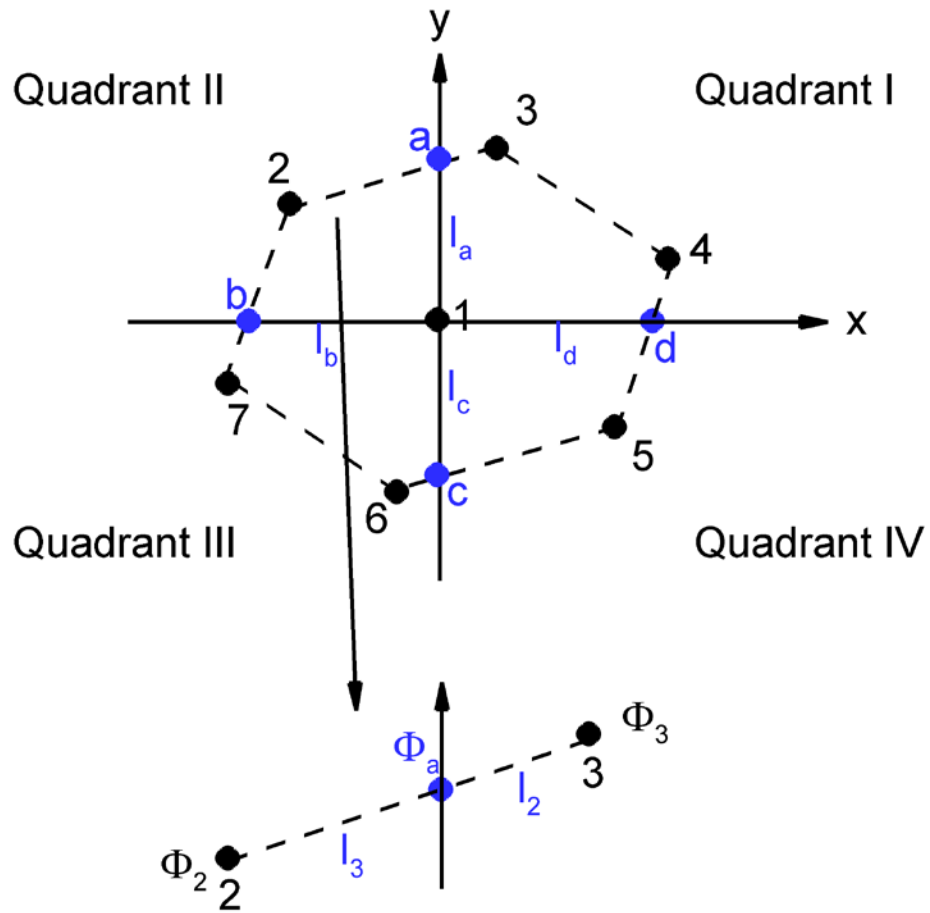


Figure 2.4 An example of the interpolation technique used to obtain electric field and E/N on an unstructured mesh.

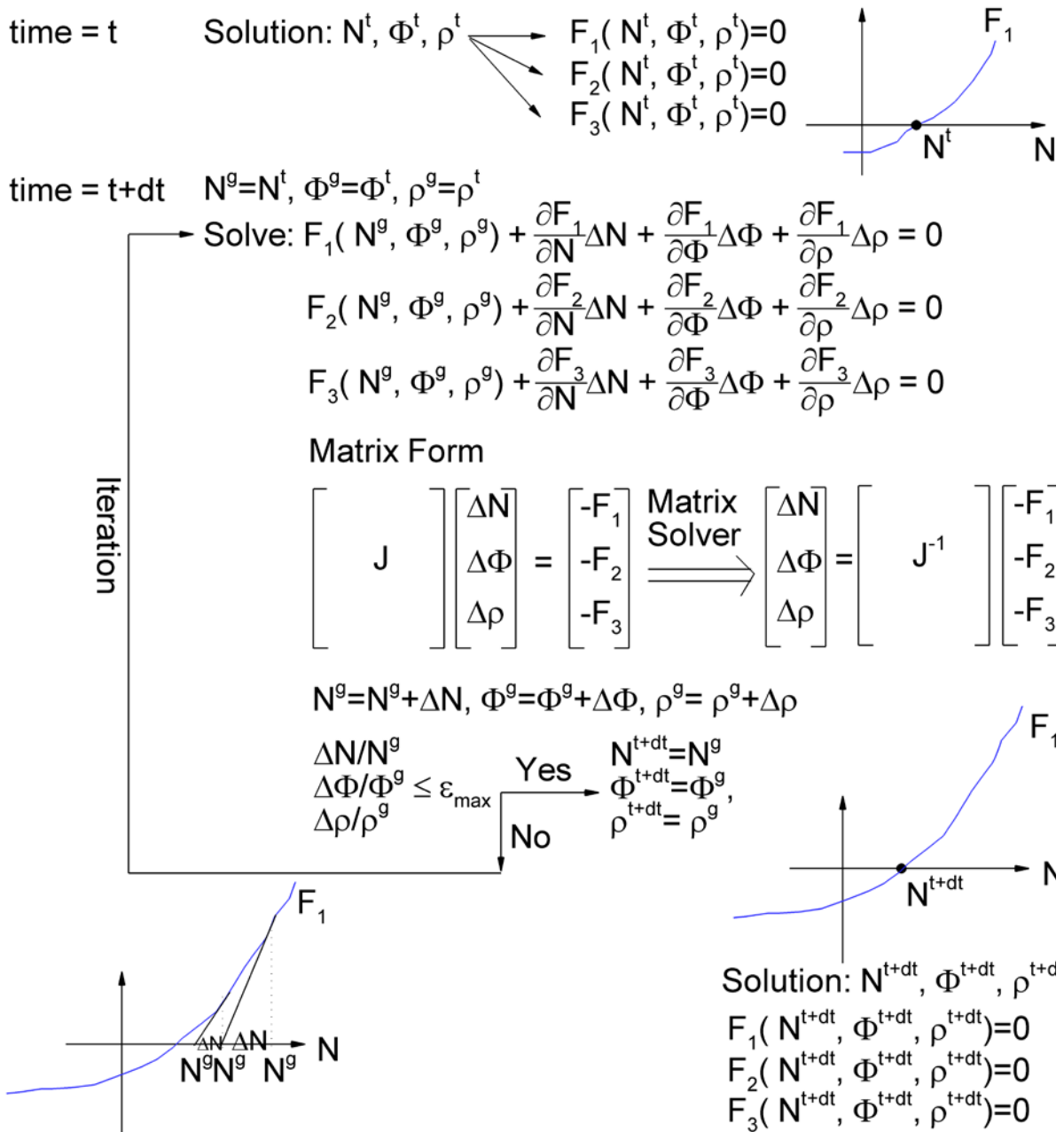


Figure 2.5 A schematic of the Newton-Raphson iterative method.

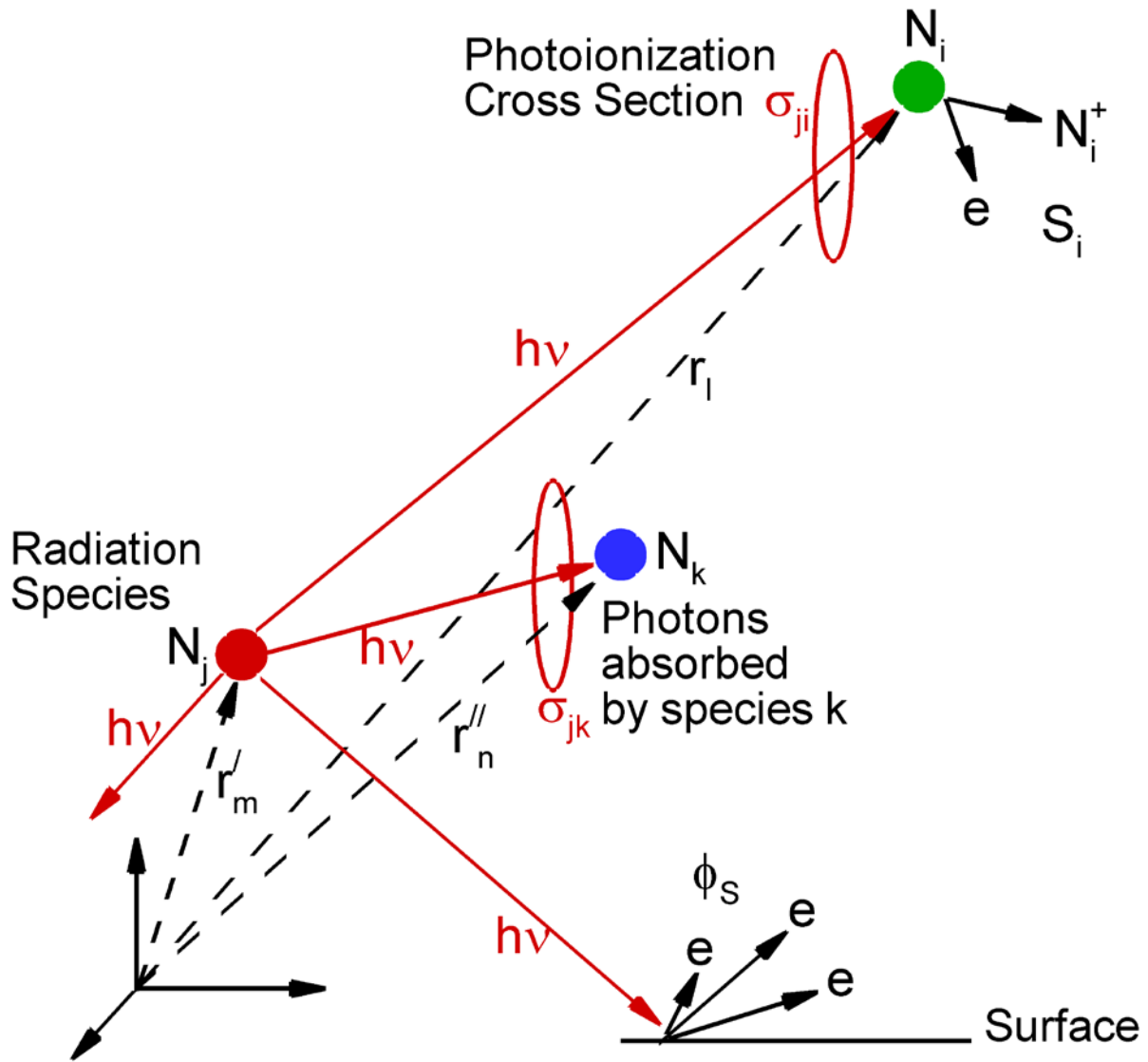


Figure 2.6 Schematic of radiation transport. Seeding of electrons far away from the avalanche is produced by photons from excited species in the ionization. Both photoionization and photoemission (ϕ_s) from the surface result from photons emitted by species j .

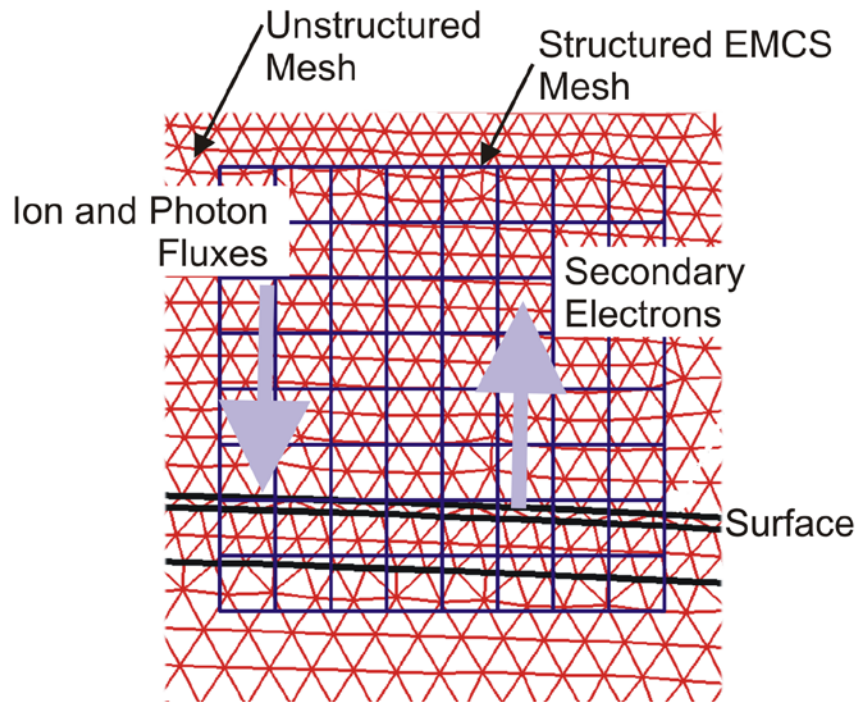


Figure 2.7 An electron Monte Carlo simulation is used to follow trajectories of secondary electrons from surfaces. The structured Cartesian mesh (CM) is overlaid onto the unstructured mesh (UM). The CM overlays only the portion of the UM in which beam electron transport is expected to be important. The resolution of the CM is chosen to be fine enough to capture the small scale feature of the UM.

- Pseudo-particle
- Emission node on Cartesian mesh

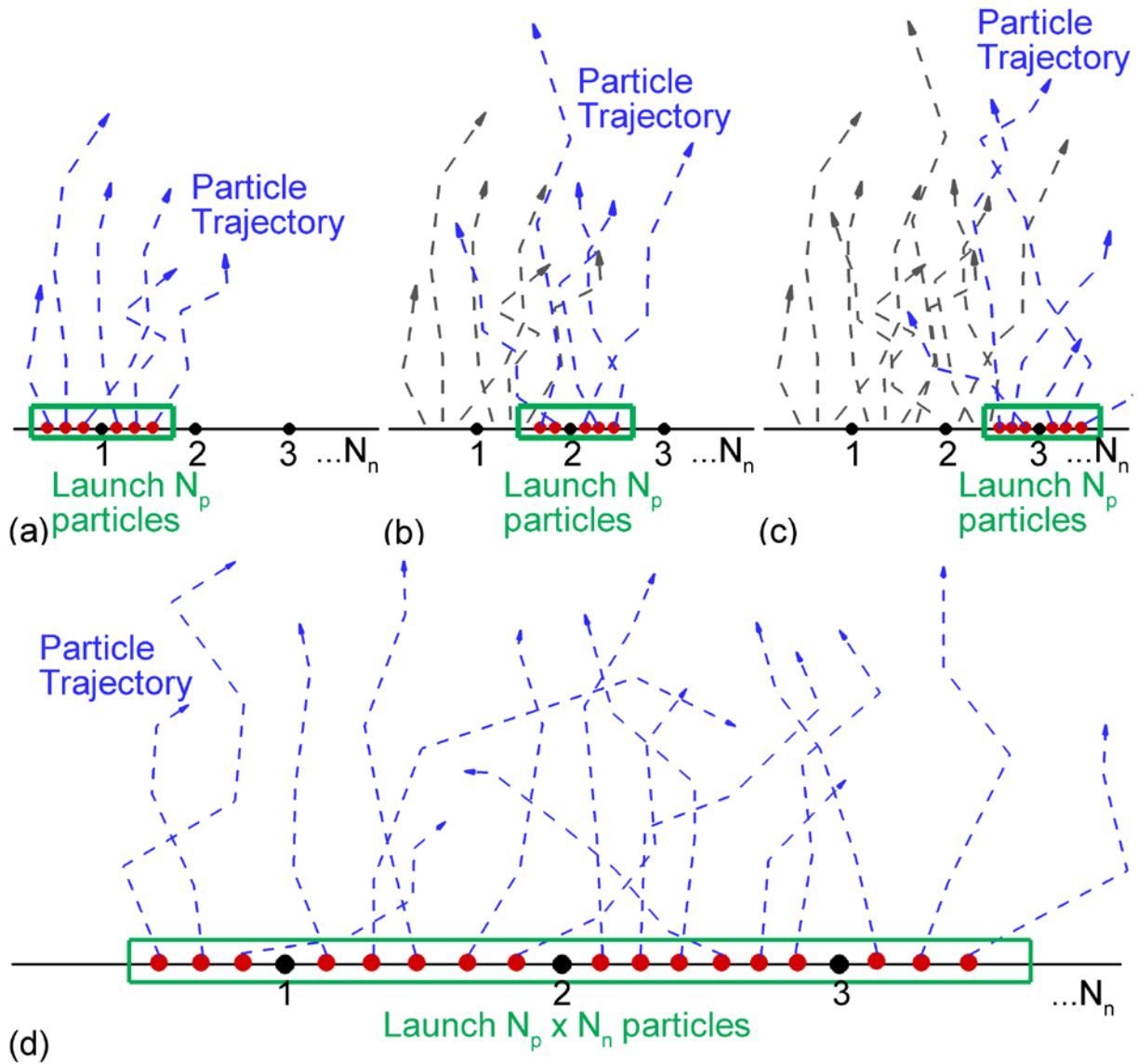


Figure 2.8 A schematic of original and optimized particle trajectory algorithms in the EMCS. In the original algorithm, particles are (a) first launched and from node 1. After all particles from node 1 are tracked and removed from EMCS domain, new particles are then released from (b) node 2 and then (c) node 3. The process repeats until particles are launched and recorded from all emission nodes. In the optimized algorithm (d), particles are simultaneously released from all emission nodes.

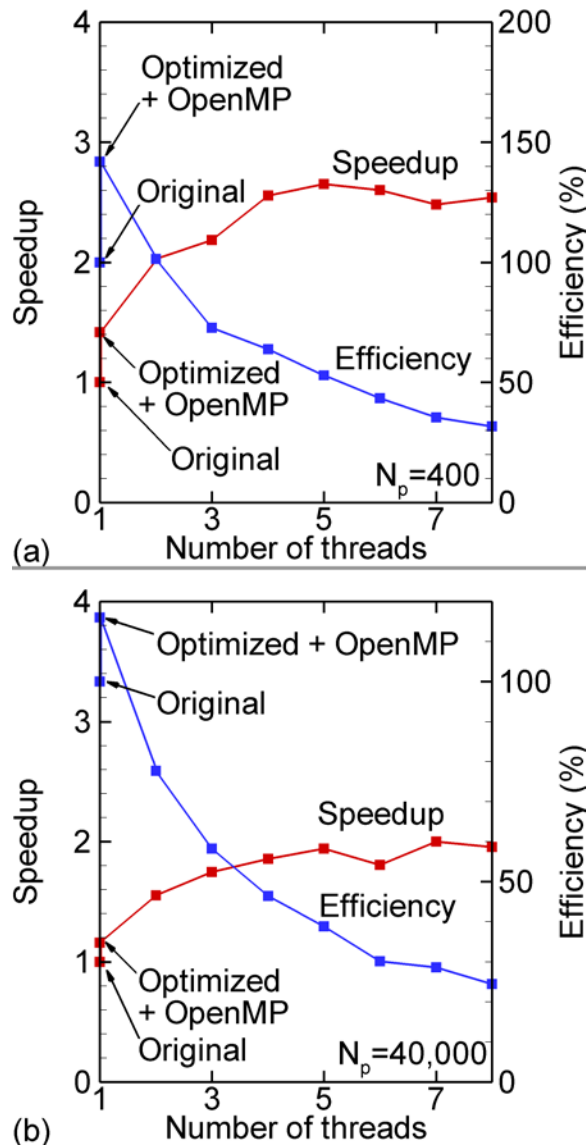


Figure 2.9 The speedup and efficiency for (a) $N_p = 400$; and (b) $N_p = 40,000$ from each emission node.

2.11 References

- [1] S. Rauf and M. Kushner, J. Appl. Phys., **85**, 3460 (1999).
- [2] J-C. Wang, N. Leoni, H. Birecki, O. Gila and M. J. Kushner, J. Appl. Phys. **113**, 033301 (2013).
- [3] B. M. Lay, R. S. Moss, S. Rauf and M. J. Kushner, Plasma Sources Sci. Technol. **12**, 8 (2003).
- [4] Z. Xiong and M. J. Kushner, J. Phys. D: Appl. Phys. **43**, 505204 (2010).
- [5] Mark. J. Kushner, J. Appl. Phys., **95**, 846 (2004).
- [6] B. M. Lay, MS Thesis, University of Illinois, 2000.
(<http://uigelz.eecs.umich.edu/theses.html>)
- [7] A. N. Bhoj, MS Thesis, University of Illinois, 2004.
(<http://uigelz.eecs.umich.edu/theses.html>)
- [8] A. N. Bhoj, PHD Thesis, University of Illinois, 2006.
(<http://uigelz.eecs.umich.edu/theses.html>)
- [9] R. A. Arakoni, PHD Thesis, University of Illinois, 2007.
(<http://uigelz.eecs.umich.edu/theses.html>)
- [10] B. M. Lay, R. S. Moss, S. Rauf and M. J. Kushner, Plasma Sources Sci. Technol. **12**, 8 (2003).
- [11] Finite Volume Method (FVM)
(<http://www.ctcms.nist.gov/fipy/documentation/numerical/discret.html#fig-vc-cc-fv>)
- [12] D. L. Scharfetter, and H. K. Gummel, IEEE Trans. Electron Devices. ED-**16**, 64 (1969).
- [13] Scharfetter-Gummel discretization scheme for drift-diffusion equations
(<http://www.utdallas.edu/~frensley/minitech/ScharfGum.pdf>)

- [14] M. J. Kushner, J. Phys. D: Appl. Phys. **42**, 194013 (2009).
- [15] Y. P. Raizer, Gas Discharge Physics, Springer, 1991.
- [16] H.C. Kim, F. Iza, S. S. Yang, M. R-Radjenovic and J. K. Lee, J. Phys. D: Appl. Phys. **38**, R283 (2005).
- [17] J. V. Dicarlo and Mark. J. Kushner, J. Appl. Phys., **66**, 5763 (1989).
- [18] OpenMP (openmp.org/wp)

CHAPTER 3 ELECTRON CURRENT EXTRACTION FROM RADIO FREQUENCY EXCITED MICRO-DIELECTRIC BARRIER DISCHARGES

3.1 Introduction

Extraction of electron current from arrays of microplasma devices is attractive due to its potential application for surface treatment of large areas with high spatial resolution.[1,2] A number of microplasma configurations have been investigated, including the cathode boundary layer (CBL) discharge [3], the capillary plasma electrode configuration (CPE) [4-6], microhollow cathode discharges (MHCD) [7,8] and dielectric barrier discharges (DBDs).[9-12] DBDs are becoming commonplace, particularly for applications at higher pressures (hundreds of Torr and above) due to their intrinsic stability against arcing. In fact, commercial plasma display panels use a DBD configuration, albeit on scales of hundreds of microns.[13-30]

One focus of this thesis is in arrays of DBDs operated at atmospheric pressure which can be used as sources of electron current for patterning dielectric surfaces. In this application, charge is extracted out of a micro-DBD (or mDBD) having an electrode structure of tens of microns in size using an auxiliary electrode separated by hundreds of microns.[31] These devices are capable of delivering narrow beams of extracted electron current tens of microns in diameter. Arrays of these mDBD devices can be used to form latent electrostatic images in the context of ion deposition

printing, charge deposition printing, ionography, electron beam imaging and digital lithography. This image transfer device may include, for example, laser printers, copiers or facsimiles.[31-33]

On larger spatial scales, these 3-electrode configurations [31-33] for microplasmas have been used at low pressure to extract charges or create plumes of excited states. For example, Pitchford *et al* [34,35] demonstrated efficient production of $O_2(^1\Delta)$ in a three-electrode microcathode sustained discharge. This configuration consisted of a MHCD acting as a plasma cathode to maintain a stable glow discharge between the MHCD and a third, positively DC biased planar electrode a few mm away.[7] Müller *et al* [36] demonstrated that one can use a large area plasma source based on surface discharge DBD system for the production and extraction of ions. A biased woven electrode is positioned on top of a flat disk of dielectric while the second grounded electrode is on its reverse side. A biased electrode in front of the DBD is used for extraction of ion current. Recently, a micro-plasma stamp [27] was developed based on the principle of mDBDs by Lucas *et al* for micrometer scale area-selective modification of surface properties. The dielectric barrier used in the micro-plasma stamp is a 600 μm thick PDMS (polydimethylsiloxane) layer patterned with circularly arranged cylindrical cavities having dimensions as small as a few microns. The atmospheric pressure microplasmas are ignited in these geometrically defined cavities which are formed temporarily by compressing the microplasma stamp and the substrate to be treated. The substrate acts as an extraction cathode.

Despite the fact that the plasmas sustained in mDBDs are relatively straight forward to generate, maintaining the system in a stable region and obtaining accurate measurements of plasma parameters are complicated and challenging due to their small spatial and temporal scales. In order to provide insights to the nonlinear plasma kinetics under such conditions, numerical simulation models have been developed to investigate plasma dynamics and their scaling [24,28,37-40].

In this chapter, the results of a numerical investigation of electron current extraction from an rf excited mDBD having an auxiliary electrode sustained in atmospheric pressure N_2 were presented. The mDBD device, shown in Fig. 3.1, consists of a cylindrical micro-cavity 65 μm in diameter in a grounded electrode, separated from an rf powered electrode by a dielectric sheet. The positively biased current extraction electrode is separated from the mDBD cavity by 400-500 μm . In this chapter, the rf driving voltage, frequency and dielectric constant of the insulator were parameterized. It was found that in properly designed devices, the vast majority of extracted current is produced in the mDBD cavity rather than in the gap between grounded electrode and top extraction electrode. Over the range of driving frequencies investigated (2.5 to 25 MHz) a pre-pulse and a single current pulse is produced at high frequency (10-25 MHz) which breaks into multiple current pulses at lower frequencies (2.5-5 MHz). Charge collection by the top biased electrode increases with increasing rf frequency, driving voltage and dielectric constant of the insulator.

The model used in this chapter is described in Sec. 3.2, followed by a discussion of the plasma dynamics and current extraction from mDBDs in Sec. 3.3. In Sec. 3.4, the dielectric charging characteristics and ionization processes in the mDBD cavity and gap are discussed. Charge collection by varying rf frequency, driving voltage and dielectric constant is discussed in Sec. 3.5. Sec. 3.6 contains our concluding remarks.

3.2 Description of the Model and Reaction Mechanism

The model used in this chapter, *nonPDPSIM*, is described in detail elsewhere [41-44] and in Chapter 2. The mDBD geometry is shown in Fig. 3.1. An rf electrode with applied voltage from 1.4 to 5.6 kV and frequencies of 2.5 to 25 MHz is buried in a printed-circuit-board having

relative permittivity $\epsilon_r = \epsilon/\epsilon_0 = 4.3$. A grounded electrode 25 μm thick is separated from the rf electrode by a 19 μm thick dielectric sheet having ϵ_r up to 20. This dielectric layer is, in the model, a perfect insulator - the conductivity is zero so that the surface charges are laterally immobile on the dielectric sheet. In reality, one can expect there will be some photon generated conductivity produced by the photon flux on the photoconductive materials used for dielectric. The cylindrically symmetric mDBD cavity is 65 μm in diameter with a 35 μm diameter opening. The top extraction electrode is biased with up to 2 kV and is separated from the grounded electrode by a 475 μm gap. A 100 k Ω ballast resistor is connected to the extraction electrode to limit the current and so prevent arcing. There are 5,700 computational nodes in the mesh of which 2,800 are in the plasma zone. The typical mesh spacing is 2 μm in the microdischarge cavity and 12 μm in the gap. Although the mDBDs are typically used in arrays, this work focuses on the scaling of a single cylindrically symmetric device.

The gas fill is 1 atm of N_2 with a small amount of O_2 as an impurity – $\text{N}_2/\text{O}_2 = 99.99/0.01$ at 300 K. This impurity reflects the estimated purity of the gas used in experiments. Including a small amount of O_2 impurity also provides an unambiguous species which can be photoionized. Due to the magnitude of the calculation, a reduced reaction mechanism containing a subset of the reactions described in [45,46] to minimize the computation time while capturing the dominant plasma hydrodynamics and chemistry is used. The reduced reaction mechanism includes N_2 , $\text{N}_2(v)$, N_2^* , N_2^{**} , N_2^{***} , N_2^+ , N_4^+ , N , N^* , N^+ , O_2 , $\text{O}_2(^1\Delta)$, O_2^+ , O_2^- , O_3 , O^- , O , $\text{O}(^1\text{D})$, O^+ and electrons. The states N_2^* and N_2^{**} are nominally $\text{N}_2(\text{A,B})$ and $\text{N}_2(\text{C})$ though the latter is treated as a lumped state including transitions higher than $\text{N}_2(\text{C})$, and N_2^{***} is nominally $\text{N}_2(\text{a}')$ and higher states.

The discharge is initiated by placing an electrically neutral electron-ion cloud centered in the mDBD cavity with peak density 10^{12} cm^{-3} and 100 μm in radius which is larger than mDBD

cavity. The precise density and radius of the initiating cloud does not affect the predicted operation of the device except during the first half cycle. A succession of rf cycles (referred to as pulses) are then computed. The time step is chosen dynamically and is typically 6×10^{-12} s during the high voltage portion of the cycle and 10^{-11} s during the low voltage portion of the cycle. Many rf cycles are computed until either quasi-steady state conditions are achieved or long term trends are discernable.

Although the gas temperature is held constant during the simulation, it is true that local gas heating can produce temperature excursions in pulsed microplasma devices. The dominant heating mechanisms are ion acceleration followed by charge exchange reactions and Franck-Condon heating following dissociative excitation during the current pulse. V-T relaxation of vibrationally excited states also contributes to gas heating after the current pulse. Since the current pulse is short compared to the entire pulse period, the large surface-to-volume ratio of these devices enables rapid heat transfer to the walls. This is facilitated by the majority of the heating occurring close to boundaries. As such, large temperature excursions are not expected.

3.3 Plasma Dynamics and Current Extraction from the mDBD

The characteristic of mDBD current extraction for a frequency of 25 MHz (pulse period of 40 ns) will first be discussed. The sinusoidal rf “peak” voltage is 1.4 kV and the top extraction voltage is 2 kV. The dielectric constant for the insulating sheet is $\epsilon_r = 20$. The time evolution of E/N (electric field/gas number density) and electron density in the mDBD cavity are shown in Fig. 3.2 over a single cycle. The electron density in the plume of extracted current is shown in Fig. 3.3. The electron temperature T_e , and electron impact ionization sources by bulk electrons, S_e and secondary electrons S_{sec} , are shown in Fig. 3.4.

The peak electron density, n_e , within the mDBD cavity is approximately $3.2 \times 10^{15} \text{ cm}^{-3}$, a value that is maximum when the potential on the rf electrode crosses zero toward negative values. The change of n_e in the mDBD cavity during the cycle is over a factor of 100. n_e in the electron plume has a maximum value of $2.5 \times 10^{12} \text{ cm}^{-3}$ 220 μm above the mDBD cavity to 10^{12} cm^{-3} 28 μm below the collection electrode, corresponding to that time when the rf voltage cross zero towards negative values. The electron density decays to negligible values within 15 ns of the peak as electrons are swept out of the gap into the collection electrode.

During the negative portion of the rf cycle, the positive ions in the mDBD cavity drift towards the dielectric and positively charge it. When the rf potential (V_{rf}) crosses from negative to positive at the beginning of the cycle ($t = 0 \text{ ns}$ in the figures), the net voltage between the top extraction electrode and the now positive dielectric is small due to the previous positive charging of the dielectric. The electrons in the mDBD drift towards the dielectric and begin to neutralize the positively charged dielectric. Before the positive peak of V_{rf} at $t = 10 \text{ ns}$, the negative charge collected on the dielectric has neutralized a sufficient amount of the positive charge that there is a net extracting field that accelerates electrons out of the mDBD cavity. A small flux of electrons, the pre-pulse, escapes from the cavity and is accelerated across the gap by the extraction electrode. This pre-pulse is magnified with large values of dV/dt hence is more prominent at higher rf frequencies.

When V_{rf} decreases to zero at $t = 20 \text{ ns}$, a negative potential still exists on the dielectric due to the previous collection of electrons. At this point, the extraction field is at maximum and an electron plume is then extracted from the cavity, which reduces the electron density in the mDBD cavity. At the same time, S_e and S_{sec} reach their maximum values ($10^{25} \text{ cm}^{-3}\text{s}^{-1}$), a consequence of an avalanche of remaining residual electrons in the mDBD cavity and by secondary electrons

emitted from the surface in the cavity. This in-cavity avalanche then enhances the current extraction to the top biased electrode. The electron plume reaches its greatest extent at 30 ns at the negative peak of V_{rf} . As this proceeds, positive ions are being collected on the dielectric, which reduces the voltage drop across the gap. The electron plume then begins to diminish and nearly extinguishes. The cycle then restarts.

The electron plume is essentially extinguished every rf cycle and so requires re-ignition each cycle. This re-ignition process is facilitated by the dynamics of E/N in the cavity. At the zero-crossing of V_{rf} at $t = 0$ ns, electrons are attracted to the center of dielectric. This conductive plasma then shields out and reduces the electric field, which in turn reduces the electron temperature T_e and S_e – they are only significant in the vicinity of the vertex of the grounded electrode where S_e up to $2.5 \times 10^{24} \text{ cm}^{-3}\text{s}^{-1}$ is produced. After the electron plume is extracted out of the cavity at $t = 20$ ns, the electron density is reduced which enables the voltage that was previously confined to the sheath to be dropped across the mDBD cavity. This enables a high T_e which avalanches the small remaining electron density, proving a source as high as $3.8 \times 10^{24} \text{ cm}^{-3}\text{s}^{-1}$. This avalanche enhances the electron plume and current extraction to the top biased electrode until the negative peak of V_{rf} is reached. Shortly after the negative peak in V_{rf} at $t = 35$ ns, the electron flux is attracted to the center of dielectric, and the conductive plasma shields the electric field, which reduces the ionization source. At this point, the ignition phase re-starts.

During the rf cycle, S_e and S_{sec} are synchronized with the dynamics of T_e . The secondary electron ionization source S_{sec} extends over a larger volume than S_e due to the longer mean free paths for the high energy electrons produced in the sheath compared to the bulk electrons accelerated in the volume. S_{sec} is also enhanced by a nearly continuous flux of UV photons incident onto all surfaces inside the mDBD cavity, including the dielectric, as discussed below.

The total charge density (ρ), positive and negative charges are shown in Fig. 3.5. Excited states $N_2(C)$ and $N_2(A,B)$ density are shown in Fig. 3.6. Before 10 ns, there is net positive charge on the dielectric and in the vicinity of the vertex of ground electrode. Secondary electrons released from the grounded electrode are due to positive ion bombardment and photons. The net positive charge on the dielectric transitions to negative charge within 10 ns. As the electrons are extracted from the cavity at $t = 20$ ns, positive ions strike the negatively charged dielectric, releasing secondary electrons. As a result, the secondary electron ionization source peaks near the discharge electrode and negatively charged dielectric when they behave cathodically. In addition to positive ions producing secondary electrons which, upon sheath acceleration, produce ionization, UV photon emission from excited states of nitrogen, also help seed the secondary electrons and re-ignite the avalanche. There can also be secondary emission from the flux of long lived excited states to these surfaces. Since the effective lifetimes of excited states are long compared to the intrapulse dynamics, at least for 25 MHz, there is a nearly continuous flux of UV photons which produce secondary electrons within the mDBD cavity. If produced during the anodic cycle (for that surface), these secondary electrons are accelerated back into the surface with little change in local plasma properties. If produced during the cathodic part of the cycle, the secondary electrons are accelerated by the sheath, and produce ionization throughout the volume of the mDBD cavity. Since S_{sec} is to some degree decoupled from the incident ion flux due to the availability of UV light, S_{sec} responds more quickly to changes in local electric field. These long lived neutral excited states become more important at lower frequencies for re-ignition when the mDBD cavity is more depleted of seed electrons.

3.4 Dielectric Charging Characteristics and Ionization Processes

As points of references, plasma properties will be discussed for the four sites (A, B, C and D) placed on the surface of the dielectric, in the cavity and in the gap, as shown in Fig. 3.1(b). The surface charge density σ_S , and the electron density, ionization source and E/N at sites A and B are shown in Figs. 3.7 and 3.8 for discharges in 1 atm of N_2 for frequencies ν_{rf} of 2.5 MHz to 25 MHz. For ν_{rf} up to 25 MHz, σ_S on the dielectric is nearly 180 degrees out of phase with V_{rf} . This is largely expected as the dielectric sheet behaves as a capacitor and the frequency is high, which maximizes the displacement current. However, due to the power dissipation in the device, this is not a purely capacitive system, and so there is a phase delay between V_{rf} , dielectric charging and surface potential. At 25 MHz, when V_{rf} increases to its positive peak at $t = 10$ ns, the negative charge density on the dielectric also reaches its peak value. However, the surface potential on the dielectric is still positive. Then σ_S slowly decreases (becomes less negative) with decreasing rf voltage. During this time, the positive potential on the dielectric decreases towards zero and then changes its polarity to negative. As the rf voltage reduces to nearly zero at $t = 20$ ns, a negative potential up to -500 V is produced due to the previously collected negative surface charges. In comparison, the discharge electrode behaves anodically to enable an electron avalanche and a large electron plume is expelled from the microdischarge cavity. When V_{rf} changes its polarity to negative, positive ions are drawn into the dielectric which charges it positively. The negative potential on the dielectric is increased (become less negative) and then transitions to positive values.

Over the range of frequencies investigated, this charging cycle does not dramatically change. However, as the frequency decreases, structure is produced in the local dielectric potential and σ_S . This oscillating structure can be attributed to *overshoot*. Since the capacitance of the

dielectric is fixed, there is a finite amount of charged particle fluence (either negative or positive) required to change the potential on the dielectric by a given amount. (Fluence, cm^{-2} , is flux integrated over time.) When this critical fluence is collected, the local potential of the dielectric builds to a sufficiently large value that it begins to retard the flux. At high frequencies, these time scales correspond to the rf period, and so there is a smooth transition from positive to negative dielectric potential. At lower frequencies, however, these dielectric charging times are shorter than the rf period. So the retarding potential on the dielectric slows down the collection of negative (or positive) charges at a time that V_{rf} is still increasing (or decreasing). The still increasing (or decreasing) V_{rf} then restarts the charge collection which produces the local minimum in the surface potential.

In addition to *overshoot* in surface charging, periodic bursts of ionization can lead to multiple peaks in current extraction. V_{rf} , local potential, E/N , electron density and ionization source at site B are shown in Fig. 3.8 for ν_{rf} of 25 and 2.5 MHz. Corresponding extracted currents collected on the top electrode are shown in Fig. 3.9. At 25 MHz, a pre-pulse electron current of 0.3 mA is collected by the extraction electrode which is then followed by a larger main current pulse. This pre-pulse is correlated with large values of dV/dt and occurs before the zero-crossing of rf voltage at 20 ns. As the frequency decreases to 15 MHz, the pre-pulse is reduced to 0.1 mA and by 5 MHz, the pre-pulse is suppressed. Before the rf voltage changes its polarity to negative, the local potential in the cavity reaches its negative peak which increases E/N and the ionization sources (S_e and S_{sec}) in the mDBD cavity. This ionization provides the electron source for the main current pulse. At 25 MHz, for example, the local peak in E/N in the mDBD cavity reaches as high as 1700 Td (1 Td [Townsend] = 10^{-17} V-cm²) slightly before V_{rf} zero-crossing at 20 ns, and the peak electron source exceeds 3×10^{24} cm⁻³s⁻¹. The corresponding electron density then reaches

$3.5 \times 10^{14} \text{ cm}^{-3}$. The conductive, high electron density plasma in the cavity then shields out the electric field, E/N decreases which then decreases the electron sources. At all frequencies, the magnitudes of S_e and S_{sec} are commensurate to each other, with S_{sec} lasting somewhat longer due to the long lived excited states which, though photoelectron production, continue to seed secondary electrons at surfaces. For example, at 25 MHz the peak electron source from bulk plasma ionization (S_e) is essentially the same as that from secondary electron ionization (S_{sec}), on the order of $3 \times 10^{24} \text{ cm}^{-3}\text{s}^{-1}$.

Shortly after the negative peak in V_{rf} at 30 ns, the local potential at site B becomes more positive due to the positive surface charges, the electron plume begins to extinguish and electron flux is attracted to the dielectric. As the frequency decreases and the period becomes longer, there is sufficient electron current extracted to deplete the cavity. The local E/N then rebounds, which produces ionization sources, which in turn repopulate the electron density in the cavity which enables another burst of electron current to be collected. If V_{rf} has not yet changed sign, the process can repeat itself.

For example, at 2.5 MHz, the period of 400 ns is sufficient for multiple cycles of electron depletion and avalanche to occur. As shown in Fig. 3.8, depletion of electrons in the mDBD cavity as V_{rf} crosses zero towards negative values at 200 ns produces a peak in E/N of 1,540 Td. This produces a burst of ionization which repopulates the mDBD cavity but also reduces E/N to about 850 Td. These electrons are extracted producing the first current pulse (see Fig. 3.9) with the local electron density decreasing from $4 \times 10^{12} \text{ cm}^{-3}$ to $3 \times 10^{11} \text{ cm}^{-3}$. The E/N then recovers to 1,260 Td, the electron source follows E/N and then a second local peak in electron density is formed for the second current pulse. The process repeats a third time before V_{rf} changes sign. The re-ignition of the plasma following each extraction is facilitated by a quasi-dc production of secondary

electrons from the dielectric and grounded electrode by UV photons from long lived excited states. Note that the same process occurs on the anodic part of the rf cycle, producing peaks in the E/N , electron density and ionization sources. These undulations are not reflected in the electron current collected at the top electrode since the net field is pointing in the opposite direction – the bursts of electron current are collected on the dielectric surface.

In general, S_e and S_{sec} follow E/N during an rf period for both 25 and 2.5 MHz, while S_{sec} is longer-lived in the cavity. However, for 25 MHz when V_{rf} cross zero at $t = 0$, S_{sec} is as large as $1.6 \times 10^{24} \text{ cm}^{-3}\text{s}^{-1}$ but S_e is negligible at site B, as shown in Fig. 3.8(a). At this time, electrons are attracted to the center dielectric due to the previous positive surface charging and the highly conductive plasma shields the local electric field, which results in the small bulk ionization source. At this time, however, a large amount of ionization by secondary electrons ionization occurs near the vicinity of the tip of the discharge electrode, boosting S_{sec} , as the electrode behave cathodically.

Note that the peaks S_e and S_{sec} are on the order of $5 \times 10^{23} \text{ cm}^{-3}\text{s}^{-1}$ at 2.5 MHz which is 6 times smaller than the peak electron ionization sources at 25 MHz. The lower electron source at 2.5 MHz can be attributed to the lower residual electron density in the cavity surviving from the prior pulse. At 2.5 MHz, the period is long enough that the the majority of electrons are extracted out of the cavity. Positive ion and UV fluxes from long lived excited states can facilitate re-ignition at 2.5 MHz by production of secondary electrons from surfaces. However these secondary electron sources are too small to trigger as large an avalanche as that produced by the higher residual electron density at 25 MHz. As a result, the peak current collection tends to decrease with decreasing frequency.

The trends in extracted and collected current from 25 and to 2.5 MHz include the loss of the pre-pulse, due in large part to the decreasing dV/dt at low frequency, and the onset of

modulation in the current at low frequency due to the cycle of extraction, depletion and avalanche at low frequency. Similar trends of oscillating currents (single current pulses at high frequency, multiple current pulses at low frequency) in DBDs were reported in the modeling results by Petrović *et al* [37], and in the experimental results by Radu *et al* [47] and J. Shin [38]. These oscillations were reported for larger parallel plate devices and at lower frequencies (kHz). However the basic sequence of events is similar – charging, depletion, ionization, extraction.

Multiple pulses of current at 2.5 MHz are also experimentally observed when using the same sandwich mDBD configuration of slightly different size and operated under similar conditions. In the experiment, the top extraction electrode is grounded, a -1 kV DC voltage is applied to both rf and discharge electrode, while rf electrode is also biased with a 1 kV ac voltage at 2.5 MHz. The experimental voltage drop between the rf and discharge electrode and current collection on the top electrode are shown in Fig. 3.10(a). From a biasing standpoint, this arrangement is equivalent to that used in the simulated results shown in Fig. 3.10(b). The results from the simulation are in basic agreement with the experiment data, although the current is smaller in experiment which can be attributed to differences in geometry and operating conditions. The predicted triple pulses of current extracted at the zero crossing of the rf voltage are corroborated by the experiment. The transition from triple pulses to double pulses is observed both experimentally and computationally.

Recall that the top electrode is biased positively and there is a ground electrode at the top of the mDBD cavity. Although the current flowing from the buried rf electrode having an rf bias must be ac, there is no requirement that the current flowing to the top electrode is ac since there is a non-capacitive path to ground through the top electrode. If the potential drop between the top extraction electrode and ground electrode is large enough there could be a dc discharge, and an

optimally designed device would either avoid this possibility with a lower extraction voltage, or limit the current with an appropriate ballast resistor. Even with a less than self-sustaining voltage on the extraction electrode, it is possible to have a quasi-dc current by virtue of the electrons injected into the gap from the mDBD cavity. The dc discharge between the grounded and top extraction electrode would then operate as an externally sustained discharge, in analogy to, for example, electron beam sustained discharges.[48]

To illustrate these scalings, the electron and positive ion density at site D (see Fig. 3.1(b)), and extracted electron current are shown in Fig. 3.11 as a function of extraction voltage on the top electrode for 25 MHz excitation on the rf electrode. With a 1 kV extraction voltage, the current on the top electrode consists of a series of pulses. The time averaged E/N (80 Td) across the gap is too small to self-sustain (or avalanche) a discharge, and so current is collected only when electrons are extracted from the mDBD cavity. The probability of recombination and attachment for this gas mixture during the transit time across the gap is small, and so the majority of the extracted current out of the mDBD cavity is swept to the top electrode. The E/N is small enough that there is only a small amount of ionization and positive charge generated in the gap.

For a 2 kV extraction voltage, the collected electron current begins as being purely pulsed, which reflects the periodic extraction of electrons from the mDBD cavity. With this time averaged E/N (170 Td), there is non-negligible ionization within the gap, which has two consequences. First, the pulsed current extracted from the mDBD cavity is amplified in crossing the gap, as shown by the pulses prior to 400 ns. Second, ionization and excitation in the gap increases the positive ion density, dominated by N_4^+ for these conditions, and excited state density. (The negative ion density due to the O_2 impurity is generally at least 2 orders of magnitude smaller.) The positive ions have a much lower drift velocity towards the grounded electrode and so are not highly modulated during

the rf cycle. A transition occurs in the current collected by the top electrode to a pulsed modulated dc current. At this time the gradually increasing positive ions perturb the local electric field, voltage and charge collection until it reaches an oscillatory steady state. On a pulse-to-pulse basis, positive ions accumulate in the gap over time, as these heavier positive ions are not able to respond to the instantaneous electric field and create a local positive potential which enhances the extraction of charge from the gap. The accumulating excited states also increase the efficiency of ionization through multistep collisions. With a 2 kV extraction bias, the positive charge density ρ^+ at site D increases monotonically until reaching a steady state at 800 ns, which leads to a pulsed modulated dc current. This pulsed modulated dc current can be avoided by using a lower extraction voltage. For example, purely pulsed electron currents are collected by applying 1 and 1.5 kV top extraction voltages, as shown in Fig. 3.11(b).

3.5 Total Charge Collection

Total charge collected per pulse and time integrated charge collection on the top electrode as a function of time for rf frequencies of 2.5 to 25 MHz are shown in Fig. 3.12. The top extraction electrode is biased with +2 kV. For early pulses and lower frequencies, the charge per pulse collected is essentially the same, 3.5×10^{-11} C/pulse, and limited by the capacitance of the dielectric layer above the rf electrode. Although more peak current is collected at higher frequency, as shown in Fig. 3.9, more charge per pulse is collected by operating at lower frequency due to the longer charge extraction period and multiple current pulses per rf cycle. Integrated current as a function of time at 25 MHz is higher due simply to the higher repetition rate. For frequencies greater than 10-15 MHz, charge collection per pulse is limited by the shorter rf period. The charge/pulse

increases with number of the pulses until a quasi-dc condition is reached due to the accumulation of excited states and ions in the gap. At this point quasi-dc current is collected.

Integrated charge collection as a function of time for different rf voltages (1.4 to 5.6 kV) at 25 MHz is shown in Fig. 3.13. The corresponding dielectric properties (V_{rf} , surface charge and surface potential) at site A and ionization characteristics (E/N , electron density and ionization sources) at site B are shown in Fig. 3.14. The magnitude of the charging of the dielectric scales nearly linearly with V_{rf} , as the discharge is dominantly capacitive – the charged particle flux to the intervening dielectric is that value that charges the dielectric to V_{rf} . The nearly linear increase of collected charge with voltage, is less clearly correlated with this capacitive current. In general, electron density, E/N and ionization sources at site B tend to increase with rf voltage. However, as the electron density increases, the local value of E/N decreases due to plasma shielding. In spite of this shielding, the electron impact sources by both bulk and sheath accelerated electrons increase with applied voltage due to non-local electron transport. The heating of electrons at the boundaries of the microcavity by the larger sheath electric fields (either by bulk Joule heating or secondary electron acceleration) convects into the center of the mDBD cavity to increase ionization rates.

The local electron density at site B reaches its minimum and ionization processes tend to start earlier at higher rf voltage. These trends are due to the surface voltage at site A reaching its negative peak value earlier at $V_{rf}=5.6$ kV which leads to a time-shift of electron current extraction and ionization process. For example, the dielectric surface potential at site A reaches its most negative potential at $t = 20$ ns and 17 ns for $V_{rf}=1.4$ kV and 5.6 kV, the corresponding ionization source S_e also peaks at $t = 21.5$ ns and 16 ns, respectively.

Charge collection on the top electrode as a function of dielectric constant ($\epsilon_r=\epsilon/\epsilon_0$) of the insulator between the discharge electrode and rf electrode is shown as a function of time in Fig.

3.15 for a frequency of 25 MHz. The dielectric properties at site A and ionization characteristics at site B (E/N and ionization sources) and C (electron density) are shown in Fig. 3.16 for $\epsilon/\epsilon_0=2, 5, 10,$ and 20 . Since the intervening dielectric acts as a capacitor whose capacitance scales with ϵ_r , its charging characteristics should scale with ϵ_r . That is, the surface charge required to charge the dielectric to the line voltage should increase linearly with ϵ_r . If I normalize charge collection by ϵ_r , differences are then attributable to transport processes. In general, charge collected per pulse normalized by ϵ_r is approximately equal (to within 50%) over a factor of ten in ϵ_r . This indicates that charge collection, at least for a small number of pulses, is limited by the series capacitance of the dielectric. Integrated charge collection then increases with increasing ϵ_r . For later pulses normalized charge collection increases with increasing dielectric constant; 2×10^{-12} C/pulse/ ϵ_r with $\epsilon/\epsilon_0=2$, increasing to 4.5×10^{-12} C/pulse/ ϵ_r with $\epsilon/\epsilon_0=20$.

The normalized charge density (surface charge density/ ϵ_r), V_{rf} and local potential at site A for different ϵ_r are shown in Fig. 3.16. The normalized charge density collected at site A is essentially the same during the rf period for all values of ϵ_r . The surface potential on the dielectric reaches a maximum magnitude of 500 V, and as ϵ_r increases, more charge is required to charge the surface to this potential, thereby necessitating an increase in current density and so electron density. Electron densities at site C reach their maximum values when the current is extracted out of the mDBD cavity. Peak electron densities scale nearly linearly with ϵ_r , up to 10^{15} cm⁻³ for $\epsilon_r=20$. As ϵ/ϵ_0 decreases from 20 to 2, the dielectric charging time decreases and so the overshoot in electron density is more prominent. The peak value of E/N , 1800-2000 Td, is largely determined by the nearly constant magnitude of surface potential which occurs when the electrons are expelled out of mDBD cavity. So this peak value is largely determined by the vacuum fields. In spite of the low electron densities in the cavity, the large value of E/N produces the maximum S_e , up to $2.3 \times$

$10^{24} \text{ cm}^{-3}\text{s}^{-1}$ for $\epsilon/\epsilon_0 = 20$. Ionization by secondary electrons has values that are essentially the same as for ionization by bulk electrons over the entire range of ϵ_r investigated.

3.6 Concluding Remarks

Dielectric barrier discharges are being used as current sources for charging of surfaces in a variety of applications, and digital printing in particular. Using results from a two-dimensional plasma hydrodynamics model, I investigated the properties of a micro-DBD with an additional charge extraction electrode sustained in atmospheric pressure N_2 with a small O_2 impurity. Properties were investigated as a function of driving voltage, frequency, dielectric constant, and extraction voltage. For the design investigated, the electron density produced within the mDBD cavity can be extracted into a plume that is collected by a dc biased electrode. The value of the extraction bias determines whether the device delivers continuous pulses of extracted current, or transitions to a pulse modulated dc current source. I found that in the pulsed mode, current extraction is ultimately limited by charging of the intervening dielectric – more charge extraction for larger dielectric constants. I also found that the shape of the current pulse is a function of frequency. At high frequencies (tens of MHz), a single current pulse is extracted during each rf cycle. At low frequencies (a few MHz), the current pulse is highly modulated into individual peaks, produced by successively charging and discharging of the intervening dielectric. Extraction of current from the mDBD cavity can deplete the electron density to such a large extent that the plasma inside the mDBD needs to be re-ignited each rf cycle. The re-ignition is facilitated, in part, by long lived excited states that provide photons which generate secondary electrons from the insides surfaces of the cavity.

In summary, this chapter aims at understanding kinetic and plasma dynamic process occurring in rf excited micro-dielectric barrier discharges used for print heads. Since it is difficult to measure plasma properties in the mDBD cavities due to their small size, high pressure and transient nature, the modeling provides valuable insights and design rules. For example, by choice of rf frequencies, rf driving voltages, and properties of bottom dielectric, electron plumes can be carefully shaped and controlled. In addition, a triple pulse of current extraction excited by rf voltage at 2.5 MHz is predicted by simulation, which shown the power of the code.

3.7 Figures

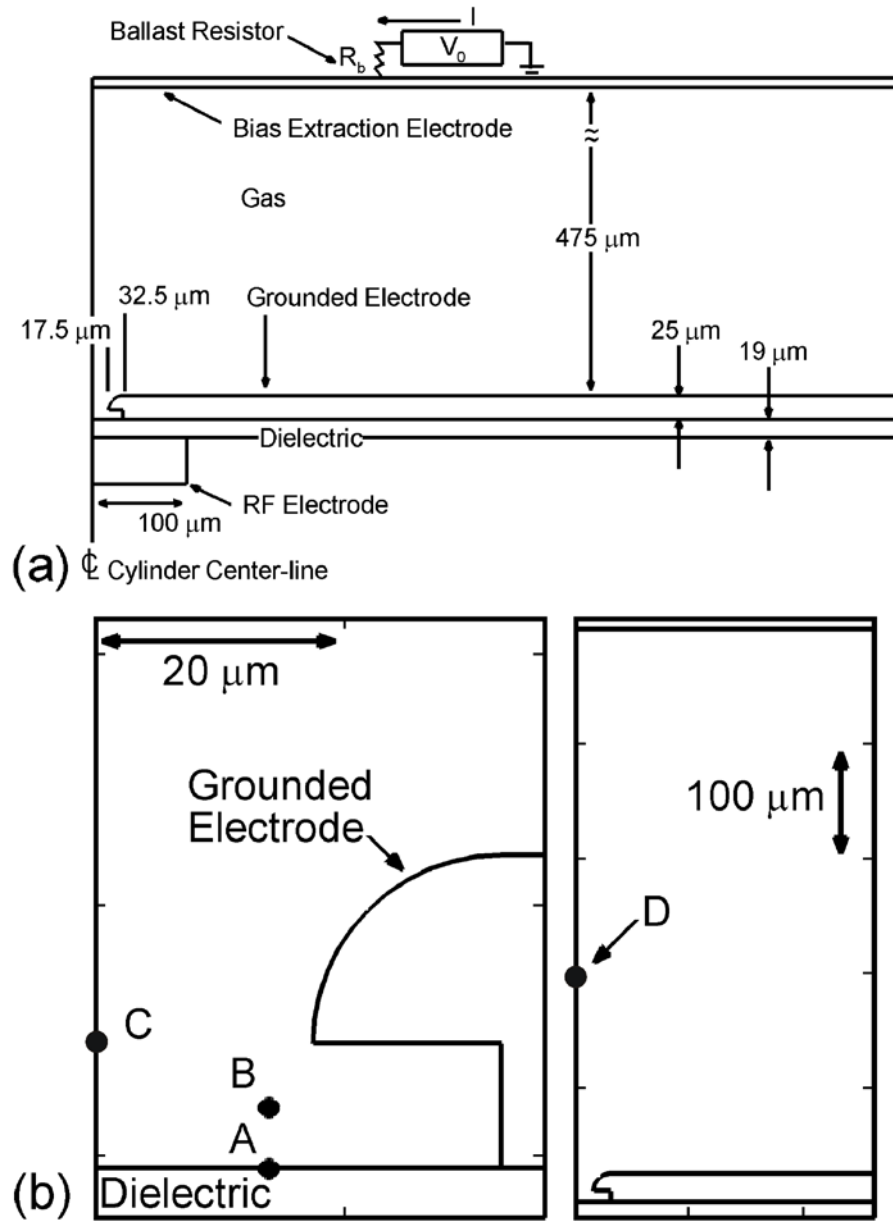


Figure 3.1 Schematic of the cylindrical symmetric mDBD device. (a) Entire device and full computational domain. (b) Enlargement of mDBD cavity and location of sites A, B, C and D that are used to provide surface properties and ionization characteristics.

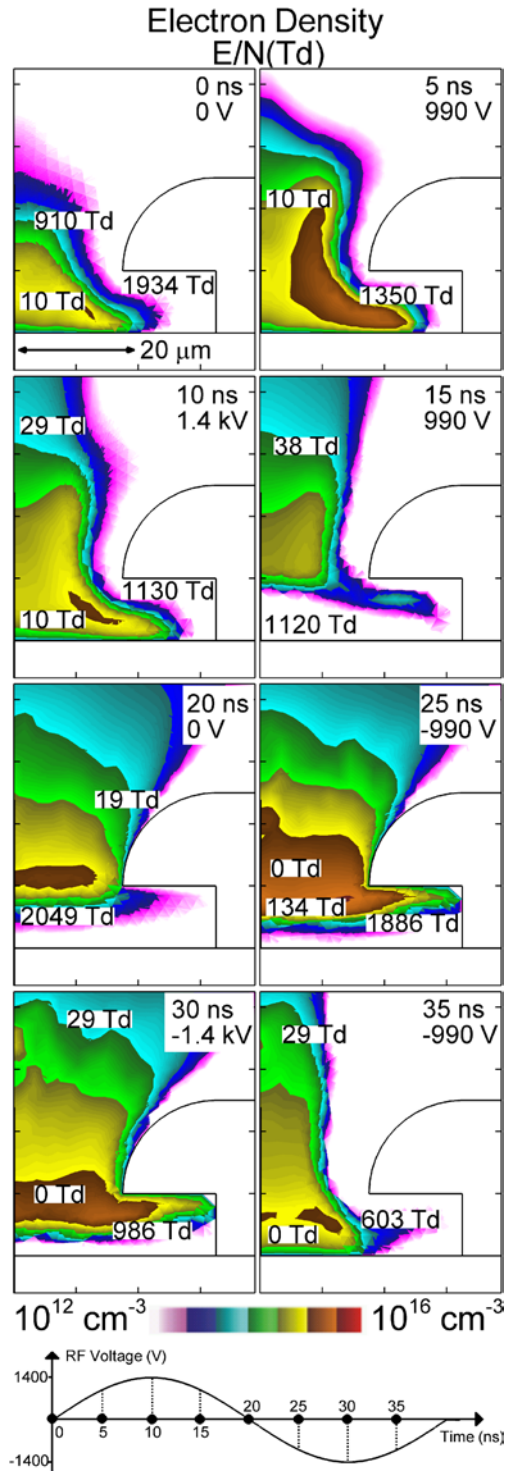


Figure 3.2 Time evolution of electron density (log scale, cm^{-3}) and E/N (at the center of contour labels, Td) in the mDBD cavity at different phases of the rf driving voltage of 1.4 kV during a 40 ns (25 MHz) cycle. The cycle begins with 0 V on the buried rf electrode. The top electrode is biased with +2 kV. At high electron density, the electric field is shielded and E/N is reduced.

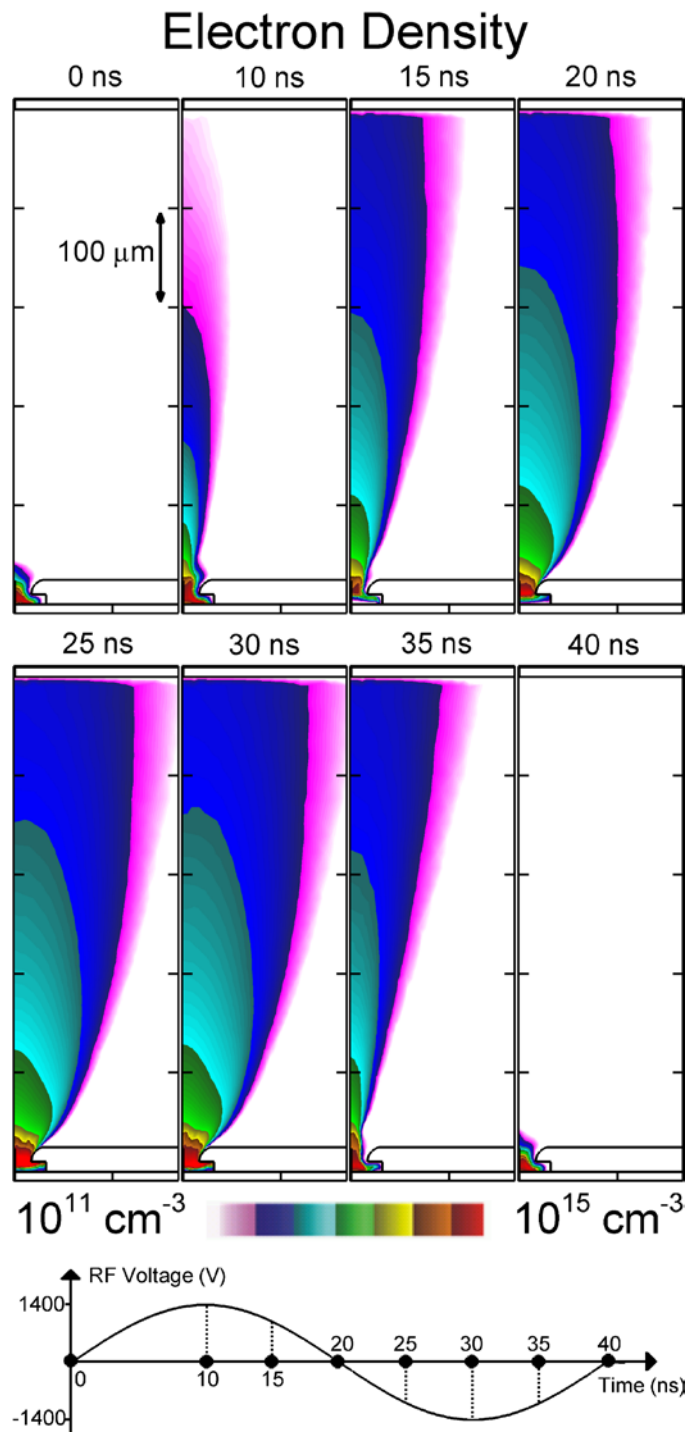


Figure 3.3 Electron density in the plume (log scale, cm^{-3}) in the gap at different phases of the rf driving voltage of 1.4 kV during a 40 ns (25 MHz) cycle.

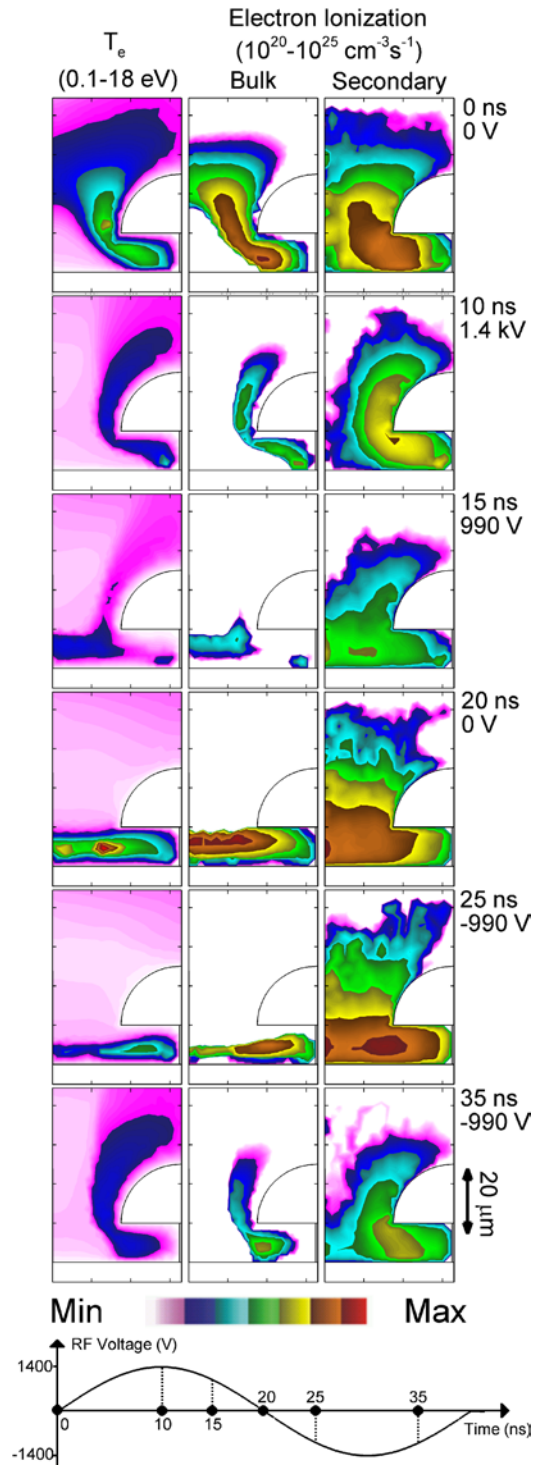


Figure 3.4 Electron temperature (eV), electron impact ionization sources from bulk electrons (S_e) and ionization source by sheath accelerated secondary electrons (S_{sec}) in the mDBD cavity during a 40 ns (25 MHz) cycle for $V_{rf} = 1.4$ kV and extraction voltage of 2 kV. The ionization sources are plotted on a log scale.

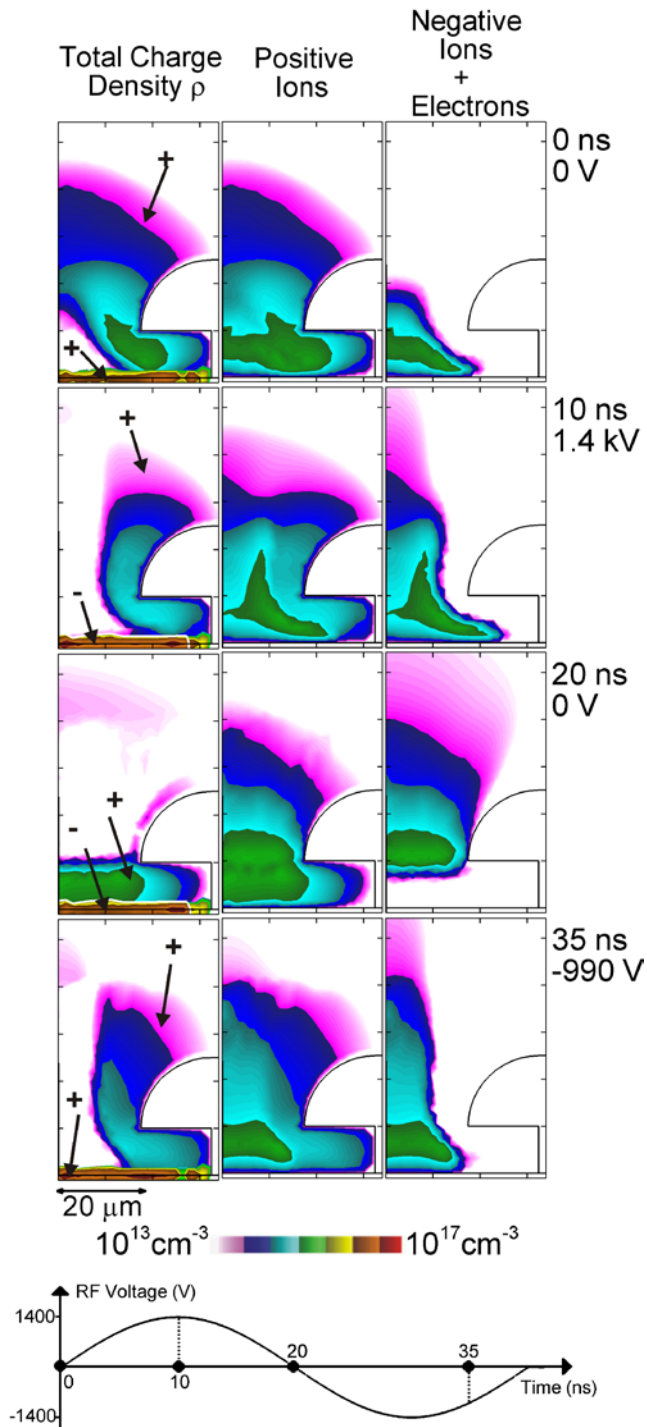


Figure 3.5 The total charge density, charge density due to positive ions and charge density due to electrons and negative ions ($\log \text{ cm}^{-3}$) in the mDBD cavity at different times during a 25 MHz cycle for $V_{rf} = 1.4 \text{ kV}$ and extraction voltage of 2 kV. Positive ions alternately strike the cathode-like negatively charged dielectric or discharge electrode and release secondary electrons for re-ignition.

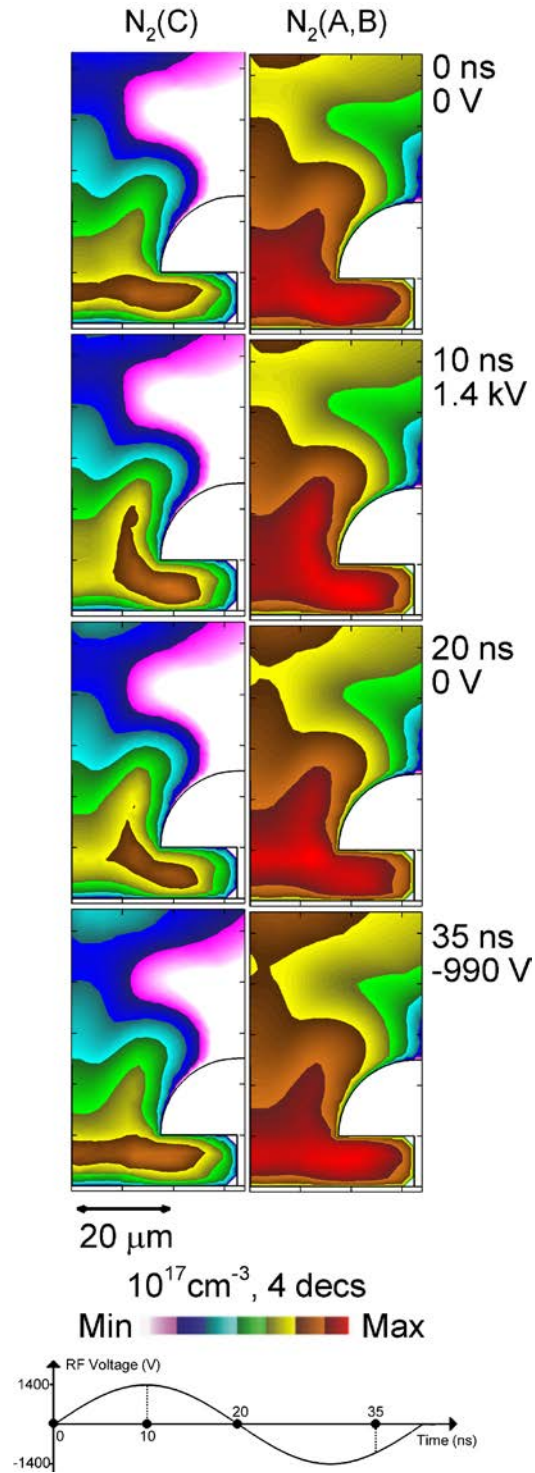


Figure 3.6 Density of excited states $N_2(C)$ and $N_2(A,B)$ in the mDBD cavity (log scale, cm^{-3}) at different times during a 25 MHz cycle for $V_{rf} = 1.4 \text{ kV}$ and extraction voltage of 2 kV. UV photons emitted from excited states of nitrogen produce secondary electrons which aid in re-ignition of the plasma especially at low frequency.

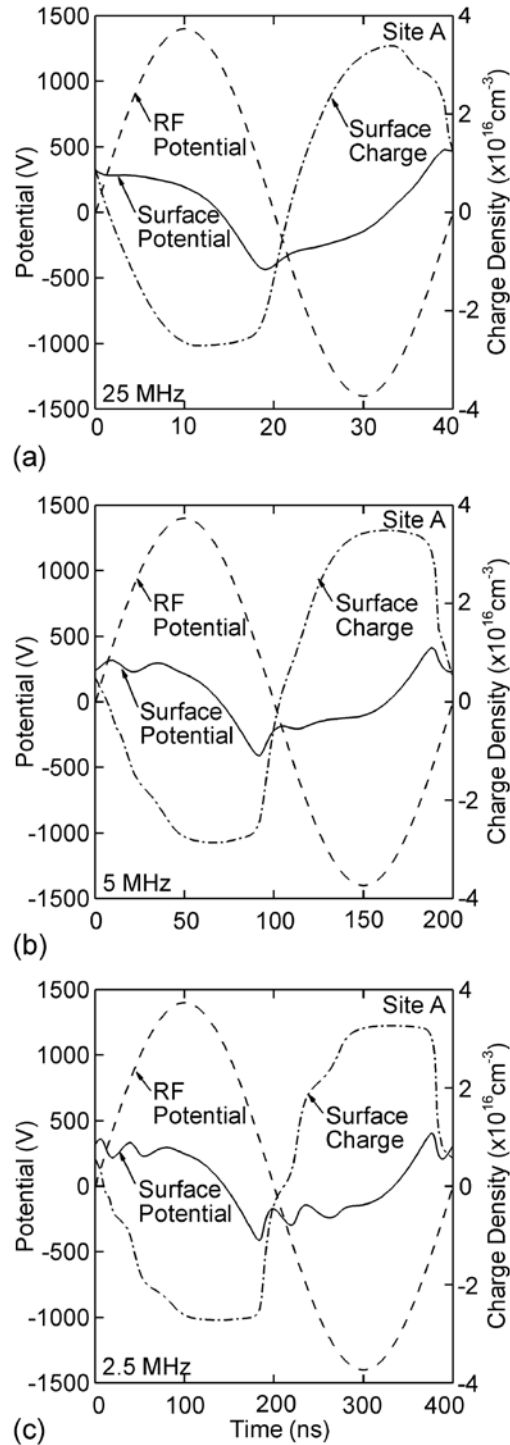


Figure 3.7 The surface charge density σ_s (dash-dotted, cm^{-3}), surface voltage on the dielectric (solid, V) and voltage on the buried rf electrodes (dashed, V) are shown for frequencies of a) 25, b) 5 and c) 2.5 MHz at site A (see Fig. 3.1) for $V_{rf} = 1.4$ kV and extraction voltage of 2 kV. Oscillations in charging of the dielectric appear at low frequencies.

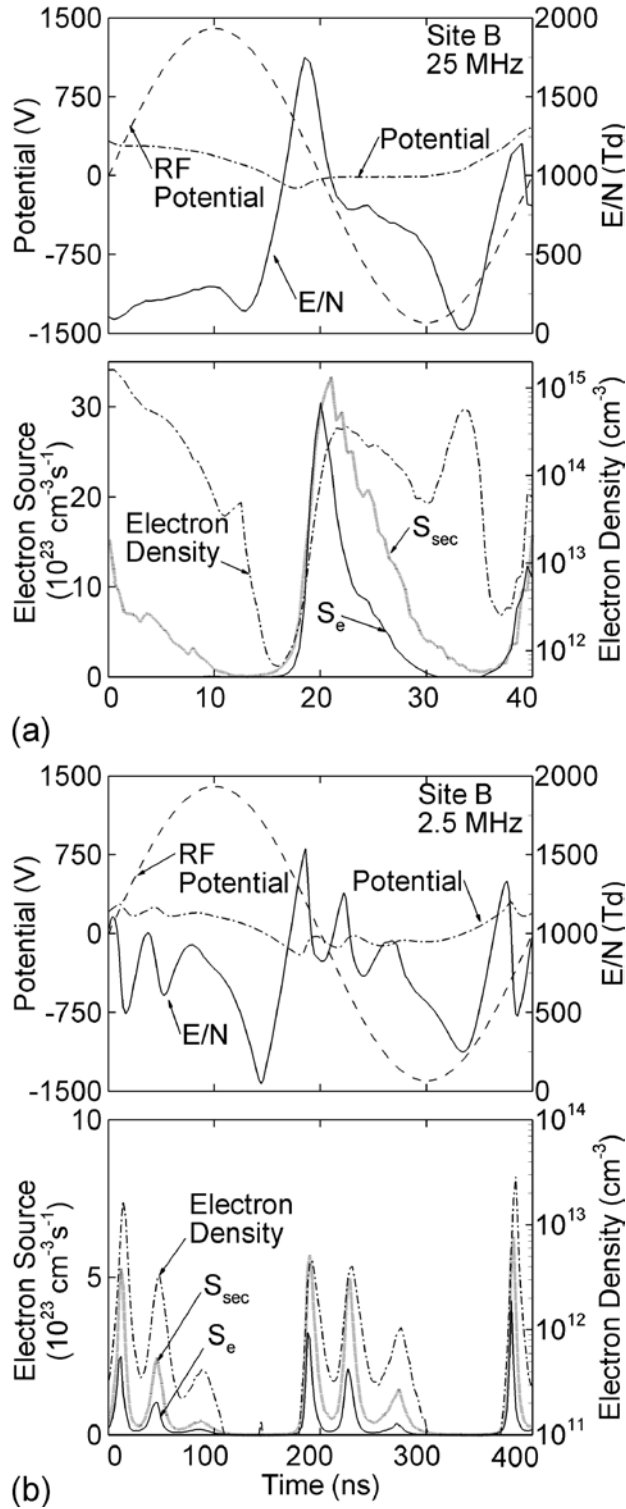


Figure 3.8 mDBD characteristic are shown at site B as a function of time (see Fig. 3.1) for $V_{rf} = 1.4$ kV and extraction voltage of 2 kV for a) 25 MHz and b) 2.5 MHz: rf voltage (dashed, V), local potential (dash-dotted, V) and E/N (solid, Td), electron density (dash-dotted, cm^{-3}) and electron ionizations source S_e and S_{sec} (solid and dotted, $\text{cm}^{-3} \text{ s}^{-1}$).

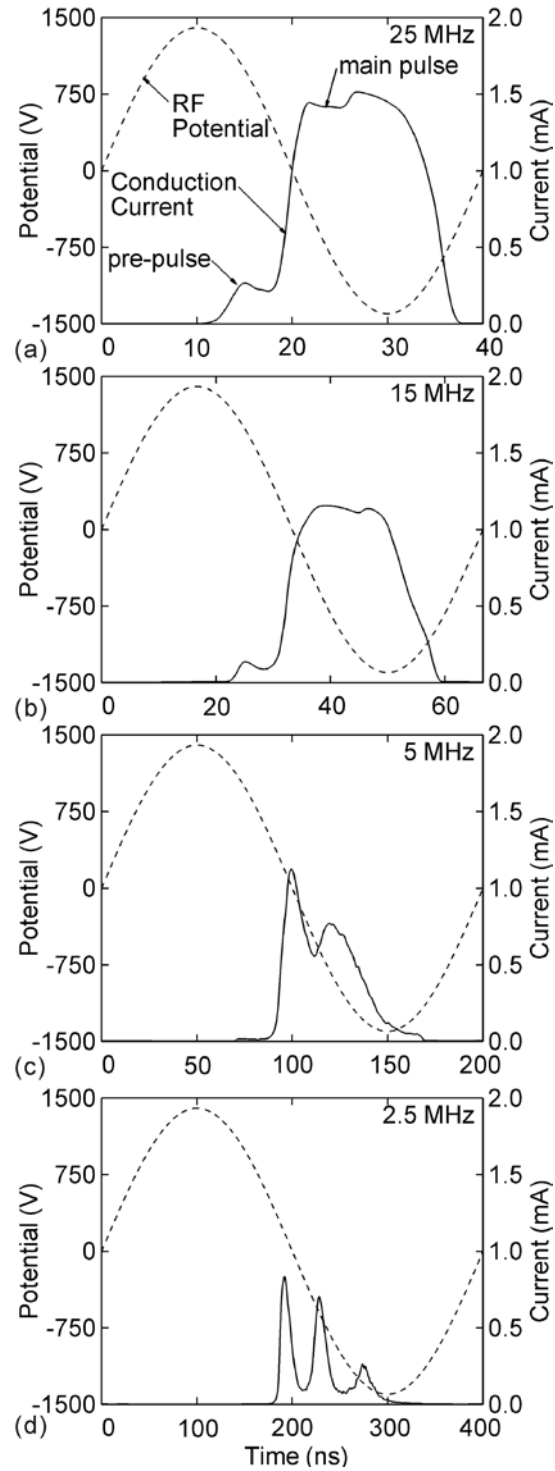


Figure 3.9 Current collection on the top electrode. a) Experimentally observed triple current pulsed obtained at 2.5 MHz and b) simulation results in a similar sandwich mDBD device for equivalent biasing.

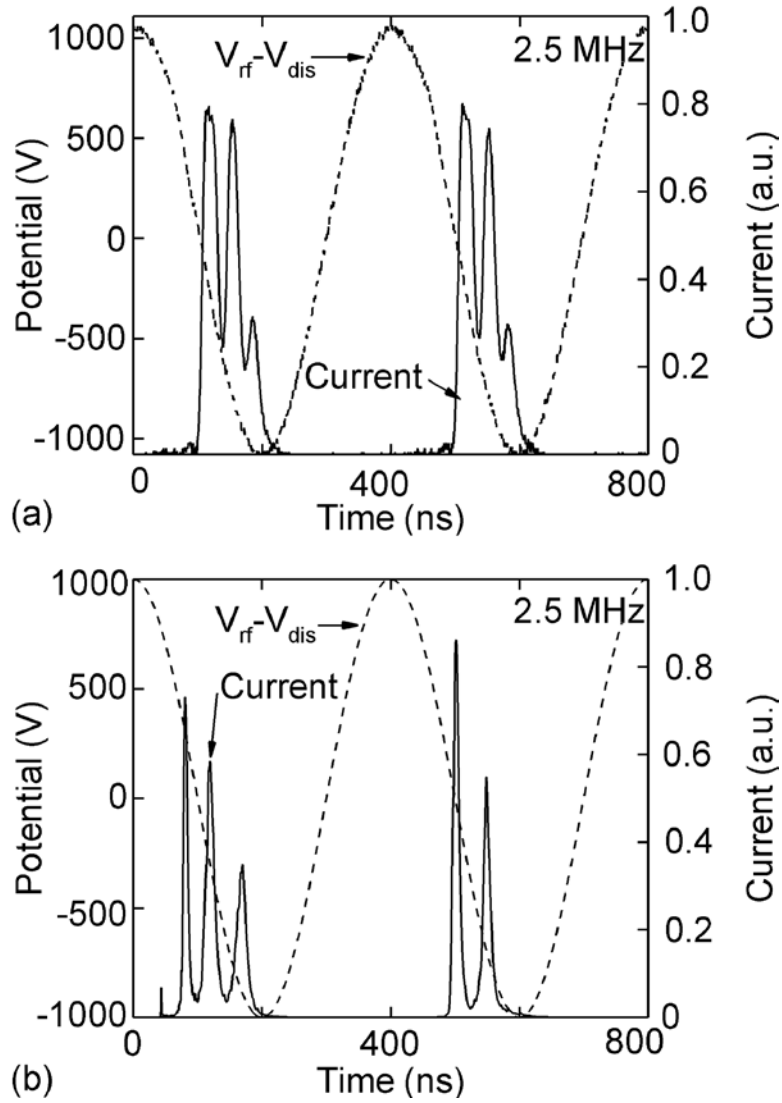


Figure 3.10 Charge density at site D and current collection on the top electrode at 25 MHz. a) Electron (solid, cm^{-3}) and positive ion density (dash, cm^{-3}) at site D for top bias voltage $V_{top} = 2, 1.5$ and 1 kV. b) Electron current collected by the top biased electrode for $V_{top} = 2, 1.5$ and 1 kV. A pulsed modulated dc current is collected at $V_{top} = 2$ kV.

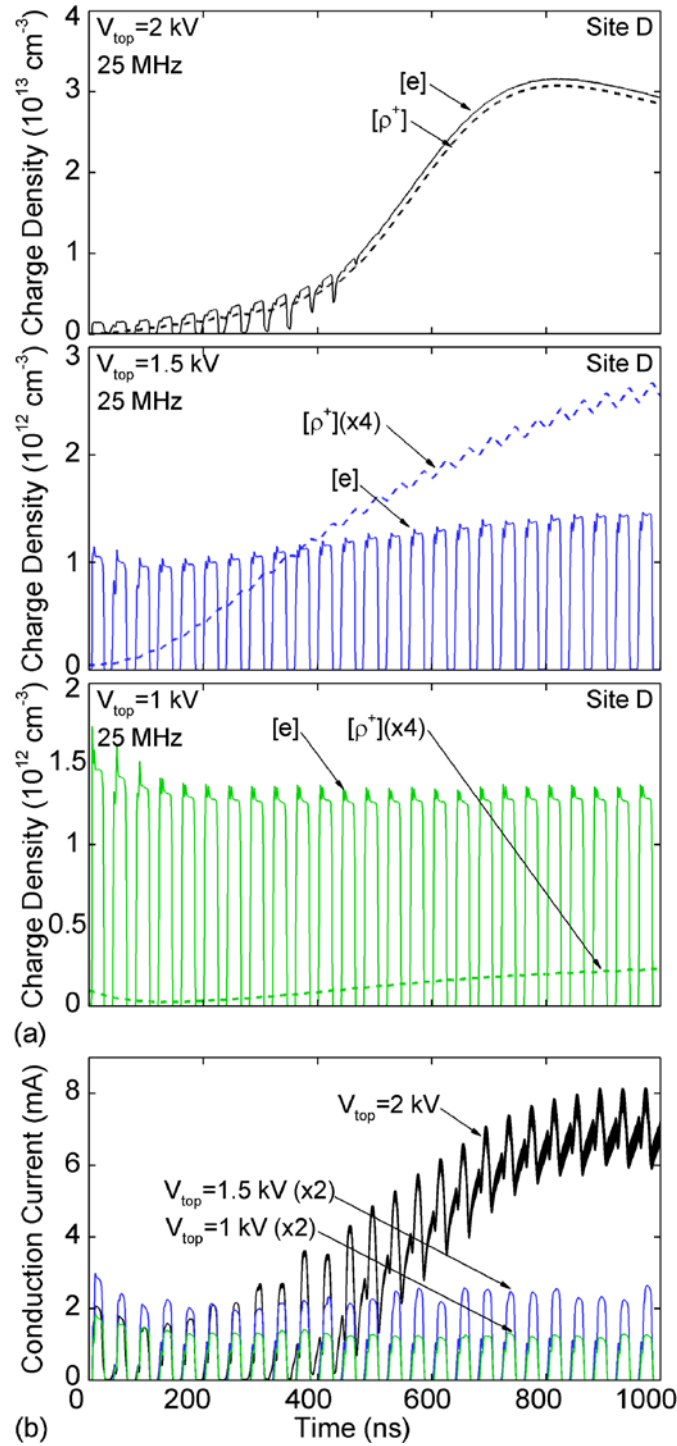


Figure 3.11 Charge collection as a function of time for 25 MHz to 2.5 MHz (1.4 kV rf bias) and a 2 kV biased collection electrode. a) Charge collected per pulse and b) time integrated charge collection. Charge collection per pulse is relatively independent of frequency until positive charge builds up in the gap at the higher frequencies, which then transitions to a modulated dc discharge.

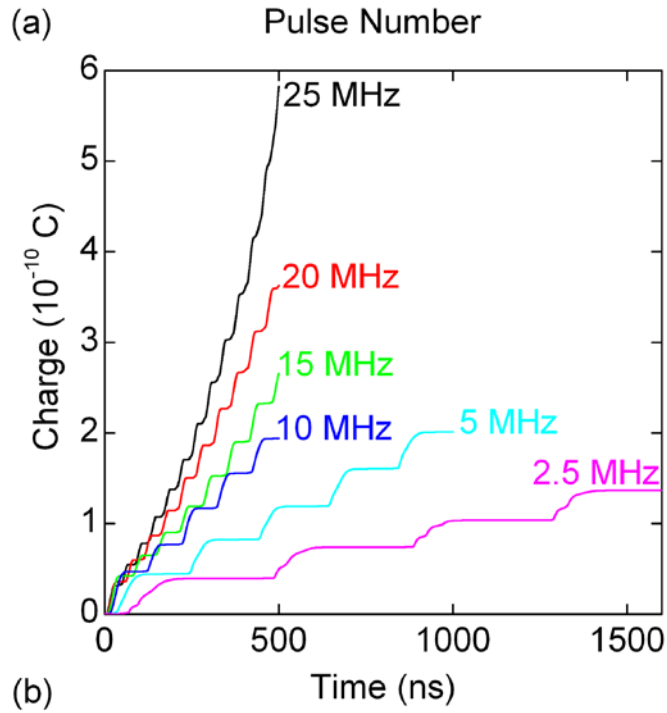
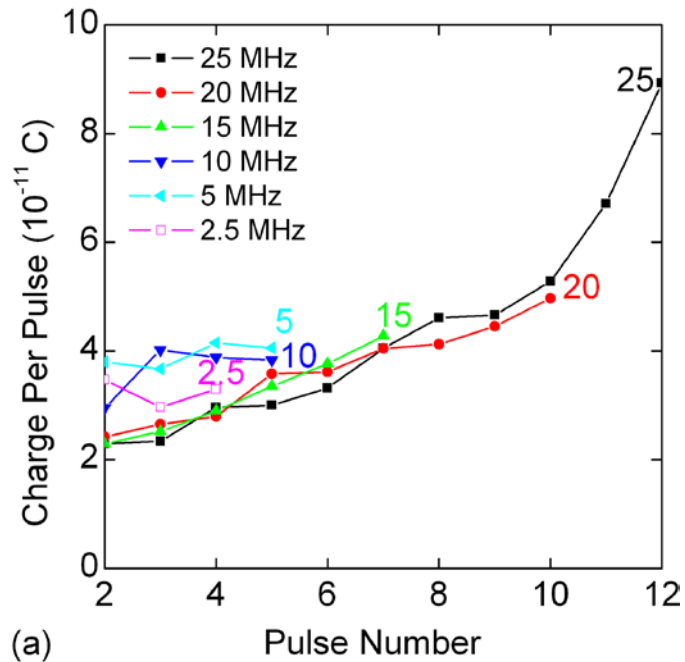


Figure 3.12 Charge collection as a function of time for 25 MHz at $V_{rf} = 1.4, 2.8, 4.2$ and 5.6 kV and a 2 kV biased collection electrode.

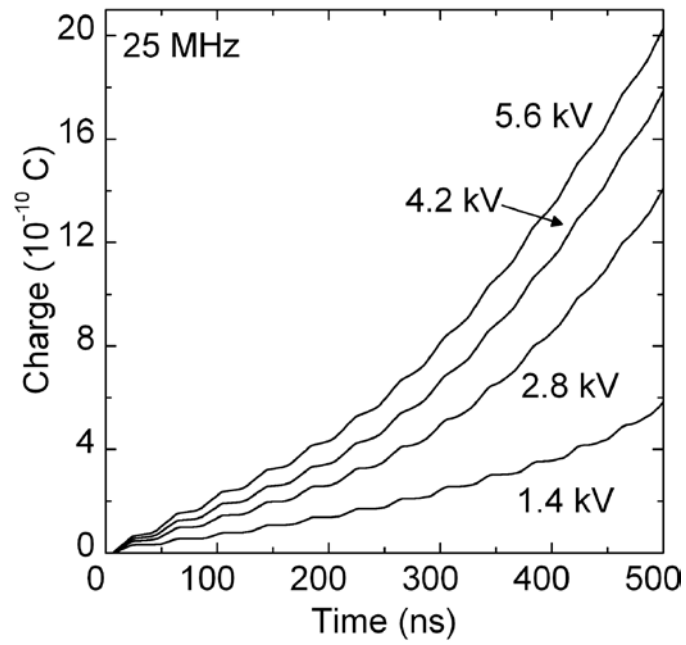


Figure 3.13 Charge collection as a function of time for 25 MHz at $V_{rf} = 1.4, 2.8, 4.2$ and 5.6 kV and a 2 kV biased collection electrode.

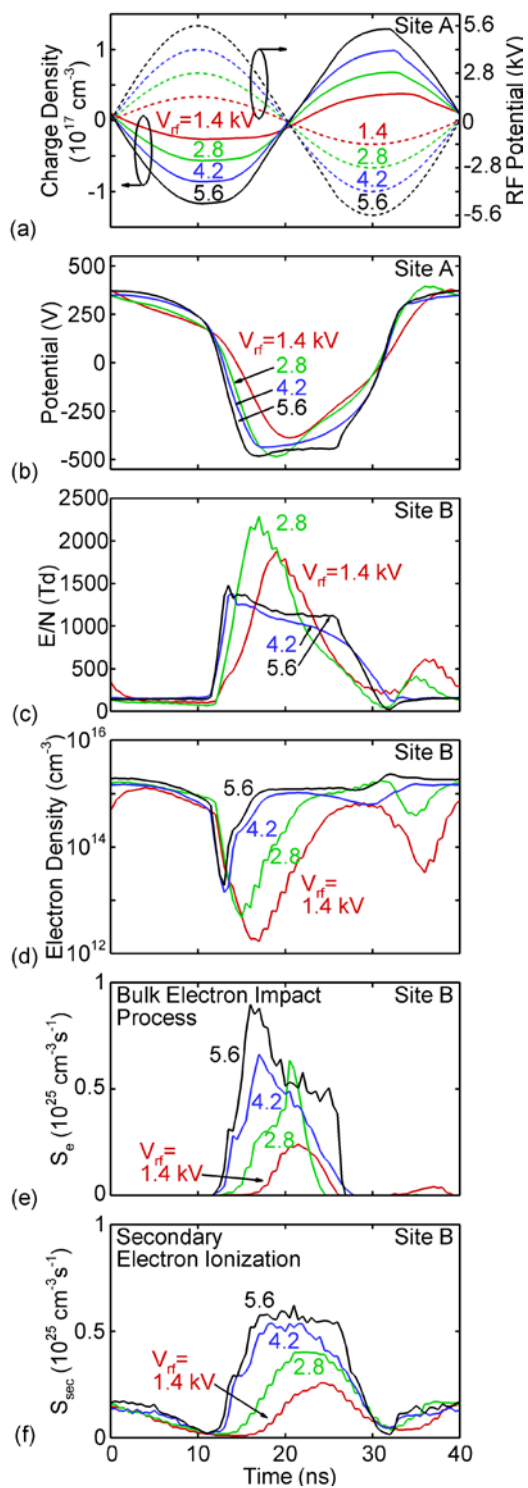
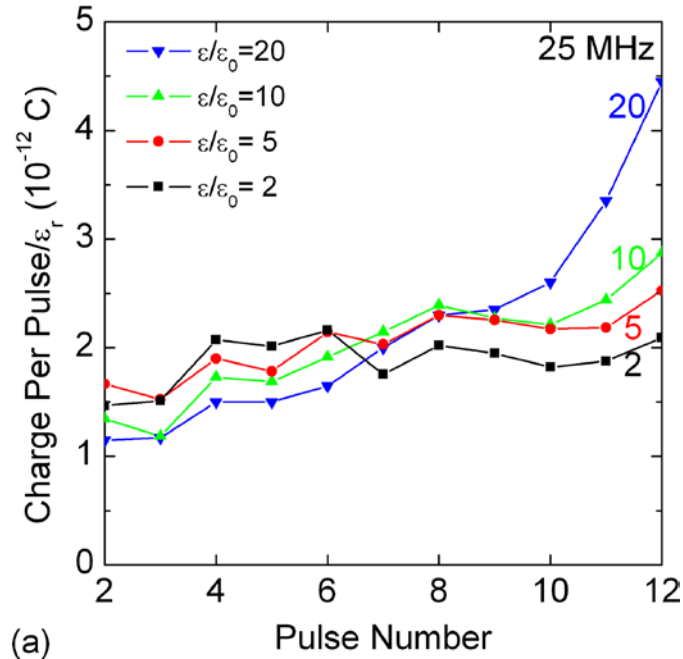
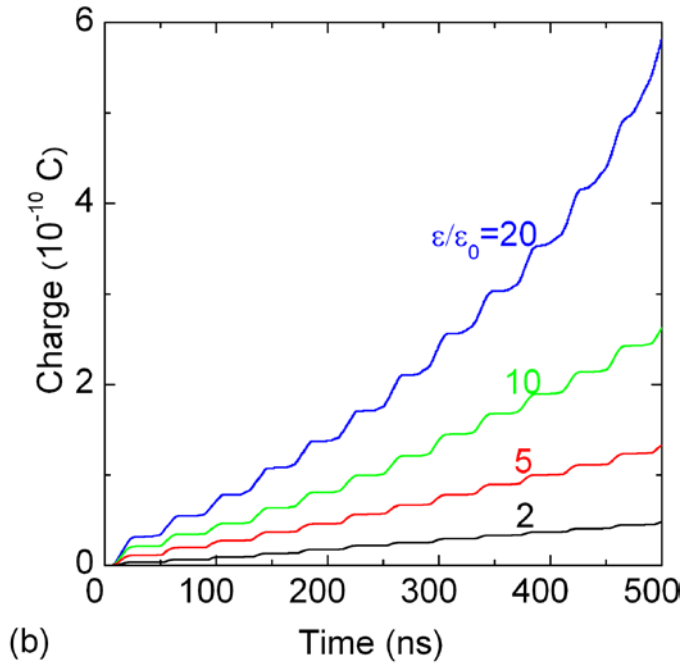


Figure 3.14 Surface properties at site A and gas phase properties at site B as a function of time at 25 MHz for $V_{rf} = 1.4, 2.8, 4.2$ and 5.6 kV. The location is noted in each frame. a) Surface charge density and applied rf voltage, b) surface potential, c) E/N , d) electron density, e) ionization by bulk electrons and f) ionization by secondary electrons



(a)



(b)

Figure 3.15 Charge collection/pulse and total charge collected by the top 2 kV biased electrode as a function of time for 25 MHz with $\epsilon/\epsilon_0=20, 10, 5$ and 2 with 1.4 kV on the rf electrode. The charge per pulse is normalized by $\epsilon_r = \epsilon/\epsilon_0$.

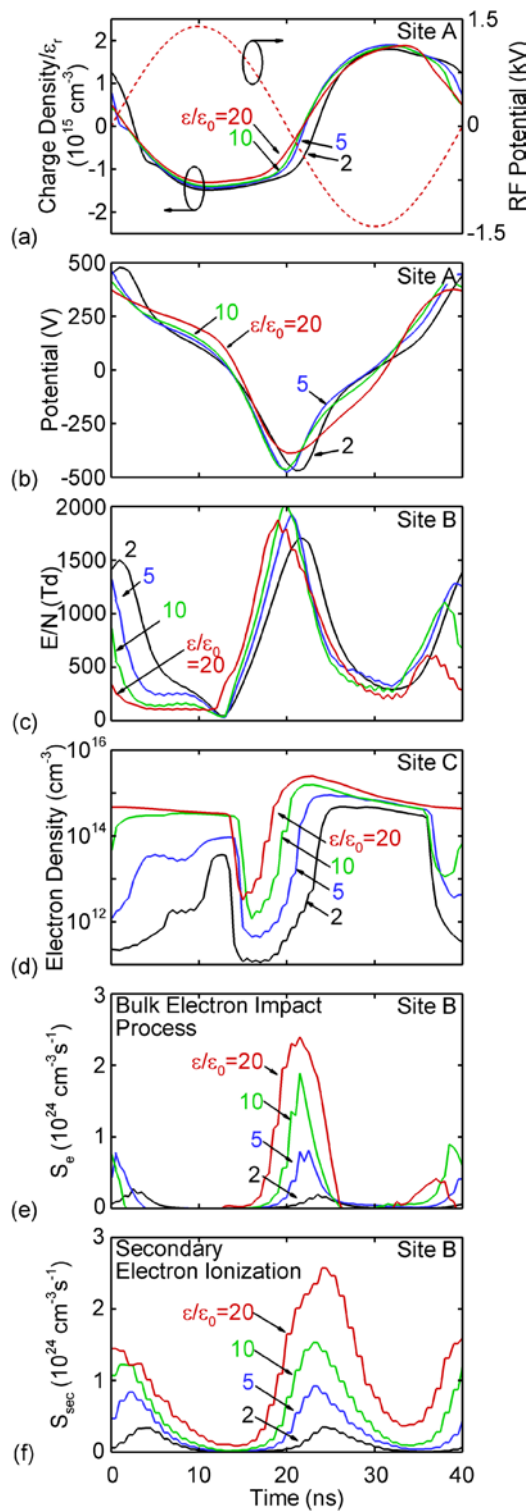


Figure 3.16 Surface properties at site A and gas phase properties at sites B and C as a function of time at 25 MHz for $\epsilon/\epsilon_0=20, 10, 5$ and 2 . The location is noted in each frame. a) Surface charge density normalized by ϵ_r and rf voltage, b) surface potential, c) E/N , d) electron density, e) ionization by bulk electrons and f) ionization by secondary electrons.

3.8 References

- [1] C. Penache, C. Gessner, T. Betker, V. Bartels, A. Hollaender and C.-P Klages, IEE Proc. Nanobiotechnol. **151**, 139 (2004).
- [2] S. Kreitz, C. Penache, M. Thomas, and C. -P. Klages, Surf. Coat. Technol. **200**, 676 (2005).
- [3] K. H. Schoenbach, M. Moselhy, and W. Shi, Plasma Sources Sci. Technol. **13**, 177 (2004).
- [4] N. S. Panikov, S. Paduraru, R. Crowe, P. J. Ricatto, C. Christodoulatos, and K. Becker, IEEE Trans. Plasma Sci. **30**, 1424 (2002).
- [5] K. H. Becker, K. H. Schoenbach, and J. G. Eden, J. Phys. D: Appl. Phys. **39**, R55 (2006).
- [6] T. S. Cho, S. H. Park, K. H. Becker, and E. E. Kunhardt, IEEE Trans. Plasma Sci. **39**, 1496 (2011).
- [7] K. H. Schoenbach, A. El-Habachi, W. Shi, and M. Ciocca, Plasma Sources Sci. Technol. **6**, 468 (1997).
- [8] P. S. Kothnur and L. L. Raja, J. Appl. Phys. **97**, 043305 (2005).
- [9] S.-J. Park, J. G. Eden, K. Jain and M. A. Klosner, Jpn. J. Appl. Phys. **45**, 8221 (2006).
- [10] S. A. Al-Bataineh, E. J. Szili, A. Mishra, S. J. Park, J. G. Eden, H. J. Grisesser, N. H. Voelcker, R. D. Short and D. A. Steel, Plasma Process. Polym. **8**, 695 (2011).
- [11] J. D. Readle, K. E. Tobin, K. S. Kim, J. K. Yoon, J. Zheng, S. K. Lee, S.-J. Park, and J. G. Eden, IEEE Trans. Plasma Sci. **37**, 1045 (2009).
- [12] S.-J. Park, P. A. Tchertchian, S. H. Sung, T. M. Spinka, J. G. Eden, IEEE Trans. Plasma Sci. **35**, 215 (2007).
- [13] J. P. Boeuf, J. Phys. D: Appl. Phys. **36**, R53 (2003).
- [14] U. Kogelschatz, Plasma Chem. Plasma Process. **23**, 1 (2003).
- [15] S. Kanazawa, M. Kogoma, T. Moriwaki, and S. Okazaki, J. Phys. D: Appl. Phys. **21**, 838

- (1988).
- [16] T. Yokoyama, M. Kogoma, T. Moriwaki, and S. Okazaki, *J. Phys. D: Appl. Phys.* **23**, 1125 (1990).
- [17] A. Fridman, A. Chirokov, and A. Gutsol, *J. Phys. D: Appl. Phys.* **38**, R1 (2005).
- [18] E. E. Kunhardt, *IEEE Trans. Plasma Sci.* **28**, 189 (2000).
- [19] H. H. Kim, *Plasma Process. Polym.* **1**, 91 (2004).
- [20] B. Eliasson, M. Hirth and U. Kogelschatz, *J. Phys. D: Appl. Phys.* **20**, 1421 (1987).
- [21] G. Borcia, C. A. Anderson and N. M. D. Brown, *Plasma Sources Sci. Technol.* **12**, 335 (2003).
- [22] M. Sira, D. Trunec, P. Stahel, V. Bursikova, Z. Navratil and J. Bursik, *J. Phys. D: Appl. Phys.* **38**, 621 (2005).
- [23] Z. Fang, X. Xie, J. Li, H. Yang, Y. Qiu and E. Kuffel, *J. Phys. D: Appl. Phys.* **42**, 085204 (2009).
- [24] J. Meunier, Ph. Belenguer and J. P. Boeuf, *J. Appl. Phys.* **78** (2), 731 (1995).
- [25] M. G. Kong, G. Kroesen, G. Morfill, T. Nosenko, T. Shimizu, J. van Dijk, and J. L. Zimmermann, *New J. Phys.* **11**, 115012 (2009).
- [26] H. Ayan, G. Fridman, A. F. Gutsol, V. N. Vasilets, A. Fridman and G. Friedman, *IEEE. Trans. Plasma Sci.* **36**, 504 (2008).
- [27] N. Lucas, A. Hinze, C. P. Klages and S. Büttgenbach, *J. Phys. D: Appl. Phys.* **41**, 194012 (2008)
- [28] J. Zhang, Y. H. Wang and D. Z. Wang, *Phys. Plasmas* **17**, 043507 (2010).
- [29] A. Chirokov, A. Gutsol, A. Fridman, K. D. Sieber, J. M. Grace and K. S. Robinson, *Plasma Chem. Plasma Process.* **26**, 127 (2006).

- [30] L. Stollenwerk, J. G. Laven and H. G. Purwins, Phys. Rev. Lett. **98**, 255001 (2007).
- [31] R. Fotland, E. Hanson, N. Leoni, P. McClelland, U.S. Patent No. 7,623,144 (24 Nov. 2009).
- [32] N. J. Leoni, O. Gila, M. H. Lee and E. G. Hanson, U.S. Patent No. 2009/0033735 (5 Feb. 2009)
- [33] M. W. Brennan, W. G. Read and S. Read, U.S. Patent No. 6,386,684 (14 May. 2002)
- [34] G. Bauville, B. Lacour, L. Magne, V. Puech, J. P. Boeuf, E. Munoz-Serrano and L. C. Pitchford, Appl. Phys. Lett. **90**, 031501 (2007).
- [35] J. S. Sousa, G. Bauville, B. Lacour, V. Puech, M. Touzeau and L. C. Pitchford, Appl. Phys. Lett. **93**, 011502 (2008).
- [36] S. Müller, R. J. Zahn, J. Grundmann, Plasma Process. Polym. **4**, S1004 (2007).
- [37] D. Petrović, T. Martens, J. van Dijk, W. J. M. Brok and A. Bogaerts, J. Phys. D: Appl. Phys. **42**, 205206 (2009).
- [38] J. Shin and L. L. Raja, J. Appl. Phys. **94**, 7408 (2003).
- [39] Q. Wang, J. Sun and D. Wang, Phys. Plasmas **18**, 103504 (2011)
- [40] X. Duan, F. He and J. Ouyang, Plasma Sources Sci. Technol. **21**, 015008 (2012).
- [41] B. Lay, R. S. Moss, S. Rauf and M. J. Kushner, Plasma Sources Sci. Technol. **12**, 8 (2003).
- [42] Z. Xiong and M. J. Kushner, J. Phys. D: Appl. Phys. **43**, 505204 (2010).
- [43] D. L. Scharfetter, and H. K. Gummel, IEEE Trans. Electron Devices. **ED-16**, 64 (1969).
- [44] M. J. Kushner, J. Appl. Phys. **95**, 846 (2004).
- [45] N. Y. Babaeva and M. J. Kushner, Plasma Sources Sci. Technol. **20**, 035017 (2011).
- [46] Y. Akishev, M. Grushin, V. Karalnik, A. Petryakov and N. Trushkin, J. Phys. D: Appl. Phys. **43**, 215202 (2010).
- [47] I. Radu, R. Bartnikas, and M. R. Wertheimer, IEEE Trans. Plasma Sci. **31**, 1363 (2003).

- [48] A. A. Ionin, Y. M. Klimachev, A. A. Kotkov, I. V. Kochetov, A. P. Napartovich, L. V. Seleznev, D. V. Sinitsyn, and G. D. Hager, *J. Phys. D* **36**, 982 (2003).

CHAPTER 4 CHARACTERISTIC OF A RF MICRO-DIELECTRIC BARRIER DISCHARGE ARRAY

4.1 Introduction

Arrays of micro-DBDs (or mDBDs) having dimensions of tens of μm operating at atmospheric pressure using rf voltages have been developed for large area-selective surface treatment and production of photons, excited states or charge species.[1-11] mDBD characteristics are determined by the geometry of the aperture, material, repetition rate and pulse shape, the latter two of which can in principle be independently controlled for each aperture.[7,10-17] One such example of independent control of light emitting mDBDs is the commercial plasma display panel (PDP).

mDBD arrays also hold potential for inexpensive latent image production in electrographic printing. Leoni *et al* developed an electrographic apparatus consisting of arrays of individually addressable mDBDs from which plumes of electron current only tens of microns in diameter are extracted for forming a latent image.[18] The mDBD is typically operated in nitrogen or in inert gas to avoid the production of negative ions which reduces the current extraction. These electron beams deposit charge on the dielectric imaging surface. The charge is then either directly the basis of adhering toner particles to the surface or is transferred to another surface. During formation of the latent negative charge previously deposited on the imaging surface can repel the incoming electron current, thereby spreading and increasing the diameter of the initially narrow electron beam extracted from the mDBD. This divergence reduces the quality of the latent image.[18,19]

In addition to the interaction between mDBDs through dielectric charging, plumes of charge extracted from the mDBD apertures can also directly interact with each other or with the remnants of charge from previous discharge pulses. Although not a topic of this chapter, combinations of indirect interactions with charged surfaces and direct interaction between DBD plumes, either attraction or repulsion, can result in self-organized patterns.[20-25]

In this chapter, I discuss results from a numerical investigation of a 3-aperture array of mDBDs sustained in atmospheric pressure N_2 with an O_2 impurity. The model geometry of mDBD aperture, shown in Fig. 4.1, is patterned after those developed for electrographic printing.[18] I found that the divergence of the extracted current can be delayed by increasing the permittivity of the target surface to produce a longer charging time. Accumulation of positive charge in the gap on a pulse-to-pulse basis helps to extract electrons from the mDBD cavity. With higher oxygen impurity content, electron attachment begins to dominate which reduces the extraction field and ultimately reduces the collected surface charge density. At rf frequencies up to 25 MHz, charge extraction is limited by the duration of the cathodic portion of the cycle. At lower frequencies having periods longer than the charging time of the intervening dielectric, electron current is limited by charging of the dielectric. The model used in this chapter is described in Sec. 4.2 and followed by a discussion of N_2 plasma dynamics sustained in a single mDBD in Sec. 4.3. In Sec. 4.4, characteristic of mDBD arrays are discussed, and Sec. 4.5 contains our concluding remarks.

4.2 Description of the Model and Reaction Mechanism

In this chapter, a two-dimensional, fluid hydrodynamic simulation platform, *nonPDPSIM*, was used and is described elsewhere [26,27] and Chapter 2 in detail. The mDBD is a sandwich of alternating electrodes and dielectrics. (See Fig. 4.1.) An rf biased metal electrode is embedded in

a dielectric substrate (relative permittivity $\epsilon_r = \epsilon/\epsilon_0 = 4.3$) 50 μm below the dielectric surface. This rf electrode is biased with -2 kV DC and a 1.4 kV AC potential with frequencies up to 25 MHz. A negatively DC biased discharge electrode (-2 kV) 25 μm thick sits on the top of the dielectric layer (19 μm thick and $\epsilon_r = 20$) and has a 35 μm opening which exposes the underlying dielectric. A less-negatively-DC-biased screen electrode, 40 μm thick, biased with -1950 V is separated from the discharge electrode by another dielectric (25 μm thick and $\epsilon_r = 20$) and acts as an anode switch to extract charges and narrow the current beam. The extracted electron current is accelerated towards a grounded electrode covered with a 25 μm dielectric sheet with ϵ_r up to 12.5. This dielectric-covered grounded electrode is separated from the screen electrode by 410 μm gap. The lateral spacing between the mDBDs apertures are tens to hundreds of microns. The side boundaries in the simulation are grounded and placed far from the mDBDs apertures using a progressively coarser mesh so that the potential calculation will not be affected by the side boundaries. The top and bottom boundaries are also grounded, as in actual device. All the dielectrics used in the model are perfect insulator – the conductivity is zero and the surface charges on dielectrics are laterally immobile.

In this chapter, the mDBD is filled with N_2 at 1 atm with a small amount of O_2 serving as an impurity at room temperature 300 K. This selection of gas mixture reflects that used in experiments. The ratio of N_2/O_2 varies from 99.99/0.01 to 90/10. A reduced reaction mechanism contains a subset of the reactions described in [28,29] to limit the magnitude of calculation. The reduced reaction mechanism includes N_2 , $\text{N}_2(\text{v})$, N_2^* , N_2^{**} , N_2^{***} , N_2^+ , N_4^+ , N , N^* , N^+ , O_2 , O_2^* , O_2^+ , O_2^- , O_3 , O^- , O , O^* , O^+ and electrons. The states N_2^* and N_2^{**} are nominally $\text{N}_2(\text{A,B})$ and $\text{N}_2(\text{C})$ though the latter is treated as a lumped state including transitions higher than $\text{N}_2(\text{C})$, and N_2^{***} is nominally $\text{N}_2(\text{a}')$. The discharge is initiated by placing a plasma cloud 100 μm in radius centered

in each mDBD cavity with a peak electron density of 10^{12} cm^{-3} . Many rf cycles are then computed until either quasi-steady state conditions are achieved or long term trends are discernable. Each aperture in an actual array is circular which would require a 3-dimensional model to resolve. Our model, being 2-d, resolves side-by-side apertures as slots in a Cartesian geometry.

4.3 mDBD Plasma Properties

The plasma dynamics of a single aperture mDBD in similar geometry have been previously investigated [27], and so the fundamental properties of single mDBDs will be briefly discussed. The operating conditions are 1 atm $\text{N}_2/\text{O}_2 = 99.99/0.01$ at 300 K. This impurity reflects the actual purity of gas used in experiments and provides an unambiguous source of photoionization. As shown in Fig. 4.1, the rf electrodes are biased with -2 kV DC plus 1.4 kV rf voltage at 25 MHz. The discharge and screen electrodes are biased with -2 kV and -1950 V, respectively. The grounded electrode is about 400 μm above the screen electrodes, and is covered by a dielectric sheet 25 μm thick with relative permittivity $\epsilon/\epsilon_0 = 12.5$. The complete computational domain extends 1.45 mm on either side of the center mDBD. The time evolution of single aperture electron density and electric potential during an rf period is shown in Fig. 4.2(a). Electron density, electric field and potential in the mDBD cavity are shown in Fig. 4.2(b) at $t = 13.5 \text{ ns}$ when top electrode begins to extract the electron plume. The applied rf voltage is shown in Fig. 4.2(c). The cycle begins with -2 kV on the rf electrode at $t = 0 \text{ ns}$, which is same as the voltage on the discharge electrode. However, due to the positive charge deposited on the bottom dielectric on previous rf cycles, electrons are attracted toward the dielectric and begin to neutralize the positive charge. By $t = 15 \text{ ns}$, the negative charge collected on the bottom dielectric is sufficiently large that electric field vectors are reversed and an electron flux starts to escape from the mDBD cavity. The screen

electrode with a potential 50V higher than discharge electrode acts as an anode switch to help extract and focus the electron current. The re-entrant electric potential contours in the opening of the screen electrode, as shown in Fig. 4.2(b), aids in focusing the plume when extracting the electrons towards the top dielectrics.

As the rf voltage decreases to -2 kV at $t = 20$ ns, there is no net external rf field applied to the cavity while a large negative potential remains on the bottom dielectric due to the previously collected negative charges. The electron plume is then expelled out of the mDBD cavity towards the top dielectric covered extraction electrode, which negatively charges the sheet. At the same time, the plasma is re-ignited in the cavity due to the avalanche of remaining residual electrons and secondary electron emission from the surface in the cavity produced by UV/VUV photons and ions. The current extraction is then enhanced as the rf voltage becomes slightly more negative at $t = 25$ ns. When the rf voltage becomes more positive (or less negative) at $t = 34$ ns, a sufficiently large amount of positive charge is collected on the bottom dielectric that the negative charge is neutralized, the voltage drop is reduced and electron plume begins to diminish. The cycle then repeats. The electron density in the mDBD cavity is on the order of $3 \times 10^{15} \text{ cm}^{-3}$, and is of order $5 \times 10^{11} \text{ cm}^{-3}$ adjacent to the top dielectric. As the electron current beam negatively charges the top dielectric, a negative surface potential is produced and electric potential lines are trapped into the dielectric target as shown in Fig. 4.2(a) at $t = 40$ ns.

4.4 Small Arrays of mDBDs

The plasma plumes extracted from the mDBD cavities interact with the top collection surface by successively charging the surface on a pulse by pulse basis. This charges the capacitance of the dielectric sheet which produces a negative surface potential, which results in

additional lines of electrical potential being in the dielectric. The acceleration produced by the resulting electric fields opposes the incoming plume of electrons. If the charging is spatially uniform, the collection of current from the electron plumes will uniformly decrease. If the charging of the surface is spatially non-uniform or the surface is in motion, the retarding electric fields may perturb the incidence plumes in a non-uniform or asymmetric manner.

To investigate these dynamics, an array of three mDBDs were simulated with a spacing of 300 μm as shown in Fig. 4.3. The dielectric constant of the top dielectric is $\epsilon/\epsilon_0 = 1.25$, purposely chosen to be small to accelerate the consequences of charging. The voltage on the three rf electrodes are in phase with a -2 kV dc bias and a 1.4 kV rf bias at 25 MHz (period of 40 ns). The resulting electron density is shown at the peak of the electron extraction for the 1st, 3rd, 5th, 7th and 12th pulse. The electrons extracted from the mDBDs are incident onto the top dielectric target. For the initial portion of the first pulse, the potential lines in the gap are essentially uniform and parallel. The unperturbed electron plumes are accelerated vertically upward to the dielectric and begin to charge the surface, which traps the potential lines in the dielectric sheet. Meanwhile, these three electron plumes are below the space charge limit of affecting their neighbors and so are extracted independently. By 20 ns, there is enough charging of the dielectric in spots above the mDBD apertures that horizontal components of the electric field are generated, which in turn begin to warp outwards the two outside electron plumes. The center plume, seeing symmetric charging, remains nearly vertical.

As the pulsing continues, negative charging of the dielectric target continues and the retarding potential increases. By the 3rd pulse (100 ns), the potential at the dielectric surface is as large as -1160 V, half of the initial extraction potential. The potential is non-uniform and varies by 300 V laterally across the surface. With an additional two pulses (180 ns), the negative charging

and negative potential of the dielectric is sufficiently large that the center electron plume is diminished in intensity and the rate of surface charging decrease. Electric fields with components parallel to the dielectric are produced by the charging and deflect the outer plumes in the direction of largest electric field which is now towards the uncharged dielectric on the boundary. By the 12th pulse (460 ns) the center plume is extinguished as the potential difference between the top dielectric and the focusing screen electrode is insufficient to extract additional charge, and the outer plumes are deflected by more than the spacing between the mDBDs. This deflection in printing, diminishes the quality of the latent image and poses a challenge to achieving high resolution image.[18,19]

Since the onset of the divergence of the current is inversely proportional to the charging time (or the capacitance) of the top dielectric, a larger capacitance of the top dielectric having a larger charging time should delay the divergence. This expectation is illustrated in Fig. 4.4 where electron plumes and electric potential contours are shown for the same conditions as Fig. 4.3 except for the top surface having a larger dielectric constant $\epsilon/\epsilon_0 = 12.5$. With the larger permittivity and capacitance of the top dielectric, obtaining a given surface potential requires more charge accumulation, and so divergence of the current begins later. The plumes from each of the three mDBDs maintain their vertical trajectories through the first 10 pulses, and only at $t = 460$ ns, are the electron plumes beginning to become warped.

Although the majority of ionization occurs in the mDBD cavity, some ionization does occur as the electron plume transits the gap. Due to low mobility of the positive ions (dominantly N_4^+ produced by 3-body reactions of the originally produced, N_2^+) and their slow drift towards the negatively biased screen electrode, ions tend to accumulate in the gap pulse to pulse. The total charge density and electric potential are shown in Fig. 4.5 for several rf pulses. A net positive

charge density of $7.5 \times 10^{11} \text{ cm}^{-3}$ is initially produced after the first few rf cycles in the path of the electron plume. The more mobile electrons are accelerated out of the gap on a pulse –by–pulse basis leaving the positive ions that were produced in the gap. As the electron plumes are diverted by charging of the dielectric, electron impact ionization in the gap occurs in the deflected path and the accumulation of positive charge follows the trajectories of the plumes. The positive charge density that remains in the gap is insufficient to significantly perturb the potential lines, as the potential is dominantly determined by the dielectric charging. (For these conditions, the negative ion density in the gap is small, $8.5 \times 10^9 \text{ cm}^{-3}$.) However, the net positive charge density is large enough, $3.7 \times 10^{12} \text{ cm}^{-3}$, near the apertures in the screen electrodes to produce a small concavity of the potential contours. An auxiliary average electric field is produced to aid in current extraction and help focus the electron beam due to this concavity of the electric potential lines. The accumulated positive ion density near the apertures and the extracting electric field increase with successive discharge pulses. As a result, the peak electron density increases at early pulses before the surface charge on top dielectric reduces the extracting field.

With the small impurity of O_2 in the current gas mixture $\text{N}_2/\text{O}_2 = 99.99/0.01$, the influence of negative ions is inconsequential. With increasing O_2 content, however, electron attachment and negative ions begin to play more important roles. The total charge density, surface potential and time integrated electron flux after 11 pulses (450 ns) for O_2 fractions of 0.01% to 10% are shown in Fig. 4.6. The net negative charge density (ρ^-) and net positive charge density (ρ^+) shown in Fig. 4.6 are separated by a white contour line. Below 0.1% O_2 , positive ions (mainly N_4^+) accumulate close to the apertures and produce an average extracting electric field, while negative ions (mainly O^-) slowly drift to the top anode-like dielectric. The fractional electron loss due to attachment is small, and the mDBDs behave as though they are electro-positive plasma. The

concave electric potential lines close to the screen electrode help focus the electron beam.

When the gas mixture increases to 1% and 10% O₂, electron attachment becomes a significant electron loss mechanism and more negative ions are then produced along the electron extraction path. The increasing negative ion density reduces the extracting electric field by reducing the net positive charge density. By an O₂ fraction of 10%, the net negative charge extends nearly to the opening in the screen electrode and the previously concave electric potential lines are reversed to be convex. The convex electric potential lines produced by net negative charges now defocus the extracted electron beam. The time integrated electron flux on the top dielectric is then proportionately smaller and more uniform, as shown in Fig. 4.6(f). A consequence of the decrease in integrated electron current is a decrease in the surface potential on the dielectric. The surface potential on the top dielectric for O₂ fractions of 0.01% to 10% after 11 pulses is shown in Fig. 4.6(e). With an O₂ fraction < 0.1%, the negative peak surface potential remains near -900 V. When the O₂ fraction increases to 10%, the surface potential drops to -500 V.

The O₂ impurity also provides volumetric photoionization source (S_{ph}). By increasing the O₂ fraction from 0.01% to 10%, S_{ph} increases from 2.5×10^{17} to $8.2 \times 10^{19} \text{ cm}^{-3}\text{s}^{-1}$, which is still small compared to electron impact ionization sources. Having said that, this small photoionization source is fairly uniform throughout the volume of the mDBD cavity, and so serves to seed electrons that eventually avalanche in locally large electric fields. In the same way, UV photons from long lived excited states continuously seed secondary electrons by photoemission at dielectric and electrode surfaces which helps to facilitate the reignition of plasma.

The uniformity and charging of the dielectric are functions of the mDBD spacing, and this can be used to advantage depending on the application. For example, if uniform charging over large areas is desired without modulation, more closely spaced mDBDs can be used. If truly

independent charging of spots on the dielectric is desired, more widely spaced mDBDs can be used. For example, the electron density and electric potential for successive pulses are shown in Fig. 4.7(a)-(f) for a spacing between the mDBDs of 100 μm . The electron density and potential after the 12th pulse are shown in Fig. 4.7(g) for a spacing of 600 μm . The surface potentials after the 12th pulse (460 ns) for spacings between the mDBDs of 100, 300 and 600 μm are shown in Fig. 4.7(h). The repetition rate is 25 MHz (40 ns cycle). With the 100 μm spacing, the electron density in the plume adjacent to the top surface initially increases (first 3 pulses) prior to the negative charging of the surface beginning to dominate and deflecting the electron current. Decreasing the aperture spacing does not change the current extraction process. However, the three electron plumes do merge to form a single current beam as the interactions between the electron beams are not significant. Due to the merging of the plumes, the electron current is larger in amplitude and broadened in width, producing a less modulated and larger (more negative) surface potential. The peak surface potential reaches -1,060 V on the 12th pulse due to the merged electron plumes. As the spacing is increased to 600 μm , the charging of the dielectric by the electron plumes become more independent and the individual electron plumes are not significantly perturbed by the charging produced by its neighbor. The peak surface potential produced by each individual mDBD plume drops to -750 V.

Since divergence of the current occurs within 100's ns and is dependent on capacitance (charging time) of the top dielectric and accumulation of ions in the gap, the charging process should be sensitive to rf driving frequency. The electron density and electric potential after four rf cycles for frequencies of 2.5 MHz to 25 MHz are shown in Fig. 4.8. As a point of reference, the peak electron density during each rf cycle is shown in Fig. 4.4.

9(a) for site A adjacent to target dielectric (see Fig. 4.1(b) for location). The electric potential on

the surface of the top dielectric at the same time ($t = 500$ ns) and the same pulse (4th) is shown in Fig. 4.9(b) and 4.9(c). Since the top dielectric is treated here as perfect insulator, this potential profile reflects the charged particle fluence (cm^{-2} – flux integrated over time) along the surface. In reality, it is likely that UV photon illumination of the top dielectric does provide some surface conductivity that might smear out the collected charge and so the potential. At high frequency, charge extraction is limited by the shorter rf cycle, while positive ions accumulating in the gap cannot respond to such high frequency. These ions produce a positive space charge in the gap and help extract electrons out of the mDBD cavity. As a result, the peak electron density at site A initially increases due to this accumulation of positive ions which produces a larger extraction field. The electron density then decreases with increasing number of pulses as a result of negative charging of the dielectric.

With lower frequencies and longer cycles, more electrons are extracted out of the mDBD cavity into the plume during early cycles. The plume then charges the dielectric which retards the subsequent electron flux. Also, there is sufficient time for positive ions in the gap to drift downward to be collected by the screen and discharge electrodes, thereby reducing the accumulation of positive charge in the gap which would otherwise enhance electron extraction. Consequently, the peak electron density at site A decreases with increasing number of rf pulses. The charge collection on the top dielectric surface at given time tends to be larger at higher frequencies. The electric potential on the top dielectric at $t = 500$ ns is more negative at high frequency simply due to there being more charge collection as a result of the higher repetition rate. However, more charge is collected at lower frequency for given rf pulse. As a result, the surface potential is about half as negative at 25 MHz compared to 2.5 MHz. The larger current collection per pulse at lower frequency is shown by the more negative potential after 4 pulses compared to

high frequency (-1000 V at 2.5 MHz compared to -400 V at 25 MHz). Although a non-uniform voltage can be generated by the surface charges on the top dielectric sheet, the resulting electric field parallel to the surface is typically not large enough to induce a surface discharge.

The ability to independently control the rf bias to each mDBD aperture provides the opportunity to tune the profile of the surface charging. This tuning capability is demonstrated by the electron density, electric potential and surface potential shown in Fig. 4.10 for an mDBD spacing of 300 μm . Electron density and potential are shown for the 1st, 3rd, 5th, 7th and 12th pulse. The applied voltage of the center rf electrode is delayed by 2 cycles (80 ns) compared to the outer electrodes that are excited in phase. The surface potential after 500 ns (12 pulses) for the center-delayed operation is compared to fully synchronized mDBDs in Fig. 4.10(f). The charging process of center delayed case is essentially the same as that of the in-synch case. However with the center plume delayed by 2 pulses, there is proportionately less charge extracted from the mDBD and so less surface charging. With fully synched mDBDs, the surface potential is largest (most negative) above the center mDBD, a result of the outer plumes being deflected and there being contributions to surface charging at the center by the adjacent plumes. By delaying the center mDBD, there is both less deflection of the outer plumes and less charging by the center plumes. The end result is that the peak surface potential above the center mDBD is reduced by 100 V (less negative), in this case becoming slightly less negative than the other peaks.

4.5 Concluding Remarks

mDBD arrays are being developed for high definition surface treatment and charging. Using results from a 2-dimensional model, I investigated the plasma dynamics of a small array of mDBDs sustained in 1 atm N_2/O_2 mixtures, and the interaction between electron plumes through

charging of the target dielectric. After electrons are produced in the mDBD cavities and extracted onto the target dielectric surface, a negative potential is generated which deflects the incoming electron plumes. This divergence can be mitigated by increasing the dielectric constant (or charging time) of the target surface. Positive ions which accumulate in the gap also help extract charges by increasing the average extraction field. With increasing oxygen fraction, electron attachment processes begin to dominate. As a result, the electron flux extracted from mDBD cavity is additionally hindered by negative ion charge accumulation in the gap. Collection of charge on the top dielectric is then reduced with increasing oxygen content.

Uniformity of charging is a sensitive function of mDBD spacing. Reducing the mDBD spacing merges plumes and reduces modulation of the charging. Increasing spacing between the mDBD reduces the deformation of the plumes by the charging produced by adjacent plumes. The surface potential profiles can be tuned by independently controlling the timing and number of pulses from the individual mDBDs apertures. The plumes also indirectly interact with each other through the space charge they produce in the gap. This is, however, a cumulative affect. Due to the large extracting electric field and high mobility of electrons, the space charge provided by the electron density in the gap during a single pulse is not large enough to perturb the neighboring plume. However, the accumulation of low mobility ionic charge (either positive or negative) during successive pulses can produce sufficient space charge to perturb neighboring plumes. In this sense, more closely spaced mDBDs will be more perturbing to their neighbors. In all cases, charging of the dielectric and its associated electric fields ultimately dominate in perturbing the plume.

In summary, this chapter focuses on independently controlled mDBD arrays, and interaction between the electron plumes and target dielectric. The electron plumes extracted from

the mDBD arrays charge the dielectric and form latent images on the selected locations. If the surface charging and current extraction are not carefully controlled, the blooming effect becomes dominant which broadens the beam size, warps the electron plumes and reduces the resolution. This blooming effect can be mitigated by increasing the dielectric constant of the target surface. The capability of being independently controlled is also demonstrated by simulation.

4.6 Figures

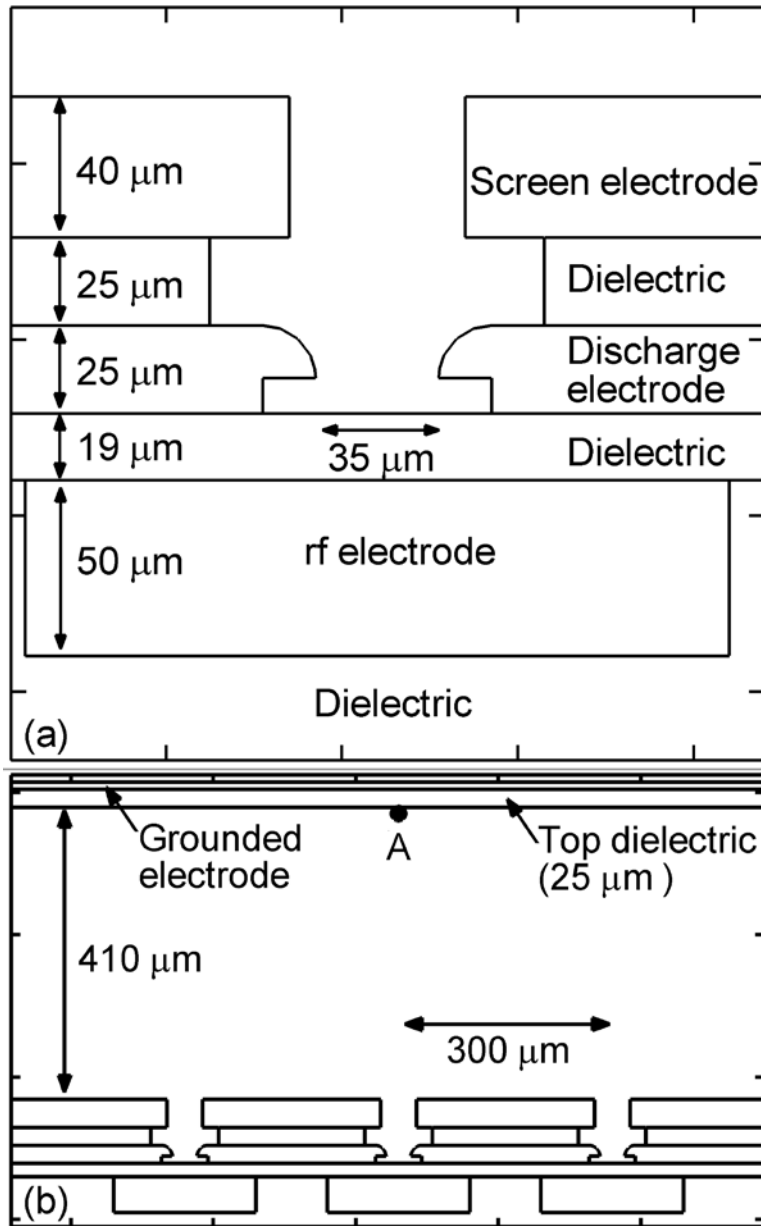


Figure 4.1 Schematic of the mDBD device. (a) A single mDBD single aperture. (b) Multiple mDBD apertures and top grounded electrode covered with dielectric.

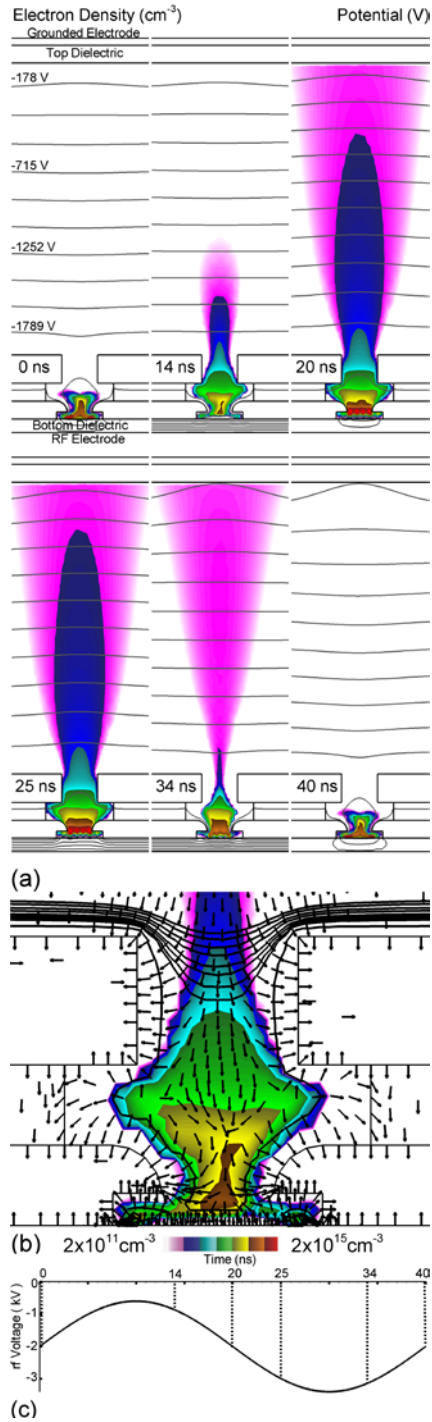


Figure 4.2 Electron current extraction produced by an rf voltage of 25 MHz. (a) Time evolution of electron density (color flood, cm⁻³) and electric potential (contour lines, V) during a 40 ns rf period. The electron density is plotted on a log-scale over 4 decades (2 × 10¹¹ – 2 × 10¹⁵ cm⁻³). (b) Electron density (color flood, cm⁻³), electric field (vector, V-cm⁻¹) and potential (contour lines, V) at t = 13.5 ns when electrons are extracted. (c) rf driving voltage. The instantaneous electric field vectors show only the orientation but not the magnitude of the field which help extract and focus the electron beam.

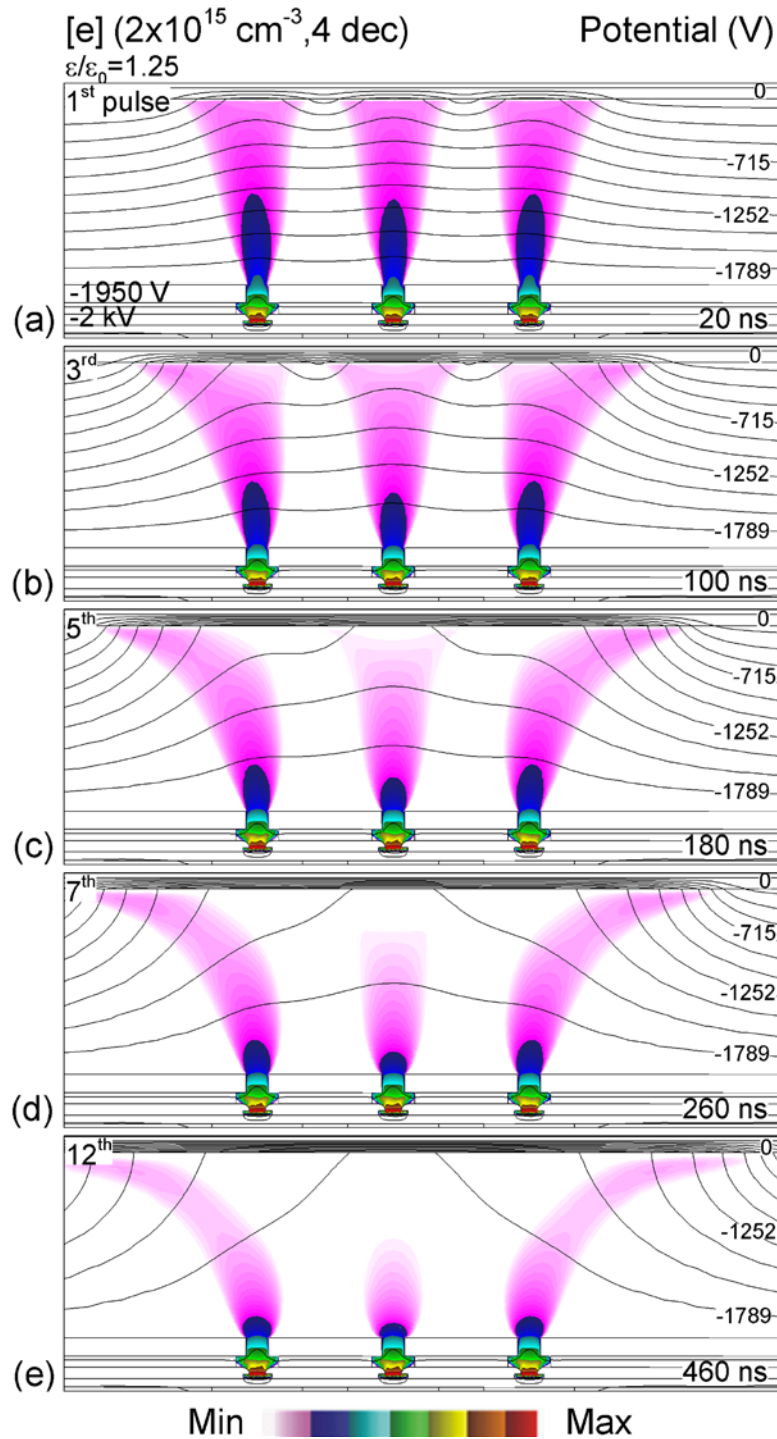


Figure 4.3 mDBD array with a spacing of 300 μm and target dielectric constant of $\epsilon/\epsilon_0 = 1.25$. Electron density (color flood, cm^{-3}) and electric potential (contour lines, V) at the peak of electron current extraction for the (a) 1st, (b) 3rd, (c) 5th, (d) 7th and (e) 12th rf pulse. The electron density is plotted on a log-scale over 4 decades ($2 \times 10^{11} - 2 \times 10^{15} \text{ cm}^{-3}$). The electron plume is largely warped toward less charged dielectric by the 12th pulse.

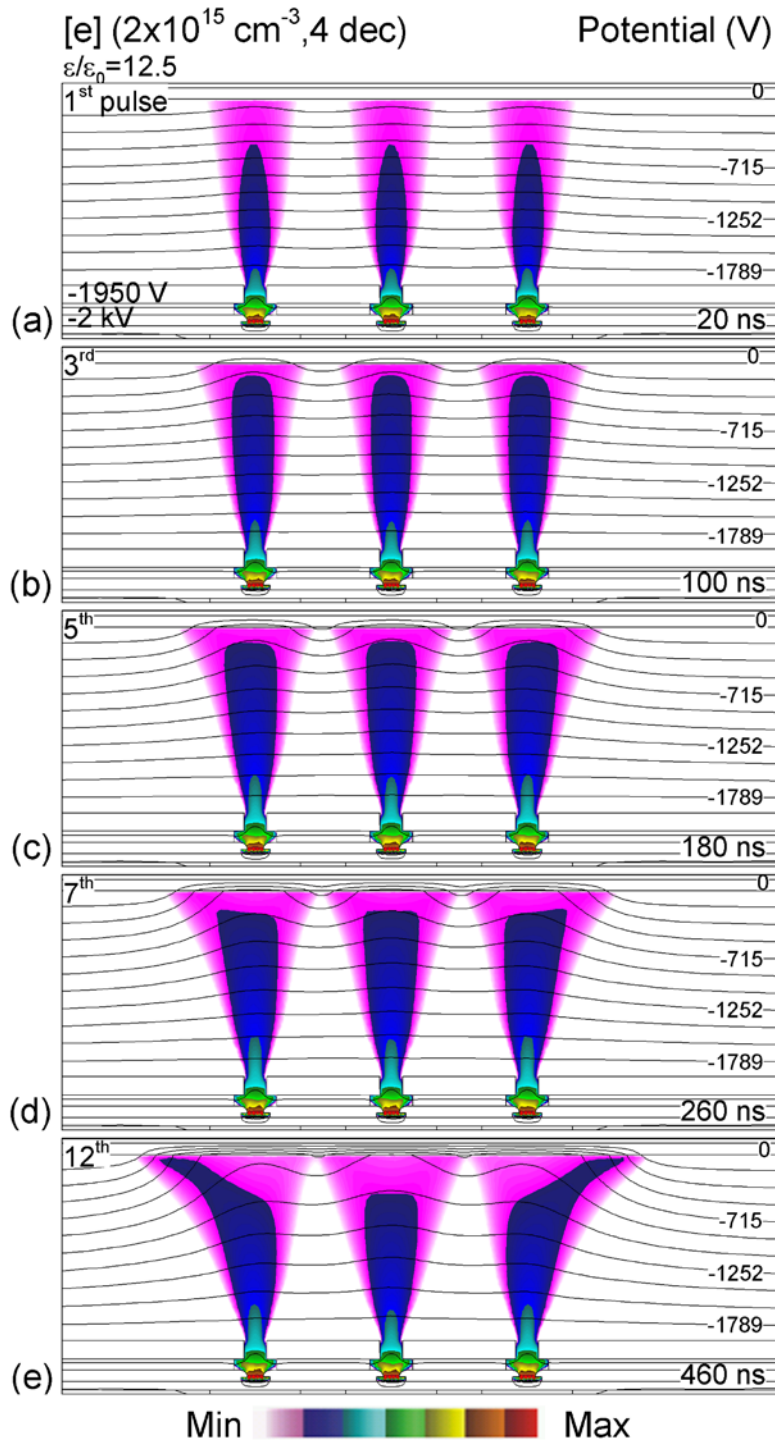


Figure 4.4 mDBD array with spacing of $300 \mu\text{m}$ and larger target dielectric constant $\epsilon/\epsilon_0 = 12.5$. Electron density (color flood, cm^{-3}) and electric potential (contour lines, V) at the peak of electron current extraction for the (a) 1st, (b) 3rd, (c) 5th, (d) 7th and (e) 12th rf pulse. The electron density is plotted on a log-scale over 4 decades ($2 \times 10^{11} - 2 \times 10^{15} \text{ cm}^{-3}$). Divergence of the current begins later due to the longer charging time of target dielectric.

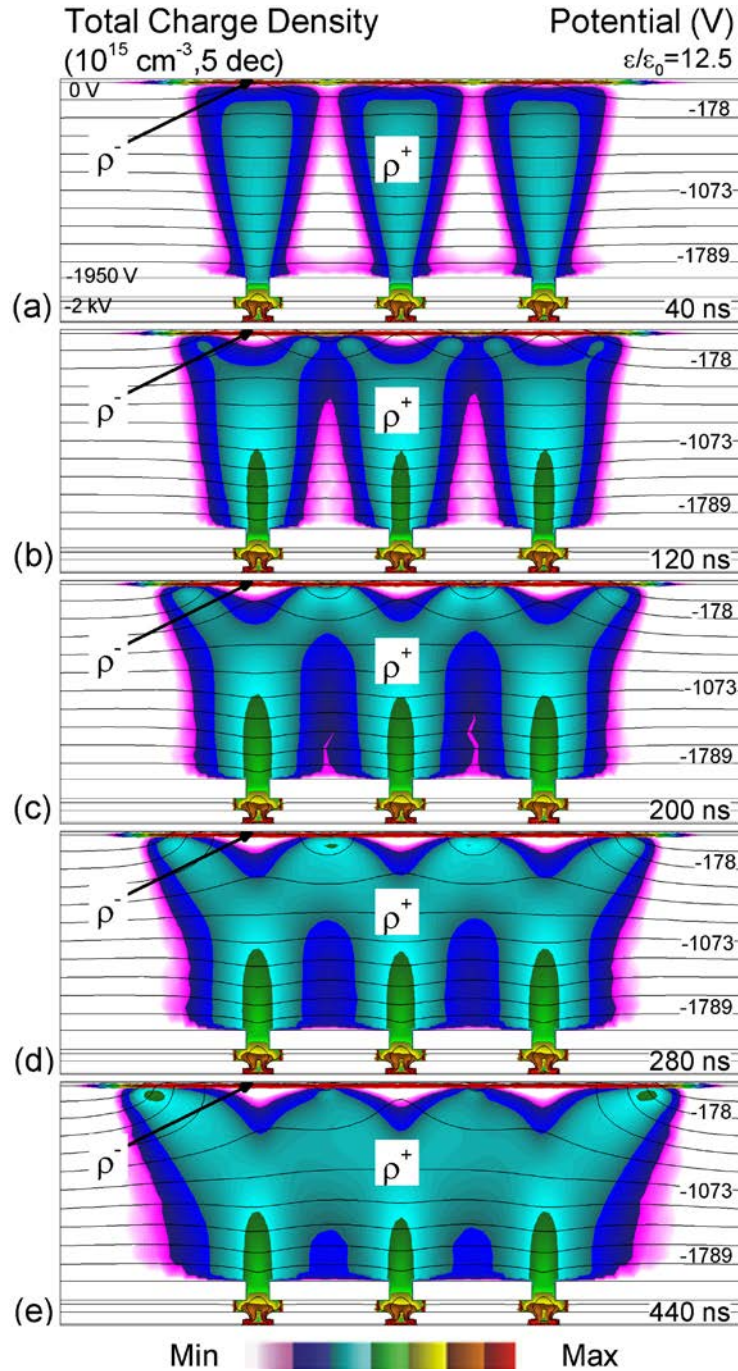


Figure 4.5 Total charge density (color flood, cm^{-3}) and electric potential (contour lines, V) for the (a) 1st, (b) 3rd, (c) 5th, (d) 7th and (e) 11th rf pulse. The charge density is plotted on a log-scale over 5 decades ($10^{10} - 10^{15} \text{ cm}^{-3}$). Electrons in the plumes are accelerated towards the top dielectric and only heavy positive ions are left in the gap. A concavity in the potential is produced by the net positive charge in the gap which helps to extract and focus the electron current beam before surface charging become dominant.

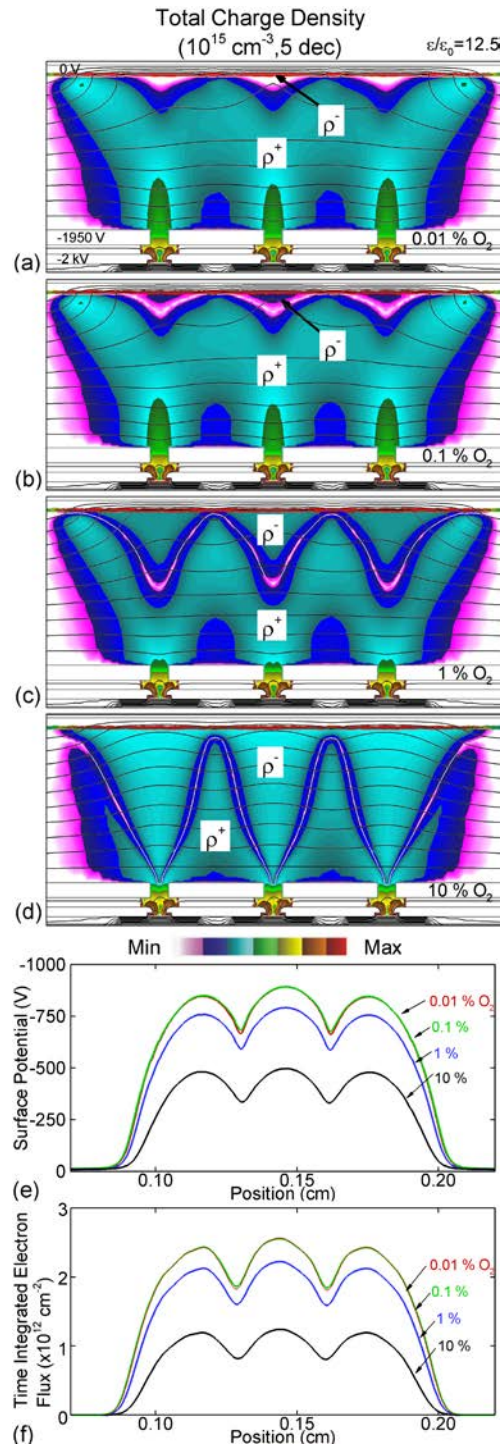


Figure 4.6 Net negative (ρ^-) and positive (ρ^+) total charge density (color floods cm^{-3}) and electric potential (contour lines, V) in a gap filled with N_2/O_2 mixtures with O_2 content of (a) 0.01%, (b) 0.1 %, (c) 1% and (d) 10%. The charge density is plotted on a log-scale over 5 decades ($10^{10} - 10^{15} \text{ cm}^{-3}$) after the 12 pulse. A white line separates regions of positive and negative charge. The resulting (e) potential (V) on the top dielectric surface and (f) time integrated electron flux (cm^{-2}) decrease with increasing O_2 content.

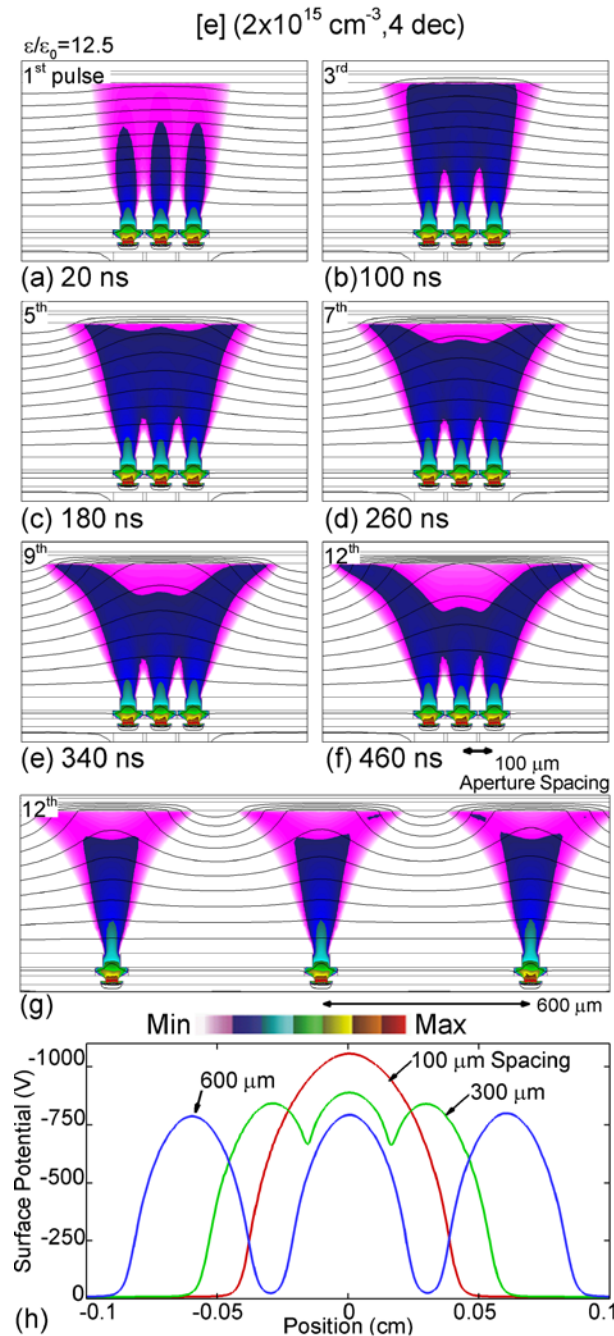


Figure 4.7 A more uniform current beam with higher intensity can be achieved by reducing the mDBD spacing. Electron density (color flood, cm^{-3}) and electric potential (contour lines, V) for (a) 1st, (b) 3rd, (c) 5th, (d) 7th, (e) 9th and (f) 12th rf pulse. The electron density is plotted on a log-scale over 4 decades ($2 \times 10^{11} - 2 \times 10^{15} \text{ cm}^{-3}$). (g) Electron density and potential after the 12th pulse for a 600 μm spacing. (h) Surface potential on top dielectric after the 12th pulse for spacing of 100 μm , 300 μm and 600 μm between the microdischarge cavities. A less modulated and higher peak potential results from merging of the closely spaced electron plumes.

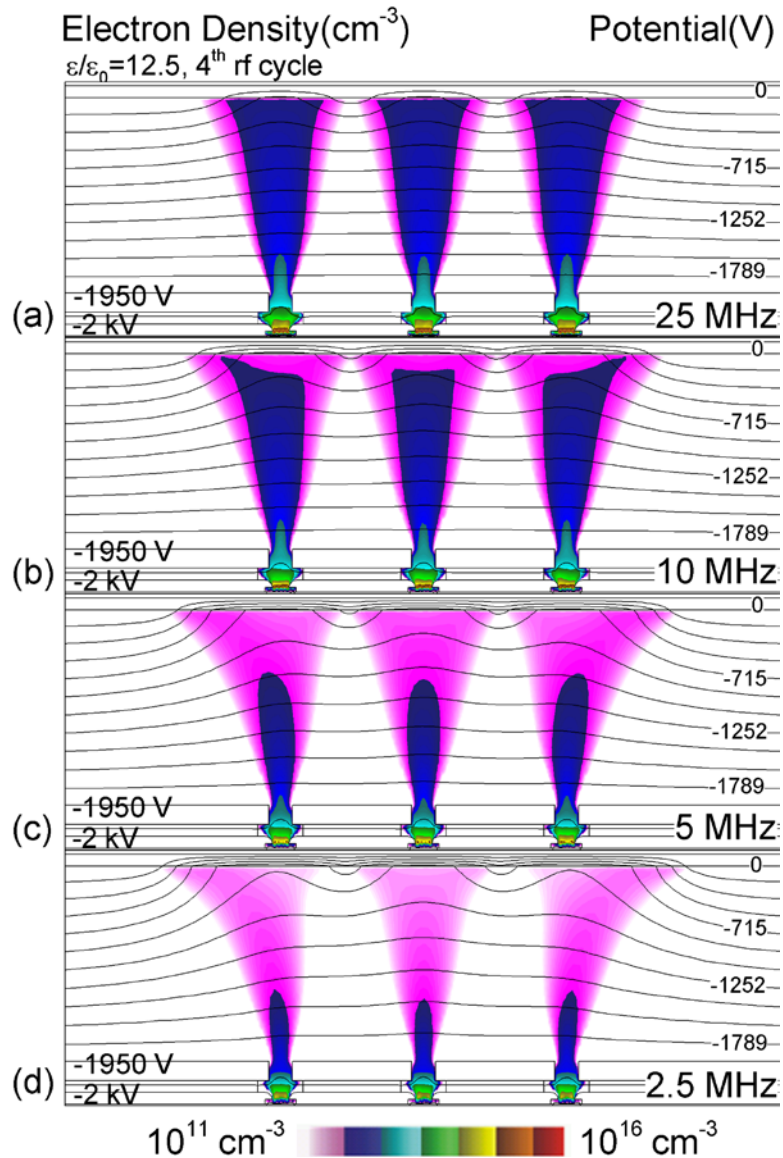


Figure 4.8 Electron density (color flood, cm^{-3}) and electric potential (contour lines, V) during peak current extraction on the 4th rf cycle for frequencies of (a) 25 MHz, (b) 10 MHz, (c) 6 MHz and (d) 2.5 MHz. The electron density is plotted on a log-scale over 5 decades ($10^{11} - 10^{16} \text{ cm}^{-3}$). More negative voltage and charge density result on the top dielectric at lower frequency due to the longer rf period.

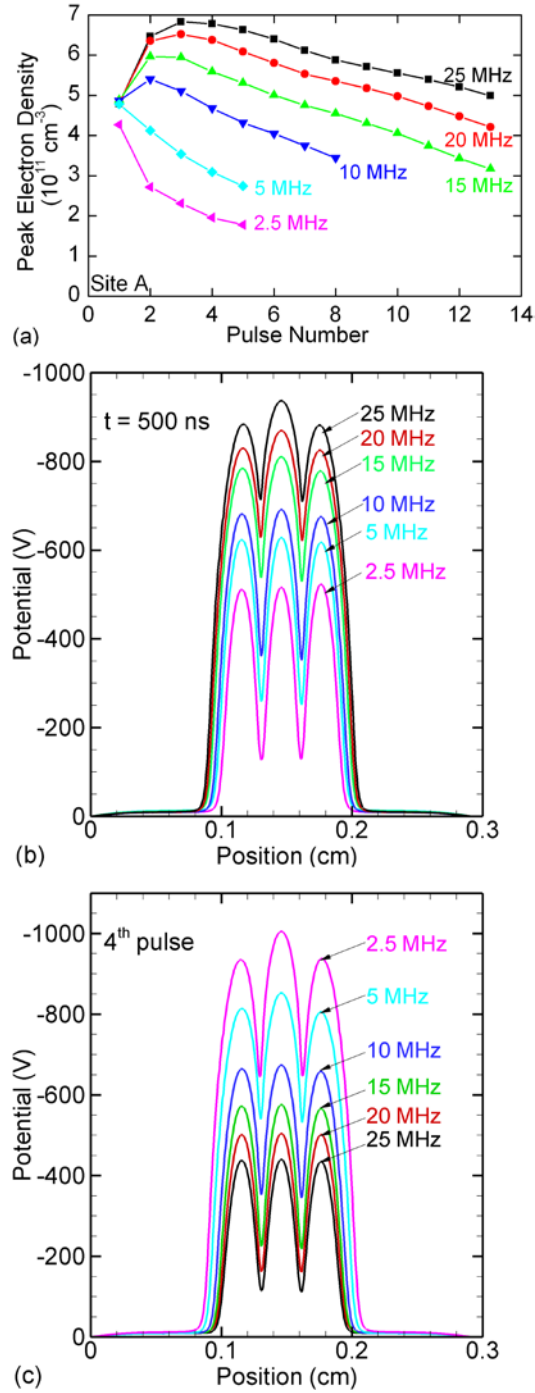


Figure 4.9 Plasma and charging characteristics for different rf frequencies. (a) Peak electron density (cm^{-3}) at site A (see Fig. 4.1) as a function of pulse number, (b) surface potential (V) at $t = 500 \text{ ns}$ and (c) surface potential after the 4th pulse. At higher frequencies, the peak electron density initially increases due to enhancements in the extracting field produced by positive ion accumulation. The electron density then decreases due to charging of the top dielectric. At lower frequencies, positive ions are collected by the screen electrode and the electron density decreases with increasing pulses.

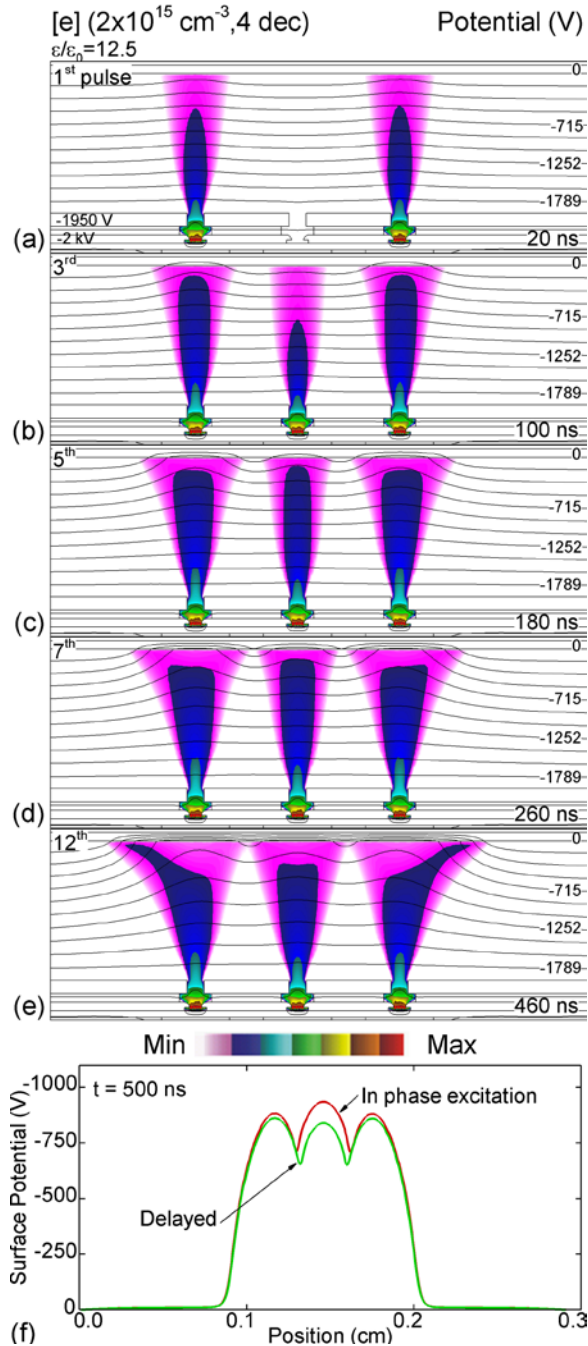


Figure 4.10 Independently controlled mDBDs demonstrated by delaying starting rf voltage on the center microdischarge by 2 rf periods. Electron density (color flood, cm^{-3}) and electric potential (contour lines, V) for (a) 1st, (b) 3rd, (c) 5th, (d) 7th and (e) 12th rf pulse. The electron density is plotted on a log-scale over 4 decades ($2 \times 10^{11} - 2 \times 10^{15} \text{ cm}^{-3}$). (f) Surface potential on the top dielectric at $t = 500 \text{ ns}$ (12th pulse) for in-phase and center delayed rf excitation. Tuning of the surface potential is enabled by controlling the onset of individual microdischarges, in this case a decrease in the potential of the center peak 100 V due to the two period delay.

4.7 References

- [1] U. Kogelschatz, Plasma Chem. Plasma Process. **23**, 1 (2003).
- [2] H. H. Kim, Plasma Process. Polym. **1**, 91 (2004).
- [3] B. Eliasson, M. Hirth and U. Kogelschatz, J. Phys. D: Appl. Phys. **20**, 1421 (1987).
- [4] G. Borcia, C. A. Anderson and N. M. D. Brown, Plasma Sources Sci. Technol. **12**, 335 (2003).
- [5] M. Sira, D. Trunec, P. Stahel, V. Bursikova, Z. Navratil and J. Bursik, J. Phys. D: Appl. Phys. **38**, 621 (2005).
- [6] Z. Fang, X. Xie, J. Li, H. Yang, Y. Qiu and E. Kuffel, J. Phys. D: Appl. Phys. **42**, 085204 (2009).
- [7] N. Lucas, A. Hinze, C. P. Klages and S. Büttgenbach, J. Phys. D: Appl. Phys. **41**, 194012 (2008).
- [8] M. G. Kong, G. Kroesen, G. Morfill, T. Nosenko, T. Shimizu, J. van Dijk, and J. L. Zimmermann, New J. Phys. **11**, 115012 (2009).
- [9] H. Ayan, G. Fridman, A. F. Gutsol, V. N. Vasilets, A. Fridman and G. Friedman, IEEE. Trans. Plasma Sci. **36**, 504 (2008).
- [10] C. Penache, C. Gessner, T. Betker, V. Bartels, A. Hollaender and C.-P Klages, IEE Proc. Nanobiotechnol. **151**, 139 (2004).
- [11] S. Kreitz, C. Penache, M. Thomas, and C. -P. Klages, Surf. Coat. Technol. **200**, 676 (2005).
- [12] J. P. Boeuf, J. Phys. D: Appl. Phys. **36**, R53 (2003).
- [13] K. H. Becker, K. H. Schoenbach, and J. G. Eden, J. Phys. D: Appl. Phys. **39**, R55 (2006).
- [14] S. J. Park, J. G. Eden, K. Jain and M. A. Klosner, Jpn. J. Appl. Phys. **45**, 8221 (2006).
- [15] J. D. Readle, K. E. Tobin, K. S. Kim, J. K. Yoon, J. Zheng, S. K. Lee, S. J. Park, and J. G.

- Eden, IEEE Trans. Plasma Sci. 37, 1045 (2009).
- [16] M. G. L. Fontanil, et al, U.S. Patent No. 5,086,257 (4 Feb. 1992).
- [17] K. D. Cho, H. S. Tae, and S. I. Chien, IEEE Trans. Electron Devices **50**, 359 (2003).
- [18] N. J. Leoni, O. Gila, M. H. Lee and E. G. Hanson, U.S. Patent No. 7,764,296 (27 Jul. 2010).
- [19] I. Kubelik, U.S. Patent No. 5,450,103 (12 Sep. 1995).
- [20] Q. Y. Nie, C. S. Ren, D. Z. Wang, S. Z. Li, J. L. Zhang, and M. G. Kong, Appl. Phys. Lett. **90**, 221504 (2007).
- [21] Y. Feng, C. S. Ren, Q. Y. Nie and D. Z. Wang, IEEE Trans. Plasma Sci. 38, 1061 (2010).
- [22] D. T. Tang, C. S. Ren, D. Z. Wang, and Q. Y. Nie, Plasma Sci. Technol. **11**, 293 (2009).
- [23] T. Shirafuji, T. Kitagawa, T. Wakai, and K. Tachibana, Appl. Phys. Lett. **83**, 2309 (2003)
- [24] V. M. Bedanov and F. M. Peeters, Phys. Rev. B **49**, 2667 (1994).
- [25] E. L. Gurevich, A. L. Zanin, A. S. Moskalenko, and H. G. Purwins, Phys. Rev. Lett. **91**, 154501 (2003).
- [26] Z. Xiong, E. Robert, V. Sarron, J.-M. Pouvesle and M. J. Kushner, J. Phys. D: Appl. Phys. **45**, 275201 (2012).
- [27] J-C. Wang, N. Leoni, H. Birecki, O. Gila and M, J. Kushner, “Electron current extraction from rf excited micro-dielectric barrier discharges”, J. Appl. Phys. 113, 033301 (2013).
- [28] R. Dorai, *Modeling of Atmospheric Pressure Plasma Processing of Gases and Surfaces* PhD Thesis University of Illinois (<http://uigelz.eecs.umich.edu/theses.html>)
- [29] Y. Akishev, M. Grushin, V. Karalnik, A. Petryakov and N. Trushkin, J. Phys. D: Appl. Phys. **43**, 215202 (2010).

CHAPTER 5 CHARGING OF MOVING SURFACES BY CORONA DISCHARGES SUSTAINED IN AIR

5.1 Introduction

Atmospheric pressure plasmas are widely employed to functionalize surfaces due to their short treatment times, room temperature operation, and ability to operate without vacuum facilities. One such application is improvement in wettability of surfaces.[1-5] By creating new surface functional groups on commodity polymer sheets, metallic foils and paper, surface tension (or surface energy, dyne/cm) can be increased to improve the bonding abilities with adhesives, coatings and solvents. As a result, the printing quality and lamination strength can be improved. For example, commodity hydrocarbon polymeric materials such as polyethylene [1,5] and polypropylene [2-5] are hydrophobic and relatively chemically inert due to their low surface energy. A common process to improve wettability and adhesion of inks to these materials is through the use of oxygen containing electric discharges to affix oxygen to their surfaces. More recent developments in the use of atmospheric pressure discharges to change surface properties are in the biomedical field. Sterilization of biomedical devices and the creation of reactive surface functionalities to optimize the biocompatibility have been proven to benefit from atmospheric pressure plasmas.[6-9]

A natural outcome of atmospheric pressure discharges in contact with dielectric or low conductivity surfaces is charging of those surfaces, and so these discharges are frequently used in electrophotographic (EP) printing processes, as discussed in Sec. 1.7.[10-17] For example, corona

discharges in air are used to sensitize the surface of the photoconductor (PC) in EP printing by electrically charging the surface to an optimum potential.[12-17] Although corona discharges sustained in the air for surface charging do have challenges (e.g., high voltage source, long term deterioration of the PC), the simplicity, high charging efficiency and low cost of corona charging devices have motivated continued research into optimizing their performance.

The polarity of the corona discharges used for surface charging of PCs depends on the characteristics of the underlying photoconductive coating and toner particles. For example, amorphous selenium coatings perform better when they are charged positively, whereas zinc oxide-resin coatings require negative charging.[13,16,17] Although there are some variation among coatings, negative coronas are most often used for surface charging of PCs. In a typical negative corona discharge, one or more thin metal wires or straight metal blade electrodes are negatively biased to 100s V dc plus a few kV of ac voltage.[10,11,15] The wires are separated from the PC by gaps ranging from hundreds of microns to a few centimeters. The underlying dielectric PC layer is in contact with the ground plane. A large electric field is produced around the wire or tip of the blade by geometric enhancement and the discharge is initialized when free electrons are accelerated by these strong electric fields to trigger an avalanche.[17,18] This process in negative coronas is particularly sensitive to surface roughness and defects in the electrode that produce additional electric field enhancement or electric field emission of electrons. In negative coronas, the net drift of electrons and negative ions is towards the underlying PC surface which charges the capacitance of the surface which in turn reduces the electric field in the gap. The surface charging terminates the discharge as long as the discharge is only sustained by a dc (or quasi-dc in a pulsed mode) voltage. The PC charging process functionally operates as a dielectric barrier discharge (DBD).

Corona discharges are used in at least two of the process steps of EP printing – the charging and transfer steps.[13-16] In the charging step, the PC surface is uniformly charged using a corona discharge produced by a corotron or scorotron, as shown in Fig. 5.1 (a). The corotron consists of parallel corona wires situated above the PC plate and below a biased electrode. A scorotron is similar to a corotron with the addition of a grid of parallel wires between the corona wires and the PC surface. After the PC surface is charged and the light-induced latent image is formed on this surface, charged toner particles electrically adhere to the latent image. Another corona device is then used to charge the back of the paper to optimize adhesion of toner particles during the transfer of particles from the PC to the paper. In both of these process steps, the underlying dielectric surface moves with speeds of hundreds of cm/s during their charging process with residence times of hundreds of microseconds underneath the corona wire. The discharge itself may last for only hundreds of ns. As a result, a non-uniform charge patterns may result due to the interaction between the corona discharge and the moving surface.

In this chapter, results from a computational investigation of a dc blade corona discharge sustained in atmospheric pressure dry air, charging both stationary and moving dielectric surfaces in a DBD configuration, as shown in Fig. 5.1 (b) and (c) are discussed. For the voltages investigated, I found that the corona discharge is initially sustained by electron impact ionization in the bulk plasma and by secondary electron emission from the cathode. When the underlying dielectric surface charges and voltage is removed from the gap, the electron impact sources from the bulk plasma diminish and the plasma is then sustained by ionization by sheath accelerated secondary electrons from the electrode. Eventually the plasma extinguishes by charging of the surface in a DBD-like manner. When the dielectric surface moves, the previously charged surface translates away from the corona electrode and is replaced by uncharged surface. This results in an

increase in voltage drop across the gap between the corona electrode and the approaching uncharged surface on only one side of the electrode. This rebound in voltage across the gap results in a re-ignition of the discharge. The charging uniformity is sensitive to the material properties of the dielectric sheet, and the subsequent re-ignition of the discharge is sensitive to the previous charging cycle. An oscillatory charging pattern is predicted.

The model used in this chapter is described in Sec. 5.2 and followed by a discussion of plasma dynamics of corona and surface charging on a stationary surface in Sec. 5.3. The characteristics of charging of a moving surface are discussed in Sec. 5.4 followed by our concluding remarks in Sec. 5.5.

5.2 Description of the Model and Reaction Mechanism

The model used in this chapter, *nonPDPSIM*, is described in detail in Chapter 2 and Refs. [19,20]. To enable investigation of plasma-surface interactions during charging with moving surfaces, an idealized corona device has been modeled, as shown in Fig. 5.1(b) and (c). The device consists of a metal cathode corona blade biased with negative dc voltage up to a few kV. The metal blade has a thickness of 100 μm and a height of a few mm. The radius of curvature of the blade tip is 50 μm . An underlying dielectric sheet (100 μm thick and $\epsilon_r = \epsilon/\epsilon_0 = 5$) is separated from the corona tip by a 200 μm gap in the base case. This dielectric target (intended to represent paper or a photoconductor layer in EP printing) serves as a perfect insulator (the conductivity is zero) so the surface charges are laterally immobile on the dielectric sheet. The PC is in contact with the grounded electrode and is initially uncharged. The mesh consists of about 12,800 computational nodes of which about 9,000 are in the plasma zone. The finest mesh spacing is 9 μm in the gap between the corona tip and dielectric sheet. The lateral side boundaries in the

simulation are placed far from the corona wire so that the potential calculation will not be affected. Although corona wires are typically used in arrays in EP applications, I investigated a single corona source using Cartesian geometry to study possibly asymmetric plasma-surface interactions on stationary and moving surfaces.

The moving surface was computationally addressed in the following manner. The numerical mesh points on top of the surface in contact with the plasma are chosen to be evenly spaced. These mesh points are identified during code initialization and sifted into an array based on horizontal position. The surface is moved every $\Delta t = \Delta x/v$ s, where Δx is the mesh spacing on the surface and v is the horizontal speed of the surface. Assuming that the surface is moving right-to-left, motion of the surface consists of translating the properties of the mesh point (e.g., chemical composition, surface charge density) one location to the left. The properties of the leftmost mesh point are translated out of the computational domain and no longer affect the simulation. The properties of the rightmost mesh point are set to the initial or prescribed conditions, which in this case is a zero surface charge density.

The gas is 1 atm of dry air and the gas temperature is held constant at 300 K. Due to the magnitude of the calculation, I use a reduced reaction mechanism containing a subset of the reactions described in Refs. [21,22] to minimize the computation time. The reduced reaction mechanism includes N_2 , $N_2(v)$, N_2^* , N_2^{**} , N_2^{***} , N_2^+ , N_4^+ , N , N^* , N^+ , O_2 , $O_2(^1\Delta)$, O_2^+ , O_2^- , O_3 , O^- , O , $O(^1D)$, O^+ and electrons. The states N_2^* and N_2^{**} are nominally $N_2(A,B)$ and $N_2(C)$ though the latter is treated as a lumped state including transitions higher than $N_2(C)$. N_2^{***} is nominally $N_2(a')$ though it is also a lumped state accounting for higher levels. The discharge is initiated by placing an electrically neutral electron-ion cloud with a peak density of 10^{12} cm^{-3} and radius of 200 μm around the corona tip. The time step is typically 5×10^{-12} s.

5.3 Corona Properties and Charging of a Stationary Surface

The characteristics of the blade corona discharge and charging of the underlying stationary dielectric surface will first be discussed. The corona was first biased to -3 kV and the dielectric constant of the underlying insulating sheet in contact with ground was $\epsilon_r = 5$. The time evolution of the electron density and electric potential during the surface charging process is shown in Fig. 5.2. The electron impact ionization sources by bulk electrons S_e and beam-like secondary electrons S_{sec} are shown in Fig. 5.3. Due to the high gap-averaged electric field of 136 kV/cm ($E/N \approx 556$ Td, $1 \text{ Td} = 10^{-17} \text{ V-cm}^2$) between the corona tip and dielectric surface, and the geometrically enhanced electric field at the corona tip, an electron avalanche occurs within a few ns. Ionization is provided by lower energy bulk electrons, and by electrons emitted from the cathode blade through ion and photon secondary emission and accelerated by the large sheath potential. Before the dielectric is charged and while the full applied potential is dropped across the gap (0.1 ns in Fig. 5.3), the rate of ionization directly underneath the blade corona by bulk electrons, $10^{23} - 10^{24} \text{ cm}^{-3}\text{-s}^{-1}$, dominates. Ionization from secondary electrons is generally 2 orders of magnitude smaller due to the small ion flux at this time producing a low rate of secondary emission, and the lack of a fully formed sheath at the cathode. Electrons drifting towards the underlying dielectric sheet negatively charge the surface. As the plasma channel becomes conductive and the dielectric charges, the electric potential is shielded by the bulk plasma while electric potential lines are trapped in the dielectric due to the surface charging. At $t = 2 \text{ ns}$, plasma densities of up to 10^{15} cm^{-3} are generated at the corona tip which fully form the sheath. The electron density at mid-gap is on the order of $2 \times 10^{13} \text{ cm}^{-3}$.

As the discharge proceeds, the charging of the lower surface reduces the voltage drop and

E/N between the corona blade and the dielectric, and so decreases the rate of electron impact ionization from bulk plasma electrons in the gap beneath the tip. However, electron impact ionization from sheath accelerated secondary electrons still occurs due to UV photon and positive ion bombardment of the negatively biased corona blade. At $t = 3$ ns, this ionization source at the tip, S_{sec} , is up to $3 \times 10^{24} \text{ cm}^{-3}\text{-s}^{-1}$. At this stage, the corona discharge is primarily sustained by secondary electron ionization processes.

The voltage drop in the gap directly underneath the corona tip is reduced by charging of the capacitance of the PC. However, there is still a large potential drop between the corona blade and the uncharged surface of the PC to the left and right of the centrally charged PC surface. The conductive plasma in the gap results in the majority of the voltage between the corona tip and the uncharged dielectric being dropped across the edge of the plasma and the uncharged PC surface. The result is a surface ionization wave (SIW) at the edge of the plasma which propagates laterally outwards with a speed of $5 \times 10^6 \text{ cm-s}^{-1}$. The E/N at the surface in the SIW is 330 Td, which supports an ionization rate of $9 \times 10^{21} \text{ cm}^{-3}\text{-s}^{-1}$. As the SIW propagates, the underlying PC is charged. The spreading of the discharge on the surface is symmetric as there is uncharged dielectric on both sides of the blade and this produces SIWs propagating in both directions. By 60 ns, the SIWs dissipate as the finite voltage drop in the plasma (and distance from the corona blade) reduces the E/N in the SIW below the self-sustaining value. At this time, the dielectric surface underneath the corona blade is fully charged to a distance of 0.1 cm on either side of the blade. This charging process is similar to those occurring in conventional DBDs.[23-26]

The time evolution of the surface charge density and electric potential on the PC surface is shown in Fig. 5.2(b). (The surface charge densities are slightly smoothed to reduce the noise in the charging due to the randomness of the Monte Carlo simulation used for secondary electrons.)

The PC surface is rapidly charged during the first 20 ns. The charging during the first 5 ns is directly under the corona blade by ionization in the bulk plasma above the PC. After the first 5 ns, charging is largely due to the propagation of the oppositely directed SIWs. Charging largely terminates by about 40 ns and the SIWs have completely dissipated by 60 ns. At this time, the discharge terminates. The peak voltage on the PC surface underneath the corona tip after the termination of the discharge is -2.7 kV for an initial corona bias voltage of -3.0 kV.

Strictly speaking, conventional negative corona discharges are sustained by the high electric field near the surface of a small radius-of-curvature electrode due to geometrical field enhancement.[27-28] This geometrical field enhancement decreases with distance from the tip of the corona blade (or wire) and local ionization rates scale exponentially with the local electric field. At a critical distance from the tip, the electric field is sufficiently small that electron impact ionization is reduced below self-sustaining. At that point in an attaching gas such as air, the electrons are consumed by formation of negative ions and current continuity is then carried by drift of the negative ions.[27-30]

In this particular geometry and in most EP applications of corona, the PC surface is still within the high electric field region, and so the transition to a classical corona discharge where current is dominantly carried by negative ions does not occur. The proximity of the ionization by sheath phenomena is therefore important. For example, the electron density and electric potential with and without ionization by sheath accelerated secondary electrons, S_{sec} , are shown in Fig. 5.4(a). At $t = 30$ ns before the discharge terminates, S_{sec} provides a higher ionization source and electron density in the gap which helps maintain the discharge and charges the underlying dielectric more negatively. The surface charge density and potential on the PC after the discharge has been terminated for both cases are shown in Fig. 5.4(b). With S_{sec} , the surface potential reaches

–2.7 kV and charging extends to ± 1 mm. Without S_{sec} , the surface potential reaches only –2.2 kV and charging extends only to ± 0.75 mm. The ionization resulting from secondary electron emission enables the discharge to be sustained for a longer time and so more fully charge the PC.

Although the PC surface is close to the corona tip and current continuity is provided primarily by drift of electrons in geometry, negative ions are still formed during the charging process— O^- through dissociative attachment to O_2 and direct attachment to form O_2^- . The time evolution of electron density, total negative ion density, electric potential, surface charge density and potential on PC surface is shown in Fig. 5.5. The sequence begins at 50 ns when the discharge has nearly terminated due to surface charging and the reduction in voltage across the gap. The low electron temperature in the gap, 0.5 eV is well below the self-sustaining value and so attachment to O_2 dominates. At 50 ns, the electron density of $7 \times 10^{12} \text{ cm}^{-3}$ begins to decay through recombination, attachment and drift onto the PC surface. At this time, the peak negative ion density is $1.6 \times 10^{13} \text{ cm}^{-3}$ near the corona tip. By 200 ns, the electron density has decayed to $3 \times 10^9 \text{ cm}^{-3}$ while the negative ion density is $3 \times 10^{12} \text{ cm}^{-3}$. At this time, the recombining plasma consists mostly of negative and positive ions. This plasma then slowly decays dominantly by ion-ion recombination. The surface charge density and surface potential change very little from 50 ns to later times in spite of the large remaining ion density. First, the electric field in the gap is small and so there is little drift of ions to the surface. Second, the drift of ions to the surface is largely ambipolar. That is, the negative and positive ions drift at the same rate. As a result, there is not a net current to the surface to further charge the PC.

During the active discharge, the peak value of volumetric photoionization source S_{ph} is on the order of $10^{19} \text{ cm}^{-3}\text{-s}^{-1}$, which is small compared to electron impact ionization sources. Having said that, this photoionization source and photoemission produced by UV photons from long-lived

excited states continuously provide seed secondary electrons at the dielectric and electrode surfaces. Subsequent avalanche by these secondary electrons then help maintain the discharge through either sheath accelerated secondary electrons at the cathode or by helping to maintain the SIW. For example, the electron density and electric potential with and without volumetric photoionization and photoemission from the corona wire and PC surface during surface charging (at $t = 30$ ns) are shown in Fig. 5.6. The surface charge density and potential on the PC after the discharge is terminated are also shown in Fig. 5.6. Although the contribution of S_{ph} is small and the change in peak electron density is small, the plasma density is more uniform when including the photoionization. Due to the somewhat lower impedance of the discharge due to photoemission at the cathode surface, the final potential and surface charge density with S_{ph} are nominally higher than for discharges without S_{ph} .

After initiation of the discharge, the applied voltage is divided between the sheath at the electrode, the plasma column, the avalanche front, the surface sheath capacitance after the discharge strikes the surface, and the capacitance of the PC as the surface charges. For a given surface charge, the voltage drop in the dielectric ΔV_d is inversely proportional to the capacitance (per unit area) of the PC, $\epsilon_r \epsilon_0 / d$. By controlling the capacitance of the PC, the sheath voltage, electron impact ionization rates and so spreading of the plasma along the surface can be controlled and optimized. For example, the electron density and electric potential at $t = 60$ ns before the discharge terminates, and the surface charge density and potential on PC surface after the termination of discharge are shown in Fig. 5.7 for PCs having $\epsilon_r = 5, 10,$ and 20 . For the PC having a large capacitance, the voltage across the gap remains large for a longer period of time since the higher capacitance of the PC requires a longer time to charge. As a result, the discharge for $\epsilon_r = 5$ at $t = 60$ ns has a smaller electron density and begins to terminate earlier than the discharge on a

PC surface with $\epsilon_r = 20$. At this time, the maximum electron density at mid-gap is $5.9 \times 10^{12} \text{ cm}^{-3}$ for $\epsilon_r = 20$ compared to $5 \times 10^{11} \text{ cm}^{-3}$ for $\epsilon_r = 5$. Since the terminal electrical potential of the surface after charging is approximately the same for all ϵ_r , the maximum surface charge is then in proportion to ϵ_r . The larger capacitance requiring more current to charge the PC results in a longer discharge pulse (a longer RC time constant) and produces a higher electron density. However, the spatial extent of the surface charge is a weak function of ϵ_r . The SIW that laterally extends charge on the surface is driven, in part, by the horizontal component of the electric field at the surface of the PC. Although the surface charge is larger with larger ϵ_r , the surface potential is nearly the same. As a result, the horizontal component of the electric field that drives the SIW is a weak function of ϵ_r .

5.4 Charging of a Moving Surface

When a corona discharge is used for continuous surface charging, the underlying dielectric is in motion during the charging process. For a stationary uncharged target, the charging process by a dc (or quasi-dc) corona discharge behaves like a DBD. The charging of the surface is symmetric on either side of the corona tip. Surface charging reduces the electric field in the gap which then terminates the discharge. In the case of a moving surface, as the dielectric surface underlying the discharge moves, surface charge is translated away from the corona electrode on one side while uncharged dielectric translates towards the corona electrode on the other side. As a result, the incoming uncharged (or partially charged) surface restores the voltage drop in the gap that had previously been reduced by surface charging. This restoration of voltage may then reignite the plasma which then charges the fresh incoming surface.

At atmospheric pressure, the plasma formation and decay times can be as short as tens of ns, whereas the residence time of the moving charged surface before the plasma is reignited may be a few hundred microseconds. The surface moves in an almost quasi-static fashion which is much slower than the spreading of the plasma. As a result, it is difficult to address the surface moving at its actual speed in the model while also simulating plasma processes having sub-ns timescales with nearly many ps timesteps. Given that the plasma does terminate due to surface charging, it may not be necessary to address the entire time while the surface charge is moving after the discharge terminates and before it reignites. To address the continuous motion of the PC the following technique was used in the first cases investigated.

The PC surface was assumed to enter from the right and exit to the left in Fig. 5.8. The plasma is first simulated until charging of the dielectric terminates the discharge, producing a symmetric charging pattern. This surface charge density is then translated to the left in 100 μm increments, which brings in uncharged PC from the right while extending the region of charged surface to the left. This results in an asymmetric electrical potential distribution, as shown in Fig. 5.8(a). This asymmetric potential compresses contours of electric potential into the cathode and produces a progressively larger electric field at the corona electrode on the side of the electrode facing the incoming charged surface. The translation of the surface continues until the electric field is large enough to re-ignite the plasma, which occurs here for a shift of the surface to the left of 500 μm . This re-ignition process, illustrated by the time evolution of electron density, electric potential, and ionization sources from bulk and secondary electrons, is shown in Fig. 5.8(b). This sequence is for the second discharge which follows translation of the first symmetrically charged surface to the left. Time $t = 0$ corresponds to when the second discharge re-ignites, approximately the time shown in Fig. 5.8(a). At $t = 40$ ns, ionization for the second discharge is dominated by

sheath processes (both bulk and secondary emission) at or near the cathode, and by restarting of the SIW. The ionization sources are $10^{21} - 10^{22} \text{ cm}^{-3}\text{-s}^{-1}$. The electron source in the bulk plasma is generally comparable with the source from secondary electron ionization at the corona tip.

The reignited discharge is asymmetric, with plasma preferentially produced on the side of the corona electrode facing the uncharged dielectric where the voltage drop across the gap is the largest. Note that at the time of re-ignition, there is a small secondary electron ionization source at the surface of the PC. These secondary electrons are produced largely by photo-electron emission at a time that the charging of the surface produces a larger horizontal component of the electric field than a vertical component, which would otherwise accelerate the secondary electrons back into the surface. These secondary electrons are then accelerated parallel to the surface for about 100 – 200 μm prior to impacting the PC. A small ionization source then results.

At $t = 50 \text{ ns}$, the second discharge is fully developed. The plasma density is generally smaller (10^{12} cm^{-3} at mid-gap) compared to the first discharge pulse (10^{13} cm^{-3} at mid-gap) as the bulk electric field is smaller for at least two reasons. First, re-ignition occurs when the voltage drop across the gap is less than the initial charging voltage due to the prior charging of the dielectric. Second, the effective gap length for the first pulse is the geometrical vertical distance between the tip of the corona bar and the surface of the PC, 200 μm , which produces a gap-averaged $E/N = 556 \text{ Td}$. For re-ignition, the effective gap length is along the electric field line originating on the cathode at the site of the maximum electric field and ending on the uncharged surface entering from the right. This distance is 300 μm at re-ignition, producing a gap averaged $E/N = 270 \text{ Td}$. After the second discharge pulse fully develops, the conductive plasma at the side of the corona tip shields the electric field and diminishes the electron source in the bulk plasma. The re-ignition is then dominated by the secondary electron ionization source, S_{sec} . As the SIW charges one side

of the surface and reduces the electric field in the gap, the second discharge pulse then starts to extinguish. This general sequence of events is repeated as fresh, uncharged PC surface is translated towards the corona electrode from the right.

The total surface charge density and surface potential on the PC surface before and after re-ignition of secondary discharge are shown in Fig. 5.9 while initial surface charge density is shifted up to 700 μm . The total surface charge density and surface potential on the dielectric after 5 discharge pulses (4 re-ignitions) are shown in Fig. 5.10. In general, the discharge cannot be reignited until the surface is translated to the left by at least 300 - 500 μm . With each successive re-ignition, the surface is incrementally charged over another 100-200 μm . The maximum surface charge incrementally produced with each re-ignition is about the same compared to the initial pulse, with perhaps a small increase. Although there is a bit of statistical noise in the charging, there is also a periodic maximum in the surface charge density and potential. In a continuous charging process, the following basic sequence is repeated: ignition, surface charging, SIW, discharge termination, motion of the surface, restoration of gap voltage and re-ignition. The requirement for re-ignition is to have a critically large E/N , which produces a rapid avalanche which in turn charges the surface. The resulting SIW extends the charging beyond the point that the surface must reach to create the critical E/N . This process of re-ignition and SIW naturally produces a periodic charging pattern.

The pattern of the surface potential and its peak value are expected to be sensitive to the design of corona device (speed of surface movement, voltage waveform and dielectric materials) since the re-ignition strongly depends on feedback from the previous surface charging cycle. For purposes of demonstration, the time evolution of electron density and electric potential of a corona discharge onto a continuously fast-moving surface are shown in Fig. 5.11(a). The corresponding

total charge density and electric potential on the moving surface are shown in Fig. 5.11(b). The blade corona is biased with -3 kV dc and the underlying dielectric moves from right to left at a speed that is commensurate with the spreading of the plasma by the SIW. The moving dielectric continuously translates uncharged fresh surface towards the blade corona. When the voltage drops between the blade corona and uncharged surface rebounds, an electron avalanche occurs, and the corona discharge is then reignited. The charged surface translating to the left terminates the discharge on the left side of the electrode while the corona blade continuously sees the fresh surface underneath the tip as the surface enters from the right. The end result is that the discharge continuously and uniformly charges the underlying dielectric, and the surface charging is asymmetric with respect to the corona electrode but more uniform. The oscillatory charging pattern on the surface results from discrete re-ignition events which in turn result from the rapid charging of the surface and the relatively slow moving surface. A more uniform surface charging might be obtained by using a gas mixture with long lived excited states capable of continuously emitting UV/VUV photons which produce photoemission on a fast moving surface. This photoemission will help maintain the SIW in a continuous manner.

In addition to controlling the capacitance of PC dielectric, the peak surface potential can also be adjusted by varying the gap distance between corona tip and the underlying surface. The electron density and electric potential during the charging process at $t = 20$ ns are shown in Fig. 5.12(a) for varying the applied dc voltage (V_a) and gap size (d_g) while keeping the ratio constant ($V_a/d_g = 15$ kV/mm). V_a varies from -1.5 kV to -4.5 kV for gaps of 100 μm to 300 μm . The surface charge density and surface potential after the discharge has terminated are shown in Fig. 5.12(b). Although the gap averaged E/N is the same in all cases, the geometrically enhanced electric field significantly increases with increased dc voltage on the corona tip. As a result, the

higher electric field produced at the corona tip biased with -4.5 kV with the larger gap produces a more intense ionization source, a higher electron density and wider region of surface charging. The larger voltage also requires more current and a longer time to charge the surface of the PC which provides more time for the SIW to propagate to charge more surface. Surface charging with the lower voltage and smaller gap is more confined.

5.5 Concluding Remarks

Corona discharges sustained in atmospheric pressure air are important in many EP printing technologies to charge the underlying dielectric PC surfaces. I computationally investigated the behavior of an idealized corona discharge and surface charging when the PC surface is stationary and in motion. It was found that electron impact ionization by electrons in the bulk plasma initialize the discharge underneath the corona tip, however prior to the discharge terminating, ionization is provided dominantly by sheath accelerated secondary electrons. Electrons negatively charge the underlying dielectric, trapping electric potential lines in the dielectric and removing voltage from the gap. The electrons carry the vast majority of current to the dielectric in this particular geometry with little contribution from negative ions. On a stationary dielectric, a surface ionization wave spreads outwards from the corona tip on both sides and symmetrically charges the surface, while the discharge is sustained by the sheath accelerated secondary electrons. The discharge is terminated when the electric field for the SIW is reduced by virtue of the distance the SIW has traveled from the corona electrode. When the dielectric surface is in motion, surface charges and the potential they produce are translated away from the corona wire. The voltage between the corona electrode and the incoming uncharged surface rebounds, and an electron avalanche is re-ignited on one side of the blade. The corona discharge process then repeats to form

an oscillatory charging pattern. The charging pattern can be made less oscillatory by using a fast-moving surface or a gas mixture capable of continuously providing seed electrons to maintain the discharge.

In summary, atmospheric pressure corona discharges used in EP printing technologies are investigated in this chapter. The charging process on a moving surface and plasma dynamics are discussed in detail. A periodic charging pattern observed in the experiments produced by moving surface are also predicted in the simulation results. Although the speed of moving surface in the simulation is a few hundred times faster compared with the moving speed in real printing applications, the modeling still improves our understanding of the underlying physics.

5.6 Figures

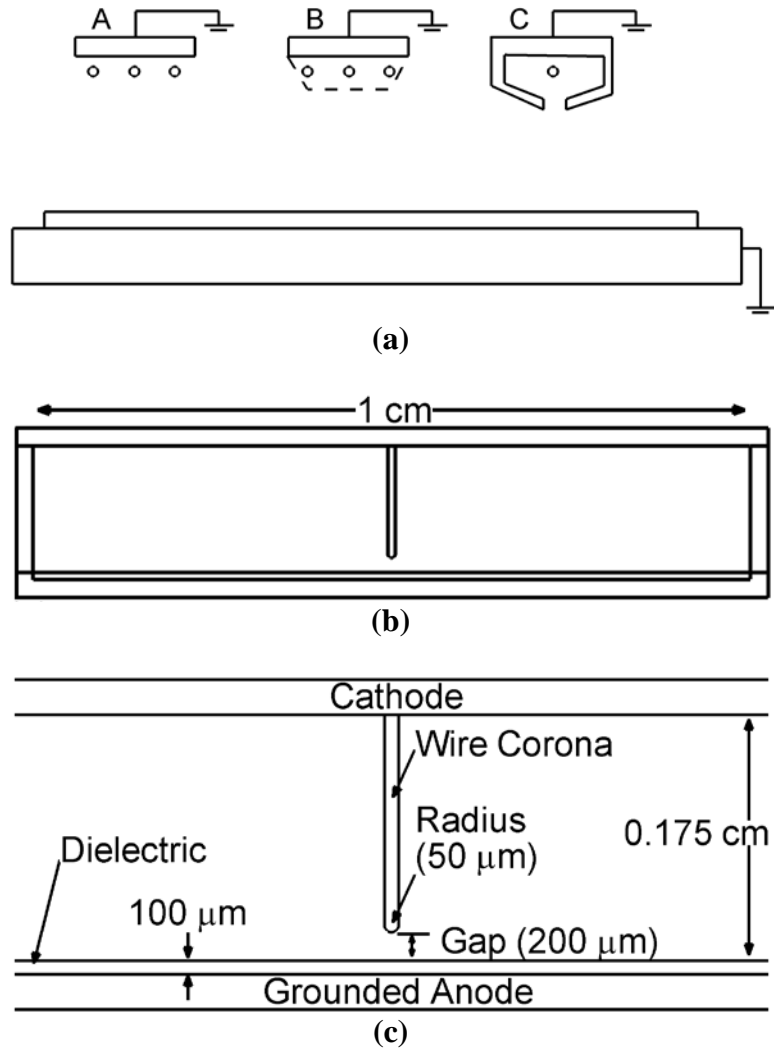


Figure 5.1 Schematics of corona devices. (a) A, B and C are 3-wire corotron, scorotron and shielded corotron, respectively.[16] (b) Entire device and full computational domain of negatively dc-biased blade corona discussed in this chapter. (c) Enlargement of corona electrode and underlying ground electrode covered with a dielectric photoconductor (PC).

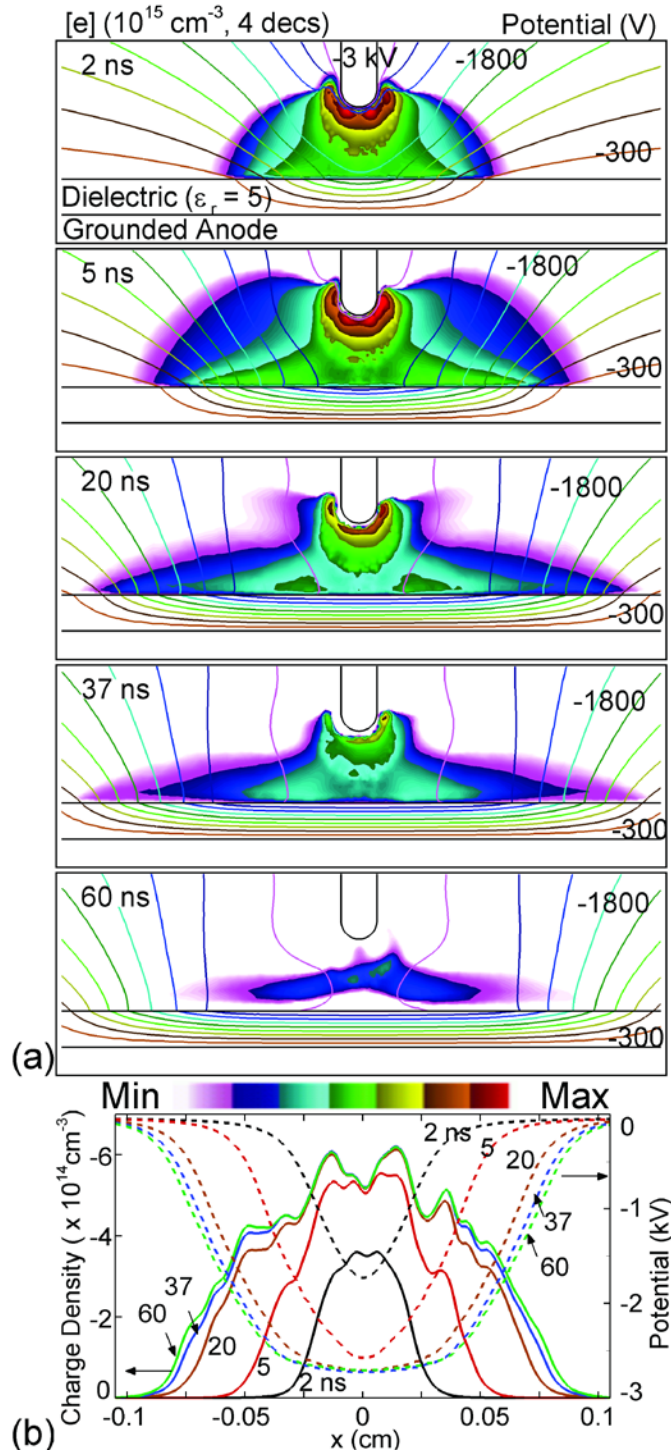


Figure 5.2 Charging of PC surface by a dc biased corona blade. (a) Time evolution of electron density (color flood, cm^{-3}) and electric potential (contour lines, V) produced by a -3 kV dc biased corona blade. (b) Time evolution of surface charge density (solid, cm^{-3}) and surface voltage (dashed, V) on the PC dielectric. The electron density is plotted on a log-scale over 4 decades ($10^{11} - 10^{15} \text{ cm}^{-3}$). The discharge is terminated by surface charging.

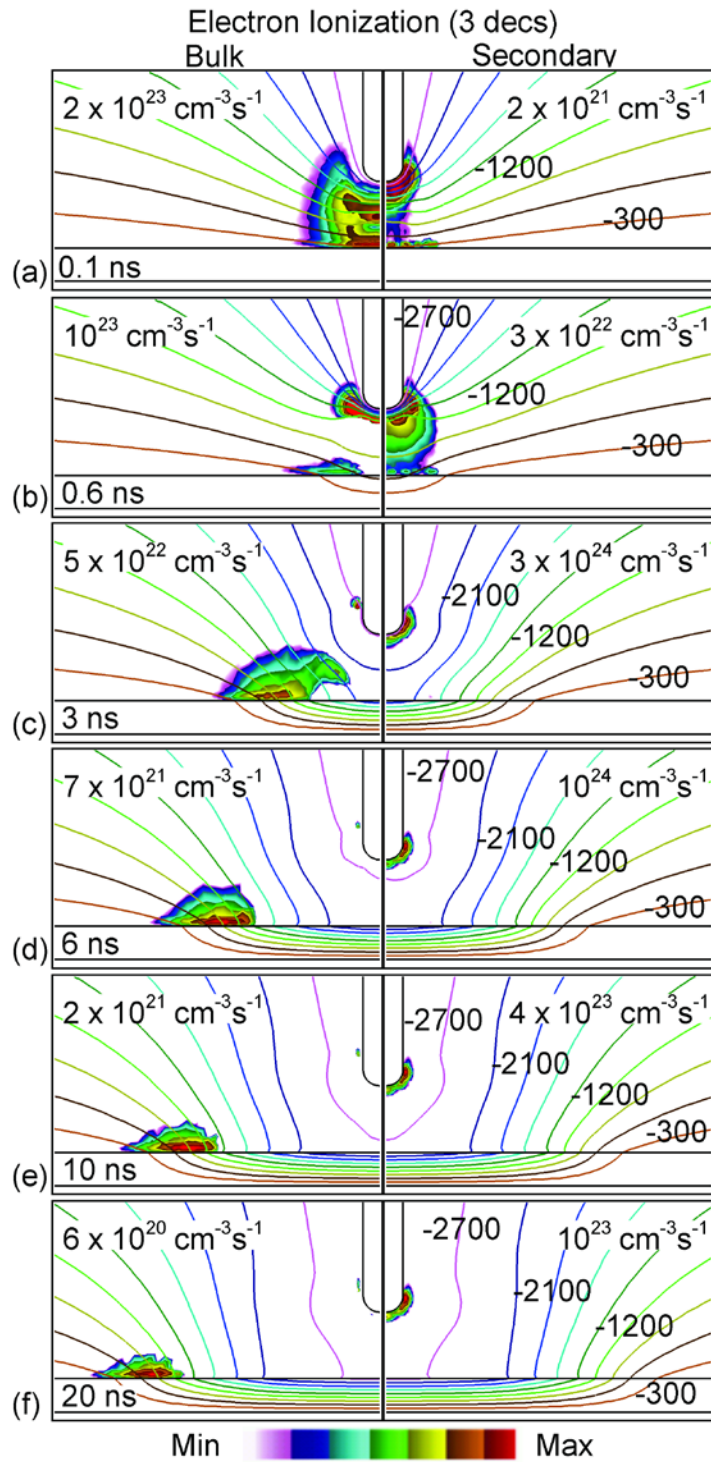


Figure 5.3 Electron impact ionization sources from bulk electrons (Se), and ionization source by sheath accelerated secondary electrons (Ssec) at different times after initiation of the discharge. The ionization sources are plotted on a log scale over 3 decades. The charging of the surface far from electrode results from a surface ionization wave.

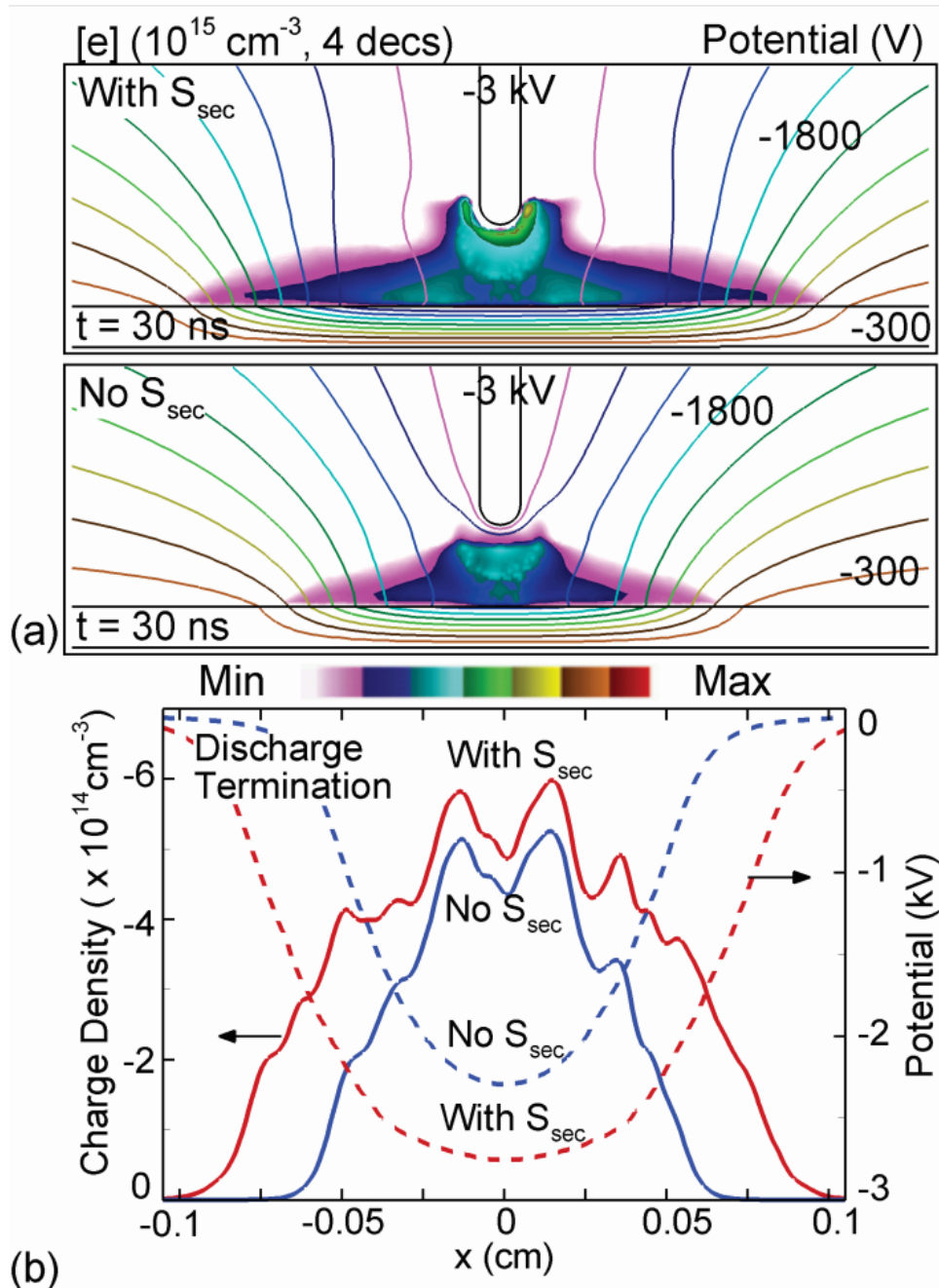


Figure 5.4 Ionization by secondary electrons S_{sec} helps maintain the corona discharge. (a) Electron density (color flood, cm^{-3}) and electric potential (contour lines, V) produced by a -3 kV dc biased wire corona at $t = 30 \text{ ns}$ with and without ionization sources by sheath accelerated secondary electrons (S_{sec}). (b) Surface charge density (solid, cm^{-3}) and surface voltage (dashed, V) with and without S_{sec} showing the contribution of secondary electrons.

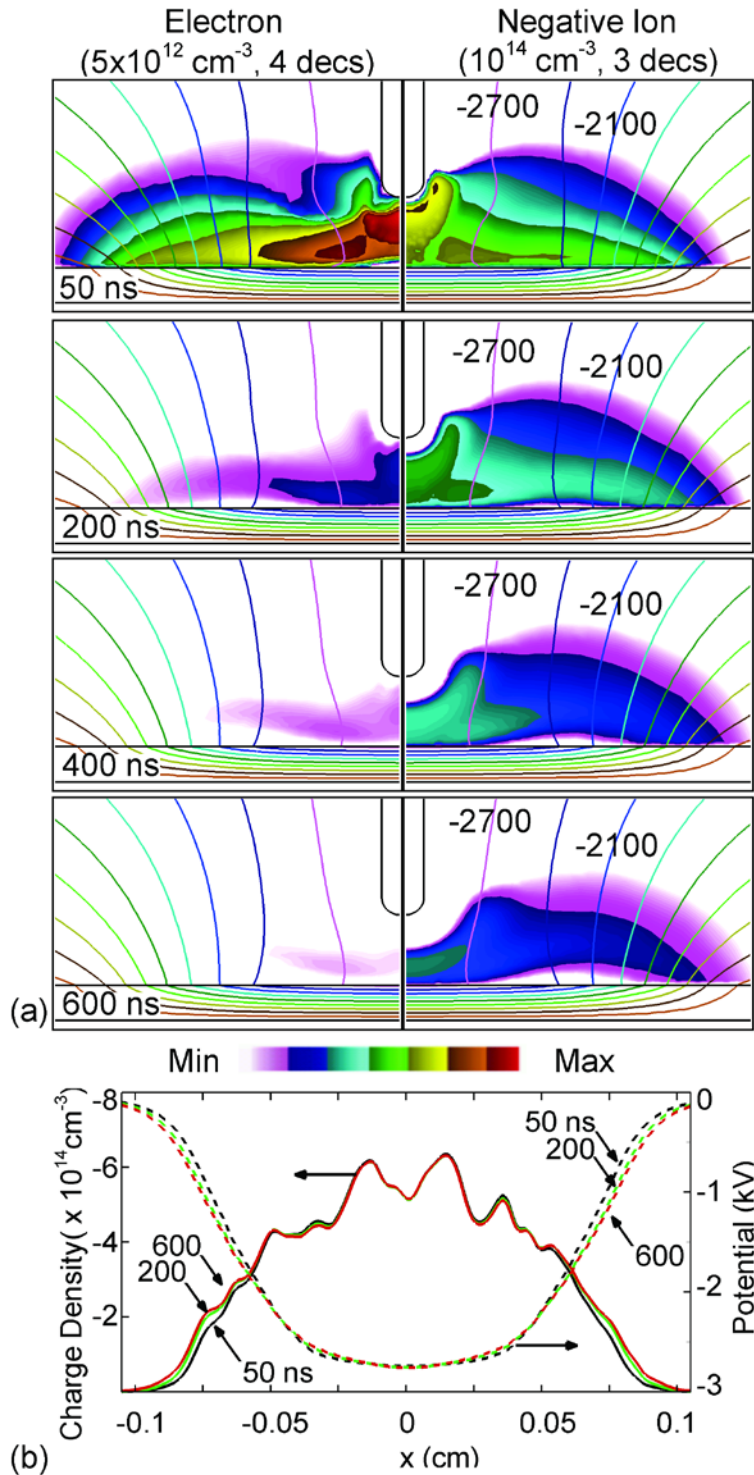


Figure 5.5 Residual electrons and negative ions produce nominal charging of the PC after the discharge is terminated. (a) Time evolution of electron and negative ion density (color flood, cm^{-3}), and electric potential (contour lines, V) at $t = 50, 200, 400$ and 600 ns . (b) Time evolution of surface charge density (solid, cm^{-3}) and surface voltage (dashed, V) at $t = 50, 200$ and 600 ns .

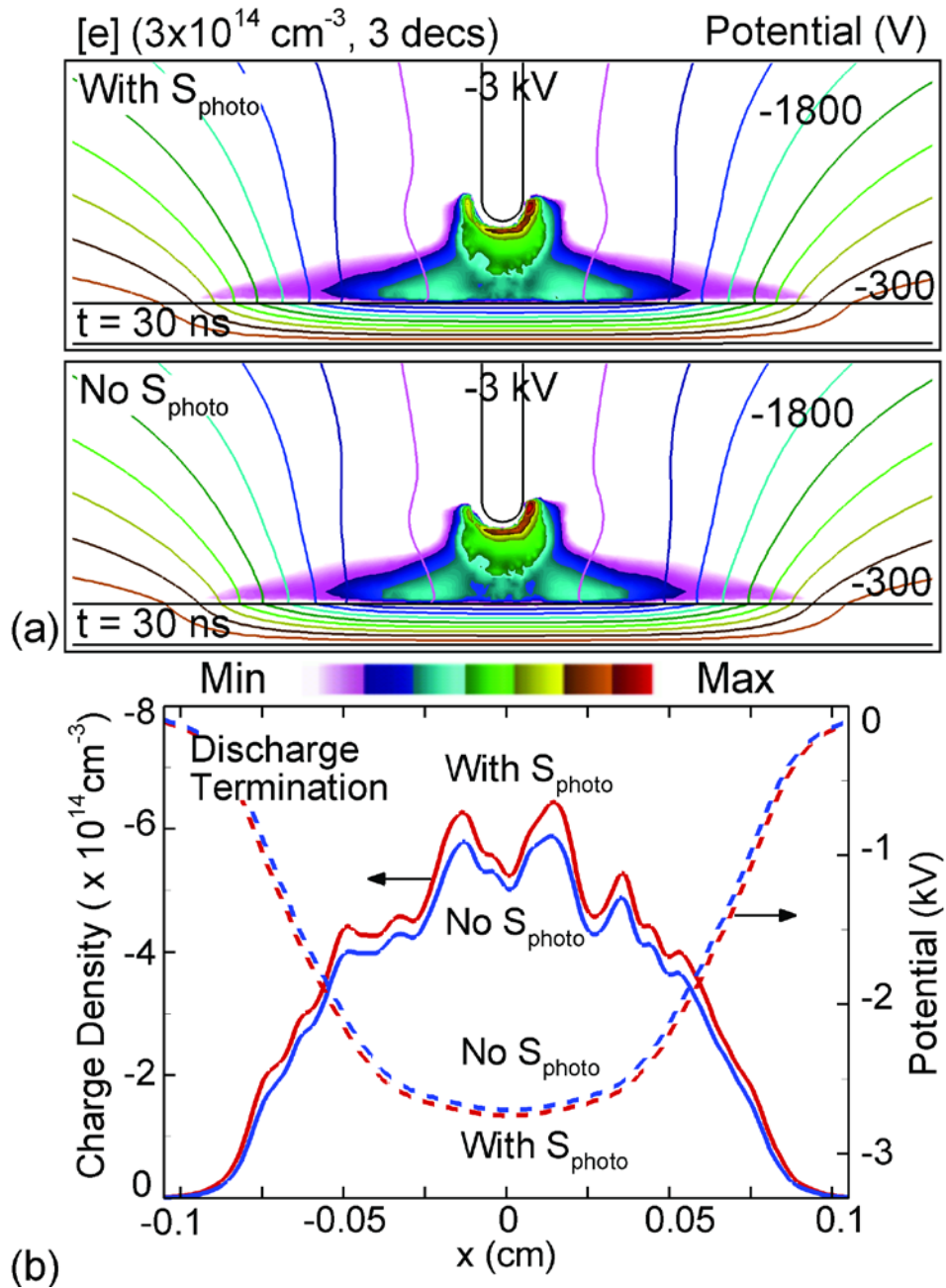


Figure 5.6 Plasma properties produced by a -3 kV dc biased wire corona at $t = 30 \text{ ns}$ with and without volumetric photoionization source S_{ph} and photoemission from the corona and PC surface. (a) Electron density (color flood, cm^{-3}) and electric potential (contour lines, V). (b) Surface charge density (solid, cm^{-3}) and surface voltage (dashed, V).

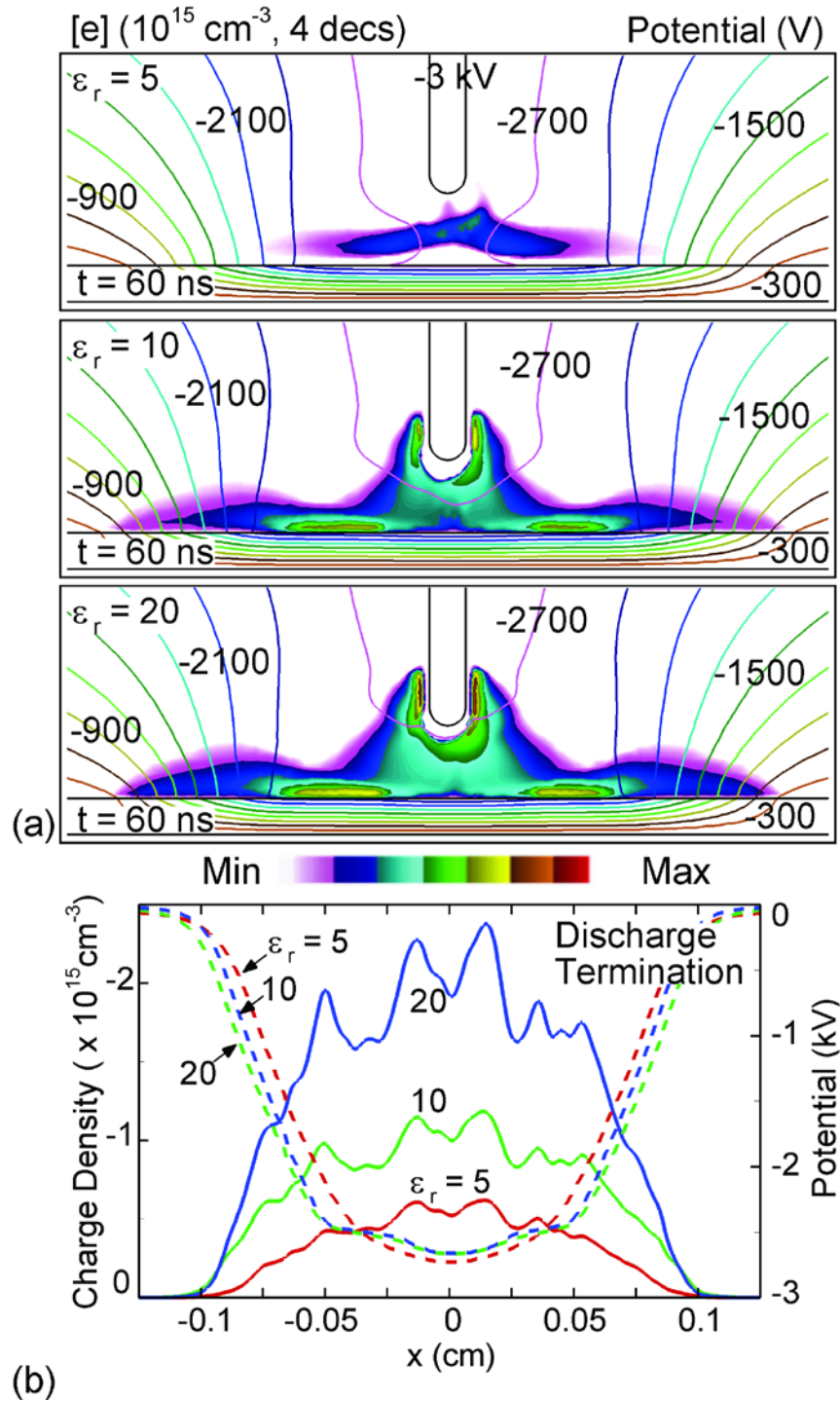


Figure 5.7 Plasma properties produced by a -3 kV dc biased wire electrode at $t = 60 \text{ ns}$ on dielectric sheets with relative permittivities ϵ_r of 5, 10, and 20. (a) Electron density (color flood, cm^{-3}) and electric potential (contour lines, V). (b) Surface charge density (solid, cm^{-3}) and surface voltage (dashed, V) on the dielectric surface after termination of the discharge.

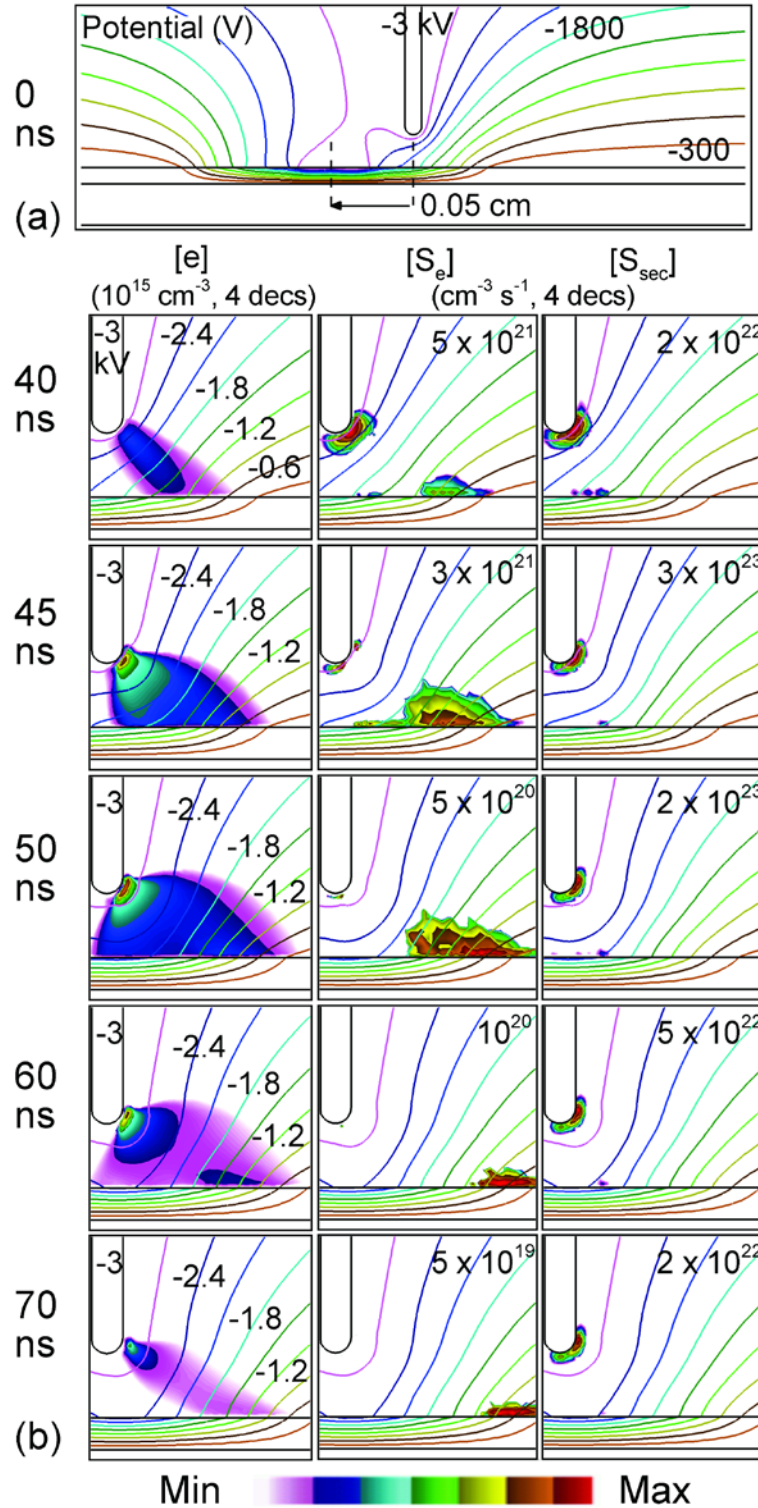


Figure 5.8 Time evolution of electron density (flood, cm^{-3}), ionization sources from bulk electrons S_e , ionization by secondary electrons S_{sec} (flood, $\text{cm}^{-3}\text{-s}^{-1}$) and electric potential (contour lines, V) produced during reignition after the first symmetric surface charge density was shifted to the left by 500 μm .

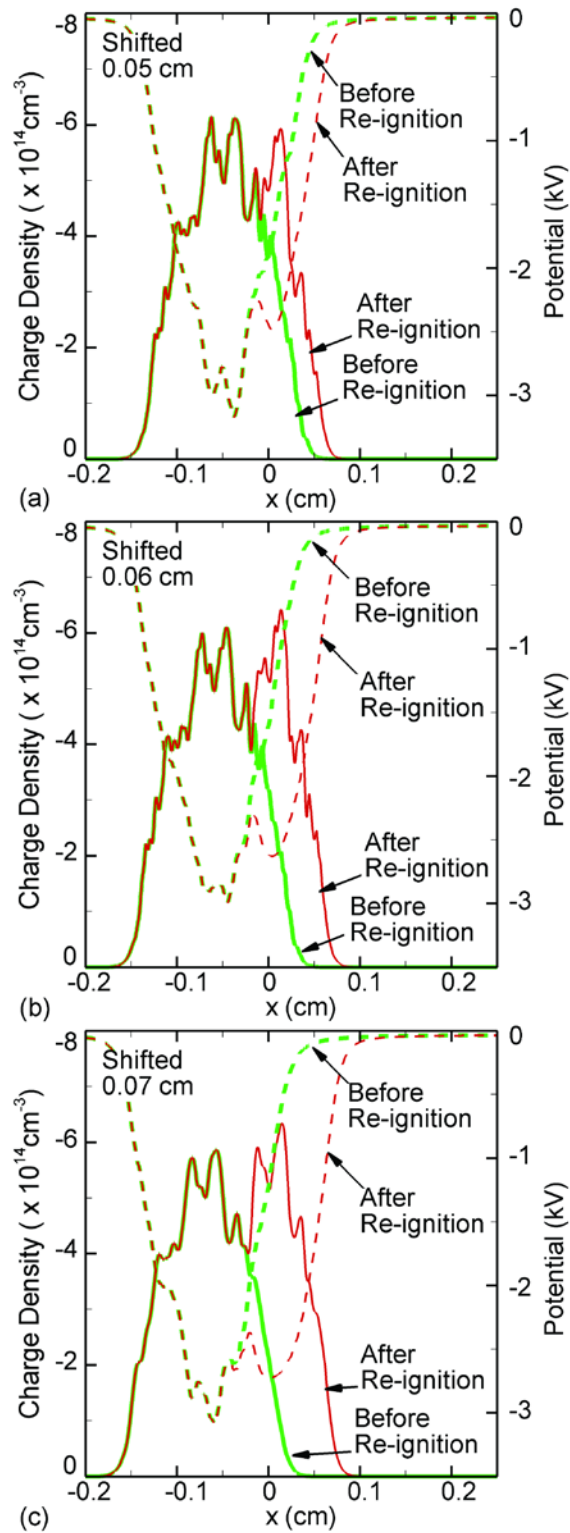


Figure 5.9 The total surface charge density (solid, cm^{-3}) and surface potential (dashed, V) before and after re-ignition of the secondary discharge with a shift of initial surface charge density by (a) 500 μm , (b) 600 μm , and (c) 700 μm .

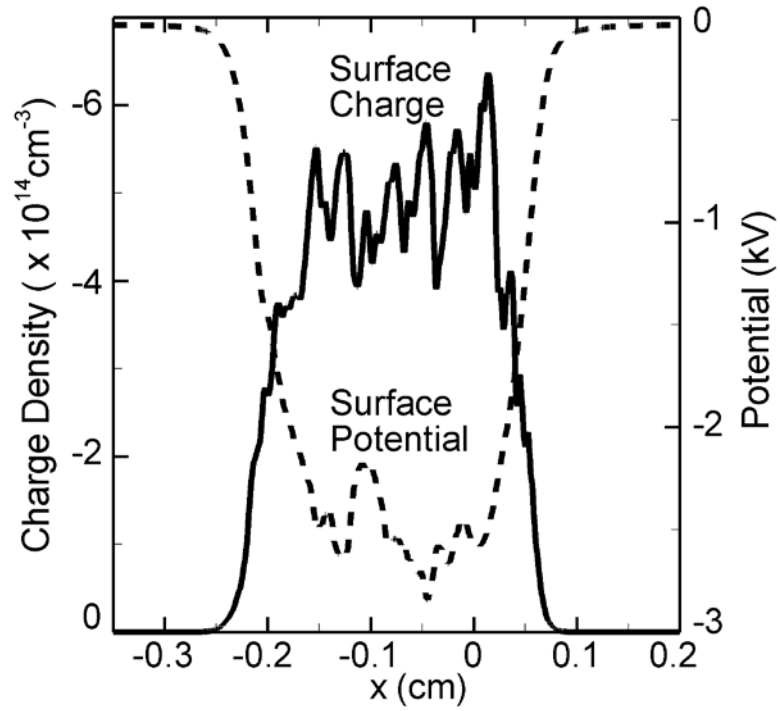


Figure 5.10 The total charge density (solid, cm^{-3}) and surface potential (dashed, V) on the dielectric surface after 5 discharge pulses (4 re-ignitions).

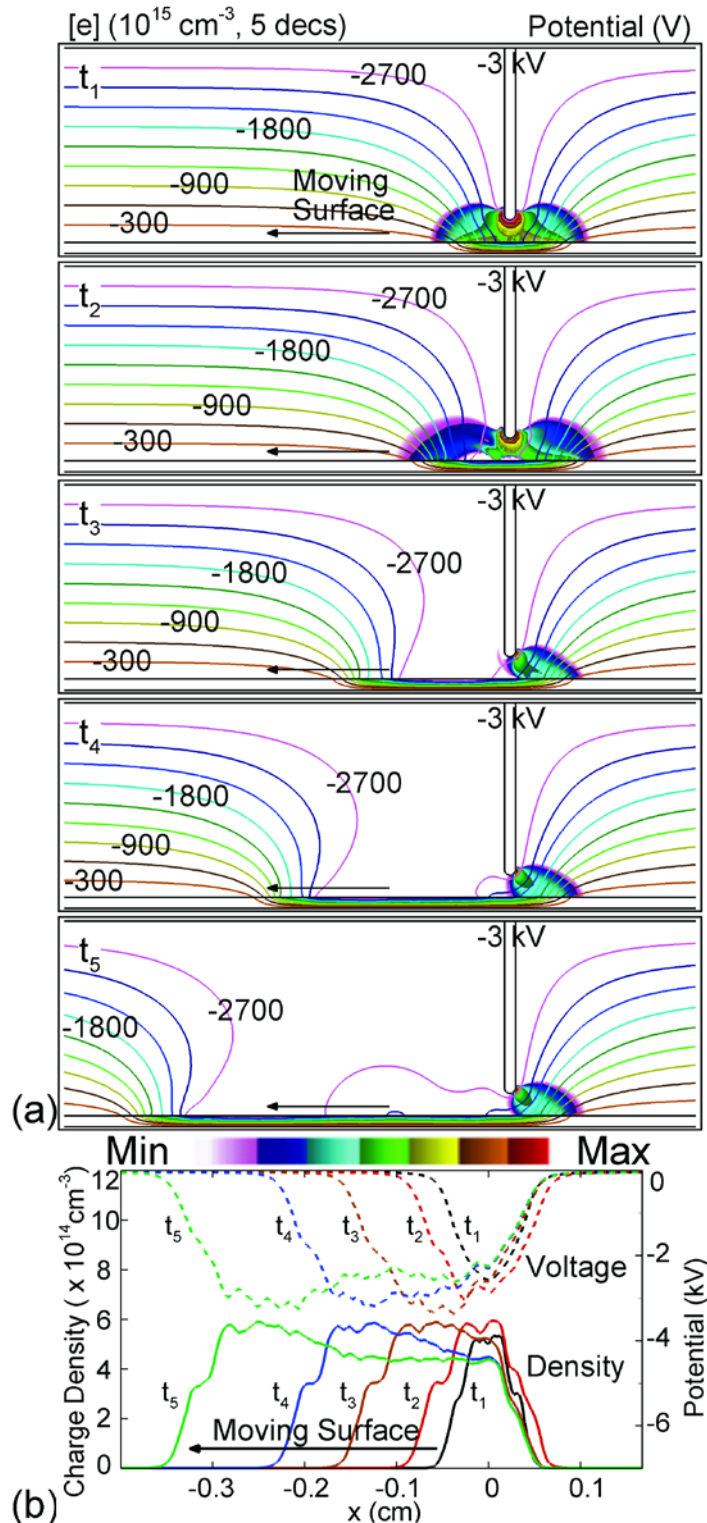


Figure 5.11 Time evolution of (a) electron density (flood, cm^{-3}) and electric potential (contour lines, V) and (b) total surface charge density (solid, cm^{-3}) and surface potential (dashed, V) on a rapidly moving surface. The discharge is continuously re-ignited by the rapidly moving surface in a quasi-dc manner.

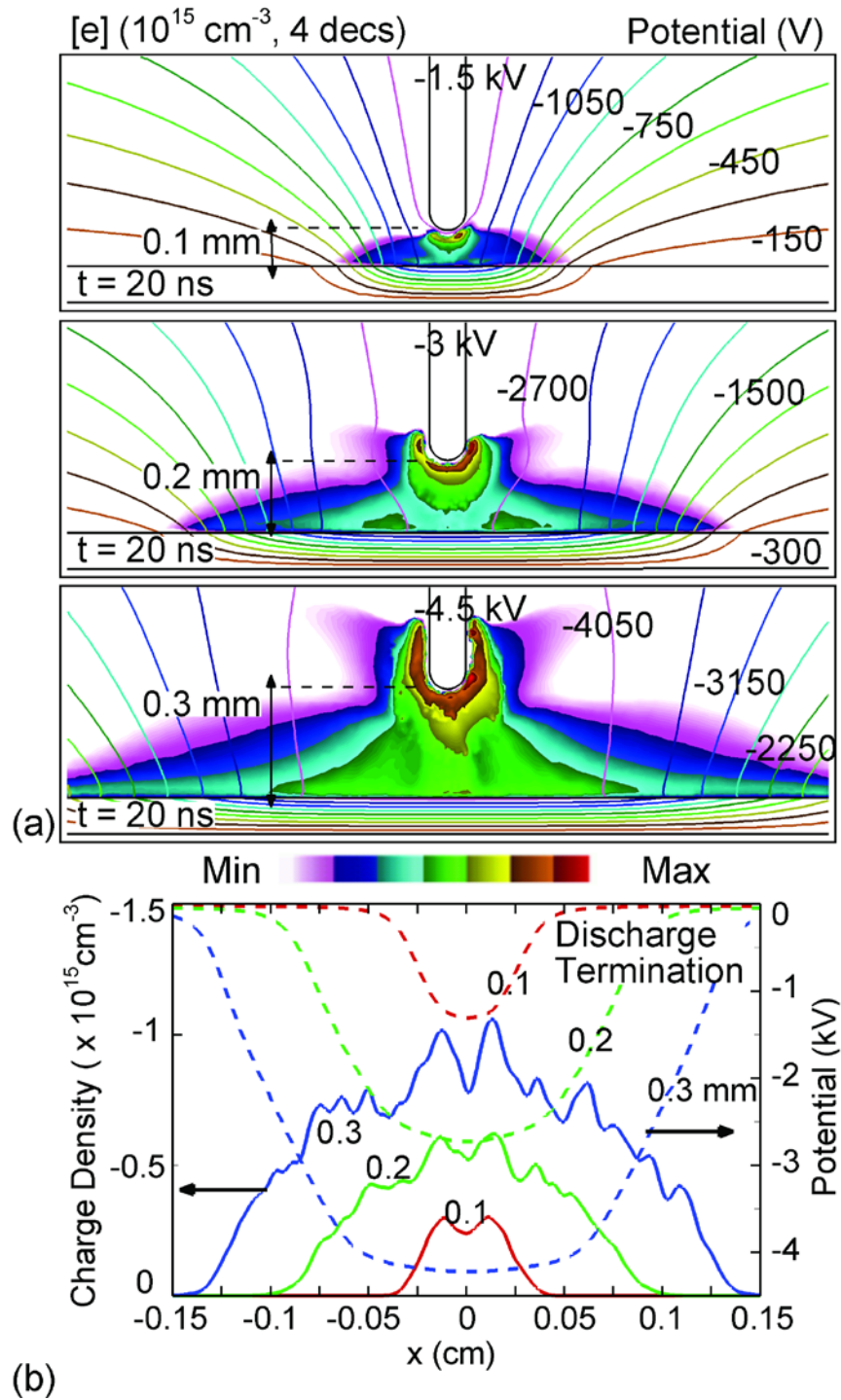


Figure 5.12 Time evolution of (a) electron density (flood, cm^{-3}) and electric potential (contour lines, V) during the charging process at $t = 20 \text{ ns}$ and (b) total surface charge density (solid, cm^{-3}) and surface potential (dashed, V) after the termination of discharge for $V_a/d_g = -1.5 \text{ kV}/0.1 \text{ mm}$, $-3 \text{ kV}/0.2 \text{ mm}$ and $-4.5 \text{ kV}/0.3 \text{ mm}$, where V_a is the applied dc voltage and d_g is the gap size.

5.7 References

- [1] S. F. Miraläi, E. Monette, R. Bartnikas, G. Czeremuskin, M. Latrèche, and M. R. Wertheimer, *Plasmas Polym.* **5**, 63 (2000).
- [2] F. Massines, G. Gouda, N. Gherardi, M. Duran and E. Croquesel, *Plasmas Polym.* **6**, 35 (2001).
- [3] L.-A. O'Hare, S. Leadley, and B. Parbhoo, *Surf. Interface Anal.* **33**, 335 (2002).
- [4] S. Guimond, I. Radu, G. Czeremuskin, D. J. Carlsson, and M. R. Wertheimer, *Plasmas Polym.* **7**, 71 (2002).
- [5] M. Sira, D. Trunec, P. Stahel, V. Bursikova, Z. Navratil and J. Bursik, *J. Phys. D: Appl. Phys.* **38**, 621 (2005).
- [6] Q. Zhang, C. Wang, Y. Babukutty, T. Ohyama, M. Kogoma and M. Kodama, *J. Biomed. Mater. Res.* **60**, 502 (2002).
- [7] C. Geßner, V. Bartels, T. Betker, U. Matucha, C. Penache and C-P. Klages, *Thin Solid Films* **459**, 118 (2004).
- [8] P-L. Girard-Lauriault, F. Mwale, M. Iordanova, C. Demers, P Desjardins and M. R. Wertheimer, *Plasma Process. Polym.* **2**, 263 (2005).
- [9] C. Sarra-Bournet, S. Turgeon, D. Mantovani and G. Laroche, *J. Phys. D: Appl. Phys.* **39**, 3461 (2006).
- [10] M. H. Lee, N. J. Leoni, H. Birecki and O. Gila, U.S. patent 2011/0216126 (Sep. 8, 2011).
- [11] O. Gila, N. J. Leoni and J. Nielsen, U.S. patent 2012/0272896 (Nov. 1, 2012).
- [12] J. Kurokawa, K. Nojima, N. Sohmiya, U.S. patent 5,499,078 (12 Mar 1996).
- [13] D. M. Pai and B. E. Springett, *Rev. Mod. Phys.* **65**, 163 (1993).
- [14] L. B. Schein, *J. Vac. Sci. Technol. A* **25**, 1256 (2007).

- [15] C. B. Duke, J. Noolandi, and T. Thieret, *Surf. Sci.* **500**, 1005 (2002).
- [16] R. M. Schaffert, *Electrophotography* (Focal Press, London, 1965).
- [17] J. S. Chang, P. A. Lawless, and T. Yamamoto, *IEEE Trans. Plasma Sci.* **19**, 1152 (1991).
- [18] E. M. van Veldhuizen and W. R. Rutgers, *Proceedings of Frontiers in Low Temperature Plasma Diagnostics IV*. Limburg (NL) (Univ. of Technology, Dep. of Applied Physics, Eindhoven, 2001).
- [19] B. Lay, R. S. Moss, S. Rauf and M. J. Kushner, *Plasma Sources Sci. Technol.* **12**, 8 (2003).
- [20] J-C. Wang, N. Leoni, H. Birecki, O. Gila and M, J. Kushner, *J. Appl. Phys.* **113**, 033301 (2013).
- [21] R. Dorai, *Modeling of Atmospheric Pressure Plasma Processing of Gases and Surfaces*, PhD Thesis University of Illinois (<http://uigelz.eecs.umich.edu/theses.html>).
- [22] Y. Akishev, M. Grushin, V. Karalnik, A. Petryakov and N. Trushkin, *J. Phys. D: Appl. Phys.* **43**, 215202 (2010).
- [23] S. Celestin, K. Allegraud, G. Canes-Boussard, N. Leick, O. Guaitella and A. Rousseau, *IEEE Trans. Plasma. Sci.* **36**, 1326 (2008).
- [24] S. Celestin, G. Canes-Boussard, O. Guaitella, A. Bourdon and A. Rousseau, *J. Phys. D: Appl. Phys.* **41**, 205214 (2008).
- [25] S. Celestin, Z. Bonaventura, O. Guaitella, A. Rousseau and A. Bourdon, *Eur. Phys. J. Appl. Phys.* **47**, 22810 (2009).
- [26] F. Pechereau, J. Jansky and A. Bourdon, *Plasma Sources Sci. Technol.* **21**, 055011 (2012).
- [27] D. S. Antao, D. A. Staack, A. Fridman and B. Farouk, *Plasma Sources Sci. Technol.* **18**, 035016 (2009).
- [28] Y. P. Raizer, *Gas Discharge Physics* (Springer, Berlin, 1991).

- [29] M. Goldman, A. Goldman and R. S. Sigmond, *Pure & Appl. Chem.* **57**, 1353 (1985).
- [30] J. Chen and J. H. Davidson, *Plasma Chem. Plasma Process.* **23**, 83 (2003).

CHAPTER 6 ATMOSPHERIC PRESSURE MICRODISCHARGES PRODUCED BY CONDUCTIVE CHARGE ROLLER

6.1 Introduction

Atmospheric pressure microdischarges have been frequently used in area-selective surface patterning [1–3] and surface charging in printing technologies.[4–9] For example, a radio frequency (rf)-excited micro-dielectric barrier discharge (or mDBD) array having dimensions of tens of micrometers operating at atmospheric pressure has been developed for high-resolution electrostatic latent image production.[10–13]. This mDBD configuration used in the electrostatic image transfer process to generate the charged particle beams is referred to as a charge deposition print head, or “print head.” The print head is the most essential component in an ionographic image device.

As the atmospheric pressure discharge is directly in contact with dielectric material, the plasma charges the dielectric surface and removes the voltage, and then the plasma extinguishes due to the charging of the dielectric surface. This charging process is widely used in electrophotographic (EP) printing technologies.[4–9] A Corona discharger is one of the main implementations used in a print engine to sensitize the surface of the photoconductor (PC) by electrically charging the PC surface to a predetermined potential. A corona discharger has the advantages of a simple structure, a high charging efficiency, and the low cost of a charging device. It also has drawbacks that impose challenges on the printing industry, such as high electric power consumption, the mass production of ozone and NO_x along with the corona charging, and the

damage to the charging element (e.g., photoconductor)—the last of which causes image deterioration.[5–9]

In addition to the corona discharge, a contact charging method, wherein a rotatable charge roller (CR) is in contact with a rotating photoconductive drum, has been studied for surface charging in the EP community.[14–17] The schematic of a charge roller and photoconductor drum is shown in Fig. 6.1(a). A typical charge roller consists of a biased metal shaft covered by a few layers of alternative conductive and resistive elastomer coatings to prevent arcing. These resistive and semi-insulating layers that are a hundred microns thick have conductivities of $\sigma = 10^{-10} - 10^{-4} \Omega^{-1} \text{ cm}^{-1}$. [4,15] The photoconductive (PC) dielectric layer is in contact with a ground electrode. As a negative dc voltage of a few hundred to a few thousand volts is externally applied to the metal shaft and charge roller, a large electric field is produced in the converging air gap between the charge roller and the photoconductor. Free electrons in the space produced by cosmic radiation or electric field current emission from the CR surface are accelerated by the strong electric field in the gap to trigger an avalanche, and so form microdischarges. These microplasmas charge the PC surfaces and trap the potential lines in the PC dielectric. If the CR is biased with a dc or quasi-dc voltage in a pulse mode, the plasma is then terminated by the surface charging as in a DBD manner.

Although a contact charge roller is capable of operating with a lower voltage source and of generating less ozone, a non-uniform periodic surface charging pattern (shown in Fig. 6.1(b)) and an “alligator pattern”[17] produced by a rotatable CR on a moving (rotating) PC surface degrade the quality of the printing image. A number of causes are found to produce the undesirable non-uniformity of the charge pattern. For example, a highly resistive CR, or a CR with local non-uniform conductivity that stems from electrical irregularity in the elastomer layer, is found to reduce the local voltage drop in the gap, which prematurely terminates the discharge and charging

process. As a result, the surface is charged non-uniformly. These charging failures can be alleviated by optimizing the voltage waveform applied to the CR shaft or by using proper materials for the elastic layers and surface layers on the CR.[4,15,17] Having said that, the non-uniform charging pattern on a moving PC surface is still a major charging failure, which has motivated continued investigation into further understanding and improving the performance.

In this chapter, I present the results of a numerical investigation into microdischarges sustained in atmospheric pressure dry air, and the charging of both stationary and moving dielectric PC surfaces by a conductive charge roller in a print engine. The devices of interest are shown in Fig. 6.1. For surface charging of a stationary PC surface, I found that the photoemission and photoionization are significant in the initiation and charging process. After field emission current is locally injected from an emission node, microplasmas are initiated at the smaller gap by remote seed electrons. The plasma laterally spreads outward on the PC surface, charging the underlying dielectric. The discharges are then terminated by the surface charging. Without the remote electrons, the microplasmas are directly initiated underneath the field emission node if the local E/N is sufficient. As the surface is in motion, the rapidly moving PC surface brings in an uncharged surface and re-establishes the E/N in the gap. The rebound in E/N then re-ignites the microplasma. With a high applied voltage and a rapidly moving surface, self-pulsing microplasmas are produced to form a periodic surface charging pattern. At certain operation conditions, a Townsend-like discharge can be produced, and a uniform surface charging is achieved.

The model used in this chapter is described in Sec. 6.2 and followed by a discussion of plasma dynamics in the gap and charging of a stationary PC surface in Sec. 6.3. The characteristics

of the charging of a moving surface are discussed in Sec. 6.4, and Sec. 6.5 contains our concluding remarks.

6.2 Description of the Model and Reaction Mechanism

The charge roller and the charging of PC dielectric in a DBD manner were computationally investigated using the modelling platform, *nonPDPSIM*. The model is the described in Chapter 2 and Refs. [12,18]. Sources of electrons from the surface include field-enhanced thermionic emission and secondary electrons produced by ion and photon fluxes. The secondary emission coefficients used in this chapter were 0.15 for all of the positive ions and up to 0.01 for photon flux.

To emphasize the dynamics of microplasmas on a stationary PC surface affected by field emission current, photoionization, and the conductivity of the charge roller, an idealized device has been modeled and shown in Fig. 6.1(c) and Fig. 6.1(d) (the geometry shown in Fig. 6.1(d) is vertically expanded by a factor of 2 for clarity). The device consists of a metal electrode biased with negative dc voltage up to a few kV. The conductive charge roller in the model is treated as a dielectric with high conductivity up to $10^{-2} (\Omega\text{-cm})^{-1}$. The photoconductor sheet in contact with the charge roller and ground electrode has a thickness of $100 \mu\text{m}$ and an electrical dielectric thickness (d/ϵ_r) of $6 \mu\text{m}$ where d and ϵ_r are the thickness and dielectric constant of the photoconductor sheet. This PC dielectric serves as a perfect insulator (the conductivity is zero) so that the surface charges on the dielectric sheet are immobile and not neutralized by the conduction process (a.k.a. dielectric relaxation). Plasma is initiated by a field emission current density of $10^{-3} \text{ A}\cdot\text{cm}^{-2}$ from emission node A, B, or C, which is $85 \mu\text{m}$, $135 \mu\text{m}$, or $177 \mu\text{m}$ above the PC surface, respectively. The emission node represents a surface roughness of a few microns on the charge

roller. The mesh consists of approximately 8,000 computational nodes, of which 3,000 nodes are in the plasma zone. The finest mesh spacing is 2 μm in the gap between the emission node and underlying PC dielectric sheet.

The gas fill is 1 atm of dry air – $\text{N}_2/\text{O}_2 = 80/20$, and the gas temperature is held constant at 300 K through the simulation. The gas phase reaction mechanism used in this chapter contains a subset of the reactions described in Refs. [19,20] to minimize the computation time. The species included in the reduced reaction mechanism are: N_2 , $\text{N}_2(\text{v})$, N_2^* , N_2^{**} , N_2^{***} , N_2^+ , N_4^+ , N , N^* , N^+ , O_2 , $\text{O}_2(^1\Delta)$, O_2^+ , O_2^- , O_3 , O^- , O , $\text{O}(^1\text{D})$, O^+ , and electrons. The states N_2^* and N_2^{**} are nominally $\text{N}_2(\text{A,B})$ and $\text{N}_2(\text{C})$, though the latter is treated as a lumped state including transitions higher than $\text{N}_2(\text{C})$, and N_2^{***} is nominally $\text{N}_2(\text{a}')$. I assume that the generation of UV/VUV radiation is produced by the relaxation of high-lying excited states of N_2 , and that the photons are absorbed by O_2 .

In a real EP printing application, the PC sheet is moving during the charging process, and the microplasma is sometimes initiated by background electrons rather than a field emission current from surface roughness. To capture the characteristics of microplasmas on a moving PC surface, a more sophisticated geometry is also modeled and shown in Fig. 6.1(e), in which the vertical scale is expanded by a factor of 4 for clarity. In this geometry, the top electrode is biased up to a kV, the ground electrode is covered with a PC sheet 18 μm in thickness, and the electrical dielectric thickness (d/ϵ_r) remains 6 μm . The gap is filled with 1 atm. dry air, and the reaction mechanism used in this geometry remains the same as discussed above, but an additional electron source balanced by electron attachment processes is used to continuously generate a peak background electron density of 10^3 cm^{-3} at electron temperature $T_e = 0.1 \text{ eV}$. The microplasma is then continuously seeded by the background electrons. The moving surface was computationally

addressed elsewhere [21] in detail. Briefly, the mesh points on the moving surface in contact with the plasma zone are chosen to be evenly spaced. Assuming the surface enters from the right and moves to the left, the moving surface translates the properties of the mesh points (e.g., surface charge density in the simulation) to its left every Δt ($\Delta t = \Delta x/v$ seconds, where Δx is the mesh spacing on the surface and v is the horizontal speed of the moving surface). The total mesh consists of 8,762 computational nodes, of which 3,769 are in the plasma zone. The finest mesh spacing is 4 μm in the converging gap between the charge roller and photoconductor sheet.

6.3 Characteristics of Microplasmas and Charging of a Stationary PC Surface

The characteristics of the microplasmas initiated by a field emission with current density of 10^{-3} A-cm⁻² from emission node A (see Fig. 6.1(d)), which is 85 μm above the stationary PC sheet located on a conductive charge roller, will first be discussed. The top electrode is biased to -1.6 kV dc and the conductive charge roller is a dielectric with a high conductivity of 10^{-2} Ω^{-1} -cm⁻¹. The electrical dielectric thickness of the underlying photoconductor is $d/\epsilon_r = 6$ μm , and the secondary emission coefficient for photon flux (γ_p) is 0.01 for this particular case. The time evolution of electron density and electric potential during the charging process is shown in Fig. 6.2. The electron impact ionization sources by bulk electrons, S_e , and beam-like secondary electrons, S_{sec} , are shown in Fig. 6.3 and Fig. 6.4. The photoionization source is shown in Fig. 6.5. After an initial electron current emitted from node A, an electron avalanche occurs within 1 ns. The electrons drift along the high averaged electric field of 176 kV/cm ($E/N \approx 720$ Td, 1 Td = 10^{17} V-cm²) underneath the emission node, and the electron density is then multiplied along the trajectory of the electron plume with a peak density of 2.7×10^{10} cm⁻³ at the PC surface. The electron impact ionization source is primarily provided by lower-energy bulk electrons, S_e , on the

order of $10^{21} \text{ cm}^{-3} \text{ s}^{-1}$. The ionization source by the beam-like high-energy electrons emitted from the CR cathode, S_{sec} , is generally two orders of magnitude smaller. It is due to fewer secondary electrons being produced, and to the absence of the sheath potential at the cathode. Fewer secondary electrons are produced because of the smaller ion flux and the smaller photon flux. Although the peak value of the volumetric photoionization source, S_{photo} , is on the order of $1.8 \times 10^{16} \text{ cm}^{-3}\text{-s}^{-1}$, which is small compared to electron impact ionization sources, the photoionization source and photoemission provided by UV photons from long-lived excited states provide remote seed secondary electrons emitted from the CR surface at the smaller gap between the CR and PC sheet where the electric field is higher. At $t = 4 \text{ ns}$, these seed electrons at the small gap start to avalanche. A peak electron density of $7.4 \times 10^{11} \text{ cm}^{-3}$ is produced at a gap of $30 \text{ }\mu\text{m}$ with a high electric field of 417 kV ($E/N \approx 1660 \text{ Td}$). The peak ionization source of $10^{23} \text{ cm}^{-3}\text{-s}^{-1}$ is dominated by bulk electrons, S_e . By $t = 10 \text{ ns}$, plasma densities up to 10^{15} cm^{-3} are generated near the nip point where the charge roller is in contact with the underlying PC sheet, and this conductive plasma fully forms the sheath at the CR cathode. Meanwhile, a streamer with an electron density of 10^{14} cm^{-3} underneath the emission node A has been developed and propagated upward to the CR cathode.

As the discharge proceeds, the negative charges drift to the PC surface and remove the voltage drop across the gap. The reduced voltage drop and E/N decrease the ionization rate of the electron source from bulk plasma, S_e . However, the electron impact ionization source from the beam-like sheath-accelerated high-energy electrons becomes dominant due to the fully developed sheath and secondary electrons provided by ion flux and UV photons onto the CR cathode. At $t = 10 \text{ ns}$, the peak ionization source, S_{sec} , is as high as $2 \times 10^{24} \text{ cm}^{-3}\text{-s}^{-1}$ at the conductive CR cathode.

The voltage drop in the gap between the charge roller and photoconductor is reduced by

the charging of the PC surface. Having said that, there is still a large potential drop across the less-conductive plasma edge between the CR and the uncharged dielectric surface, which triggers a surface ionization wave (SIW) propagating along the PC surface. The SIW spreads outward from the avalanche point with a speed of $2 \times 10^6 \text{ cm-s}^{-1}$, and negatively charges the PC surface. By $t = 20 \text{ ns}$, the outward-propagating SIW and the spreading of microplasmas have already merged with the cathode-directed streamer underneath emission node A, and have started to dissipate the voltage drop across the plasma edge. As the voltage drop and E/N at the less conductive plasma edge fall below the self-sustaining value, the SIW begins to terminate.

By $t = 100 \text{ ns}$, the plasma density in the gap rapidly decays below 10^{10} cm^{-3} through electron-ion recombination, the electron attachment process, or the charging of the underlying PC surface. Part of the residue electrons laterally drift along the electric field (perpendicular to the electric potential lines) to their right at a larger gap and accelerated by the high electric field produced by the CR and the uncharged PC surface. At $t = 263 \text{ ns}$, after an electron avalanche has been re-ignited by the voltage drop between CR and the uncharged underlying dielectric, a thin plasma channel is produced with a density of 10^{12} cm^{-3} . A peak ionization rate up to $6.5 \times 10^{21} \text{ cm-s}^{-1}$ is provided by secondary electrons, S_{sec} , and bulk electrons, S_e . The plasma density in the channel is the highest near the surface, which reduces the E/N and ionization rate of S_e . The light electrons in the plasma channel rapidly drift to the PC surface and start to charge it negatively, while the positive charges are massive and accumulate in the channel. As a result, the positive charge density in the channel generally becomes 1–2 orders of magnitude larger than the electron density, which then produces a high electric field and ionization source, S_e , of $10^{21} - 10^{22} \text{ cm-s}^{-1}$. As the discharge proceeds, the intense field and ionization source stimulate a fast cathode-directed streamer propagating from the PC surface upward to the CR cathode. Meanwhile, the negative

surface charging pushes the potential lines into the PC dielectric, producing a lateral electric field that then starts to warp the plasma channel near the PC surface to the less charged region. By $t = 273$ ns, the cathode-directed streamer has already reached the CR with an electron density up to $8.5 \times 10^{14} \text{ cm}^{-3}$, ionization is provided by the electron impact ionization source up to $5.7 \times 10^{23} \text{ cm}^{-3}\text{s}^{-1}$. The negative species locally charges the underlying PC dielectric and produces a non-uniform charging pattern and a potential hump. After the re-ignition and the charging of the PC dielectric, the voltage drop between the CR and uncharged PC surface falls below the self-sustained value, and the microplasma extinguishes.

Due to the gradually narrowing gap between the conductive charge roller and PC dielectric, the microplasma is triggered at the critical point where the local voltage drop in the gap and the rate of ionization is preferable for the remote seed electrons provided by photoionization and photoemission to avalanche. Although the peak value of the volumetric photoionization source, S_{ph} , during the active discharge is on the order of $10^{19} \text{ cm}^{-3}\text{s}^{-1}$, which is small compared to the electron impact ionization source, this photoionization source and the photoemission produced by UV photons from long-lived excited states continuously provide remote seed electrons at the CR and PC surfaces to help trigger avalanches. The time evolution of surface potential produced by microplasmas initiated by current emission from nodes A, B, and C is shown in Fig. 6.6 for the secondary emission coefficient for photon flux $\gamma_p = 0.01$, and Fig. 6.7 for $\gamma_p = 0$ (no photoemission). The computational nodes in the plasma zone are truncated at $x \approx 0.04$ cm, where the corresponding gap $\approx 6 \text{ }\mu\text{m}$. The time evolution of the surface potential on the PC sheet shown in Fig. 6.6(a) reflects the corresponding plasma behavior and surface charging shown in Fig. 6.2. A microdischarge is initiated by remote seed electrons provided by photoionization and photoemission at a small gap of $30 \text{ }\mu\text{m}$ at a critical point, $x = 0.08\text{--}0.09$ cm, producing a potential

dip at $t = 5$ ns. The microdischarge and SIW spread laterally from the critical point on the PC surface with a speed of $10^6 - 10^7$ cm-s⁻¹, and negatively charge the surface to the terminal voltage of 1.2 kV – 1.6 kV. By $t = 12$ ns, the streamer initiated by the emission current from node A has been fully formed. This cathode-directed streamer triggers an SIW, which then negatively charges the surface until $t = 60$ ns, when the voltage is dissipated at the plasma edge. As the SIW is terminated, the residue electrons laterally drift to the larger gap and re-ignite the discharge at $x = 0.18$ cm at $t = 260$ ns. The microplasma spreads outward until the voltage drop between the CR and PC sheet falls below the self-sustaining value; the microplasma then starts to extinguish at $t = 290$ ns. A non-uniform charging pattern (a potential hump) is then produced by the re-ignition of this sequential pulse at the large gap.

Over the range of emission nodes (85 μm , 135 μm , and 177 μm above the PC surface) investigated for $\gamma_p = 0.01$, the charging of surface and plasma dynamics do not dramatically change. However, as the emission current is injected far from the nip point, the initiation of microplasma at the small gap is delayed by tens to hundreds of ns. This late ignition of microdischarges can be attributed to a small photon flux. Since the amount of remote seed electrons required to trigger the microplasma at the critical point (where the ionization rate is favorable) is fixed, the initiation process is sensitive to the intensity of photon flux that produces these seed electrons. As the emission current is injected from node C (177 μm above the PC sheet and 2,050 μm away from the nip point, as shown in Fig. 6.6(c)), the intensity of photon flux directly or indirectly generated by the emission current greatly decays at the critical point. As a result, the initiation of microplasma is delayed until a sufficient amount of seed electrons is produced by the photoionization and photoemission. As γ_p is reduced to 0, no photoemission electrons are provided from the CR and PC surfaces, and the microplasma is triggered only by remote volumetric seed

electrons provided by photoionization. The surface potential on the PC sheet for $\gamma_p = 0$ is shown in Fig. 6.7. The plasma dynamics and surface charging on PC dielectric do not dramatically change for $\gamma_p = 0$, and the terminal voltage produced by the plasma initiated by three nodes for $\gamma_p = 0.01$ and $\gamma_p = 0$ generally remains the same. Having said that, structures are produced in the local PC potential at the initial and final stages, and the surface potential produced by surface charging density becomes less uniform due to the lack of photoemission from the surface. The ignition of microplasma for $\gamma_p = 0$ is further delayed since the remote seed electrons are provided only by volumetric photoionization, and the critical point is slightly shifted away from the nip point.

The microdischarge produced between the conductive charge roller and the dielectric sheet is primarily initiated by photoemission or photoionization at the critical point where the local rate of ionization and voltage drop are favorable to the electron avalanche. As a result, for a gas mixture capable of producing a high photoionization source, S_{ph} , or for material that produces a large photoemission current (high γ_p), the location of the initial field emission current does not change the initiation process; the microplasma is produced at the critical point which then propagates outward and negatively charges the underlying dielectric until the voltage drop in the gap falls below the self-sustaining value. For certain gas mixtures or underlying dielectric materials used in printing, the photoionization and photoemission are barely produced during the charging process. The discharge is then triggered directly underneath the local field emission node if the local E/N is sufficient. The time evolution of electric potential and electron density triggered by a field emission current density of 10^{-3} A-cm⁻² from node A is shown in Fig. 6.8, the corresponding surface potential on the photoconductive sheet produced by the microdischarge initiated by emissions from nodes A, B, and C are shown in Fig. 6.9. Photoionization and photoemission are not considered in these cases. The surface potential corresponding to charging of PC sheet (in Fig.

6.8) is shown in Fig. 6.9(a). After an electron avalanche occurs underneath node A at $x \approx 0.14$ cm, a cathode-directed streamer is fully formed and negatively charges the underlying PC surface to -390 V at $t = 13$ ns. By $t = 40$ ns, the streamer charges and spreads on the PC dielectric surface to ± 0.02 cm. As the process proceeds, secondary electrons emitted from the cathodic CR and residue electrons in the gap trigger a sequential electron avalanche and microdischarge at $x \approx 0.11$ cm at $t = 48$ ns. The process repeats and the microplasmas spread inward to the nip point by $t = 60$ ns. Meanwhile, residue electrons also drift outward and re-ignite the plasma in the CR-PC gap until the voltage drop falls below the self-sustained value. The initiation and charging process remains the same for the emission current from node B. However, as the current is emitted from node C, the ionization rate in the gap of $177 \mu\text{m}$ is insufficient to trigger an electron avalanche, and no remote seed electrons are provided by photoionization and photoemission at the critical point. As a result, the microplasma cannot be triggered and the voltage on the PC surface remains unchanged.

With a high conductivity of $10^{-2} \Omega^{-1}\text{-cm}^{-1}$ on the current charge roller, the influence of variation of local voltage on the charge roller due to a strike of positive ions is inconsequential. Within $10^{-2} - 10^{-1}$ ns of dielectric relaxation time ($\tau_d = \epsilon/\sigma$, where ϵ and σ are the permittivity and conductivity of the charge roller, respectively), the local voltage disturbance on the CR is neutralized by the majority charge carriers (i.e., electrons in this case), and the voltage on the charge roller is basically a constant to the microdischarge. With decreasing conductivity, however, the local voltage variation on the CR begins to play more important roles. The time evolution of electron density and electric potential during the charging process for a conductivity of $\sigma = 10^{-4} \Omega^{-1}\text{-cm}^{-1}$ on the charge roller is shown in Fig. 6.10. The microdischarge is initiated by $t = 4$ ns, the upward-moving positive ions impinge onto the CR, reducing the local voltage up to 1 kV according to the strike of local ion currents. Due to the reduced conductivity of $\sigma = 10^{-4} \Omega^{-1}\text{-cm}^{-1}$, the local

variation of voltage on the CR cannot be removed until a few nanoseconds of dielectric relaxation time have passed, which is commensurate with a lifetime of microdischarges. As a result, the reducing voltage on the local surface of CR decreases the voltage drop in the gap and the rate of ionizations, the microplasma is then terminated earlier, and the local disturbance on the charge roller voltage leads to a non-uniform surface charging pattern on the PC surface. The surface potential on the PC dielectric after the discharge has been terminated for a conductivity of $\sigma = 10^{-2}$ and $10^{-4} \Omega^{-1}\text{-cm}^{-1}$ is shown in Fig. 6.10(b). With a lower conductivity on the CR, the microdischarge behaves in a dielectric barrier discharge (DBD) manner. The charging on both PC and CR surfaces removes the voltages across the gap and terminates the discharges. As a result, the PC surface is charged less negatively and non-uniformly.

6.4 Charging of a Moving Surface

When the microdischarges produced by a charge roller are used for continuous surface charging, the underlying dielectric is in motion during the charging process. For a stationary surface, the charging process by a conductive dc-biased charge roller behaves in a DBD manner; the surface charging reduces the voltage drop and ionization rate in the gap, which then terminates the discharge. When the surface is in motion, the surface charges are translated away by the moving dielectric surface on one side, while the uncharged surface is translated toward the charge roller on the other side. The incoming uncharged surface re-establishes the voltage drop in the gap, and the rebound in E/N re-ignites the plasma and charges the incoming surface. As the re-ignition and charging processes repeat to produce a self-pulsing microdischarge, a periodic charging pattern is then produced.

The time evolution of the electron density and electric potential of a continuous charging

between a conductive charge roller and a moving surface (as shown in Fig. 6.1(e)) is shown in Fig. 6.11. For the purpose of demonstration, the surface moves rapidly with a speed commensurate to the formation of the microdischarges. The conductive charge roller with a conductivity of $\sigma = 1 \text{ } \Omega^{-1}\text{-cm}^{-1}$ is in contact with an electrode biased with -1 kV dc voltage. The ground electrode is biased with a dielectric sheet 18 μm in thickness, while the electrical dielectric thickness (d/ϵ_r) remains 6 μm . The microdischarge is sustained in atmospheric dry air, and a background electron density of 10^3 cm^{-3} is continuously provided. By $t = t_1$, an electron avalanche occurs at $x \approx 0.03\text{--}0.06 \text{ cm}$ in the gap of 10–20 μm where the voltage drop across the gap and high E/N is favorable to initiation of a microplasma. Within a few nanoseconds, a conductive microdischarge is fully formed to negatively charge the surface of the underlying PC dielectric. These cathode-directed streamers laterally spread outward on the dielectric seeking out uncharged capacitances with a speed of $2 \times 10^6 \text{ cm/s}$, while the uncharged surface moves inward to the nip point. Due to the large voltage drop and the high rate of ionization between the CR and uncharged PC surface, a streamer can be ignited and fully developed within 3–5 ns. By $t = t_3$ when the microdischarge propagates to a critical E/N at a larger gap, a longer time is required to re-ignite and transform an electron avalanche into a streamer in this large gap, while the surface is still rapidly moving inward to provide a fresh, uncharged surface. As a result, the microdischarge with a plasma density up to $2.6 \times 10^{14} \text{ cm}^{-3}$ at $x \approx 0.17 \text{ cm}$ partially charges the surface and then produces a potential hump 200–300 μm in width. After the discharge is terminated by surface charging, this potential hump and surface charge density are translated to the left with the moving surface, while the uncharged surface moves in. The fresh surface then restores the E/N in the gap. At $t = t_4$, the rebound in gap potential and residue electrons re-ignite the plasma and produce a second potential hump at $x \approx 0.18 \text{ cm}$. As the discharge proceeds, the repetitive process produces a periodic self-pulsing

microdischarge at $x \approx 0.17\text{--}0.18$ cm and forms an oscillatory surface potential with an average period of 300–400 μm . At $t = t_7$, as the periodic potential and surface charges are translated to the smaller gap, a high E/N is locally re-established between the CR and less-charged surface. As a result, random microdischarges are produced in the small gap at a less-charged region of oscillatory surface potential, and a modulated periodic surface potential is formed on the PC.

Due to the high voltage and fast-moving surface, the rebound in voltage in the gap periodically produces E/N, and hence a self-pulsing microplasma. These localized microplasmas with an electron density up to 10^{14} cm^{-3} are conductive and dominated by the space charges effect. A microplasma and electric potential at periodic steady state is shown in Fig. 6.12(a); the corresponding spatial distribution of electric potential, electric field, the densities of electrons, and positive and negative ions over the cross section of a streamer are shown in Fig. 6.12(b) and 6.12(c). The characteristics of the microplasma in the charge roller are similar to those of low-pressure glow discharges. An abrupt voltage drop of 300 V within a few microns in the gap near the CR creates an electric field up to 360 kV/cm ($E/N \approx 1470$ Td). In this region, the high voltage drop results from the difference between space charge densities; the positive ion density reaches as high as 2.9×10^{14} cm^{-3} , while the electron density is generally 2–3 orders of magnitude smaller. The high E/N produces an intense electron impact ionization source of $10^{22} - 10^{23}$ $\text{cm}^{-3}\text{-s}^{-1}$, which sustains the streamer until the surface charging removes the voltage across the gap. Followed by a cathode fall, the voltage drops gradually along the gap, producing a relatively small E/N of 60–100 Td. In this region, electron, negative, and positive charge densities are on the order of 10^{12} cm^{-3} , while the density of negative charge species is slightly higher than the positive ion density near the anodic dielectric sheet. After the localized self-pulsing microdischarges periodically charge the underlying surface with a high current, the potential humps produced by the surface

charging are laterally translated to the left with the moving surface. The surface potential on the PC sheet before surface charging and after a periodic steady state has been reached are shown in Fig. 6.12(d) for a rapid moving and slowly moving (5 times slower) surface as examples. For a rapidly moving surface, an average of a 200 to 400 μm period in an oscillatory pattern is formed at steady state. The potential hump is individually produced at $x \approx 0.18\text{--}0.2$ cm where the local residue space charges, the secondary electron emission, and the rebound of local E/N by moving surface are self-adjusted to reach a periodic steady state. These simulation results are consistent with experiment observation.[17] As the surface moves relatively slower, the surface potential pattern significantly changes; the period increases to 800 – 1,000 μm , and the amplitude becomes smaller.

Since the periodic microdischarge is self-adjusted by a combination of residue space charges and the rebound in the local gap voltage, the plasma dynamics and surface charging should be sensitive to the applied voltage on the conductive charge roller. The time evolution of electron density and the electric potential of a continuous charging is shown in Fig. 6.13. The surface moves rapidly with a speed commensurate to the formation of the microdischarges, while the applied voltage on the charge roller is reduced to -700 V dc voltage. During the initial stage, the microplasma is initiated at small gap and propagates laterally to the large gap. As the discharge spreads on the PC sheet, the conductive plasma fully charges the PC surface, producing a periodic potential pattern until it reaches a critical E/N at large gap. By $t = t_2$, the plasma with a peak electron density of only $3.7 \times 10^{11} \text{ cm}^{-3}$ is produced due to the lower applied voltage. The less conductive microdischarge partially charges the underlying dielectric, while the fast-moving surface keeps translating away the previous periodic surface potential and bringing the uncharged surface inward to the charge roller. The restore of E/N by moving surface and residue electrons

(including secondary electrons by ion and photon flux) self-adjusts the position and characteristics of the microplasma. As the partially charged surface is translated to a small gap, the E/N increases, and hence triggers local electron avalanches. By $t = t_5$, a steady state of microplasma in the narrowing gap has been achieved. Microplasmas are continuously seeded by secondary electrons produced by UV photons and ion fluxes. These microdischarges of low electron density in the gap partially charge the underlying PC dielectric, the surface potential remains uniform.

The microplasma and electric potential at steady state is shown in Fig. 6.14(a), the corresponding spatial distribution of electric potential, electric field, the densities of electrons, and positive and negative ions over the cross section of the discharge are shown in Fig. 6.14(b) and 6.14(c), and the surface potential on the PC sheet at steady state is shown in Fig. 6.14(d) for a rapidly and relatively slowly moving (10 times slower) surface. After the steady state has been achieved, the dielectric is only slightly charged by the microplasma produced by a lower applied voltage. The rate of ionization on the order of $10^{21} \text{ cm}^{-3}\text{-s}^{-1}$ is insufficient to produce a conductive plasma; the electron density on the order of 10^{11} cm^{-3} peaks at the anodic dielectric while the positive ion density of 10^{13} cm^{-3} peaks at the cathodic CR. As a result, the localized space charge effect becomes less important; the electric potential gradually drops in the gap, producing a quasi-constant electric field of 100 kV/cm ($E/N \approx 410 \text{ Td}$) in the gap; and the cathode fall at the CR cathode cannot be formed due to low space charge density – the microplasma is sustained in a Townsend-like mode. This homogeneous Townsend-like discharge in a DBD has been observed at atmospheric pressure.[22–27] Having said that, the surface potential at steady state is relatively smooth and uniform compared to the periodic charging pattern produced by self-pulsing microplasmas at a high applied voltage. These Townsend-like discharges provide a solution for obtaining a uniform charging pattern. For the voltage investigated, the surface potential is not

sensitive to the speed of the moving surface as the discharge is operated in a Townsend-like mode. Although the speed of the moving surface is even slower in a real printing application, by optimizing the gas mixture, the applied voltage, and the speed of the moving surface, the Townsend-like discharge continuously seeded by secondary electrons and photoemission might be produced to form a uniform charging pattern.

6.5 Concluding Remarks

Charge rollers are the most commonly used devices for surface charging of photoconductors in EP printing technologies. I computationally investigated the properties of microplasmas in a narrowing gap between a conductive charge roller and a photoconductive dielectric. The charging of the surface of the PC is essentially performed in a dielectric-barrier-discharge (DBD) manner. With the dc-biased charge roller and a stationary dielectric target, the microplasma is terminated as voltage is removed from the gap by the surface charging on the PC dielectric. The surface potential is sensitive to the conductivity of the charge roller, photoionization, photoemission, and the location of field emission current. As the surface is in motion, the moving dielectric brings in uncharged surfaces, which restores the voltage across the gap and re-ignites the plasma. As the process repeats, a periodic self-pulsing microplasma might be produced to form an oscillatory charging pattern on the PC surface. Under certain operating conditions, a Townsend-like discharge may be obtained in the narrowing gap, the surface is partially charged by the discharge, and a quasi-constant electric field is produced. As a result, a more uniform surface charging on the dielectric may be obtained. I found that with a higher applied voltage and a rapidly moving surface, periodic avalanches form a periodic self-pulsing pattern. With a relatively smaller voltage, a Townsend-like discharge becomes dominant and a

uniform surface charging might be obtained.

In summary, this chapter focuses on atmospheric pressure microdischarges produced by conductive charge rollers used in EP printing technologies. It was found that the remote seed electrons provided by photoionization and photoemission are significant in this system due to the narrowing gap between charge roller and photoconductor. Once the remote seed electrons are produced at the narrowing gap, an electron avalanche and microplasmas could occur to charge the underlying PC surface. A more uniform surface charging might be obtained by using a smaller voltage on the charge roller, and a gas mixture with long lived excited states capable of continuously emitting UV/VUV photons which produce photoemission on a fast moving surface.

6.6 Figures

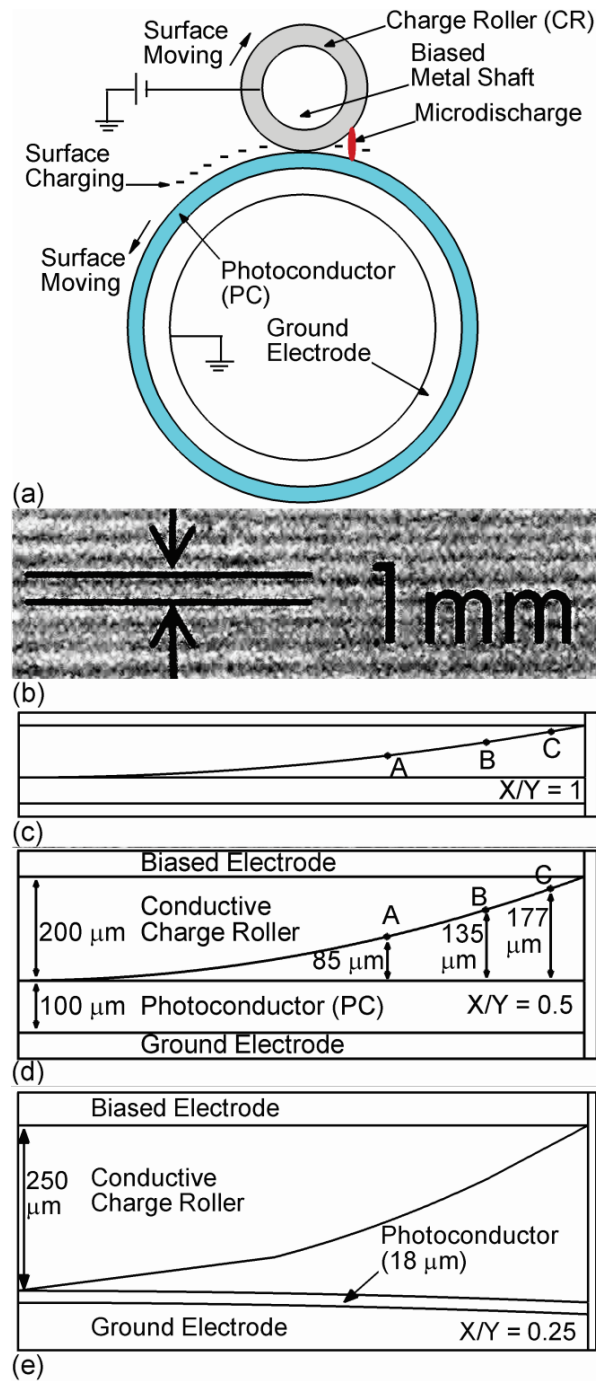


Figure 6.1 Schematic of a charge roller (CR) and a photoconductor (PC) drum. (a) Microdischarges and surface charging in the entire device consist of a cylindrical CR and a PC drum. (b) A non-uniform periodic surface charging pattern with period of 1 mm. An idealized device of its original scale is shown in (c); the idealized device with its vertical scale expanded by a factor of 2 is shown in (d). A more sophisticated geometry that is vertically expanded by a factor of 4 is shown in (e).

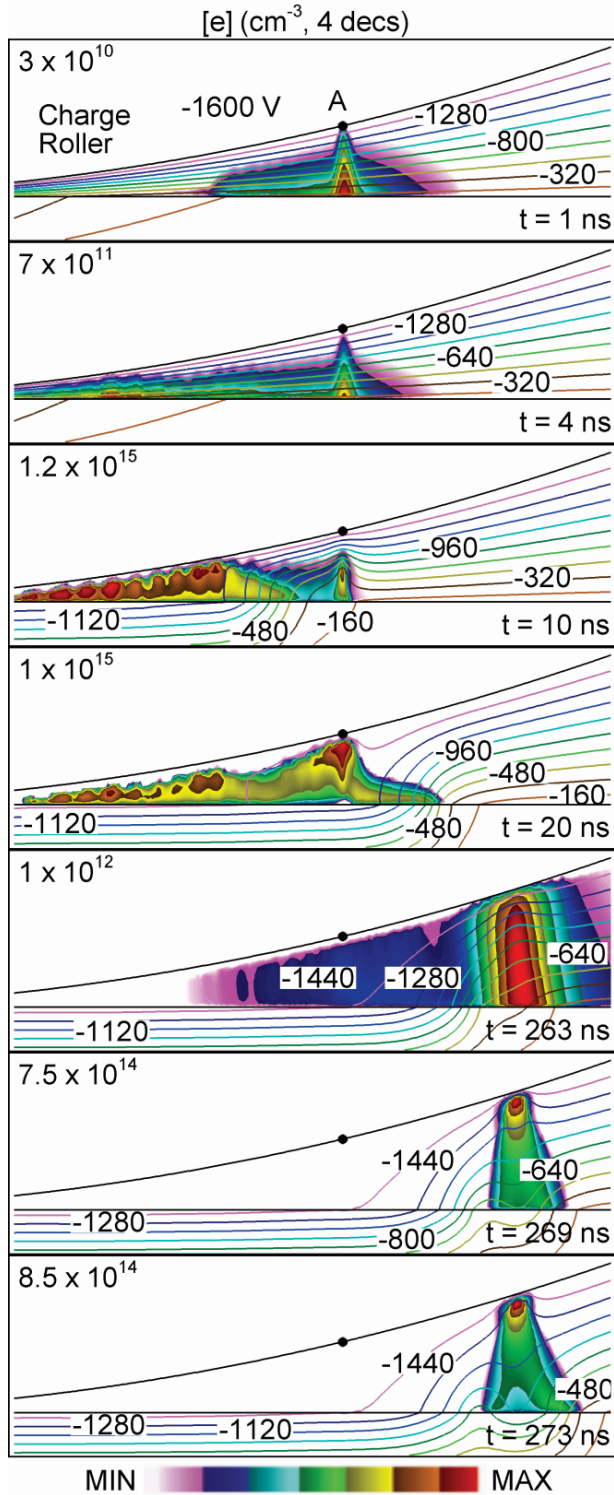


Figure 6.2 Time evolution of electron density (color flood, cm^{-3}) and electric potential (contour lines, V) produced by a -1.6 kV dc-biased conductive charge roller. The electron density is plotted on a log scale over 4 decades, the maximum density is shown in the upper-left corner of each time frame. The discharge is terminated by surface charging.

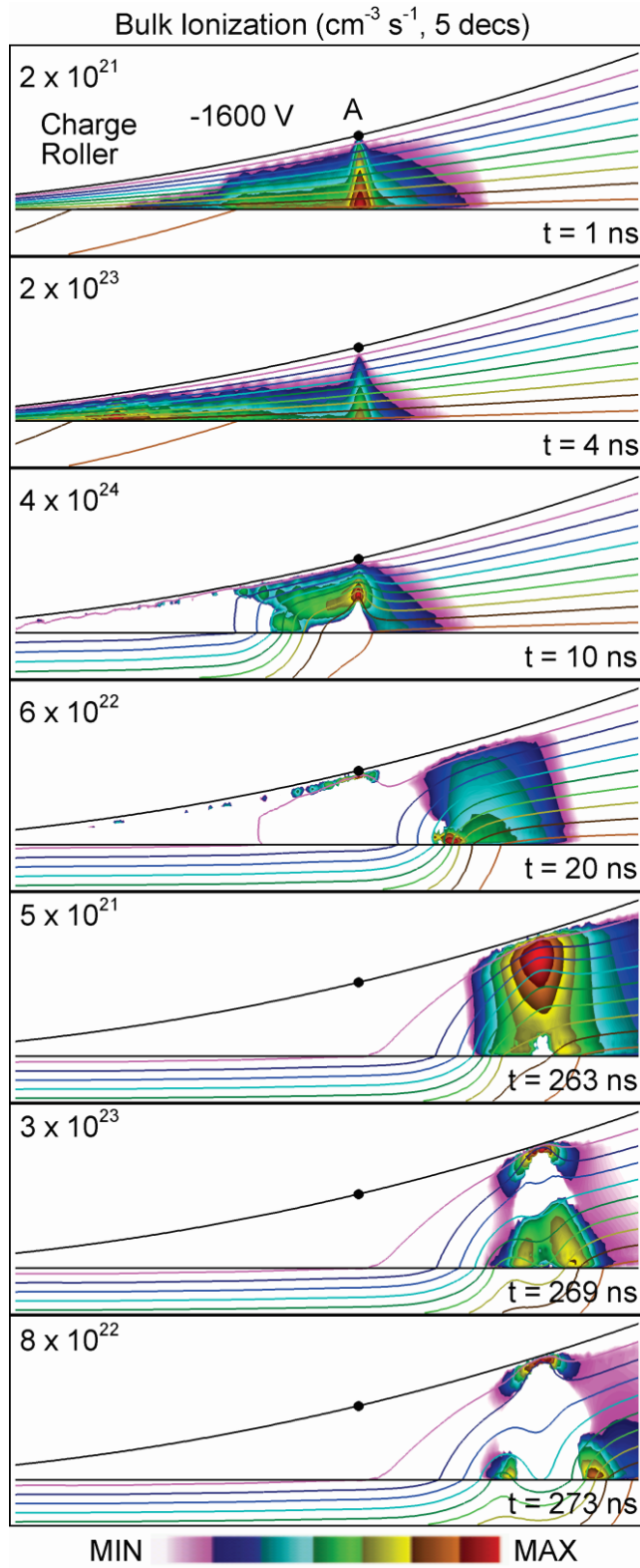


Figure 6.3 Electron impact ionization sources from bulk electrons (S_e) at different times during the charging process. The ionization sources are plotted on a log scale over 5 decades.

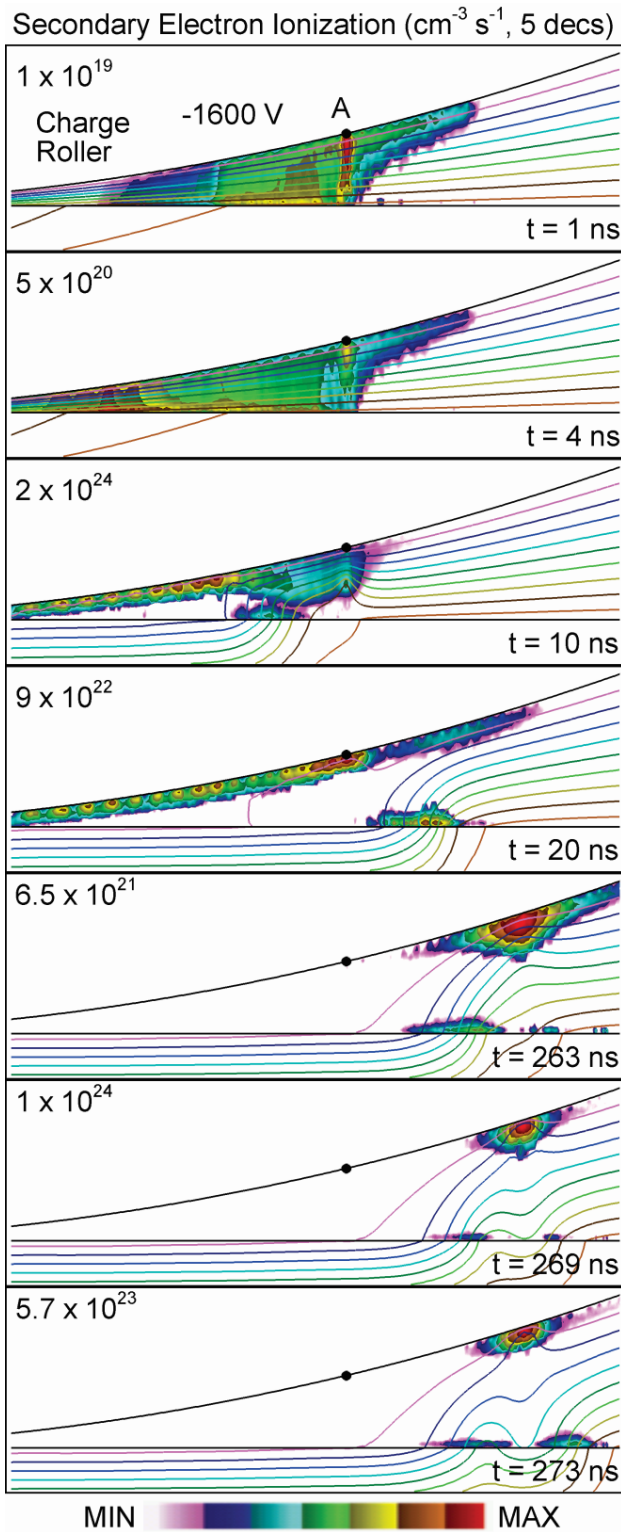


Figure 6.4 The time evolution of an ionization source by sheath-accelerated secondary electrons (S_{sec}) during the charging process. After the sheath is fully formed, S_{sec} is in general comparable to or an order of magnitude larger than S_e .

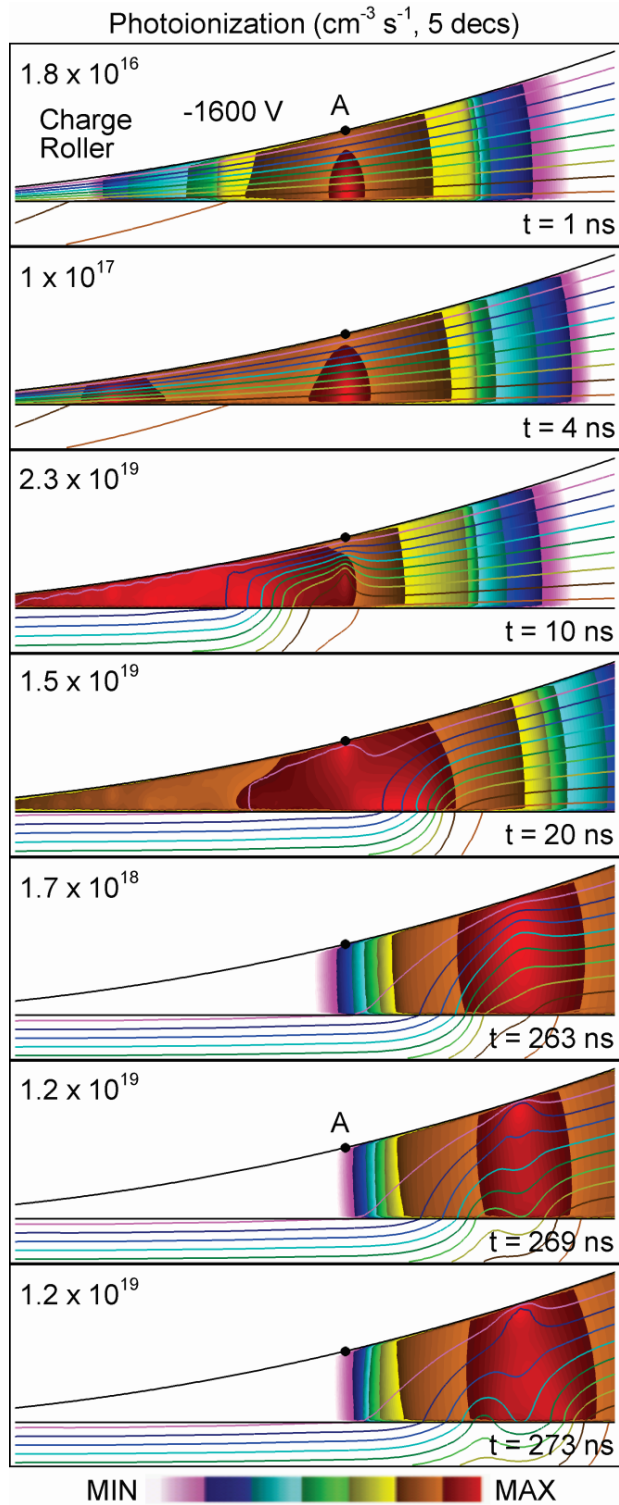


Figure 6.5 The time evolution of photoionization (S_{ph}) plotted on a log scale over 5 decades. Although relatively smaller compared to the electron impact ionization source, the remote secondary electrons provided by UV photon flux help initiate the microplasmas at the narrowing gap.

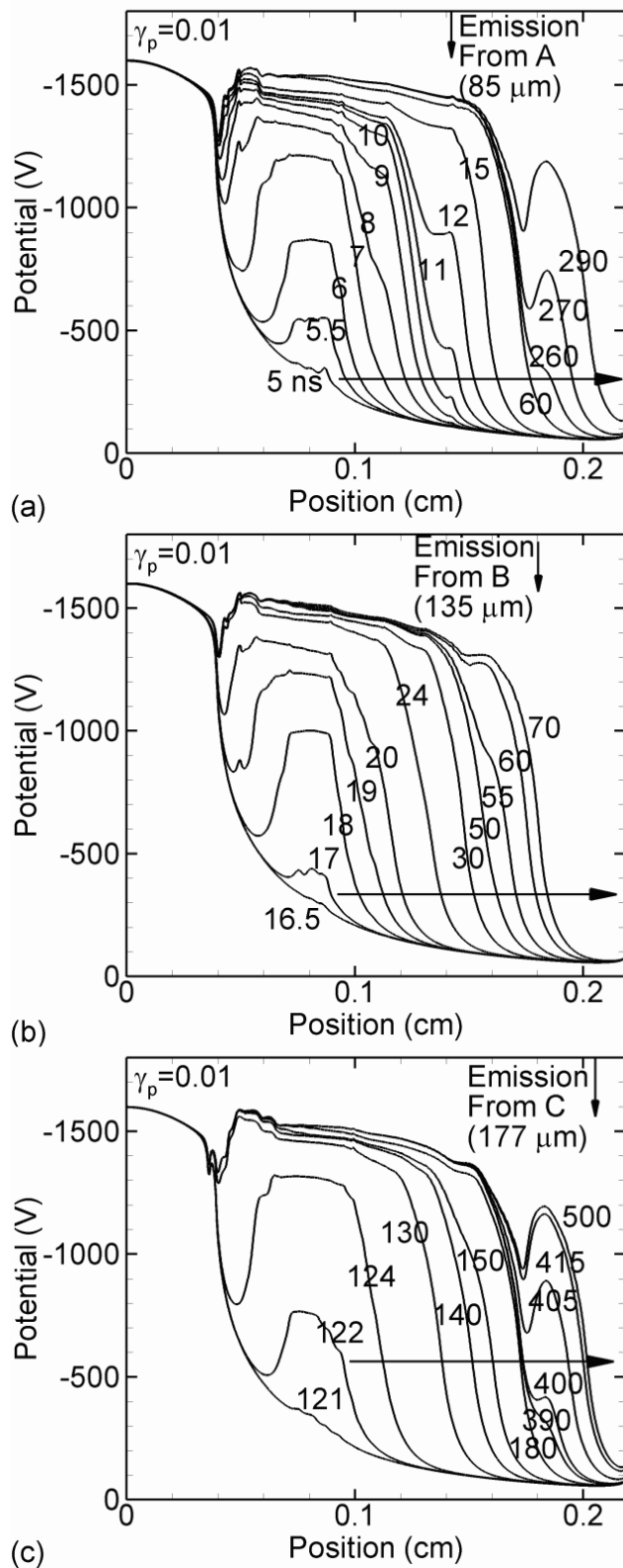
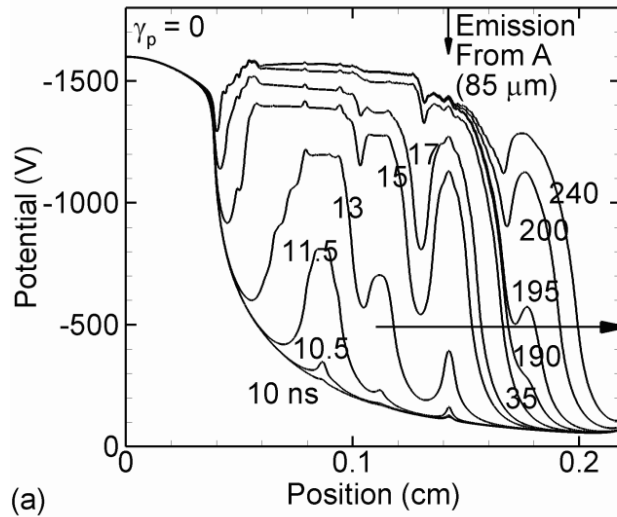
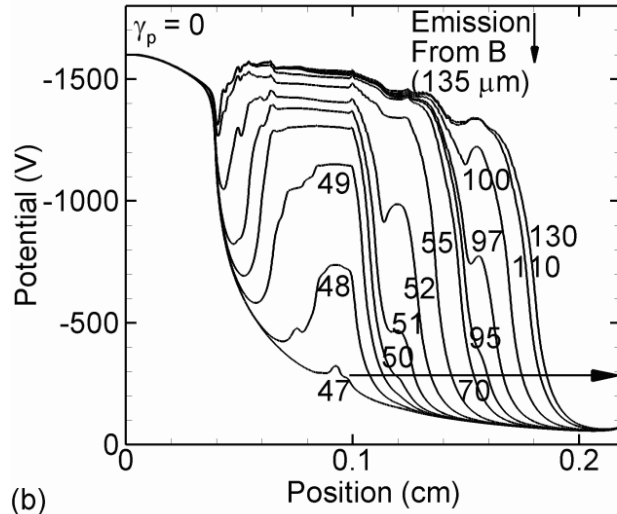


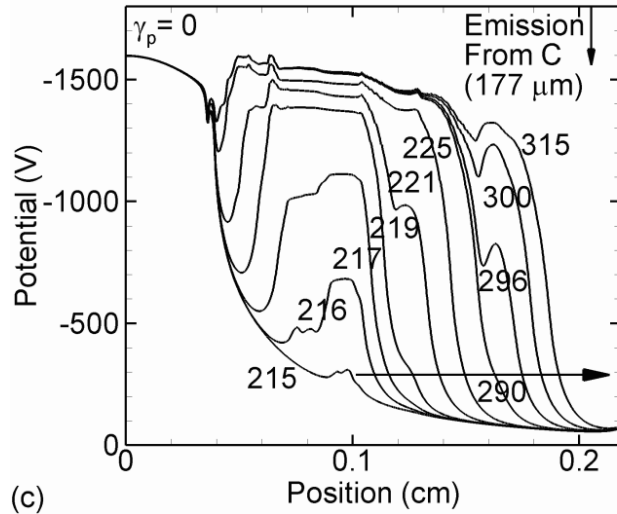
Figure 6.6 The time evolution of surface voltage (solid, V) on photoconductive dielectric for $\gamma_p = 0.01$. Microplasmas are initiated by emission current from nodes A, B, and C.



(a)



(b)



(c)

Figure 6.7 The time evolution of surface voltage (solid, V) on photoconductive dielectric for $\gamma_p = 0$ (no photoemission from surface). Microplasmas are initiated by emission current from nodes A, B, and C. The surface potential is less smooth without photoemissions.

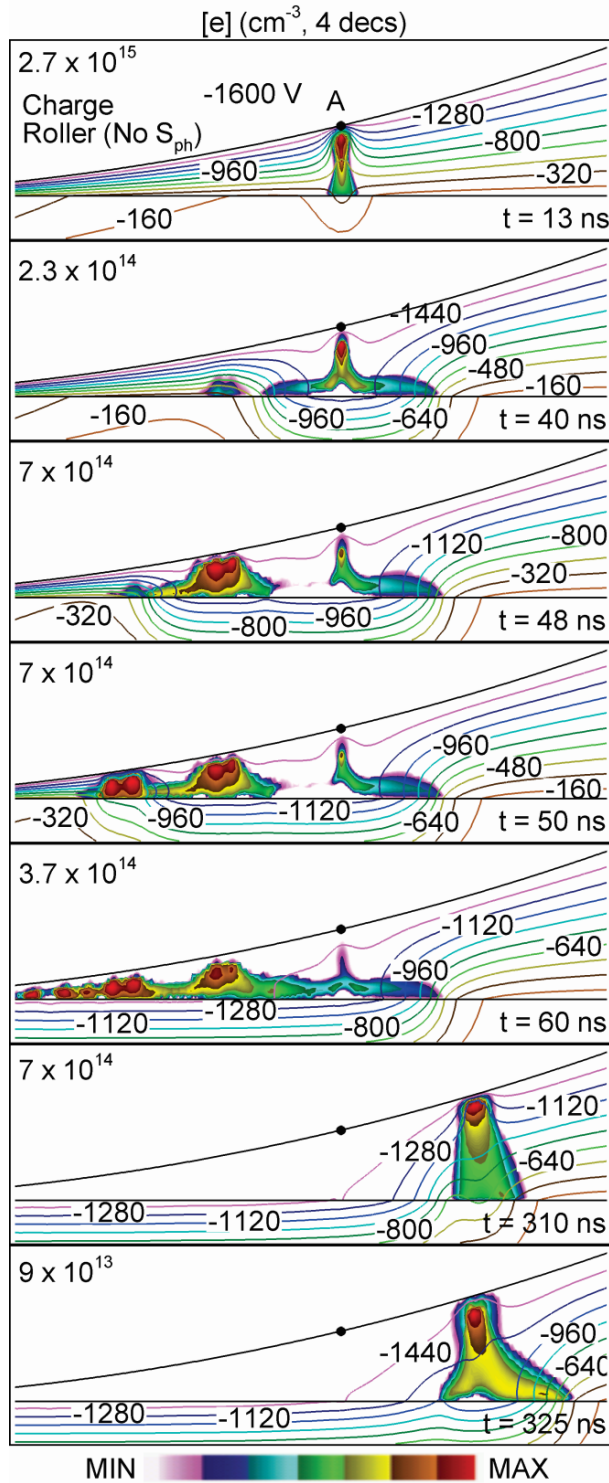


Figure 6.8 The time evolution of electron density (color flood, cm⁻³) and electric potential (contour lines, V) triggered by a field emission current density of 10⁻³ A·cm⁻² from emission node A. CR is biased with -1.6 kV dc voltage; photoionization and photoemission are not considered. The electron density is plotted on a log scale over 4 decades.

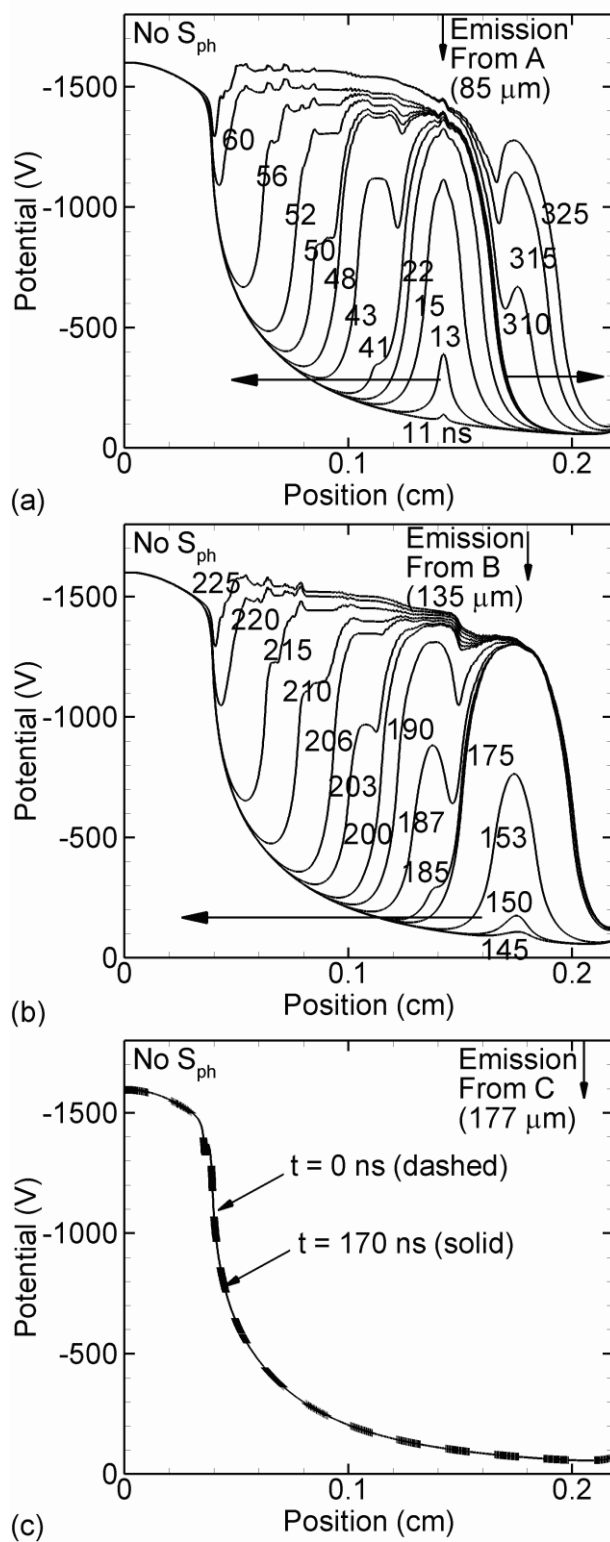


Figure 6.9 The time evolution of surface voltage (solid, V) on a photoconductive dielectric without photoionization and photoemission. Microplasmas are initiated underneath the emission node A, B, or C if the local field is sufficient.

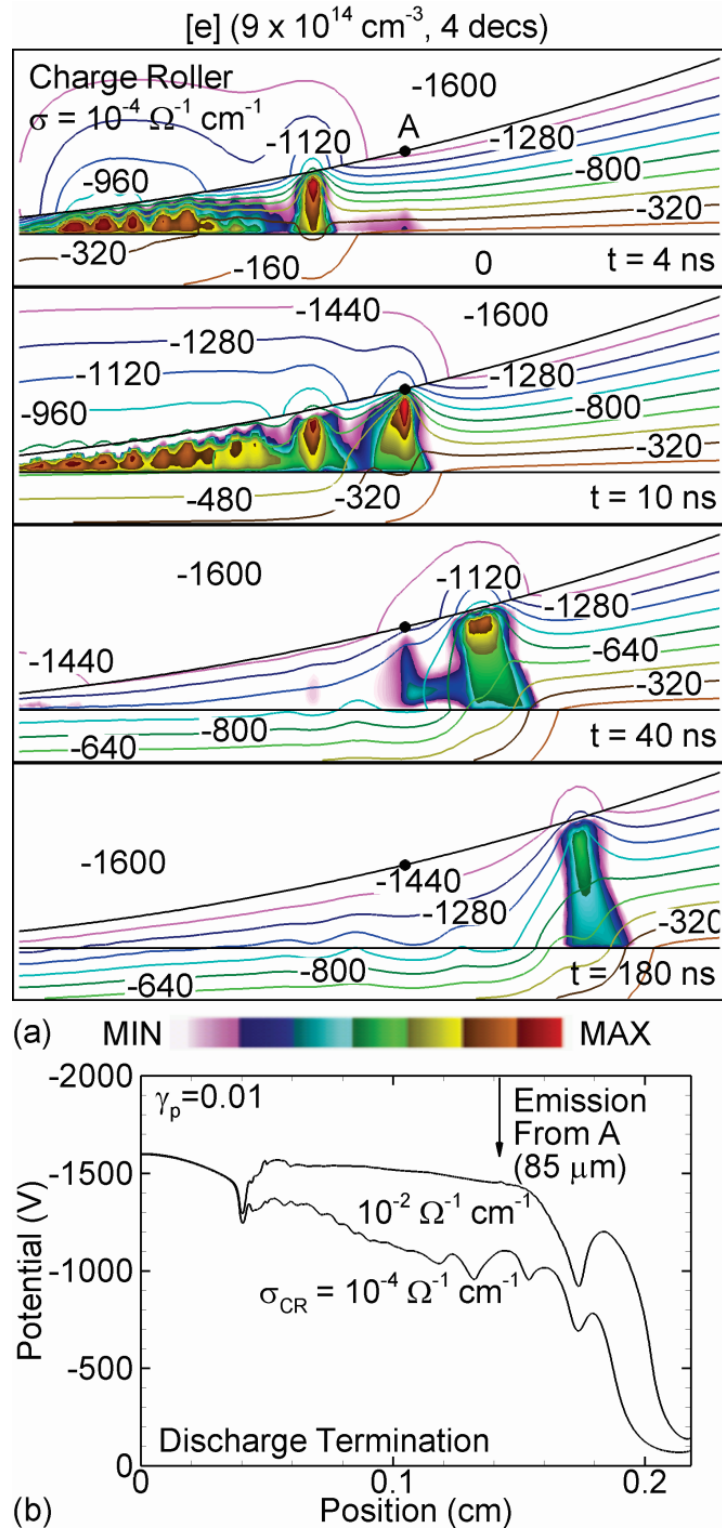


Figure 6.10 Microdischarges produced by a charge roller having a conductivity of $\sigma = 10^{-4} \Omega^{-1}\text{-cm}^{-1}$. (a) The time evolution of electron density (color flood, cm^{-3}), and electric potential (contour lines, V) at $t = 4, 10, 40,$ and 180 ns . (b) Surface voltage (solid, V) after the discharge is terminated for $\sigma = 10^{-2}$ and $10^{-4} \Omega^{-1}\text{-cm}^{-1}$.

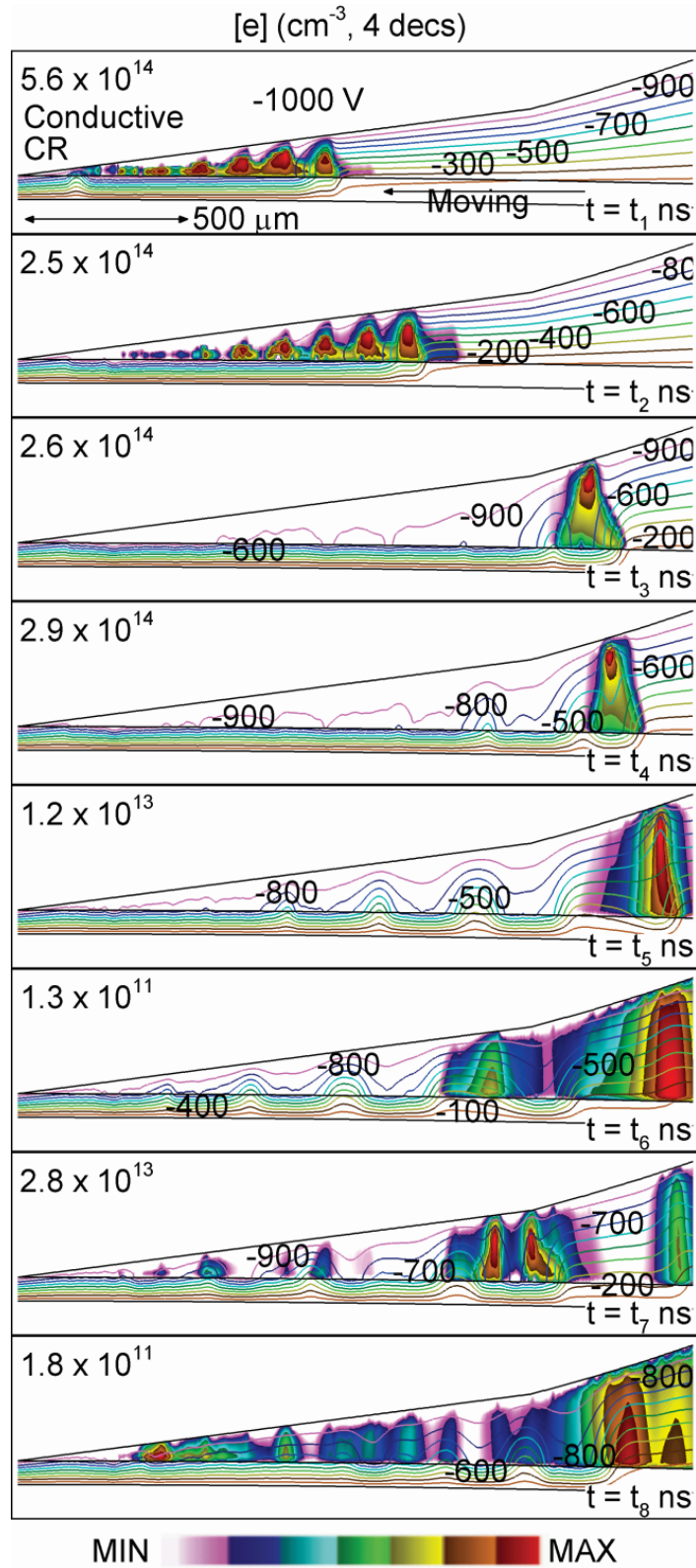


Figure 6.11 The time evolution of electron density (flood, cm^{-3}) and electric potential (contour lines, V). The discharge is re-ignited continuously by a rapidly moving surface.

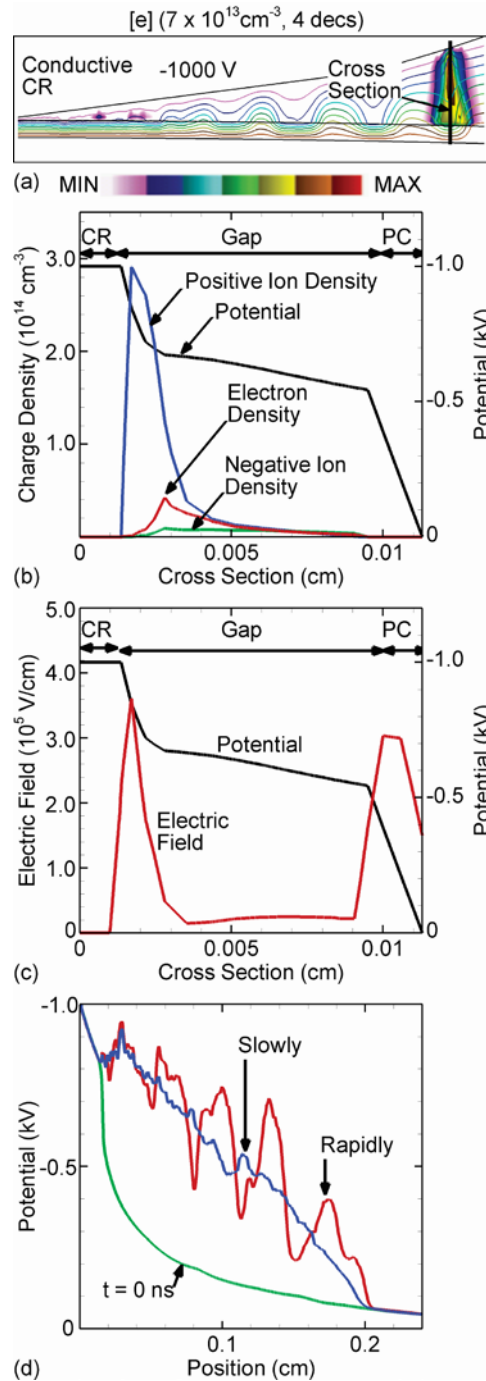


Figure 6.12 Characteristics of microplasmas and surface potential on PC dielectric at steady state. (a) The electron density (flood, cm^{-3}) and electric potential (contour lines, V). (b) The corresponding spatial distribution of electric potential and charge density over the cross section of the streamer. (c) The corresponding spatial distribution of electric potential and electric field over the cross section of the streamer. (d) The surface potential on the PC sheet before and after the steady state for a rapidly and slowly moving surface.

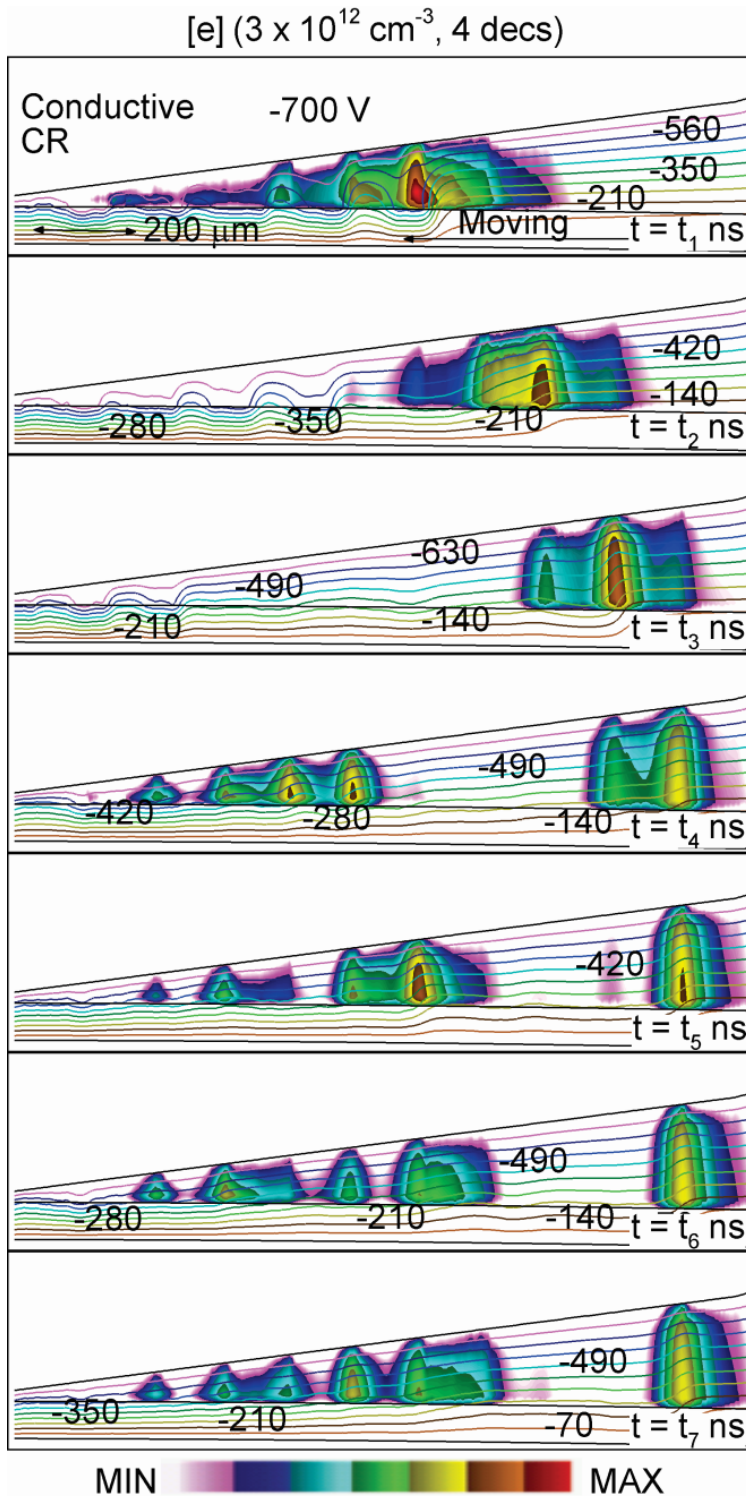


Figure 6.13 The time evolution of electron density (flood, cm^{-3}) and electric potential (contour lines, V) produced by a conductive CR biased with -700 dc voltage. The discharges of low electron density are continuously produced by lower applied voltage and seed secondary electrons.

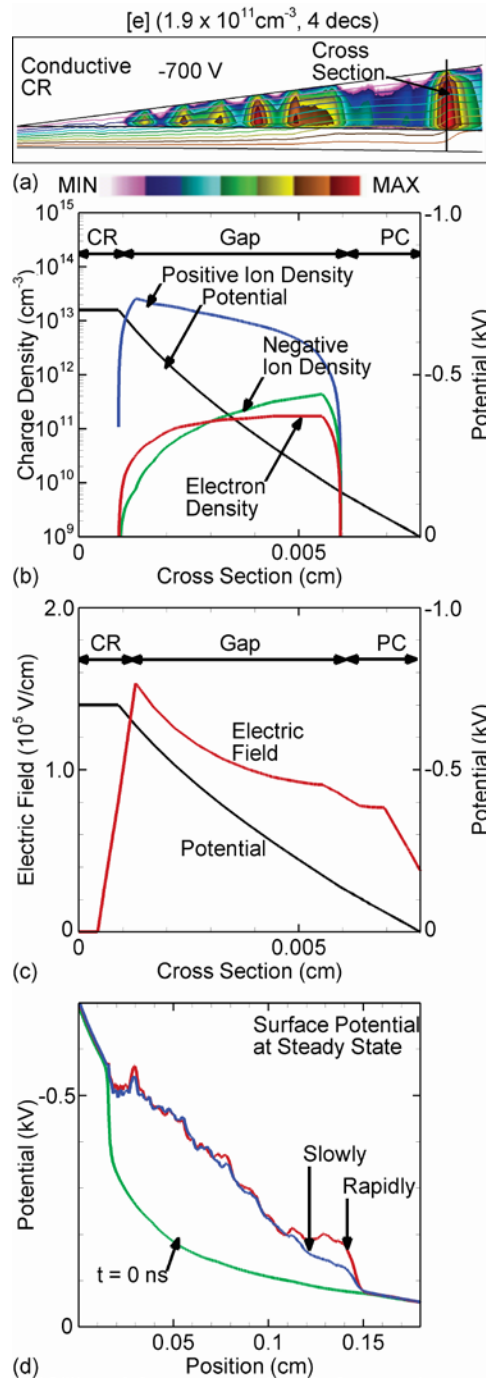


Figure 6.14 The Townsend-like discharge and quasi-constant electric field in the narrowing gap. (a) The microplasma and electric potential at steady state. (b) The corresponding spatial distribution of electric potential and the charge density over the cross section of the discharge. (c) The corresponding spatial distribution of electric potential and the electric field over the cross section of the discharge. (d) The surface potential at steady state for a rapidly and slowly moving (10 times slower) PC surface.

6.7 References

- [1] C. Penache, C. Gessner, T. Betker, V. Bartels, A. Hollaender and C.-P Klages, IEE Proc. Nanobiotechnol. **151**, 139 (2004).
- [2] S. Kreitz, C. Penache, M. Thomas, and C. -P. Klages, Surf. Coat. Technol. **200**, 676 (2005).
- [3] N. Lucas, A. Hinze, C. P. Klages and S. Büttgenbach, J. Phys. D: Appl. Phys. **41**, 194012 (2008)
- [4] J. Kurokawa, K. Nojima, N. Sohmiya, U.S. patent 5,499,078 (12 Mar 1996)
- [5] D. M. Pai and B. E. Springett, Rev. Mod. Phys. **65**, 163 (1993).
- [6] L. B. Schein, J. Vac. Sci. Technol. A **25**, 1256 (2007).
- [7] C. B. Duke, J. Noolandi, and T. Thieret, Surf. Sci. **500**, 1005 (2002).
- [8] R. M. Schaffert, *Electrophotography* (Focal Press, London, 1965).
- [9] J. S. Chang, P. A. Lawless, and T. Yamamoto, IEEE Trans. Plasma Sci. **19**, 1152 (1991).
- [10] N. J. Leoni, O. Gila, M. H. Lee and E. G. Hanson, U.S. Patent No. 7,764,296 (27 Jul. 2010).
- [11] I. Kubelik, U.S. Patent No. 5,450,103 (12 Sep. 1995).
- [12] J-C. Wang, N. Leoni, H. Birecki, O. Gila and M. J. Kushner, J. Appl. Phys. **113**, 033301 (2013).
- [13] J-C. Wang, N. Leoni, H. Birecki, O. Gila and M. J. Kushner, Plasma Sources Sci. Technol. **22**, 025015 (2013).
- [14] M. K. Tse and I. Chen, *IS&T's NIP14: International Conference on Digital Printing Technologies: Final Program and Proceedings, October 18-23, 1998, Toronto, Ontario, Canada* (IS&T, 1998).
- [15] H. Tanaka, M. Okunuki, U.S. Patent No. 5,089,851 (18 Feb. 1992).
- [16] H. Kawamoto, *NIP24: International Conference on Digital Printing Technologies:*

*September 6 – 11, 2008, Pittsburgh, Pennsylvania: Technical Program and Proceedings:
Digital Fabrication 2008 (IS&T, 2008).*

- [17] M. Kadonaga, T. Katoh and T. Takahashi, *J. Imaging Sci. Technol.*, **43**, 274 (1999).
- [18] N. Y. Babaeva and M. J. Kushner, *J. Phys. D: Appl. Phys.* **46**, 025401 (2013).
- [19] R. Dorai, *Modeling of Atmospheric Pressure Plasma Processing of Gases and Surfaces PhD Thesis University of Illinois* (<http://uigelz.eecs.umich.edu/theses.html>).
- [20] Y. Akishev, M. Grushin, V. Karalnik, A. Petryakov and N. Trushkin, *J. Phys. D: Appl. Phys.* **43**, 215202 (2010).
- [21] J.-C. Wang, D. Zhang, N. Leoni, H. Birecki, O. Gila and M. J. Kushner, “Charging of moving surfaces by corona discharges sustained in air”, submitted to *J. Appl. Phys.*
- [22] F. Massines, P. Segur, N. Gherardi, C. Khamphan and A. Ricard, *Surf. Coat. Technol.* **8**, 174 (2003).
- [23] Y. B. Gulubovskii, V. A. Mairorv, J. Behnke and J. F. Behnke, *J. Phys. D: Appl. Phys.* **36**, 975 (2003).
- [24] F. Massines, N. Gherardi, N. Naude and P. Segur, *Plasma Phys. Control. Fusion* **47**, B577 (2005).
- [25] C. Sarra-Bournet, S. Turgeon, D. Mantovani and G. Laroche, *J. Phys. D: Appl. Phys.* **39**, 3461 (2006).
- [26] N. Osawa, Y. Yoshioka, R. Hanaoka, Y. Mochizuki, Y. Kobayashi and Y. Yamada, *Electr. Eng. Jpn.* **180**, (2012).
- [27] N. Osawa and Y. Yoshioka, *IEEE Trans. Plasma Sci.* **40**, (2012).

CHAPTER 7 SIMULATION OF MICRODISCHARGE-BASED PRESSURE SENSORS

7.1 Introduction

The microscale pressure sensor is one of the earliest demonstrations of the micromachining technologies that have been successfully developed and widely used for biomedical [1-4] and industrial [5-8] applications in the past four decades.[9-11] Among all of the pressure sensor principles, the most commonly used schemes are piezoresistive [1,3,5] and capacitive [2,4,6-8] methods. These two approaches form the basis of the vast majority of microscale pressure sensors.

For a piezoresistive pressure sensor, piezoresistors having a few millimeters in diameter are generally mounted at specific locations (usually on the edge) of an edge-supported diaphragm or cantilevers where the stress variation is at a maximum. When the diaphragm deforms as a result of the pressure difference between the applied ambient pressure and the pressure in the sealed chamber, the stress of the diaphragm changes the electrical resistivity of the embedded piezoresistors. By measuring the resistivity of the piezoresistors (i.e., the stress of the diaphragms), the transverse pressure across the diaphragm (or the external pressure applied to the sensor) can be detected. The piezoresistive approach is attractive due to the simplicity of the structure (i.e., fabrication process) and the readout circuitry, since the resistive circuits generate a low output-impedance voltage. This “piezoresistivity effect” provides an easy and direct energy transduction mechanism between the mechanical and electrical signals.

Similar to the piezoresistive pressure sensor, this edge-supported flexible diaphragm is also an essential feature in a capacitive pressure sensor. Instead of measuring the stress of a deflected diaphragm, the displacement of the diaphragm deformed by external pressure is capacitively measured by another parallel electrode located on a substrate below the diaphragm in capacitive pressure sensors. As the external pressure varies, the diaphragm electrode deflects in response to the applied pressure and the averaged gap (or capacitance) between two electrodes changes; the applied pressure is then detected according to the capacitance variation. The main advantage of the capacitive method is the simplicity of structure, the high sensitivity to the external pressure, low temperature dependence, good noise performance, and decreased power dissipation.

Although piezoresistive and capacitive methods are conceptually simple, commercially available, and have been well studied by the MEMS research community, a pressure-sensing solution for extreme, hostile environments using both conventional approaches is still limited by its intrinsic nature.[7,11-12] For example, in a borehole environment for oil/gas extraction, the temperature can be several hundred degrees (°C), and the maximum pressure can be several to several hundred megapascals. The size of the device volume also has very tight constraints.[12] In such hostile environments, both methods do have challenges (e.g., strong temperature dependence, highly attenuated output signal, and intensified noise due to the reduced size), which motivates a new pressure-sensing solution.

Recently, a new pressure-sensing solution based on microdischarge has been proposed by Yogesh et al.[12-15] The microdischarge-based pressure sensors generally have three electrodes with two competing cathodes and one anode. One of the cathodes is attached to a flexible diaphragm. Microplasmas are then produced between biased electrodes in a sealed chamber filled with atmospheric pressure inner gas to avoid the production of negative ions and to prevent the

input power from being wasted in exciting the lower energy states. Argon is usually used in the chamber due to its low operating voltage and cost. When the sensor is subjected to an external pressure, the external pressure deflects the diaphragm and the attached cathode. As a result, the current produced by the microplasma between biased electrodes is redistributed due to the changing of inter-electrode spacing and internal pressure. A differential current defined by the current collection on the competing cathodes is indicative of the diaphragm deflection determined by the external pressure.

Microdischarge-based pressure sensors are attractive due to their potential advantage of operating in harsh environments with high temperature and tight constraints for the device volume. Since the electron temperature in microplasma has an average thermal energy of a few eV (1 eV \approx 11,600 K), the current collection and plasma behavior are not sensitive to the ambient temperature.[16-17] In addition, the current produced by microplasma is larger compared to devices using conventional piezoresistive and capacitive methods. The large inherent current reduces the complexity of the interface circuits, and eliminates the need for current amplification. As a result, the microdischarge-based device can be much smaller in area than the smallest capacitive and piezoresistive pressure sensors that have been reported.[12]

In this chapter, I present the results of a numerical investigation of current collection and plasma properties in a microdischarge-based pressure sensor sustained in atmospheric-pressure argon. The model geometry of the pressure sensor, shown in Fig. 7.1, is patterned after those proposed for pressure sensing. I found that after electron avalanches at the corners of an anode where the electric field is geometrically enhanced, a highly conductive plasma is generated between an anode (A) and a sensing cathode (K_2). The plasma also brings anode voltage to the reference cathode (K_1) and triggers a repetitive ionization wave (IW) propagating along A- K_1 . The

plasma sustained on both cathodes and the periodic IWs provide a pulse-modulated dc current collected on the cathodes. The current distribution on K_1 and K_2 varies with inter-electrode spacing (A- K_2) and can be optimized by adjusting the impedance connected to the electrodes.

The model used in this chapter is described in Sec. 7.2 and followed by a discussion of Ar plasma dynamics sustained in a discharge-based pressure sensor in Sec. 7.3. In Sec. 7.4, repetitive ionization waves and the current collection on cathodes are discussed. Differential current and the corresponding deflection of the diaphragm are discussed in Sec. 7.5. Sec. 7.6 contains our concluding remarks.

7.2 Description of the Model and Reaction Mechanism

A first principles computer model, *nonPDPSIM*, was performed in this chapter to improve the fundamental understanding and insight into the physical process in this device, and to provide design rules. *nonPDPSIM* is described in Chapter 2 and in Refs.[18-19]

The model geometry of the microdischarge-based pressure sensor device is shown in Fig. 7.1. The whole computational domain is shown in Fig. 7.1(a); the undeflected microdischarge chamber with a 10- μm gap is shown in Fig. 7.1(b) with its vertical scale expanded by a factor of 2 for clarity. A chamber with a 7- μm gap is shown in Fig. 7.1(c) as a deflection example. The circuit legs of three electrodes (A, K_1 , and K_2) are embedded in a glass with a dielectric constant of $\epsilon/\epsilon_0 = 3.9$. The anode (A) is adjacent to a reference cathode (K_1), and a sensing cathode (K_2) is attached to a diaphragm and separated from the anode by a microdischarge chamber. The exposed electrodes of the reference cathode (K_1) and anode (A) are 35 μm wide and 1 μm in thickness in the microdischarge chamber. The sensing electrode (K_2) with an exposed area that is 35 μm wide is directly under the anode and is separated by a 10- μm gap. The cathodes are grounded, and the

anode is biased with a 400 V dc potential. Ballast resistors of a few hundred ohms are connected to the electrodes to control the plasma behavior and current shape. A dc voltage pulse applied to the electrodes initiates a microdischarge between A-K₁ and A-K₂. When the sensor is subjected to an external pressure, the diaphragm deforms according to the pressure and changes the A-K₂ spacing, while the A-K₁ spacing remains unaffected. The changing of inter-electrode spacing then redistributes the spatial current I_{K1} and I_{K2} collected on K₁ and K₂, respectively. To reduce the pulse-to-pulse variation caused by plasma dynamics and material properties, a differential current $(I_{K2}-I_{K1})/(I_{K2}+I_{K1})$ is used as an index of external pressure.

In this chapter, the discharge is initiated with an emission current of 10^{-2} A-cm⁻² for 10 ns from the corners of 2 cathodes. The microdischarge chamber is filled with atmospheric pressure Ar at 300 K. A reduced reaction mechanism contains a subset of the Ar plasma chemistry described in A. N. Bhoj et al. [20] to reduce the magnitude of the computation. The species in the model are Ar, Ar^{*}, Ar^{**}, Ar⁺, Ar₂^{*}, Ar₂⁺, and electrons. Ar is the ground state (3s²3p⁶). The lowest excited state Ar^{*} is the Ar(3p⁵4s), which is a mix state of metastable states [Ar(1s₅), Ar(1s₃)] and radiative states [Ar(1s₄), Ar(1s₂)]. Higher excited states (Ar(3p⁵4p) or higher) are lumped into Ar^{**} states. Ar₂^{*} and Ar₂⁺ are the dimer excited state and dimer ion produced through three-body collision that is significant at atmospheric pressure. There are 7,723 computation nodes in the mesh, of which 4,025 nodes are in the plasma zone. The finest resolution of the mesh in the plasma zone is from 0.6 to 0.8 μm. Although the underlying unstructured mesh used in this investigation is static—it does not evolve during the computation—the deflection of the diaphragm and its corresponding differential current as a function of external pressure can be modeled by a series of calculations with different deformations of the diaphragm. Although the original device is a 3D design [12], our model, being 2D, resolves structure in a Cartesian geometry.

7.3 Plasma Dynamics in the Microdischarge Pressure Sensor

The characteristics of microdischarge in the chamber with a 10- μm gap (see Fig. 7.1(a)–(b)) will first be discussed. The reference (K_1) and sensing cathode (K_2) are grounded, and the anode (A) is biased with a 400 V dc voltage. A 500- Ω and two 100- Ω ballast resistors are connected to the anode and two competing cathodes (K_1 and K_2) to limit the current and so prevent arcing. The time evolution of electron density and electric potential is shown in Fig. 7.2. The time evolution of E/N (electric field/gas number density) is shown in Fig. 7.3, and electron impact ionization sources by bulk electrons, S_e , and secondary electrons, S_{sec} , are shown in Fig. 7.4 and Fig. 7.5, respectively.

The discharge is initiated with an electron current emission of 10^{-2} A-cm $^{-2}$ for 10 ns from the corners of cathodes. Due to the high averaged electric field of 400 kV/cm ($E/N \approx 1,630$ Td, 1 Td = 10^{-17} V-cm $^{-2}$) in the gap between anode (A) and sensing electrode (K_2), the electron avalanche occurs by $t = 1$ ns, and peaks at the corner of the anode where the electric field is geometrically enhanced. Ionization on the order of 10^{20} to 10^{21} cm $^{-3}$ s $^{-1}$ is provided by low-energy bulk electrons, S_e , and high-energy beam-like secondary electrons, S_{sec} , emitted from the cathodes produced by ion bombardment. Photoemission and photoionization are insignificant in the Ar plasma system. At this time, the peak electron density on the order of 4×10^9 cm $^{-3}$ does not significantly perturb the applied potential and electric field inside the chamber. After the avalanche, the bulk plasma becomes conductive and then shields the electric field and reduces E/N. The peak electron density at mid-gap is up to 10^{16} cm $^{-3}$ at $t = 7$ ns, and the corresponding local E/N drops to 500 Td. The conductive plasma transfers the anode potential to the sensing cathode (K_2) and fully forms the sheath. This high potential-drop at K_2 then produces intense electron impact ionization as high as

$2 \times 10^{24} \text{ cm}^{-3} \text{ s}^{-1}$ by sheath-accelerated secondary electrons, S_{sec} , and peaks at sensing cathode K_2 . At this time, the electron ionization source by bulk plasma, S_e , is comparable with S_{sec} . Since the reference cathode (K_1) is adjacent to the anode and separated by a 10- μm gap, the highly conductive plasma also transfers anode voltage to K_1 and forms a high voltage-drop between A- K_1 . The E/N between A- K_1 peaks at the corner of K_1 due to the geometrical enhancement. As the discharge proceeds, the positive ion flux laterally transports toward K_1 and produces secondary electrons from the edge of K_1 . By $t = 17 \text{ ns}$, the ionization source between A- K_1 by secondary electrons emitted from K_1 (S_{sec}) accelerated by the sheath potential at the edge of K_1 starts to trigger a bullet-like ionization wave (IW) propagating laterally to its left and thus stretching the local plasma between A- K_2 to reference cathode K_1 . The IW sustained by both S_e and S_{sec} is mainly seeded by field emission and secondary electrons emitted from K_1 since the photoionization and photoemission are insignificant in Ar plasma. Within 20 to 30 nanoseconds, the plasma channel produced by the first IW covers K_1 and then stops propagating at the left edge due to the absence of emitting seed electrons ahead of the plasma channel.

As the bullet-like IW propagates along K_1 , the plasma channel becomes less conductive. The local E/N and electron temperature, T_e , then increase to trigger the next IW bullet. A time evolution of the line profile of the ionization source by bulk plasma, S_e , along the mid-gap is shown in Fig. 7.4 (b). As the first IW bullet propagates to the left edge of K_1 at $t = 34 \text{ ns}$, the electron density in the plasma channel between A- K_1 drops to $3 \times 10^{14} \text{ cm}^{-3}$. The local peak E/N rebounds to 100 Td and starts to initiate a second bulk ionization source of $4 \times 10^{23} \text{ cm}^{-3} \text{ s}^{-1}$. The second S_e bullet increases in amplitude during the propagation along K_1 and then eventually two IW bullets merge within 10 to 20 nanoseconds. This process repeats and produces periodic bullet-like ionization waves propagating along reference cathode K_1 .

7.4 Periodic IW and Current Collection

As the periodic IW bullets laterally propagate to reference cathode K_1 , positive charges generated by IW transport to K_1 , which then increases positive current collection, I_{K1} , and voltage on K_1 through the ballast resistor. Microplasma sustained between A- K_2 also produces a positive current, I_{K2} , collected by sensing cathode K_2 . Although the bullet-like peak electron density (shown in Fig. 7.2) follows the IW front to reference cathode K_1 , the electron flux actually flows to the opposite direction and is collected by the anode (A). The electron current, I_A , collected by the anode reduces the voltage drop between A- K_2 through the ballast resistor, and then decreases the ion current collection on sensing electrode K_2 . For example, the periodic steady-state current collection on both cathodes, as well as a time evolution of electron density, is shown in Fig. 7.6 to demonstrate the plasma dynamics and the corresponding IV trace. At $t = t_1$, two IW bullets at K_1 produce a peak positive ion current in I_{K1} . A high electron flux transports to the anode reducing the voltage drop between A- K_2 and the current collection, I_{K2} . As the two bullets merge by $t = t_3$, fewer positive charges (electrons) are collected on K_1 (A), the voltage drop between A- K_2 rebounds, and then I_{K1} (I_{K2}) decreases (increases). At this time, the electron density drops between A- K_1 , and the rebound local E/N then triggers the third IW bullet. At $t = t_4$ the third bullet starts to propagate to K_1 , which increases I_{K1} and reduces I_{K2} . Before the third bullet merges at K_1 , the fourth bullet is generated between A- K_1 and starts to propagate by $t = t_6$. The fourth bullet further increases the I_{K1} and decreases I_{K2} . This ionization process repeats to generate periodic IW bullets and a pulse-modulated positive dc current on K_1 and K_2 . During the ionization process and IW propagation, the dc current on the cathode is sustained by the continuous ionization source at the cathode, and the pulsed current is produced by the repetitive bullet-like ionization waves. The

shape of the current pulse (i.e., pulse period and its amplitude) strongly depends on the location and frequency of newly generated IW bullets in the chamber. For this particular case, the period of the pulsed-modulated current is 25 to 30 ns, in which two IW bullets are generated during each pulse. Notice that the ion current, I_{K1} , is nearly 180° out of phase with I_{K2} over the period with a phase delay due to the electron/ion transition time.

The plasma dynamics and current collection can be controlled to optimize the signal output by adjusting the ballast resistors. A time series of current on the cathodes connected to three resistor sets (Ω_{Small} , Ω_{Median} , and Ω_{Large}) is shown in Fig. 7.7. After $t = 50$ ns, the currents are already in an oscillatory steady state. With a relatively small resistor set (250 Ω and 50 Ω on anode the cathodes, respectively) connected to the electrodes, pulsed-modulated dc ion currents of 0.4 Amps and 0.7 Amps are collected on the reference and sensing cathodes— K_1 and K_2 , respectively. I_{K1} is highly modulated by repetitive ionization waves while I_{K2} seems to be less fluctuated because the smaller resistor on the anode cannot significantly change the voltage drop between A- K_2 . By doubling the resistance to a median resistor set (500 Ω and 100 Ω on anode the cathodes, respectively), the currents are reduced by half—only 0.2-Amp and 0.4-Amp ion currents are collected by K_1 and K_2 , respectively. Both I_{K1} and I_{K2} are highly modulated by the bullet-like ionization waves, and the currents are nearly 180° out of phase with a small phase delay. Over the range of resistance investigated from small to median resistor sets, the plasma dynamics does not dramatically change: after electron avalanches a conductive plasma transfers the anode voltage to the cathodes, and the periodic bullet-like IWs are then generated and produce pulsed-modulated dc currents on the cathodes. However, as the resistance of the ballast resistor is increased to a large resistor set, the plasma density between A- K_2 drops and the plasma becomes less conductive. The electron density at steady state in the chamber connected with the large resistor set is shown

in Fig. 7.7(b). This less conductive (or more resistive) plasma cannot fully transfer the anode voltage to the reference cathode and so cannot create an intense ionization source between A-K₁. As a result, the microdischarge sustained by the anode and sensing cathode K₂ does not extend to cover K₁, and the bullet-like IWs are not triggered to provide the pulsed currents. A pure dc ion current is then collected by sensing cathode K₂, and the ion current on K₁ is almost zero.

7.5 Differential Current and External Pressure

When the microdischarge-based pressure sensor is subjected to an environment with external pressure, the diaphragm attached to sensing cathode K₂ deforms due to the difference between the internal chamber pressure and the external applied pressure. The deflection of the diaphragm increases (or A-K₂ spacing decreases) with external pressure, while A-K₁ spacing remains unaffected. As a result, the changing of inter-electrode spacing redistributes the current I_{K1} and I_{K2} collected on reference electrode K₁ and sensing electrode K₂. Having said that, the output signals of I_{K1} and I_{K2} are not directly used to measure the changing of inter-electrode spacing due to the pulse-to-pulse variation caused by noise, plasma dynamics, and material properties; a differential current $(I_{K2} - I_{K1})/(I_{K2} + I_{K1})$ is used as an index of external pressure.

Given that the underlying unstructured mesh used in the model does not evolve during the calculation, the deformation of the diaphragm as a function of external pressure and its corresponding current collection are modeled by a series of computations with different deflections of the diaphragm in this investigation. The internal chamber pressure also increases with deflection of the diaphragm in the model, assuming that $P \times V$ is a constant where P and V are internal pressure and volume in the discharge chamber, respectively. The time series of current collection on cathodes (I_{K1} and I_{K2}) and its differential current $(I_{K2} - I_{K1})/(I_{K2} + I_{K1})$ for deflection

up to 3 μm is shown in Fig. 7.8. As the diaphragm is deformed by the external pressure, the changing of the inter-electrode spacing and internal pressure perturb the E/N between electrodes. The location and frequency of the generation of new IW bullets strongly depend on the local variation of E/N. As a result, the deflected diaphragm redistributes the temporal and spatial variations of current collection on each cathode, the pulse period seems to decrease with increasing, and the time series of I_{K1} is always nearly 180° out of phase with I_{K2} . Over the range of deflections investigated, the plasma dynamics does not dramatically change. The averaged differential current as a function of deflection and external pressure is shown in Fig. 7.8. The deflection of the diaphragm corresponding to external pressure (0.12 $\mu\text{m}/\text{MPa}$ or 0.012 $\mu\text{m}/\text{atm}$) is obtained using Electrostatic Finite Element Analysis (FEA) performed with COMSOL assuming that a 5 μm thick diaphragm is attached to sensing cathode K_2 . [12] In general, the averaged differential current decreases with increasing deflection and then rebounds after a deflection of 1.5 μm (123.3 atm. applied pressure). It is highly expected that the differential current is not a linear function of deflection since the system is too complicated (as it involves multi-time scale electron/ion behavior and the changing of inter-electrode spacing and internal chamber pressure). The phase difference between I_{K1} and I_{K2} also shifts due to the changing of the electron transition time results from the deflection of diaphragm. The “phase shift” significantly changes the pulse shape of differential current and adds another nonlinearity to the signal output as the diaphragm deforms. Having said that, the device of interest is demonstrated to be feasible in measuring the external pressure, and an operating regime of 123.3 atm. is computationally obtained in this investigation.

7.6 Concluding Remarks

A microdischarge-based pressure sensor has been proposed for harsh environments with high ambient temperature and tight constraints for device volume. I computationally investigated the behavior of microplasma in the discharge chamber and current collection on the competing cathodes. I found that, following the electron avalanche in the geometrically enhanced electric field at the edge of the anode, a conductive plasma is generated within tens of nanoseconds. The microplasma transfers the anode voltage to sensing cathode K_2 , creating a high-voltage sheath and an intense electron impact ionization source that provides an ion current I_{K2} . Meanwhile, the conductive plasma creates a high voltage-drop between A- K_1 . The secondary electrons and field emission from reference cathode K_1 accelerated by the large potential at A- K_1 help trigger a bullet-like ionization wave propagating to K_1 . As the plasma channel along A- K_1 becomes less conductive, the local voltage and E/N rebounds and creates a new ionization bullet propagating to its left. The process repeats to generate periodic bullet-like ionization waves (IWs) and a pulse-modulated dc current on cathodes. The current shape can be optimized by adjusting the ballast resistor connected to the electrodes. As the resistance exceeds a critical value, the IW cannot be triggered and hence only a dc current can be collected on K_2 . I also found that the current collection varies with inter-electrode spacing (A- K_2) that is changed by the deflection of the diaphragm due to the external pressure; generally the differential current decreases with increasing deflection and then rebounds at a 1.5- μm deflection. Since I_{K1} and I_{K2} are nearly 180° out of phase, which adds another complexity to the differential current, a smaller resistor on the anode might be preferable.

In summary, this chapter aims at understanding the plasma dynamics, transport of charge species and current collection in the microdischarge-based pressure sensors. It was demonstrated by the simulation results that the differential current used as an index of external pressure varies

with deflection of the diaphragm. Although it does not monotonically changes with deflection due to the nonlinearity and phase difference between currents on both cathodes, it provides design rules for new device. For example, two-competing-anodes should be used in the new device instead of two-competing-cathodes to avoid the phase difference between current collections.

7.7 Figures

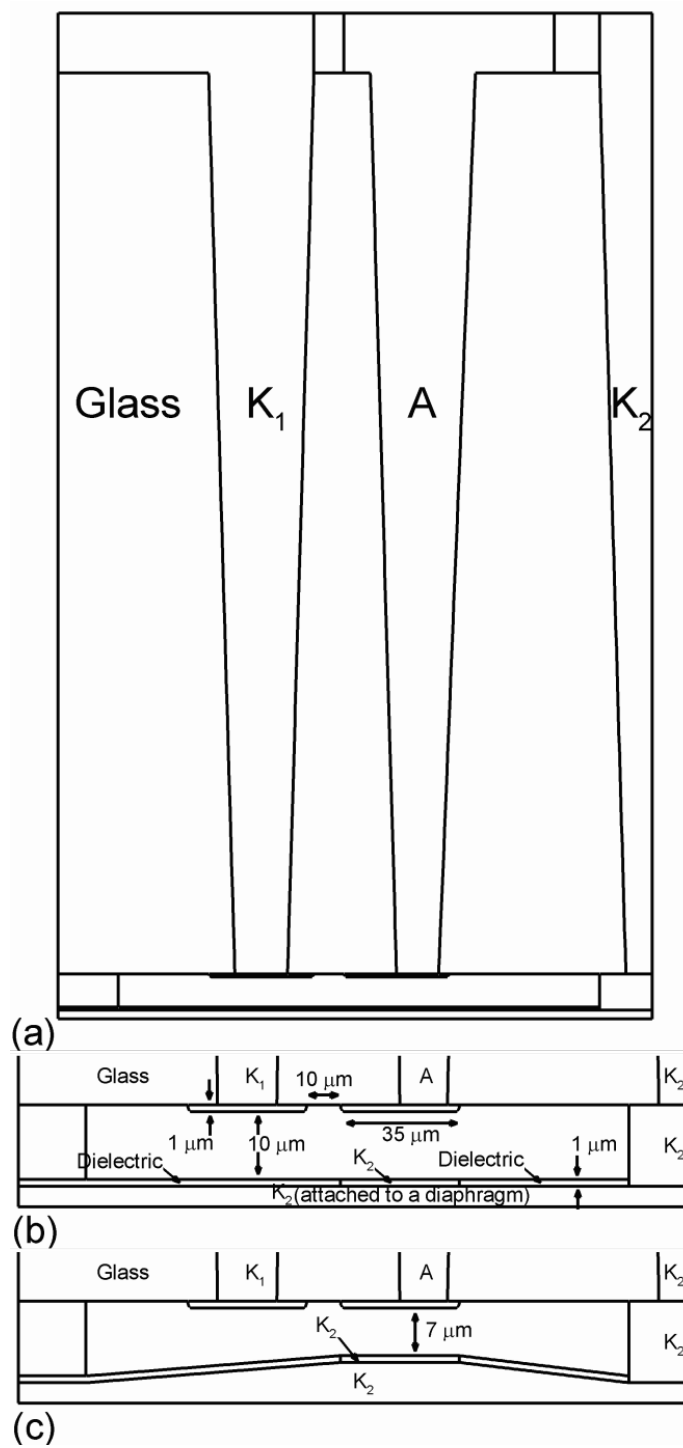


Figure 7.1 Schematic of the microdischarge-based pressure sensor device. (a) The whole computational domain. (b) The deflected microdischarge chamber with a 10- μm gap. (c) A deflection example of a discharge chamber with a 7- μm gap (i.e., 3- μm deflection). The vertical scale for Fig. 7.1(b) and 7.1(c) is expanded by a factor of 2 for clarity.

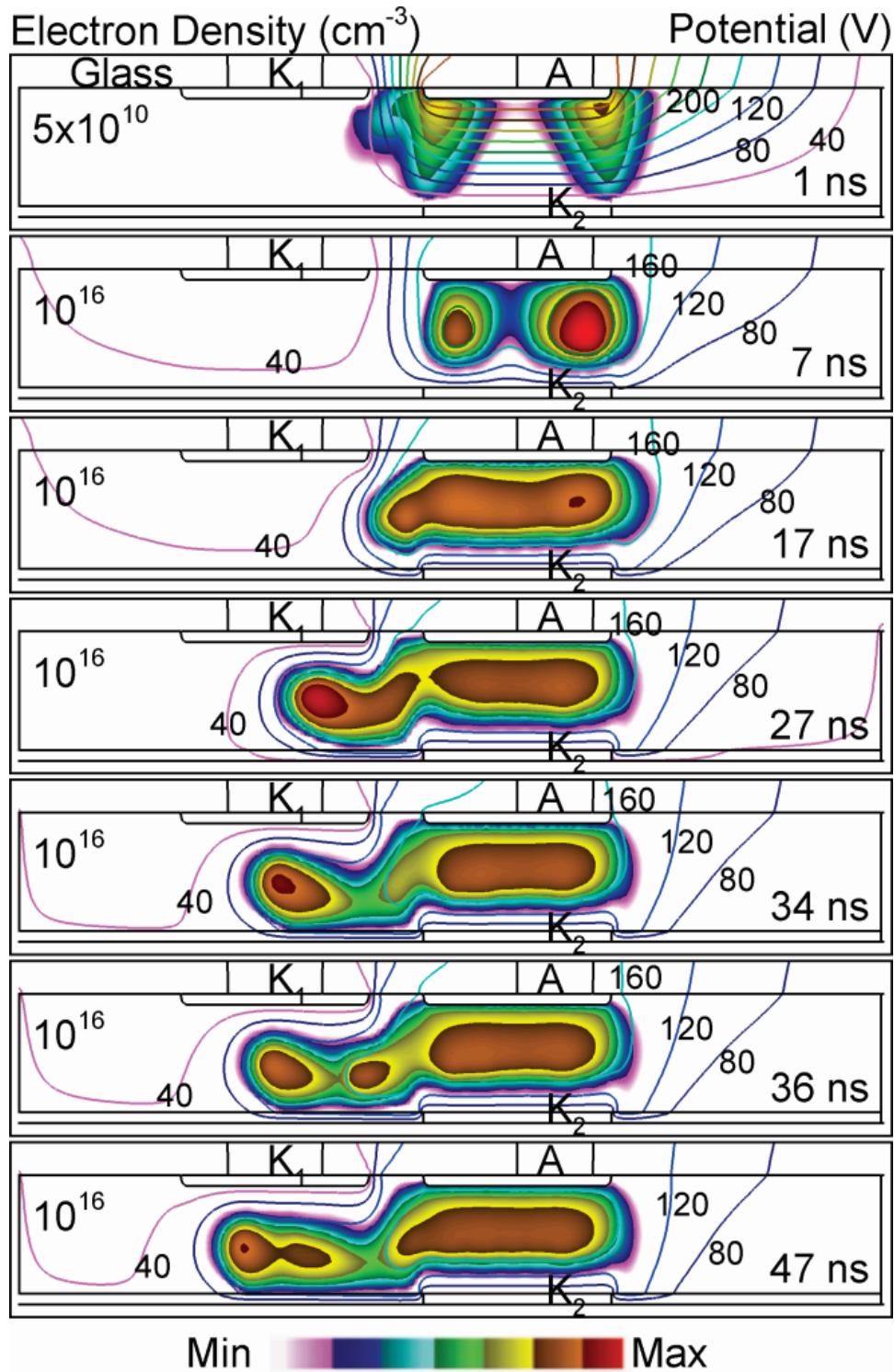


Figure 7.2 Time evolution of electron density (color flood, cm^{-3}) and electric potential (contour lines, V) produced by a 400 V dc-biased anode in the microdischarge-based pressure sensor. The electron density is plotted on a log-scale over 4 decades. The density shown on the left in the figures is the maximum level of electron density.

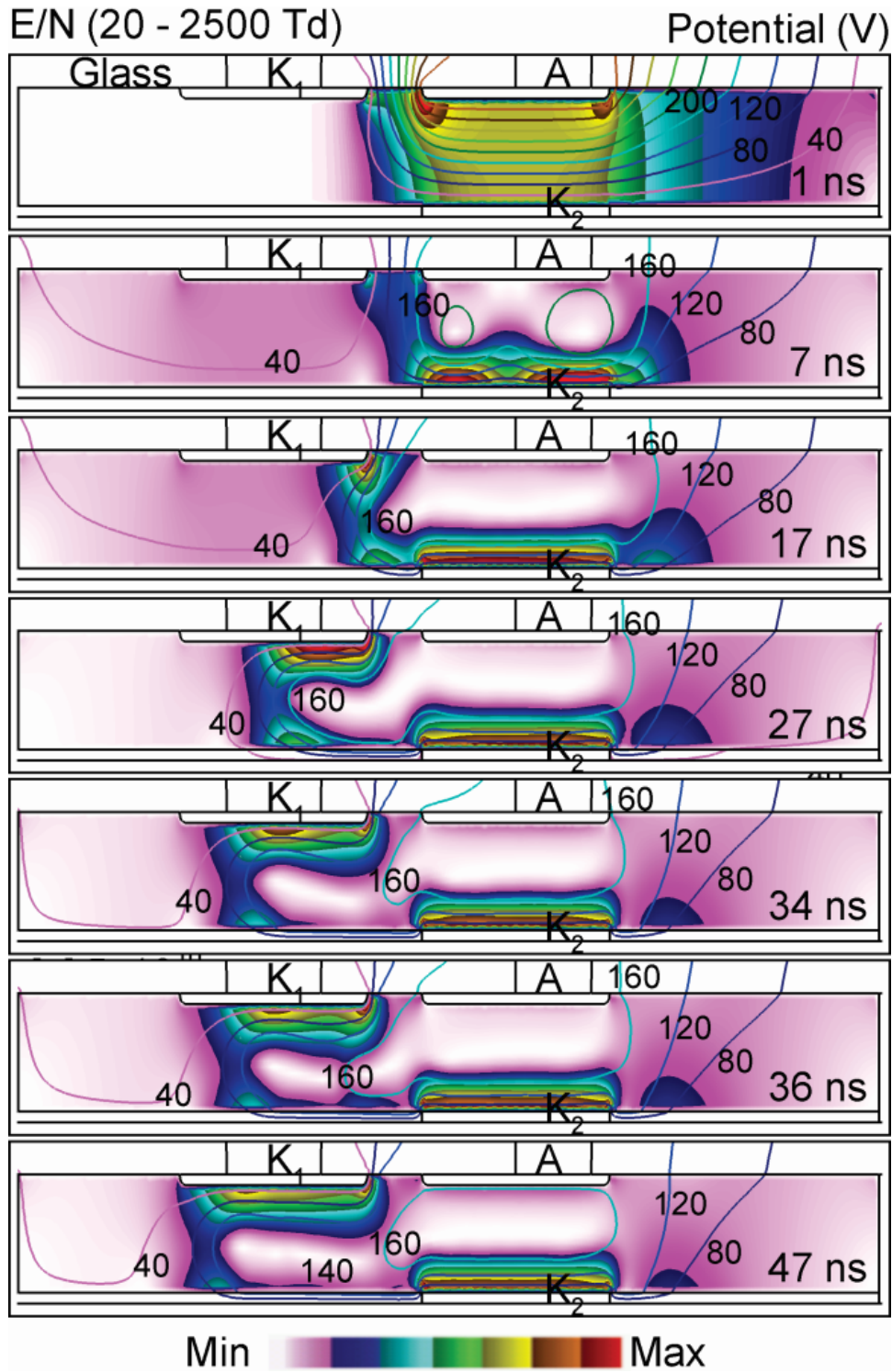


Figure 7.3 Time evolution of E/N (color flood, Td) and electric potential (contour lines, V) produced by a 400 V dc-biased anode in the microdischarge-based pressure sensor. The E/N (Td) is plotted on a linear scale from 20 to 2,500 Td.

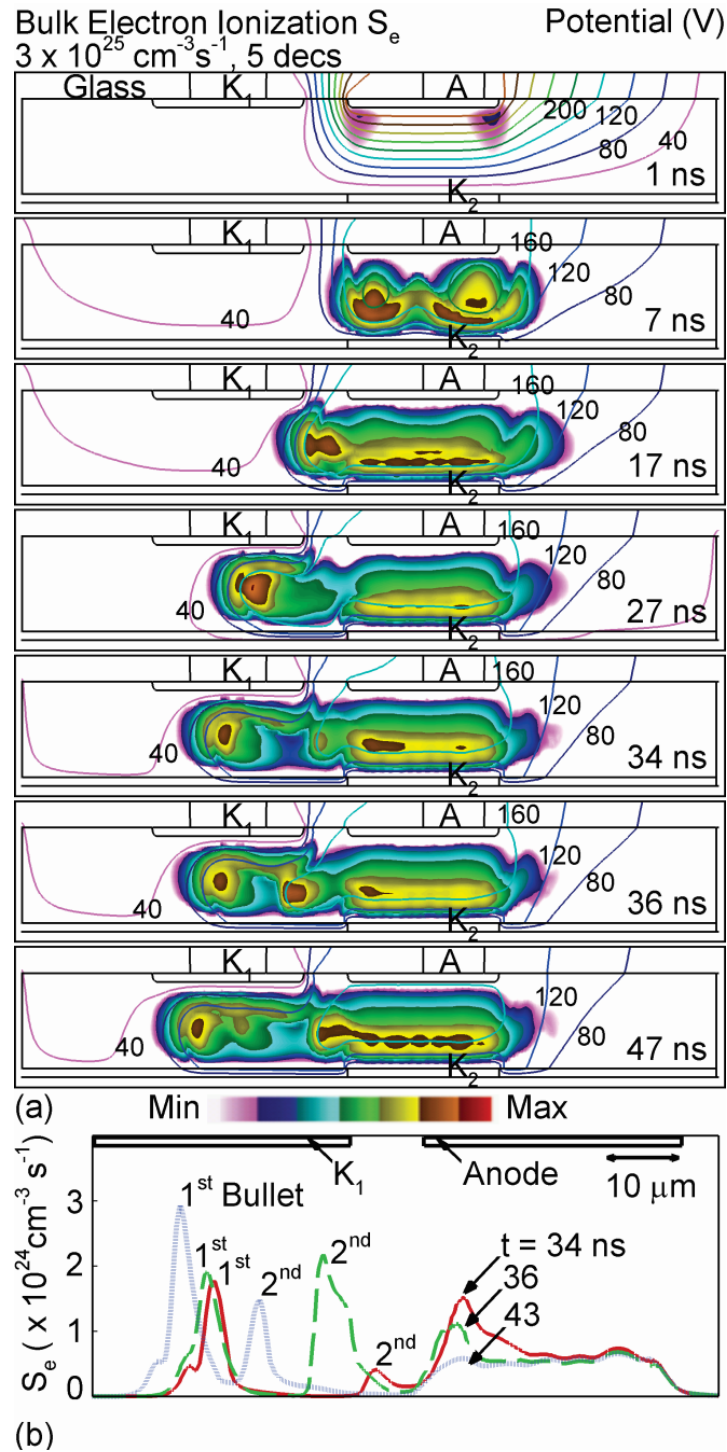


Figure 7.4 Electron impact ionization from bulk electrons (S_e). (a) The time evolution of electron impact ionization S_e (color flood, $\text{cm}^{-3} \text{ s}^{-1}$) and electric potential (contour lines, V). The ionization source is plotted on a log-scale over 5 decades. (b) A line plot of ionization source S_e at mid-gap in the chamber at $t = 34 \text{ ns}$, 36 ns , and 43 ns . Bullet-like ionization waves propagate to the left.

Secondary Electron Ionization S_{sec} Potential (V)
 $3 \times 10^{25} \text{ cm}^{-3} \text{ s}^{-1}$, 5 decs

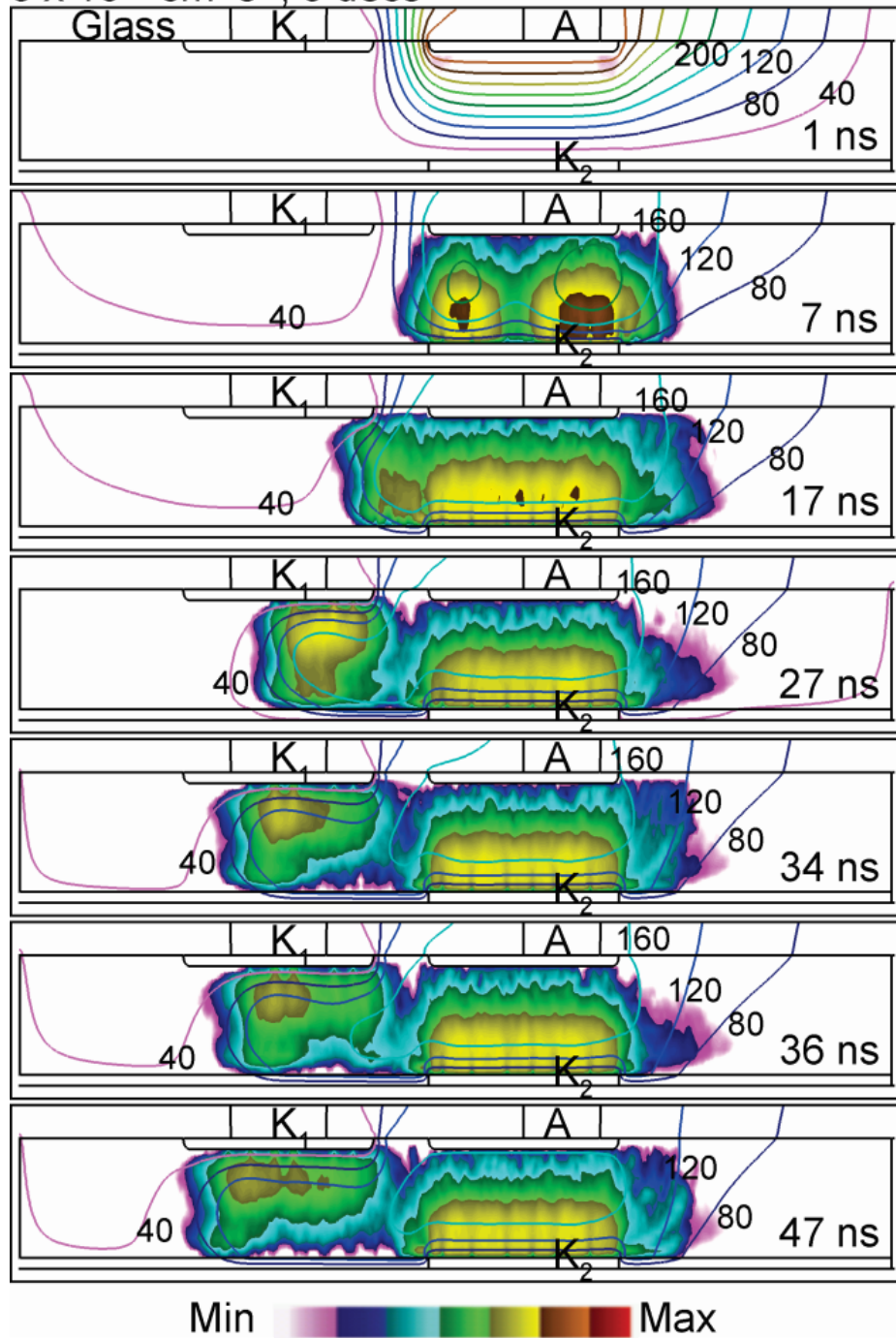
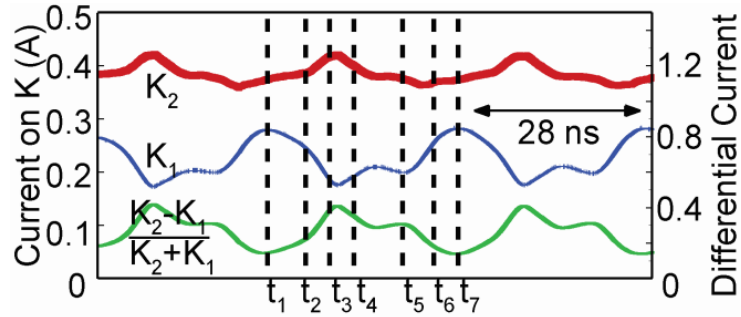
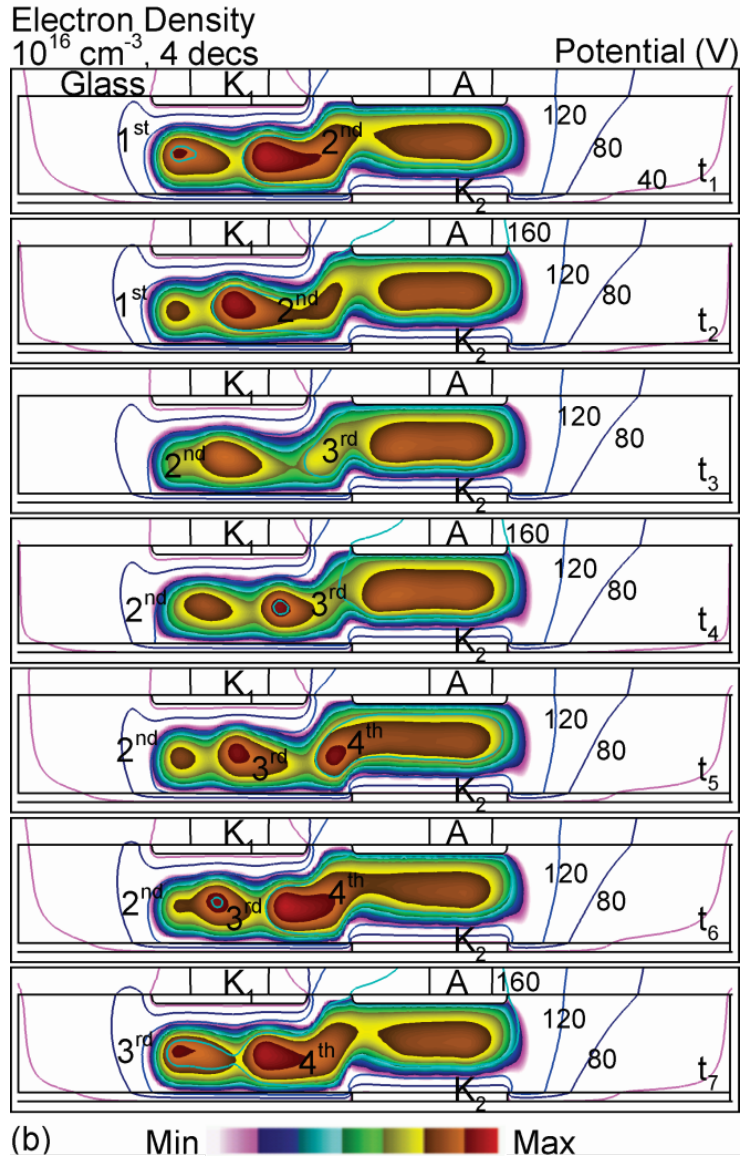


Figure 7.5 The time evolution of ionization by secondary electrons S_{sec} (color flood, $\text{cm}^{-3} \text{ s}^{-1}$) and electric potential (contour lines, V). The ionization source is plotted on a log-scale over 5 decades. The secondary electrons emitted from K_1 help trigger the ionization waves between A- K_1 .



(a)



(b)

Figure 7.6 The periodic steady-state current collection and its corresponding electron density. (a) I_{K1} , I_{K2} , and their differential current as a function of time. (b) A time evolution of electron density (color flood, cm^{-3}) and electric potential (contour lines, V). The electron density is plotted on a log-scale over 4 decades.

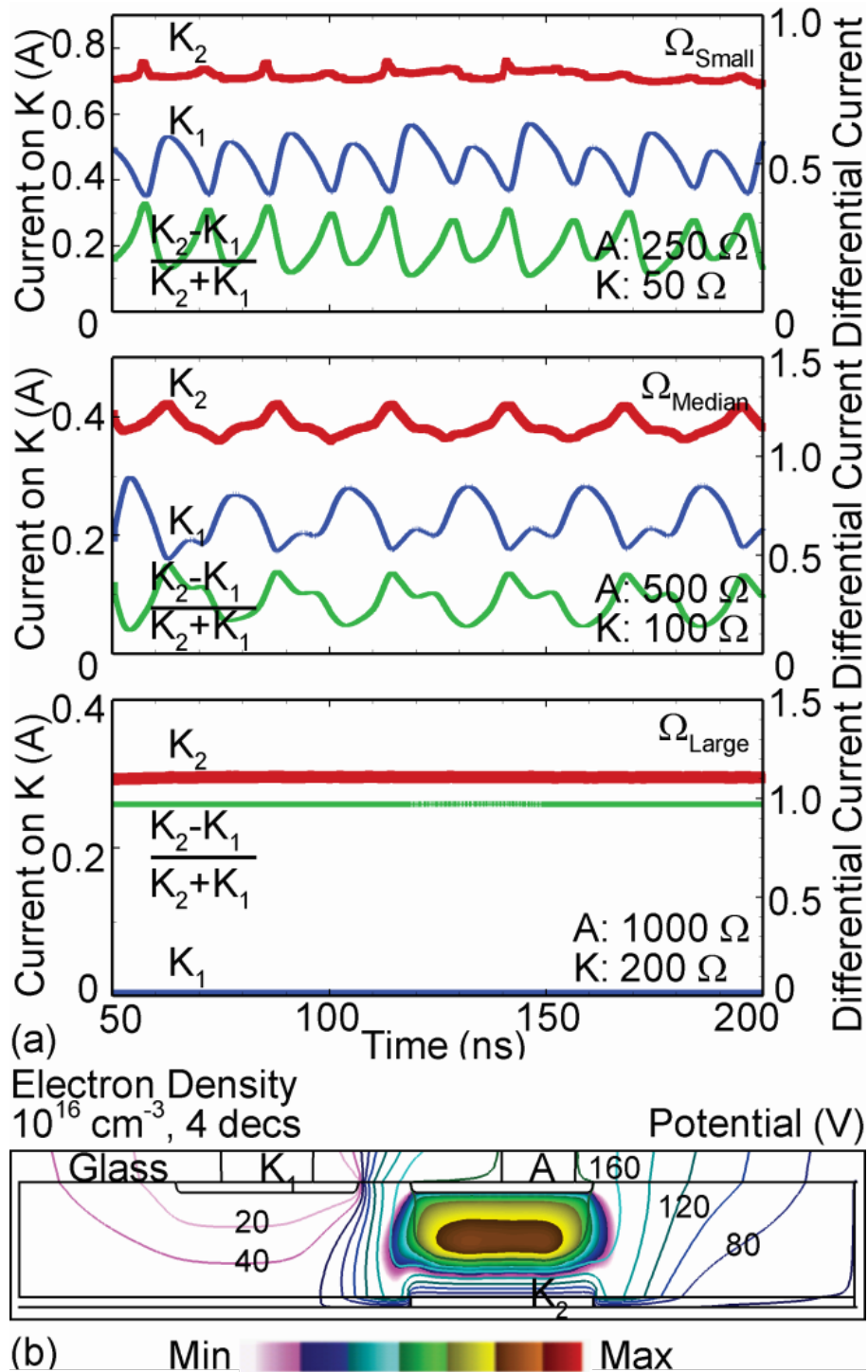


Figure 7.7 The current collection and plasma dynamics can be shaped to optimize the signal output by adjusting the ballast resistor. (a) A time series of current collected on the cathodes connected to three resistor sets (Ω_{Small} : 250 Ω on the anode and 50 Ω on cathodes; Ω_{Median} : 500 Ω on the anode and 100 Ω on cathodes; Ω_{Large} : 1,000 Ω on the anode and 200 Ω on cathodes). (b) Electron density at steady state sustained by electrodes connected to Ω_{Large} .

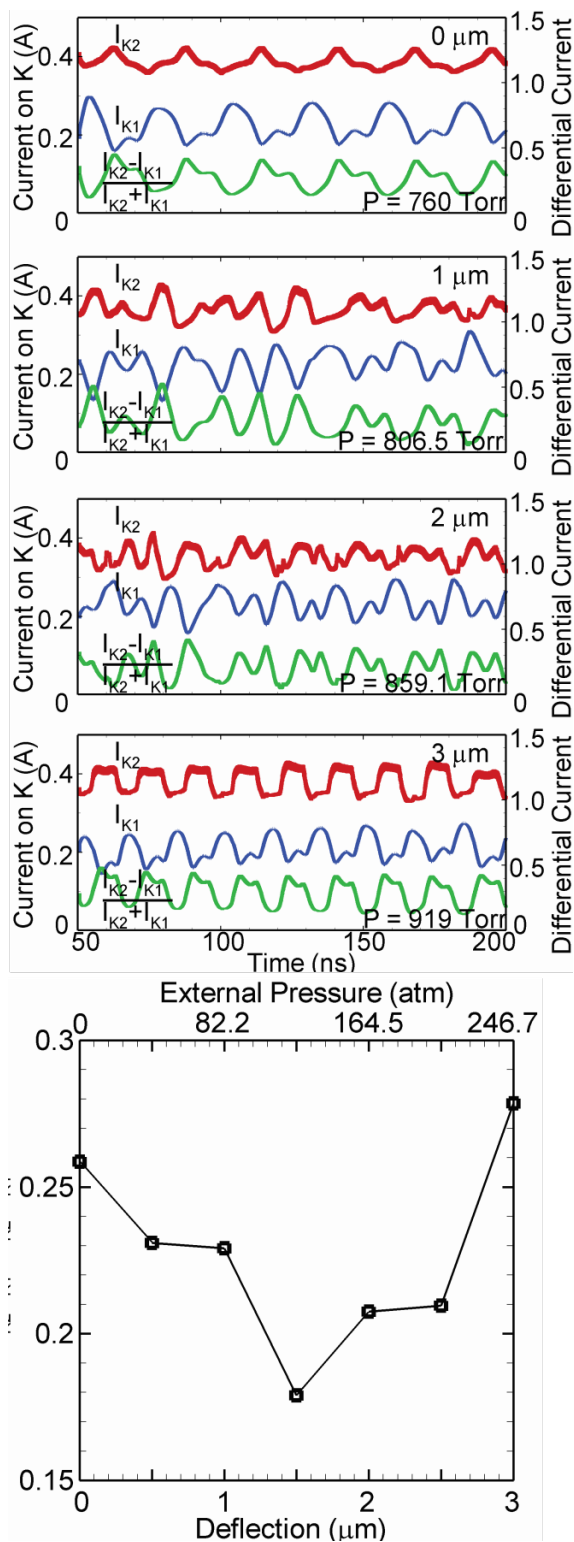


Figure 7.8 The time series of current collection on cathodes (I_{K1} and I_{K2}) and its differential current $(I_{K2} - I_{K1}) / (I_{K2} + I_{K1})$ for deflection up to $3 \mu\text{m}$. The external applied pressure (atm.) corresponding to the deflection is shown on the top x-axis.

7.8 References

- [1] W. H. Ko, J. Hyncek and S. F. Boettcher, *IEEE Trans. Electron Devices*, **26**, 1896 (1979).
- [2] A. Ginggen, Y. Tardy, R. Crivelli, T. Bork and P. Renaud, *IEEE Trans. Biomed. Eng.* **55**, 1374 (2008).
- [3] K. H. Kim, B. H. Kim and Y. H. Seo, *J. Micromech. Microeng.* **22**, 035022 (2012).
- [4] K. Takahata, Y. B. Gianchandani, and K. D. Wise, *J. Microelectromech. Syst.* **15**, 1289 (2006).
- [5] S. Sugiyama, M. Takigawa and I. Igarashi, *Sensors and Actuators* **4**, 113 (1983).
- [6] M. A. Fonseca, J. M. English, M. V. Arx and M. G. Allen, *J. Microelectromech. Syst.* **11**, 337 (2002).
- [7] D. J. Young, J. Du, C. A. Zorman and W. H. Ko, *IEEE Sensors J.* **4**, 464 (2004).
- [8] H. K. Lee, S. I. Chang and E. Yoon, *J. Microelectromech. Syst.* **15**, 1681 (2006).
- [9] Y. B. Gianchandani, C. Wilson and J.-S. Park, "Micromachined Pressure Sensors: Devices, Interface Circuits, and Performance Limits," in *The MEMS Handbook*, ed: M. Gad-el-Hak, CRC Press, 2006, pp. 3.1–3.44.
- [10] C. Liu, *Foundations of MEMS*, 1st edition, (2005).
- [11] N. Yazdi, F. Ayazi and K. Najafi, *Proc. IEEE* **86**, 1640 (1998).
- [12] C. K. Eun, X. Luo, J.-C. Wang, Z. Xiong, M. J. Kushner and Y. Gianchandani, "A microdischarge-based monolithic pressure sensor", to be published in *J. Microelectromech. Syst.*
- [13] Y. B. Gianchandani, S. A. Wright, C. K. Eun, C. G. Wilson and B. Mitra, *Anal. Bioanal. Chem.* **395**, 559 (2009).
- [14] S. A. Wright and Y. B. gianchandani, *J. Microelectromech. Syst.* **18**, 736 (2009).

- [15] S. A. Wright, H. Z. Harvey and Y. B. Gianchandani, *J. Microelectromech. Syst.* **22**, 80 (2013).
- [16] M. J. Kushner, *J. Phys D: Appl. Phys.* **38**, 1633 (2005).
- [17] C. G. Wilson, Y. B. Gianchandani, R. R. Arslanbekov, V. Kolobov, and A. E. Wendt, *J. Appl. Phys.* **94**, 2845 (2003).
- [18] Z. Xiong, E. Robert, V. Sarron, J.-M. Povesle and M. J. Kushner, *J. Phys. D: Appl. Phys.* **45**, 275201 (2012).
- [19] J-C. Wang, N. Leoni, H. Birecki, O. Gila and M. J. Kushner, *J. Appl. Phys.* **113**, 033301 (2013).
- [20] A. N. Bhoj and M. J. Kushner, *J. Phys. D: Appl. Phys.* **37**, 2510 (2004).

CHAPTER 8 SUMMARY AND FUTURE WORK

Atmospheric pressure microdischarge-based technologies have been widely developed for industrial applications. This thesis focused on the plasma dynamics and plasma-surface interaction in devices of interest such as print head in iconography, corona discharges and charge rollers in electrophotography, and microdischarge-based pressure sensors. By using a 2-D multi-fluid simulation platform, *nonPDPSIM*, I can improve the fundamental understanding of nonlinear plasma behaviors and provide design rules to optimize the performance of devices. Summary and future works of each chapter are discussed in Sec. 8.1. This is followed by the list of publications in Sec. 8.2.

8.1 Summary and Future Work

8.1.1 Electron current extraction from mDBD arrays

Chapter 3 discussed the investigation of property of micro-DBDs (mDBDs) used as current sources for charging of surfaces. The mDBD with an additional charge extraction electrode is sustained in atmospheric pressure N_2 with a small O_2 impurity and driven with radio frequency (rf) waveforms of up to 25 MHz. Following the avalanche in the mDBD cavity, the plasmas can be produced and extracted into a plume that is collected by the dc-biased extraction electrode. It was found that the charge collection can be controlled by a choice of driving voltages, frequency, dielectric constant, and extraction voltage. If operated with a low rf frequency (a few MHz), the current is highly modulated due to successive charging and discharging of the intervening

dielectric. The extraction of current depletes the plasma in the mDBD cavity to the extent that the plasma needs to be reignited each rf cycle. The reignition is in part facilitated by photoemission from the inside surface of the cavity. Chapter 4 summarized the plasma dynamics of a small array of independently controlled mDBDs sustained in 1 atm N₂/O₂ mixtures and the interaction between the current extracted from the mDBD array and the dielectric target. After the electrons are extracted onto the dielectric surface, the negatively charged surface starts to deflect the incoming electron plumes. This dielectric effect can be mitigated by increasing the dielectric constant of the target surface. The adjacency of the mDBDs apertures and the positive ions accumulated in the gap also help shape the plume and extract charges by increasing the average extraction field. It was found that the oxygen fraction is an important factor. With increasing oxygen content, electron attachment process begins to dominate and electron current extraction is reduced by negative ion charges accumulated in the gap. The surface potential profiles can be independently controlled by a choice of spacing between mDBD and applied voltage waveform on mDBD array.

The work of current extraction from independently controlled mDBD array discussed in Chapter 3 and Chapter 4 arose from the need to produce a large current with high resolution. High current extraction is desirable in a print head for high-speed printing and the high resolution is required, but limited by extracted current beam size and blooming (dielectric effect) on the dielectric surface. However, the devices modeled in these studies are simplified, and the target surface is stationary. To more accurately simulate the system, future works and recommendations are listed as follows:

- In real printing applications, the target surface is moving. Therefore, the main focus of future work should be on plasma dynamics and its interaction with a moving surface.

- In a real printer, the air flows with moving surface. The airflow should also be taken into consideration using time-slicing techniques.
- It was proposed that increasing the extraction voltage and gas pressure, while keeping the ratio of E/N constant, can reduce the size of electron beam. This approach should also be addressed in future research.
- In the simulation, the voltages applied to both screen electrode and discharge electrode remains constant. In reality, the potential on both electrodes varies with the electron current extraction due to the voltage drop across the ballast resistors connected to the electrodes. It should also be taken into account.
- It was found in the experiments that the bottom dielectric was burned and melted, and this damage of the material can be attributed to the gas heating or ion bombardment. However, the temperature of gas, ion and material are held constant during the simulation, and the heat transfer is not calculated. In the future work, these issues should be addressed.

8.1.2 Corona discharge and conductive charge roller

Chapter 5 discussed an investigation of idealized corona discharge sustained in atmospheric pressure air used in electrophotographic (EP) printing technologies to charge the underlying dielectric photoconductors (PC) surface. After an electric discharge is produced around the corona wire, electrons drift toward and negatively charge the dielectric surface. The surface charging traps the electric potential lines into the dielectric and reduces the voltage drop across the gap between the corona wire and the dielectric surface. On a stationary dielectric, the discharge is terminated when surface charging reduces the electric field. In real printing applications, this underlying surface is in motion. The moving dielectric translates away the surface charging from

the corona wire. The incoming uncharged surface then restores the electric field in the vicinity of the corona wire, which in turn reignites the discharge. This charging process repeats to form an oscillatory charging pattern on the moving surface. Chapter 6 discussed the properties of atmospheric pressure microplasmas in a narrowing gap between a dc-biased charge roller (CR) and photoconductor (PC). After the microdischarges are produced in the gap, electrons drift downward and negatively charge the underlying PC surface, which then remove the voltage drop across the gap if operated with a dc or quasi-dc voltage on the CR. In real printing applications, both the CR and PC are rotating. The rotating PC surface brings in an uncharged surface, which produces a rebound in the voltage drop and reignites the plasma. With a higher applied voltage and a rapidly moving surface, an oscillatory charging pattern is formed by self-pulsing microdischarges.

Charging of a moving surface by corona discharges and charge rollers were discussed in Chapters 5 and 6. To improve the performance, future works and recommendations are listed as follows:

- The speed of a moving surface used in the model is as high as a few km/s. However, in a real printer, the underlying dielectric surface moves at a speed of hundreds of cm/s – the residence time of the moving surface may be a few hundred microseconds. Therefore, the simulation results might not be able to accurately reflect the real plasma dynamics and surface charging mechanism. However, it is difficult to address the surface moving at its actual speed, while also simulating plasma processes with many picosecond time steps in the current model. To address this issue, focus of future work should be on the development of new numerical schemes, better approximation method or parallelization of the code to accelerate the simulation.

- In real printing applications, the corona wire and the conductive charge roller are biased with a few kV dc plus ac voltages to optimize the performance, and the charge roller consists of layers of different dielectric properties. In the future work, an extensive parametric study should be carried out.
- Airflow and heat transfer should also be taken into consideration.
- When the PC surface is in motion, the surface charging is translated toward the CR. As the charging surface is in contact with the conductive CR, the interaction between the surface charges and CR is still unknown. This issue should be discussed in the future.

8.1.3 Microdischarge-based pressure sensor

Chapter 7 discussed the investigation of the behavior of plasmas in the microdischarge-based pressure sensor and current collection. Following the electron avalanche in the geometrically enhanced electric field at the edge of the anode in this sensor, a conductive microdischarge is initiated between an anode (A) and two competing cathodes (a reference cathode, K_1 , is adjacent to the anode, and a sensing cathode, K_2 , is attached on the flexible diaphragm) within tens of nanoseconds. As the external pressure deflects the diaphragm and changes the inter-electrode spacing, the current collected by the two competing cathodes are redistributed. It was found that a periodic bullet-like ionization wave (IW) is generated in the chamber, which produces a pulse-modulated dc current collected on K_1 and K_2 . The current shape can also be optimized by adjusting the impedance connected to electrodes.

The model geometry used in this chapter is idealized, recommendation for future works are listed as follows:

- In the experiments, parasitic capacitors provide an additional voltage source which is not included in the model. The largest gap size (the gap before the diaphragm was deformed) used for simulation is 10 μm , while a 30 μm gap is used in the experiments. As a result, the current collection as a function of time in the simulation is not quantitatively consistent with experiment data. In the future, the parasitic capacitors should be taken into account.
- The gas heating and airflow in the device are not considered in the current model. In the future work, heat transfer, airflow, and temperature effect should be discussed.
- The differential current is not monotonically proportional to the deflection of the diaphragm due to the nonlinear characteristics and the phase difference between currents collected on two cathodes. In the new design of microdischarge pressure sensor, a two-anode device might be a better choice.

8.2 Publications

Research presented in this thesis has resulted in the following peer-reviewed journal articles, patents, conference proceedings, and presentations.

Referred Journal Articles

- [1] J.-C. Wang, Z. Xiong, C. Eun, X. Luo, Y. Gianchandani and M. J. Kushner, “Simulation of Microplasma based pressure sensors”, in preparation.
- [2] J.-C. Wang, S. Chang, N. Leoni, H. Birecki, M. Lee, T. Anthony, O. Gila and M. J. Kushner, “Atmospheric pressure microdischarges produced by conductive charge rollers”, in preparation.
- [3] J.-C. Wang, D. Zhang, N. Leoni, H. Birecki, O. Gila and M. J. Kushner, “Charging of moving

surfaces by corona discharges sustained in air”, submitted to J. Appl. Phys.

- [4] C. K. Eun, X. Luo, J.-C. Wang, Z. Xiong, M. J. Kushner and Y. Gianchandani, “A microdischarge-based monolithic pressure sensor”, accepted by J. Microelectromech. Syst.
- [5] J.-C. Wang, N. Leoni, H. Birecki, O. Gila and M. J. Kushner, “Characteristics of a radio-frequency micro-dielectric barrier discharge array”, *Plasma Sources Sci. Technol.* **22**, 025015 (2013).
- [6] J.-C. Wang, N. Leoni, H. Birecki, O. Gila and M. J. Kushner, “Electron current extraction from radio frequency excited micro-dielectric barrier discharges”, *J. Appl. Phys.* **113**, 033301 (2013).
- [7] J.-C. Wang, N. Leoni, H. Birecki, O. Gila and M. J. Kushner, “Electron current from an rf microdielectric barrier discharge”, *IEEE Trans. Plasma Sci.* **39**, 2168 (2011).

Patents:

- [1] Y. Gianchandani, C. Eun, X. Luo, M. J. Kushner, Z. Xiong, J. C. Wang, 2013, “Microdischarge-based transducer”. U.S. Patent Application 61/837,514, filed June 20, 2013. Patent Pending.

Conference Proceedings and Presentations:

- [1] J.-C. Wang, S. Chang, N. Leoni, H. Birecki, M. Lee, T. Anthony, O. Gila and M. J. Kushner, “The charging of photoconductors in print engines by microplasmas”, 8th APSPT, Hsinchu, Taiwan, 2013.
- [2] J.-C. Wang, X. Luo, Y. Gianchandani and M. J. Kushner, “Plasma dynamics in micro-discharge based pressure sensor”, AEC All Projects Review, Houston, TX, USA, 2013.

- [3] J.-C. Wang, Z. Xiong, C. Eun, X. Luo, Y. Gianchandani and M. J. Kushner, “Simulation of microdischarge-based pressure sensor”, 13th Engineering Graduate Symposium (EGS), Ann Arbor, MI, USA, 2013.
- [4] J.-C. Wang, Z. Xiong, C. Eun, X. Luo, Y. Gianchandani and M. J. Kushner, “Simulation of microdischarge-based pressure sensor”, LNF Users Symposium, Ann Arbor, MI, USA, 2013.
- [5] J.-C. Wang, Z. Xiong, C. Eun, X. Luo, Y. Gianchandani and M. J. Kushner, “Simulation of microplasma based pressure sensors”, AVS 60th International Symposium & Exhibition, Long Beach, CA, USA, 2013.
- [6] J.-C. Wang, Z. Xiong, C. Eun, X. Luo, Y. Gianchandani and M. J. Kushner, “A microdischarge based pressure sensor”, 4th Annual MIPSE Graduate Student Symposium, Ann Arbor, MI, USA, 2013.
- [7] J.-C. Wang, S. Chang, N. Leoni, H. Birecki, M. Lee, T. Anthony, O. Gila and M. J. Kushner, “Atmospheric pressure microdischarges produced by charge rollers”, Hewlett Packard Labs, Palo Alto, CA, USA, 2013. (Invited Talk)
- [8] J.-C. Wang, S. Chang, N. Leoni, H. Birecki, M. Lee, T. Anthony, O. Gila and M. J. Kushner, “Glow-like atmospheric pressure micro-discharges produced by charge rollers”, 40th IEEE International Conference on Plasma Science (ICOPS), San Francisco, CA, USA, 2013.
- [9] J.-C. Wang, N. Leoni, H. Birecki, O. Gila and M. J. Kushner, “Micro-plasma discharges from charge rollers in print engines”, 65th Gaseous Electronics Conference (GEC), Austin, TX, 2012.
- [10] J.-C. Wang, S. Chang, M. Lee, T. Anthony, N. Leoni, H. Birecki, O. Gila and M. J. Kushner, “The role of micro-plasmas from charge rollers in print engines”, 3rd Annual MIPSE Graduate Student Symposium, East Lansing, MI, USA, 2012.

- [11] J.-C. Wang, N. Leoni, H. Birecki, O. Gila and M. J. Kushner, “Plasma dynamics and charging characteristics of a single nozzle ion head”, NIP 28 and Digital Fabrication 2012, Quebec City, Canada, 2012.
- [12] J.-C. Wang, N. Leoni, H. Birecki, O. Gila and M. J. Kushner, “Charging of surfaces with a wire corona discharge: simulations of plasma hydrodynamics with moving surfaces”, NIP 28 and Digital Fabrication 2012, Quebec City, Canada, 2012.
- [13] J.-C. Wang, M. J. Kushner, N. Leoni, H. Birecki and O. Gila, “Computer simulation of the charging process of rollers in print engines with atmospheric pressure plasmas”, Gordon Research Conference on Plasma Processing Science (GRC), Smithfield, Rhode Island, 2012.
- [14] J.-C. Wang, N. Leoni, H. Birecki, O. Gila and M. J. Kushner, “Characteristics of arrays of independently controlled rf micro-dielectric barrier discharges“, 64th Gaseous Electronics Conf. (GEC), Salt Lake City, UT, 2011.
- [15] J.-C. Wang, M. J. Kushner, N. Leoni, H. Birecki and O. Gila, “Numerical simulations of dielectric barrier discharges in a high resolution ion print head”, 27th Intl. Conf. on Digital Printing Technologies, Minneapolis, MN, 2011.
- [16] J.-C. Wang, N. Leoni, H. Birecki, O. Gila and M. J. Kushner, “Electron current extraction and interaction of rf mdbd arrays”, 2nd Annual MIPSE Graduate Student Symposium, Ann Arbor, MI, USA, 2011.
- [17] J.-C. Wang, N. Leoni, H. Birecki, O. Gila and M. J. Kushner, “Interaction of multiple rf micro-dielectric barrier discharges”, 20th International Symposium on Plasma Chemistry (ISPC), Philadelphia, PA, USA, 2011.

- [18] J.-C. Wang, N. Leoni, H. Birecki, O. Gila and M. J. Kushner, “Independently controlled rf micro-dielectric barrier discharge arrays”, 38th IEEE International Conference on Plasma Science (ICOPS), Chicago, Illinois, USA, 2011.
- [19] J.-C. Wang, N. Leoni, H. Birecki, O. Gila and M. J. Kushner, “Arrays of independently controlled rf excited micro-dielectric barrier discharges”, 6th International Workshop on Microplasmas (IWM), Paris, France, 2011.
- [20] J.-C. Wang, N. Leoni, H. Birecki, O. Gila and M. J. Kushner, “Electron current extraction from rf micro-dielectric barrier discharges”, 57th American Vacuum Society International Symposium (AVS), Albuquerque, NM, USA, 2010.
- [21] J.-C. Wang, N. Leoni, H. Birecki, O. Gila, E. G. Hanson and M. J. Kushner, “Electron current extraction from rf micro-dielectric barrier discharges”, 1st Annual MIPSE Graduate Student Symposium, Ann Arbor, MI, USA, 2010.
- [22] J.-C. Wang, N. Leoni, O. Gila and M. J. Kushner, “Extraction of electron current from micro-dielectric barrier discharges”, Gordon-Kenan Research Seminar on Plasma Processing Science (GKRS), New London, NH, USA, 2010. (Invited Talk)
- [23] J.-C. Wang, N. Leoni, H. Birecki, O. Gila, E. Hanson and M. J. Kushner, “Modeling of micro-dielectric barrier discharges”, 37th IEEE International Conference on Plasma Science (ICOPS), Norfolk, VA, USA, 2010.
- [24] J.-C. Wang, N. Leoni, O. Gila and M. J. Kushner, “rf excited micro-dielectric barrier discharges with electron current extraction”, Plasma Science Center (PSC) 1st Annual Meeting, Ann Arbor, MI, USA, 2010.

APPENDIX: AUTHOR'S BIOGRAPHY

Jun-Chieh Wang was born in Taipei, Taiwan, in 1981. He received his B.S (2003) and M.S (2005) in Physics from National Cheng Kung University (NCKU), Tainan, Taiwan. After graduation, he worked for the Plasma and Space Science Center (PSSC) and Department of Physics at NCKU, where his research focused on theoretical and computational plasma physics in the areas of fusion plasma and ionosphere plasma phenomenon. Jun-Chieh Wang joined the Department of Electrical Engineering and Computer Science at the University of Michigan in 2009 to pursue graduate studies. Under the guidance of Professor Mark Kushner, his research has focused on modeling of atmospheric pressure low-temperature plasmas with applications to microdischarges in printing technologies and pressure sensors. His graduate work has resulted in 4 peer-reviewed journal publications, 1 pending patent application, and 24 conference proceedings or presentations. Jun-Chieh Wang also received the best paper award at the 8th Asian-Pacific International Symposium on the Basics and Applications of Plasma Technologies (APSPT) in 2013. Upon graduating with a Ph.D. from the University of Michigan in July 2014, Jun-Chieh Wang will be working as an electrical engineer with Applied Materials, Inc. in Santa Clara, California.